CRANFIELD UNIVERSITY

Mahrukh Mahrukh

# COMPUTATIONAL MODELLING OF THERMAL SPRAYING PROCESSES

SCHOOL OF ENERGY, ENVIRONMENT AND AGRIFOOD

Full-Time PhD Student

PhD
Academic Year: 2013-2016

Supervisors: Prof Sai Gu and Dr Ilai Sher
March 2016

CRANFIELD UNIVERSITY

SCHOOL OF ENERGY, ENVIRONMENT AND AGRIFOOD

Full-Time PhD Student

PhD

Academic Year 2013 - 2016

Mahrukh Mahrukh

# COMPUTATIONAL MODELLING OF THERMAL SPRAYING PROCESSES

Supervisors: Prof Sai Gu and Dr Ilai Sher
March 2016

This thesis is submitted in partial fulfilment of the requirements for the degree of PhD

# ABSTRACT

The main aim of this project is to model the effects of varied injection parameters on the gas dynamics and droplet dynamics of the HVSFS and SP-HVOFS processes for improving the droplet breakup and evaporation to enhance the nanoparticles heating and deposition efficiency. Thermal spraying processes are widely used to generate thermal-, corrosion-, and wear-resistant layers over the machine parts, to increase the durability of the equipment under severe environmental conditions. The liquid feedstock is used to achieve nanostructured coatings. It is used either in the form of a suspension or a solution precursor. The suspension is a mixture of solid nanoparticles suspended in a liquid medium consisting, for instance, of water, ethanol, or isopropanol. This dispersion mechanism in a liquid carrier provides adequate flowability to the nanoparticles, which cannot be handled by conventional gas-based feeding systems, whereas the solution precursor is mixed at the molecular level; hence, more uniform phase composition and properties are expected in the sprayed coatings as compared to the suspension and conventional powder spraying.

Firstly, experiments are conducted to analyse the effects of different precursor concentrations, solvent types and injection nozzles on the size and morphology of synthesized nanoparticles. The results indicate that the particle size increased with increasing precursor concentration due to the variations in the physical properties of the mixture solution. The higher precursor concentrations had an adverse effect on the droplet atomization and evaporation process that led to bigger size particle formation. The use of aqueous solvent has some limits and with higher precursor concentration the surface tension increases that resulted in the reduction of droplets' disintegration, and thus bigger size precursor droplets generate larger nanoparticles. A mixture of aqueous-organic solvents and pure organic precursors are preferred to improve the process efficiency of the nanoparticles size and morphology. Furthermore, the nanoparticles size can be controlled by using liquid feedstock atomization before injecting into the HVOF torch. A new effervescent injection nozzle is

designed and compared to different types of existing injection nozzles, to see the variations in the droplet disintegration, and its effects on the performance of the HVOF torch processes. It is detected that the atomization would result in smaller size particles with homogeneous morphology. In a numerical study, different droplet injection types are analysed to see their effects on the gas and droplet dynamics inside the HVOF torch. The group-type injection (GTI) and effervescent-type atomization (ETI) are used effectively to overcome the heat losses and delays in the droplet evaporation. These approaches reduce the thermal and kinetic energy losses in the suspension-fed-HVOF torch, thereby improving the coating formation.

The effects of using multicomponent water-ethanol mixture injection in the HVOF torch are also modelled, and its impact on the droplet breakup and evaporation are studied. The organic solvents have a low heat of vaporization and surface tension, and can effectively be used in the HVOF spraying process over the water-based solvents. Furthermore, nanoparticles are suspended in the liquid feedstock and injected into the HVOF torch. The effect of increasing nanoparticles' concentration in the feedstock and its consequence on the gas dynamics, droplet breakup and evaporation are analysed. The augmentation in the nanoparticles loading in the suspension droplets can decrease the droplet breakup and evaporation rate because the required heat of vaporization increases significantly. Moreover, the size of injection droplet affects the droplet fragmentation process; bigger sized droplets observed a delay in their evaporation that resulted in coating porosity. The results suggest that smaller droplet sizes are preferred in coating applications involving a higher concentration of nanoparticles with high melting point.

Further, the gas flow rates (GFRs) are regulated to control the droplet dispersion, atomization and evaporation inside the solution precursor fed-HVOF torch. The size of the droplet diameter is decreased by an increment in the GFR, as higher combustion rates increase the combustion flame enthalpy and kinetic energy. Moreover, the increase in the oxygen/fuel flow rates dilutes the injected precursor. It reduces $ZrO_2$ concentration in the process and decreases

the rate of particle collision; as a result, non-agglomerated nanoparticles can be obtained.


## KEYWORDS

High-velocity oxygen fuel spraying process; Suspension; Solution precursor; Multicomponent droplets; Effervescent atomization; Nanoparticles

# ACKNOWLEDGEMENTS

All thanks to Allah Almighty for giving me the strength to start and complete my PhD work.

I would like to thank my supervisors Prof. Sai Gu and Dr Ilai Sher, Co-supervisors Dr Spyros Kamnis and Dr Hosein Torabmostaedi for guiding me in accomplishing the task.

I would also like to thank my husband Mohammad Ali for his endless support and patience. I am grateful to my friends and family for encouraging me towards success.

I would like to acknowledge both the financial assistance of a research studentship from the NED University of Engineering & Technology Karachi (Pakistan) and the financial support of the UK Engineering and Physical Sciences Research Council (EPSRC) project grant: EP/K027530/1.

I would like to acknowledge the experimental work performed in the Xian Jiaotong University of China under the guidance of Prof. Chang-Jiu Li and Dr Shan-Lin Zhang. This work is funded by “European Seventh Framework programme-Marie Curie Actions-People International Research Staff Exchange Scheme”, under project grant-268696.

# TABLE OF CONTENTS

# LIST OF FIGURES

# LIST OF TABLES

# LIST OF EQUATIONS

# LIST OF ABBREVIATIONS

| | |
|---|---|
| ALR | Air-to-Liquid mas flow rate Ratio |
| APS | Air Plasma Spraying |
| CC | Combustion Chamber |
| C-D | Convergent-Divergent |
| CFD | Computational Fluid Dynamics |
| DJ | Diamond Jet |
| DPM | Discrete Phase Model |
| EB-PVD | Electron Beam Physical Vapour Deposited |
| EDM | Eddy Dissipation Model |
| ETI | Effervescent-Type Injection |
| GFR | Gas Flow Rates |
| GLR | Gas-to-Liquid mass flow rate Ratio |
| GTI | Group-Type Injection |
| HVOF | High-Velocity Oxygen Fuel |
| HVSFS | High-Velocity Suspension Flame Spraying |
| LFR | Liquid Flow Rate |
| LISA | Linearized Instability Sheet Atomization |
| O/F | Oxygen/Fuel |
| Oh | Ohnesorge number |
| P-E | Pure Ethanol |
| P-W | Pure Water |
| SEM | Scanning Electron Microscope |
| SMD | Sauter Mean Diameter |
| SP-HVOFS | Solution Precursor High-Velocity Oxygen Fuel Spraying |
| SPS | Suspension Plasma Spraying |
| SPPS | Solution Precursor Plasma Spraying |
| SPTS | Solution Precursor Thermal Spraying Process |
| SST | Shear Stress Transport |
| STI | Surface-Type Injection |
| TAB | Taylor Analogy Breakup |
| TBC | Thermal Barrier Coating |
| TEM | Transmission Electron Microscopy |
| $TiO_2$ | Titanium dioxide (Titania) |
| W-E | Water-Ethanol |
| We | Weber number |
| YSZ | Yttria Stabilized Zirconia |
| ZnP | Zirconium n-Propoxide |
| ZrN | Zirconium Nitrate |
| $ZrO_2$ | Zirconium dioxide (Zirconia) |

# 1 BACKGROUND AND APPLICATIONS

## 1.1 Introduction

The process of thermal spraying is used for coating purposes by means of spraying melted, semi-melted, and heated material onto a prepared surface. It has been utilized in a broad range of applications for coating machine parts under severe environmental conditions. The thermal spray process is used for the formation of wear, corrosion, and thermal resistant layers on machine parts for increasing the durability of the equipment [1], [2]. The major advantages of these coating techniques are the usage of diverse ceramic and metallic materials [3]–[6]. There are varieties of coating materials available for thermal spraying, including metals, metal alloys, ceramics, plastic, and composites. Thermal sprayed coatings are aimed at resisting wear by friction, resistance to erosion-corrosion, and to increase parts fatigue and creep resistant ability, whereas, the Thermal Barrier Coating (TBC) has low thermal conductivity, high melting point and better resistance to corrosion and oxidation at elevated temperatures [7]–[9].

High Velocity Oxygen Fuel (HVOF) thermal spraying and plasma jet spraying are the most widely used methods for generating coatings. HVOF heats the feedstock with the help of combustion flame while plasma spraying uses high-temperature electrical arcs for heating the coating material. The selection of the coating process is based on the application requirements. Recently the use of nanoparticles has been made possible to increase the strength of coatings. Lima and Marple [1] showed that reduction in grain sizes from conventional micrometre levels to nanostructured levels can significantly enhance the mechanical strength of materials. In the conventional thermal spraying processes, the use of powder feedstock limits the size of injected particles, whereas the liquid precursor thermal spraying breaks this size limit, giving much better results over conventional powder spraying. Researchers have experimentally and numerically examined the flow behaviour of liquid feedstock on gas dynamics and particle dynamics during thermal spraying processes [10]–[18].

The HVOF process efficiency mainly depends on the type of torch, coating material, nanoparticles injection parameters, type of liquid used for suspension or solution preparation, and the distance between the torch and the substrate. For increasing the effectiveness of this process, the optimization of these parameters is essential. The flow physics inside the HVOF torch cannot be studied experimentally. The Computational Fluid Dynamics (CFD) techniques are widely used to understand the phenomenon of thermal spraying inside the torch. Various models are implemented to understand the complex flow physics, combustion chemistry, flames and jets formation, and propagation involved in the thermal spraying processes [19]–[29].

Research is also underway on the development of numerical models and techniques for simulating suspension and solution precursor thermal spraying including plasma and HVOF spray techniques [10], [30]–[39]. A significant amount of work is required to understand and model the complex mechanism of injecting liquid feedstock and its coupling with the hot flame and jet. Different modelling steps are involved in the liquid feedstock spraying, droplet breakup, evaporation and droplet interaction with hot flames and combustion gas. Analysis can be undertaken by generating a multi-scale model. A review of the most recent work in this area is illustrated in Chapter 2, to better understand the flow physics and modelling procedures.

## 1.2 Aims

The purpose of the current project is to carry out the research and development related to the suspension and the solution precursor HVOF thermal spraying. The present work is dedicated to model the High Velocity Suspension Flame Spraying (HVSFS) and the Solution Precursor High Velocity Oxygen fuel Spraying (SP-HVOFS) processes using CFD techniques.

The main aim of this project is:

- To model the effects of varied injection parameters on the gas dynamics and droplet dynamics of the HVSFS and SP-HVOFS processes for improving the droplet breakup and evaporation to enhance the nanoparticles heating and deposition efficiency.

The work has been initiated by developing a CFD model that captures the effect of suspended nanoparticles on the gas dynamics and suspension's droplet dynamics inside HVOF thermal spraying processes. The current modelling setup analysed the impact of different injection parameters on droplet breakup and evaporation, and on the gas dynamics inside the HVOF torch. The study of this phenomenon is not possible experimentally, as the flow is confined within the combustion chamber (CC) and the barrel sections of the HVOF torch, which cannot be seen and analysed experimentally.

## 1.3 Objectives

The following studies are performed and considered as the goals of the current project to understand the flow physics inside the HVOF torch systems using the suspension and solution precursor injection:

- Experimentally analyse the difference in the nanoparticles size and morphology using various solute concentrations, solvent types, and injection nozzle types.
- Model and validate droplet atomization by a new effervescent-type nozzle and also modelling the effervescent atomization inside the HVOF torch.
- Model the multicomponent droplet injection in the HVSFS torch, for the purpose of studying its effect on the process flow dynamics.
- Model aerodynamic breakup and evaporation of suspension droplets carrying suspended nanoparticles in the HVSFS torch.
- Model the effect of increasing gas flow rates (GFR) inside the SP-HVOF thermal spraying torch.

These study cases have been set up, and the results are analysed to understand the steps included in combustion gas dynamics, droplets breakup and evaporation in the HVSFS and the SP-HVOFS processes.

## 1.4 Methodology

***Experimental***

- A new effervescent nozzle is designed for the atomization of liquid feedstock injection inside the HVOF torch.
- The experiments are performed using the new effervescent nozzle for the solution precursor injection inside the CH-2000 HVOF torch, (HVOF torch and all injection nozzles are designed and made in Xi'an Jiaotong University, China).
- The experiments are performed using three different injection nozzles: (i) plain-orifice; (ii) angular injection; (iii) effervescent atomization. The effects of varied nozzle types on the nanoparticles morphology and size distribution are analysed.
- The effects of different solvent types over nanoparticles formation are investigated by using different types of solvent in the solution precursor including (i) pure water (P-W); (ii) pure ethanol (P-E); (iii) water-ethanol mixture (W-E).
- The effects of three different solution concentrations are also considered (i) 0.05M, (ii) 0.075M and (iii) 0.1M.

***Numerical***

- The second main approach to problem solving is numerical, and different **Fluent** models (Ansys Inc. 14.5.0) are used to capture the flow physics inside the HVOF torch including Diamond Jet (DJ) DJ2700 torch (Sulzer/ Oerlikon Metco, Switzerland) and CH-2000 torch.
- The turbulence models used in this study are the Realizable $k-\varepsilon$ and the Shear Stress Transport (SST) $k-\omega$ models.
- The simulation of combustion dynamics is performed using Eddy Dissipation Model (EDM) from **Fluent**.
- The modelling of the suspension or solution precursor droplet injection, aerodynamic breakup, heating and vaporization is performed using the discrete phase modelling (DPM) from **Fluent**.

- The Linearized Instability Sheet Atomization (LISA) model is utilized to model the effervescent atomization and a Taylor Analogy Breakup (TAB) model is used to capture secondary breakup of droplets.

## 1.5 Thesis Outline

The aim and objectives of the present research work are highlighted in Chapter 1. Chapter 2 includes the in-depth literature review to understand the modelling required for the HVSFS and SP-HVOFS processes. In Chapter 3, all modelling equations are included that are used to simulate the gas combustion, droplet interaction, breakup and evaporation inside the HVOF torch. The numerical solver **Fluent** code is used for all the modelling. In Chapter 4, experiments are conducted to see the improvement in the droplets atomization and nanoparticles coating generation using the new atomization nozzle. Moreover, its results are also compared to without atomization injection nozzles. The new effervescent-type injection (ETI) nozzle is used to improve the performance of the HVOF torch and nanoparticles deposition. In Chapter 5, the modelling of the ETI nozzle is performed to analyse the variations in droplet sizes using varied injection parameters.

Chapter 6 presents a model to capture the multicomponent droplet breakup and vaporization mechanism inside the HVSFS torch using different mass fractions of water and ethanol. In Chapter 7, a model is developed to analyse the effects of increasing solid nanoparticles concentration in the liquid feedstock and its impact on the gas dynamics and droplet dynamics in the HVSFS process. In Chapter 8, the effects of three different injections types on the flow physics of HVSFS process are analysed. In Chapter 9, simulations are performed to see the impact of increasing GFRs over the gas and droplet dynamics inside the SP-HVOFS torch. In Chapter 10, the overall research outcomes are summarised.

## 1.6 Limitations

The present research comprises the numerical approach to understand the droplet atomization, breakup, and evaporation mechanism inside the HVOF torch using liquid feedstock injections. Also, the effect of using different injection

types (with/without atomization) and various injection parameters including mass flow rates, pressure, and droplet size over the final nanostructured coatings are further analysed, giving some useful insights regarding the liquid feedstock thermal spraying process. However, there are two major limitations:

1. Suspension flame spraying is a complex process involving flame combustion, droplet evaporation and fragmentation, along with the nanoparticles release and heat transfer between nanoparticles and the surrounding hot gas. Such modelling work is very challenging, and in present work no experimental and modelling comparison from the published literature is presented to validate the present modelling.

The reason for this limitation is that it is difficult to compare the in-flight behaviour of suspension droplets in the HVOF torch by experiments, as the HVOF internal flow physics is impossible to analyse experimentally, and this is one of the reasons that researchers used pure modelling work for clear understanding of the process [10], [14], [18]. Also, comparison of the present modelling work is not possible as this is a novel study that analysed the effect of suspended nanoparticles using nanofluids theoretical models on the liquid droplets' breakup and evaporation inside the HVOF torch; no research has presented this kind of work.

2. The detail analysis of steps including in the salt decomposition, species chemical reaction/oxidation and seed particle nucleation/growth are out of scope of this work. Moreover, the present work does not cover the solid particles' in-flight behaviour inside the HVOF torch; it is purely based on the suspension or solution precursor droplets' behaviour inside the HVOF torch. Thus, the effects of varying concentration on the nanoparticle characteristics velocity and temperature are not included.

The study of chemical reaction and nucleation is out of scope of this work and only focus is given towards the solution precursor's droplets disintegration and evaporation inside the HVOF torch. Also, present study only deals with the effect of suspended nanoparticles on the liquid feedstock behaviour in the HVOF process. The study ignored the actual presence of nanoparticles

throughout the process simulation and was restricted to the analysis of the suspension droplets disintegration and evaporation processes.

On the basis of droplet dynamics in the HVOF torch, it is concluded that poor disintegration and incomplete evaporation of suspension would result in poor heating and partial melting of the suspended nanoparticles that would, in turn, create defects in the final coatings [11], [12].

## 1.7 Publications

1. Mahrukh, M., Sher, I., and Gu, S. Numerical Analysis of an Effervescent Atomization in Solution Precursor Thermal Spraying Process. *ILASS 2016*.
2. Mahrukh, M., Kumar, A., and Gu, S. Effects of Angular Injection, and Effervescent Atomization on High-Velocity Suspension Flame Spray Process, *Surface and Coatings Technology* (Submitted Revision-2, 2016).
3. Mahrukh, M., Kumar, A., Gu, S., and Kamnis, S. Computational development of a novel aerosol synthesis technique for nanostructured Zirconia coating, *Industrial & Engineering Chemistry* (Submitted Revision-1, 2016).
4. Mahrukh, M., Kumar, A., and Gu, S. Experimental Study on using Different Precursor Concentrations, Solvent Types and Injection Types on Zirconia-Based Coating. *Surface and Coatings Technology* (Submitted, 2016).
5. Mahrukh, M., Kumar, A., Gu, S., Kamnis, S., and Gozali, E. Modelling the effects of concentration of solid nanoparticles in liquid feedstock injection on High-Velocity Suspension Flame Spray process, *Industrial & Engineering Chemistry,* (2016) 55: 2556-2573*.* DOI: 10.1021/acs.iecr.5b03956.
6. Gozali, E., Mahrukh, M., Gu, S., and Kamnis, S. Numerical investigation on the effects of nanoparticles on liquid feedstock behaviour in High-Velocity Oxygen Fuel (HVOF) suspension spraying, *Surface and Coatings Technology*, (2015) 280: 370-377. DOI:10.1016/j.surfcoat.2015.09.012
7. Gozali, E., Mahrukh, M., Gu, S., and Kamnis, S. Numerical analysis of multicomponent suspension droplets in High-Velocity Flame Spray process, *Journal of Thermal Spray Technology*, (2014) 23: 940-949. DOI: 10.1007/s11666-014-0106-1.

# 2 LITERATURE REVIEW

## 2.1 Introduction

Many researchers have worked out to model the thermal spray process using CFD techniques. The present project further adds the knowledge of modelling the effects of varied injection parameters over the droplet breakup and evaporation inside the liquid fed-HVOF thermal spraying process. Current advancements in the coating industry are moving towards spraying nanoparticles for dense and thick coating with excellent bonding strength. The use of powder feedstock limits the size of injected particles and the thickness of coating formation, and this limit can be broken by the use of liquid feedstock. Hence, an immense amount of work is performed to analyse the suspension and solution precursor spraying using plasma and HVOF techniques.

For better understanding the flow physics and modelling procedures of the HVOF, HVSFS and SP-HVOFS processes a brief literature review is presented here. A small review section for plasma spraying is included to understand the difference between the two techniques and to compare the HVOF and plasma thermal spraying. Other thermal spraying procedures are not included as they are out of the scope of this research. Furthermore, a small review is added related to the selected material and its utilisation in numerical studies. For the atomization of the suspension and solution precursor in the HVOF flame one more section is added to review different atomization techniques and their modelling.

### 2.1.1 Suspension Plasma Spraying vs. Solution Precursor Plasma Spraying

The development of suspension and solution plasma spraying is briefly addressed in this work as the major topic focuses on the suspension and solution-based HVOF thermal spraying. The need for a discussion of Suspension Plasma Spraying (SPS) and Solution Precursor Plasma Spraying (SPPS) is to compare the spraying processes and coating outcomes. Also, the literature related to suspension and solution HVOF spraying is minimal. It is required to consider the in-depth review of the SPS and SPPS processes to

understand the behaviour of the suspension and solution breakup, evaporation, precipitation, and deposition processes [40].

Many scientists performed experiments and numerical studies related to SPS, and SPPS in [41]–[50]. The major difference between these two processes is defined in the literature. In the SPPS, a homogeneous solution of metal salts in water or organic solvent is produced and used as injection feedstock into the plasma jet; whereas, in SPS the sub-micrometre solid metal or ceramic particles are dispersed in water or organic solvents to form a suspension for injecting it into the plasma jet [51].

The TBC obtained from SPS shows a coating microstructure with medium porosity and high segmentation crack density [47], [50]. Tingaud et al. [52] presented these conclusive points to consider for the efficient output of the SPS process and different references also agree and confirm the following points:

I. A mechanical injector can be used to decrease the plasma jet perturbation during suspension injection as the utilization of an atomizer increases the plasma jet fluctuations and decreases its efficiency [51], [53], [54].
II. The organic solvent evaporates easily, compared to that of the water-based solvents, due to their lower value of the enthalpy of vaporization, and this enables the formation of dense coatings [54]–[57].
III. Suspended nanoparticles size distribution must be controlled, and smaller sized particles produce a denser coating due to better heating and melting of submicron size or nanosized particles [56], [58], [59].
IV. The injection momentum of the suspension streams must be higher than the plasma jet, to penetrate the droplets into the plasma jet core [51], and lower the dispersion of the liquid and confine the droplets into the plasma plume, hence reducing the loss of material.
V. Fluctuations in the plasma arc affect the suspension behaviour inside the plasma jet, and the selection of a mono-atomic gas can reduce these fluctuations [54].
VI. Benefits of the SPS process include the short standoff distance as the generated particles in the plasma plume may cool if the spray distance

increases. By these means the plasma heat has significantly transferred to the substrate and improves the microstructure of the coating [53], [58], [59].

Furthermore, it is found that the particle temperature and velocity are significant parameters to control the microstructure features including micro-cracks, porosities and deposition rate in the SPS process. The particle velocity is controlled by the plasma torch parameters (gas flow rate, gas composition) while the particle temperature is controlled by the feedstock parameters (particle size, feed rate, solid content) [39], [60].

By computational modelling of the time-dependent phenomena of SPS, Vardelle et al. [37], discussed the effect of plasma fluctuations during the injection of the liquid precursor, highlighting that transient analysis of the plasma arc fluctuation and its contact with the injected liquid would be more realistic. Meillot et al. [48] use the volume of fluid model for the injection of P-W into the plasma plume while assuming that the plasma flow is laminar and has no fluctuations. It was illustrated that breakup modes are truly dependent on the Weber number (We) [37], [48]. Meillot et al. [49] also developed a model to compare the drop-wise injection, and continuous injection of Yttria-Stabilized Zirconia (YSZ) suspended particles in the plasma flow and then validated it experimentally. They found that continuous liquid injection made it possible to reach the core of the plasma jet, which eventually allows the complete heating and melting of the ceramic particles. The coating behaviour changes as the injector position and pressure are varied; the optimized value of pressure and the down-drop position of the injector develop better coating thickness and reduce roughness, whereas high injection pressures will decrease the efficiency of plasma spraying. This model only considers the hydrodynamic breakup of the injected liquid, i.e., no considerations are given to the droplet evaporation or heating.

Another study found that the plasma arc fluctuation has an enormous effect on the deviation of liquid droplets [61]. The model illustrates that large droplets (size>10μm) easily penetrate into the plasma jet, and experience less deviating effects during plasma fluctuations than small droplets (size=10μm). They also

confirmed that a particular value of We is required for droplets disintegration [37], [48], [51], [61]. Furthermore, fragmentation is also dependent on the size of the initial droplet, and droplet path that it follows during the spray.

In SPS, extra work is required [58], [62]. This includes the addition of suitable dispersion material for making a stable suspension for controlling particle agglomeration (or settling down) in the reservoir; also, constant stirring is essential to reduce this problem. The addition of different products to the liquid phase is required to adjust the viscosity and/or surface tension of suspension. Moreover, viscosity increases as per increment in the suspended particles that led to the requirement of higher pumping power [42], [50], [58], [62]–[64].

Whereas the solution precursors are stabilized homogeneous solutions, and their viscosity depends on the concentration of the solution, no extra addition of dispersion material or constant stirring is required to stabilize the precursor solution. SPPS allows an excellent chemical homogeneity of coatings [50]. The SPPS is a single-step process, as the precursor droplet evaporation, decomposition, crystallization, and coating formation occurs in one step [51]. Chen et al. [35] experimentally found that the solvents having low surface tension, low boiling and evaporation points will generate dense coating compared to other solvents. Another study [65], analysed that increased solution concentration would enhance the viscosity of solution precursor, but decrease the surface tension. The higher concentrated precursor forms solid particles that are melted and generate dense coating, whereas, the lower concentration led to shell formation resulting in the soft porous coating [65].

The SPPS involved on-site generation of fine particles (50–500nm) and the splats formation of sizes from 200–2000nm and showed nanoporosity and a homogeneous microstructure [66]. The TBC generated by SPPS showed vertical cracks, dense ultrafine splats regions, and uniform dispersed porosity [45]. Bertolissi et al. [43] studied the size of the solution droplets in the SPPS by laser shadowgraph technique. They examined the droplet breakup and solvent evaporation processes using water and ethanol solvents. These processes are more efficient when the ethanol-based solution is injected into plasma gas

mixtures while with the water-based solutions residual liquid droplets were detected over the substrate. It is concluded that residual liquid droplets at the substrate turned into non-pyrolized inclusions and later by plasma heat converted into the porous sponge-like structure [43]. It is highlighted that the amount of non-decomposed or partially pyrolized precursor droplets can be controlled by primarily droplet injection moments density, spray droplets fragmentation, and precursor concentration [42], [45], [46].

Basu et al. modelled the droplet disintegration phenomena [30]. The solution of zirconium acetate dissolved in water is injected axially and transversely into the plasma jet. They stated that droplets fragmentation is divided into three steps: (i) aerodynamic breakup, (ii) heating of droplet up to vaporization, (iii) precipitation and internal droplet pressurization. They suggest that droplets disintegration has an enormous effect on the quality of substrate's coating. Their findings show that small droplets melted properly and led to denser coating while large droplets damage the coating features. So it is important to breakup larger droplets into smaller ones, by reducing surface tension and preferring axial injection. Furthermore, they concluded that small droplets (<5 microns) undergo coating deposition and show less non-pyrolized material over the substrate [30]. The smaller particles reach the substrate as molten splats resulting in denser coatings. The model predicts the surface precipitation of larger droplets (>5microns) will lead to internal pressurization and in situ droplet atomization. Hence, it arrives at the substrate as the non-pyrolized precursor and in the form of broken shells [30], [46]. Moreover, the axial injection of liquid ceramic precursor droplet into a plasma jet was modelled by Basu and Cetegen [32]. The key features of the model are to capture the phenomenon of liquid droplet vaporization and precipitation. They analysed that precipitation of small droplets (10μm and less) started rapidly while the large size droplets such as 20 and 40μm undergo variation in shell thickness, and then droplet destruction occurs due to the increase in the internal pressure.

The SPPS produces unique microstructures, ultrafine splats, nanometres, and micron-sized porosity, and through thickness vertical cracks [44]. It consists of 1–2μm particles that arrive at the coated surface in various stages of conversion

from the aqueous precursor to the fully molten ceramic end product. Efficient heating of the precursor led to dense deposits while increasing amounts of partially pyrolyzed precursor (poorly heated) resulted in greater porosity. The SPPS coating durability tested in the furnace-cycling-tests shows 2.5 times the spallation-life of air plasma coatings (APS) and 1.5 times the life of electron beam physical vapour deposited (EB-PVD) coatings. The conductivity of SPPS coatings is lower than EB-PVD and higher than the best APS coatings [44].

The injection droplet size, velocity, angle, plasma conditions, and mass diffusivity of solute into a solvent can play a significant role in the vaporization, and the solute concentration builds up near the droplet surface [31]. Moreover, the use of atomization for solution precursor injection will further improve the solid particles morphologies hence forming dense coatings [67]. It is further analysed that the disintegration of droplets can increase the efficiency of the thermal spraying process which is achieved by using an atomizer or mechanical injector [67]. Depending on the availability and application requirements, different atomization gases and processes can be used for atomizing the liquid streams. One method is to introduce atomizing-gas by gas envelope around the liquid jet injection. The high-velocity oxygen exerts a force on the liquid jet and atomized liquid streams into fine droplets. The nanoparticles obtained after this type of atomization had a narrow particle size distribution, from 10–20nm [67].

In summary, the need of liquid feedstock is to inject the submicron or nanosize particles into the core of the plasma jet. However, a liquid precursor in the form of suspension requires special treatment before feeding into the plasma jet. On the other hand, solution precursors are effectively used without manufacturing the nanosize particles for making the suspension, and ease the overall process of injection. Nevertheless, the SPS coating layers are free of non-pyrolized material; however SPPS may encounter these problems. The above review of experimental and numerical studies is to understand the behaviour of the suspension and solution precursor under high-temperature plasma jet, and the droplet breakup, evaporation, and injection processes. The plasma jet is not modelled, and experiments related to this technique are not covered in this thesis.

### 2.1.2 High-Velocity Suspension Flame Spraying vs. Solution Precursor High-Velocity Oxygen Fuel Spraying

The fluctuations in the plasma arc have an enormous effect on the deviation of smaller liquid droplets [61] and cannot overcome by increasing the feedstock injection velocity or pressure; whereas, increment in the liquid feedstock injection pressures will decrease the efficiency of plasma spraying [49]. Moreover, the surface precipitation of larger droplets led to the deposition of the non-pyrolized precursor in the form of broken shells over the substrate [30], [46]. However, the benefits of the low-temperature HVOF flame with small flame fluctuations, compared to plasma, resulted in the uniform solute concentration within the droplets, thus promoted solid particles with thick shell morphologies [34]. Moreover, the particle velocities are much higher in the HVOF process; consequently, higher coating densities can be achieved compared to arc spray, air plasma and vacuum plasma spray processes [3].

The development of nanostructured coating requires nanosize powder particles to be injected inside a thermal spray torch; hence, the use of liquid feedstock is the safest and easiest way of feeding these nanoparticles into the torch. Recently this technique has been developed for injecting the liquid feedstock carrying the nanometre size to 10µm sized powder particles in the thermal spraying torch [13], [16], [68]. The suspension-based HVOF spraying (i.e. the HVSFS process), uses a nanosized powder in the form of liquid suspension [13]. For liquid feedstock injection, the HVOF torches are modified, and liquid feedstock is injected with the aid of suspension or solution feeder and injector [68]. Normally, the HVOF applications use axial internal injection systems [42], [63], [69]. The suspension spraying works well for several applications including TBCs, tribofunctional and wear-resistant coatings, biofunctional coatings, fuel cell development, and creating coatings for catalytically active surfaces [68], [70]–[72].

In the HVSFS process, the suspension liquid is injected into the spray flame and under the action of combustion gas thermal energy and high-velocity the suspension precursor droplets disintegrated, evaporated and released the nanoparticles inside the torch. These nanoparticles and nano-agglomerates

heated, melted and accelerated towards a prepared surface hence produce a coating layer on the substrate. The advantage is that the precursor can be nanosized (not possible with standard dry powder feeders) and the coatings can be thin, smooth and finely structured, even nanostructured [73]. Although different coating morphologies can be obtained, the coating microstructural features are governed by the injected feedstock [11], [74].

The HVSFS process has been established by the researcher as being completely melted which resulted in small and well-flattened lamellae (thickness range 100nm to 1µm) [74]. Three kinds of system are used to compare the microstructural features, micromechanical properties, and dry sliding tribological behaviour of $Al_2O_3$ coatings, including atmospheric plasma spray, HVOF and HVSFS. The same GTV TopGun-G torch is used for HVOF and HVSFS systems with different injection schemes. It is observed that fully melted particles are deposited on the substrate with nanoparticles suspension generating dense coating with a small thickness. The coating is tested and exhibits low porosity as compared to atmospheric plasma spray and HVOF coating and shows higher protective layers. Furthermore, the sliding wear resistance of HVSFS coating is much greater than conventional spraying, because the presence of small lamellae and a smaller interlamellar crystal size allows microscale plastic deformability, and forms more stable and protective tribofilms compared to conventional coatings [74].

Numerical analysis of the HVSFS process is investigated by Dongmo et al. [14] using a TopGun-G torch (GTV, Düsseldorf). They model and discuss the HVSFS process in which both liquid ethanol droplets (300µm) and solid Titania ($TiO_2$) particles (0.5–50µm) are injected from the gun inlet as discrete phases. They also modified the injection phenomena by simulating the flow with a 30° angle of injection. The results showed that solid particles and liquid droplets moved with different velocities in the domain due to differences in their properties. The evaporation of ethanol droplets shows significant cooling of the combustion gases at a 0° injection angle while injection at a 30°angle improves the rate of ethanol evaporation inside the CC and cooling is reduced. The disadvantage of angular injection highlighted in this study is the impingement of

droplets and particles on the CC walls and increased residence time of particles in the CC. An optimized HVSFS torch designed was analysed by Dongmo et al. [10] with the help of three-dimensional CFD modelling. They concluded that the modification in the TopGun-G's CC, by giving it a conical shape, increases the process efficiency and contributes to avoiding nanoparticles contact with the CC walls. These studies ignored the effect of nanoparticles loading on properties of P-E and its evaporation process; nor considered the nanoparticles' suspension effects on combustion gas dynamics.

Recently Jadidi et al. [75] also perform the numerical modelling of suspension HVOF spray. The suspension droplets were assumed to be a mixture of solid particles [mullite powder ($3Al_2O_3.2SiO_2$)], ethanol, and ethylene glycol. To simulate the droplet breakup, Taylor Analogy Breakup model is applied. After the completion of droplet breakup, and solvent evaporation/combustion, the solid suspended particles are tracked through the domain to determine the characteristics of the coating particles [75]. This study also ignored the effect of nanoparticles suspension on the droplet fragmentation and evaporation processes, as the nanoparticles are injected into the HVOF torch domain as a separate entity.

The liquid feedstock in the form of a solution precursor is utilized in HVOF spraying to generate dense coatings [34], [76]–[78]. The use of solution precursor over suspension purely depends on the application requirements, although solution precursor offers some key benefits over suspension spraying. Solution precursors are made by dissolving metal salts, organometallic, or liquid metal precursors in a solvent [63]. The solution precursor is mixed at the molecular level. Therefore, more uniform phase composition and properties are expected in the sprayed coatings, compared to suspension spraying and conventional powder spraying [77]. Furthermore, the SP-HVOFS process eliminates the heavy manufacturing of nanosized powders required in the HVSFS process.

The SP-HVOFS method has also been studied by some scientists experimentally and numerically. Solution precursor is used for the coating of an

Inconel alloy layer for generating finely structured and highly bonded coatings. The results show that the coating obtained from SP-HVOFS has better resistance to erosion and thermal shocks, and has good surface quality, adhesion, and ductility over the powdered feedstock system [76]. The coating created by solution precursor spraying is denser, and no cracks are observed [42]. Chen et al. studied the deposition of $Al_2O_3$-$ZrO_2$ ceramic coatings by SP-HVOFS process. Both nanocrystalline $ZrO_2$ and amorphous $\gamma$-$Al_2O_3$ are observed by performing as-sprayed coating characterizations, using X-ray diffraction and transmission electron microscopy (TEM). The coatings consist of ultrafine splats (2–5μm), spherical particles and hollow shell structures, and have high density with a thickness of 40μm [78].

Till today, very few researchers have modelled the SP-HVOFS process. Modelling of this process has proved that droplets injected into the HVOF jet undergo strong shear breakup due to high relative velocities hence producing smaller secondary droplets [33], [34], [78]. Basu and Cetegen [34] modelled the injection of precursor solution droplets into the HVOF flame jet; their model includes analysis of droplet breakup, vaporization, solute precipitation and pressurization in the liquid core surrounded by the solute. They noted that smaller droplets evaporated rapidly and become solid particles upon rapid heating while larger droplets form precipitate shells with the liquid core inside. The coating generated by this approach is denser than conventional processes [34]. As compared to DC plasma, HVOF jet has lower temperatures that allows slower vaporization of the droplets and allows longer times for solute diffusion prior to precipitation. This leads to more uniform solute concentration and promotes solid particle and thick shell morphologies [34].

The studies related to the SP-HVOFS process are few and more research is required. This thesis provides more insight to understand the liquid feedstock behaviour inside HVOF torch systems. The above literature review of the HVSFS and SP-HVOF is undertaken to understand and model the flow process dynamics, and improve the efficiency of these processes by using new injection techniques and varying injection parameters. The modelling techniques are based on the previous research work and the literature reviews for specific

models used in this work are covered in Chapter 3. The literature review related to the SP-HVOFS is specifically highlighted here for performing experiments in Chapter 4 and numerically simulating this process in Chapter 5 & 9. The studies on the HVSFS process are highlighted to understand the flow process dynamics; thus, analyzing the flow details by varying injection parameters. The HVSFS case studies are detailed in Chapters 6, 7, and 8.

### 2.1.3 Coating Material: Titania and Zirconia

The base liquid (solvent) and nanoparticles material (solute or suspended particles) are selected for experimental, and numerical work and suspension and solution precursors are injected into the HVOF thermal spraying torch by injection nozzle (Chapters 4, 5, 6, 7, 8 and 9). The two materials used here are Titania ($TiO_2$) and Zirconia ($ZrO_2$). Firstly, the Zirconium nitrate (ZrN) [$Zr(NO_3)_4.5H_2O$] salt solution in P-W, P-E and a mixture of W-E is used, and experiments are performed to see the effect of varied solvent mixture composition and solute concentration on the final coating morphology (Chapter 4). Secondly, the $TiO_2$ nanoparticles suspended in the P-E solvent are used for the numerical analyses of the HVSFS torch (Chapters 7 and 8). Thirdly, the solution mixture of 0.5M Zirconium n-propoxide (ZnP) 70wt.% in n-propanol diluted with ethanol for the production of $ZrO_2$ nanoparticles' coating is utilized to investigate the droplets disintegration and evaporation in the high GFR operated SP-HVOFS torch (Chapter 9).

$TiO_2$ can be used effectively in gas sensor applications. Also, it is widely used as food pigments, in paints, and cosmetics. Further, it works well for the formation of corrosion resistant coatings. $TiO_2$ is also utilised in the development of heterogeneous catalysis and photocatalysis. It is preferably used in solar cells for the production of hydrogen and electrical energy. $TiO_2$ is a very useful photocatalyst for the decomposition and diminution of environmental water and air pollutants [79]–[83].

$ZrO_2$ is a dense material ($\rho$=6100kg/m$^3$), having a high-temperature of fusion (2710°C) and low thermal conductivity (k=1.8W/m/K); $ZrO_2$ is widely used in coatings applications as it has excellent thermal, mechanical and chemical

stability. The coatings generated by $ZrO_2$ nanoparticles have high strength, high fracture toughness, high hardness, good wear resistance, and better friction behaviour. It is chemically durable and thermally stable, having low thermal conductivity, with a high refractive index and low optical absorption. $ZrO_2$ coatings with nanocrystalline grain structure result in enhanced mechanical properties and it is used in a variety of applications from TBC to improved tribological properties [84], [85].

The solvents utilized in the preparation of suspension and solution precursor are P-W, P-E and a mixture of W-E, i.e. inexpensive solvents. Water is selected for safety and ease-of-use purposes, ethanol to improve the heating value of combustion gases once they lose their energy by liquid feedstock evaporation. The solution precursor using water or ethanol as solvents form nanoparticles by the gas-to-particle conversion process [86]. The disadvantage of this method is that the generated nanoparticles are much bigger, irregular in shape, hollow or fragmented [87].

For the suspension solution the surface tension of water, ethanol and their mixture is based on the addition of nanoparticles. At high nanoparticles concentrations, the surface tension of the suspension solution increases with increasing particle concentration, compared to that of the base fluids (see details in Chapter 7). This is expected due to the increase in the 'Van der Waals force between the accumulated particles at the liquid-gas interface, which increases the surface free energy and cause the surface tension to increase' [88]. Similar kinds of analysis are observed for the viscosity of the nanofluids, which increases with the nanoparticles loading [42], [50], [58], [62]–[64]. The thermophysical property tables generated from Perry's chemical engineers' handbook [89] and used in the present work are shown in **Table 6-2** and **Table 7-2**.

### 2.1.4 Effervescent Atomization of Liquid Feedstock

In the HVSFS and SP-HVOFS spraying processes the size of nanoparticles' coating depends on parameters including flame temperature and velocity, solution feed rate, liquid precursor concentration, liquid precursor solvent

properties, and atomization of precursor streams. It has been further determined that nanoparticles size and morphology are significantly dependent on the solution concentration, viscosity and surface tension of liquid solvent [35], [42], [50], [55], [58], [62]–[64], [67], [90], [91]. Moreover, the atomization of droplets is essentially required for water-based precursor solutions carrying high solute concentrations or suspension loadings to improve process efficiency for generating dense nanosized coating. The atomization of liquid feedstock can be controlled by the atomizer nozzle design and its injection parameters [92]–[94].

A brief literature review is added and from previous studies, the best possible techniques are applied to atomize the liquid. Many researchers have analysed the phenomena of atomization, and some specific work is highlighted here. The theory explained by Castleman [95] states that atomization is due to the aerodynamic interaction between the liquid and gas leading to unstable wave growth on the liquid jet surface. The fast moving air strikes the water jet; hence, a portion of the liquid mass is drawn out into fine ligaments, and turns into small droplets. The higher the air speed, the smaller the size of ligaments and droplets [95]. The atomization of liquid jet is a step-wise process [96]. The near field jet breakup process is dominated by the shedding of liquid sheets and ligaments; the far field has a secondary breakup phenomenon in which the disintegrated liquid lumps from the jet are fragmented by the high-velocity air jets.

Depending on the availability and application requirements, different atomizing gases and processes can be used for the atomization of the liquid streams. The nitrogen flow atomizes the precursor stream at the tip of the liquid-carrying capillary. The syringe pump is used for liquid injection with a flow rate of 50µl/s, and atomizing nitrogen GFR are set to 0.028l/s, respectively. By using this atomization technique, the droplets size distribution observed from Phase-Doppler Particle Analyser (PDPA) is between 1–20µm with droplets velocities ranging from 5–30m/s [67].

Another type of atomization method is effervescent atomization; this technique is twin-fluid atomization, in which a small amount of gas is injected into the

liquid before the exit orifice to form a bubbly mixture of gas and liquid. On emerging from the nozzle, due to the pressure difference, gas bubbles rapidly expand and shatter the liquid into ligaments and fine droplets [92]–[94], [97]–[102]. This method offers the advantage of smaller droplet size at low injection pressure and atomizing even high-viscosity liquids effectively. Increasing air-to-liquid mass flow rate ratio (ALR) and gas input pressure will lead to a finer spray. However, high ALR and high gas input pressure result in higher energy consumption, so optimization is required for the best overall operation [102]. Moreover, the efficiency of an effervescent atomizer decreases with increasing ALR. Also, the droplets' size and distribution are dependent on the solution concentration, viscosity and surface tension, as extensively analysed by researchers [93], [101], [103], [104].

Researchers also presented the numerical modelling of effervescent atomization's internal and external flow regimes [93], [101], [102], [104]–[107]. Esfarjani and Dolatabadi [106], [107] studied the effect on droplets disintegration and two-phase flow structure in the effervescent atomizer. They analysed that the aeration level and mixing between the gas and liquid was enhanced by increasing the ALR. They also concluded that effervescent atomizers can operate independently of liquid physical properties such as density and viscosity. This analysis was performed by using a wide range of nanoparticles types and concentrations for the SPS process and no effects on the performance of the effervescent atomizer were observed [106], [107].

A three-dimensional model based on the Navier-Stokes equation was developed by Qian et al. [93], to capture the external two-phase flow of the effervescent atomizer. They analysed the effect of varied injection parameters on the Sauter Mean Diameter (SMD). Based on extensive computations, and by using curve fitting techniques, a fitting formula is obtained that relates the droplet SMD to the operating conditions, including injection pressure, ALR, injector exit diameter, and liquid physical properties including viscosity and surface tension [93]. Their results showed that liquid viscosity has little effect on droplet size and its distribution, and the effervescent atomizer can work efficiently even with highly viscous fluids. Also, smaller liquid density and

surface tension will give finer droplet atomization. According to the definitions of the Weber number ($\mathrm{We} = \frac{\rho_c v_{rel}^2 d}{\sigma}$) and Ohnesorge number ($\mathrm{Oh} = \frac{\mu}{\sqrt{\rho \sigma d}}$), they consist of the properties of fluid such as droplet density ρ, surface tension σ and droplet viscosity μ, and hence the atomization phenomena can easily be studied by these dimensionless numbers [104], [105].

A similar effervescent nozzle is modelled with an impinging plate fitted downstream of the spray [99]. They concluded that the plate had a noticeable influence on the droplets' mean size and size distribution. They also simulated the effect of atomizer operating conditions on particle characteristics and SPS. Moreover, their model can predict the nanoparticles' trajectory, velocity, temperature and size during the Radio Frequency SPS. The disintegration of droplets is influenced by the varied ALR, atomizer orifice exit diameter and injection pressures. Smaller values of ALR would decrease the atomization while the larger orifice diameter would result in larger liquid droplets, and the smaller value of the injection pressure could also affect the atomization process adversely. Hence, for increasing the efficiency of effervescent atomization higher values of ALR and injection pressure with smaller orifice exit diameter should be used [93], [99], [101], [104], [108].

The modelling of effervescent atomizers is also presented by Broukal and Hájek [109]. In their study the primary breakup is based on the Euler-Lagrange approach, coupled with Lund's model, to track the liquid droplets by discrete phase model (DPM); with improved Lund's model according to Xiong et al. [108], [110], [111], while the secondary breakup is governed by Reitz's Wave model [112], [113]. The SMD obtained from this model shows significant dissimilarity when compared to experimental results; they concluded that it can be caused by the wave model, which fails to predict the droplet breakup at lower values of We.

Fung et al. [114] experimentally and numerically analysed the spray atomization under low pressure. The primary atomization LISA model (**Fluent**) was utilised to capture the atomized flow from a nasal spray device; while TAB model was used to capture the secondary breakup of droplets. Moreover, the experiments

were performed to characterize the external flow by high-speed camera imaging and particle/droplet image analysis to validate the numerical results. They concluded that controlling the liquid sheet constant and spread parameter in the LISA model would predict the spray cone shape and droplet size distribution for low-pressure applications (3–5bar).

In the present research, for atomizing the suspension or solution precursor into fine droplets inside the HVOF torch's CC, a new ETI nozzle is designed based on previous studies [93], [94], [102]. It is determined that the atomization of precursor droplets inside the HVOF torch is a requisite for successful nanoparticles dense coatings because the injections of liquid precursor without atomization resulted in large-sized nanoparticles and may produce porous coatings. Further, a numerical model is used to see the effect of effervescent atomization on HVOF flow dynamics (see Chapters 4, 5 and 8).

## 2.2 The Research Gap

The present literature highlights the following research gaps:

- The effect of increasing nanoparticles concentrations over the gas flow dynamics and droplet dynamics inside the HVSFS torch have not been taken into consideration. Previous studies have ignored the impact of nanoparticles loading on the properties of P-E, and its disintegration and evaporation processes in the HVOF torch.
- The effects of varied injection parameters and injection types over the flow physics in the HVOF torch remain to be investigated for the purpose of increasing the effectiveness of the injection process.
- The effervescent-type twin-fluid atomization nozzle for the injection of the suspension and solution precursor in the HVOF flame has been investigated in this research for the first time.
- The new ETI nozzle is designed for the CH-2000 HVOF torch, and the coating morphologies are compared with the plain-orifice and angular injection nozzles. It is a novel study conducted to see the effects of atomization and no-atomization of solution droplets on the HVOF flame dynamics and deposition of nanoparticles.

# 3 COMPUTATIONAL MODELLING

## 3.1 Introduction

The HVOF thermal spraying process is used for spraying metallic particles and, with some modifications in the gun, can be used for ceramic particles [13], [15]. Based on Chapter 2's literature review, different modelling techniques are utilized to analyse the behaviour of liquid feedstock (suspension and solution) in the HVOF spraying process. The employed turbulent, combustion, discrete phase, flow and spray models are validated against experimental data, and demonstrated satisfactory predictions [20], [21], [23], [29], [115]–[120]. The **Fluent** code is used for modelling all processes, including suspension and solution HVOF flame dynamics, and modelling of varied liquid feedstock injection types (surface, group and effervescent) [120].

## 3.2 Problem Description

The two HVOF gun geometries used in this study are the DJ2700 torch from Sulzer/Oerlikon Metco, Switzerland [115], [116] and the CH-2000 torch from Xi'an Jiaotong University, China (for CH-2000 details, see Chapter 4, section-***4.2.2***) [121]–[123].

The geometric parameters and schematic representation of the computational domain for DJ2700 are shown in **Figure 3-1** and **Table 3-1**. The total inlet radius of the CC is $R_{CC}$=9.1mm, with length $L_{CC}$=23.8mm (section-**I**). The radius at the nozzle throat is $R_T$= 4.2mm, with the extended diverging section acting as the barrel of the gun with length $L_B$= 66.2mm (section-**II**) and exit radius of $R_B$=6.215mm. The free jet domain length ($L_{FJ}$) is set to 200–500mm (section-**III**), to see the flow dynamics in the far field region after the gun's outlet. The torch geometry considered in the numerical simulations is axisymmetric. The premixed oxygen/fuel (O/F) is injected into the DJ2700 torch; the resulting hot combustion gases are accelerated inside the convergent-divergent (C-D) nozzle and flow through the barrel section towards the exit of the gun. The droplet injection mass flow rate and injection velocities are selected on the basis of previous work [115], [116], [119]. The geometry in **Figure 3-1** is used in different case studies to see the effects of using multicomponent droplets injection

(Chapter 6), and varied nanoparticles solid loading with various injection types (Chapters 7 & 8) on the flow physics of the HVSFS process. Moreover, the effects of increasing O/F GFR in the SP-HVOFS process are also analysed using the same DJ2700 torch (Chapter 9).

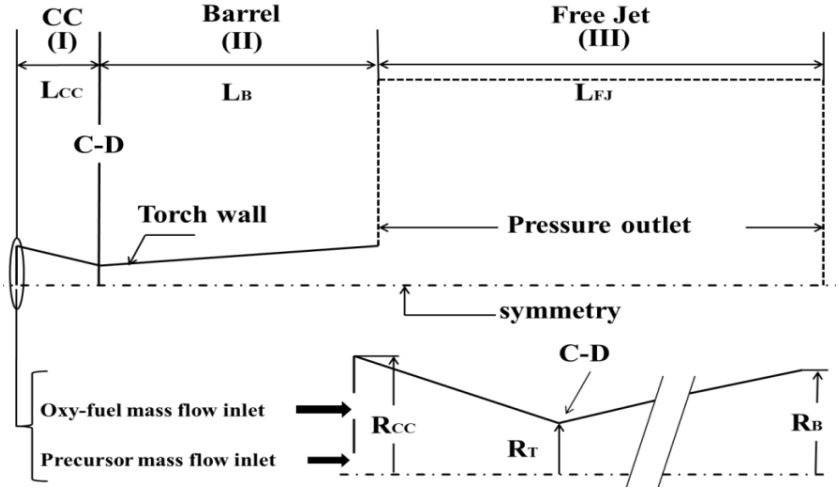


**Figure 3-1** Schematic of the HVOF gun illustrating spatial domain with the boundary conditions having three sections; **I**-Combustion Chamber (CC), **II**-Barrel, **III**-Free jet region [The domain sections marked as (**I**) Combustion Chamber (CC), (**II**) Barrel and (**III**) Free jet regions, and the vertical line separating the CC and Barrel sections which is the Convergent-Divergent (C-D) nozzle throat region, are used throughout the text]

**Table 3-1 Geometric Parameters of DJ2700 HVOF torch**

| Geometric Parameters | Symbol | Dimension (mm) |
|---|---|---|
| (I) Combustion chamber length | $L_{CC}$ | 23.8 |
| Combustion chamber radius | $R_{CC}$ | 9.10 |
| Nozzle throat radius | $R_T$ | 4.20 |
| (II) Barrel length | $L_B$ | 66.2 |
| Barrel exit radius | $R_B$ | 6.215 |
| (III) Free jet length | $L_{FJ}$ | 200–500 |

### 3.2.1 Governing Equations

The governing equations for the two-dimensional model in the Cartesian tensor form are:

Mass conservation:

$$\frac{\partial \rho}{\partial t} + \frac{\partial}{\partial x_i}(\rho u_i) = 0 \qquad \textbf{(Eq-3-1)}$$

Momentum conservation:

$$\frac{\partial}{\partial t}(\rho u_i) + \frac{\partial}{\partial x_j}(\rho u_i u_j) = -\frac{\partial p}{\partial x_i} + \frac{\partial}{\partial x_j}(\tau_{ij})_{eff} + \frac{\partial}{\partial x_j}(-\rho \acute{u}_i \acute{u}_j) \quad \textbf{(Eq-3-2)}$$

Energy, transport:

$$\frac{\partial}{\partial t}(\rho E) + \frac{\partial}{\partial x_i}[u_i(\rho E + p)] = \frac{\partial}{\partial x_j}\left(k_{eff}\frac{\partial T}{\partial x_j} + u_i\,(\tau_{ij})_{eff}\right) + Sh \quad \textbf{(Eq-3-3)}$$

Where the deviatoric stress tensor is given by

$$(\tau_{ij})_{eff} = \mu_{eff}\left(\frac{\partial u_j}{\partial x_i} + \frac{\partial u_i}{\partial x_j}\right) - \frac{2}{3}\mu_{eff}\frac{\partial u_i}{\partial x_i}\delta_{ij} \quad \textbf{(Eq-3-4)}$$

The governing equations stated above are used in the numerical simulations in Chapters 5, 6, 7, 8 and 9.

### 3.2.2 Turbulence Modelling

The Realizable $k-\varepsilon$ turbulence model explained in the present section is used in the numerical simulations of Chapters 4, 5, 6, 7, and 8. The Shear-Stress Transport (SST) $k-\omega$ model is used in Chapter 9 to capture the turbulence in the SP-HVOFS torch.

#### 3.2.2.1 Realizable $k-\varepsilon$ model

The Realizable $k-\varepsilon$ model improves the standard $k-\varepsilon$ model, as it has the new equation for the turbulent viscosity $(\mu_t)$. The turbulence dissipation rate $(\varepsilon)$ has been derived from an exact equation for the transport of the mean-square vorticity fluctuation. It introduces a variable $C_\mu$ instead of a constant. The Realizable $k-\varepsilon$ model provides improved predictions for the spreading rate of both planar and round jets; it also exhibits superior performance for flows involving rotation, boundary layers under strong adverse pressure gradients, separation, and recirculation. Realizable $k-\varepsilon$ demonstrates a superior ability to capture the mean flow of the complex structures [124]. One limitation of the realizable $k-\varepsilon$ model is that it produces non-physical turbulent viscosities in situations when the computational domain contains both rotating and stationary fluid zones (e.g., multiple reference frames, rotating sliding meshes). In the present work no sliding mesh or multiple reference frames are used thus this limit is ignored.

In the present work, the Realizable $k-\varepsilon$ model is used for modelling the turbulence in the HVOF flame jet, including compressibility effects [19], [21], [115], [117], [125].The transport equations of Realizable $k-\varepsilon$ model are given as in [120], [126], [127]:

$$\frac{\partial}{\partial t}(\rho k)+\frac{\partial}{\partial x_i}(\rho k u_j)=\frac{\partial}{\partial x_i}\left[\left(\mu+\frac{\mu_t}{\sigma_k}\right)\frac{\partial k}{\partial x_j}\right]+P_k+P_b-\rho\varepsilon-Y_M+S_k \quad \textbf{(Eq-3-5)}$$

$$\frac{\partial}{\partial t}(\rho\varepsilon)+\frac{\partial}{\partial x_j}(\rho\varepsilon u_j) \quad \textbf{(Eq-3-6)}$$
$$=\frac{\partial}{\partial x_j}\left[\left(\mu+\frac{\mu_t}{\sigma_\varepsilon}\right)\frac{\partial \varepsilon}{\partial x_j}\right]+\rho C_1 S_\varepsilon-\rho C_2\frac{\varepsilon^2}{k+\sqrt{\upsilon\varepsilon}}+C_{1\varepsilon}\frac{\varepsilon}{k}C_{3\varepsilon}P_b+S_\varepsilon$$

In these equations, $P_k$ represents the generation of turbulence kinetic energy due to the mean velocity gradients, and $P_b$ is the generation of turbulence kinetic energy due to buoyancy. For high-Mach-number flows, compressibility affects turbulence through the dilatation dissipation; neglecting this would fail to predict the observed decrease in spreading rate with increasing Mach numbers for compressible mixing and other free shear layers. Here, $Y_M$ represents the contribution of the fluctuating dilatation in compressible turbulence to the overall dissipation rate. $C_2$ and $C_{1\varepsilon}$ are constants; $\sigma_k$ and $\sigma_\varepsilon$ are the turbulent Prandtl numbers; and $S_k$ and $S_\varepsilon$ are user-defined source terms.

The turbulent eddy viscosity is given as:

$$\mu_t=\rho C_\mu\frac{k^2}{\varepsilon} \quad \textbf{(Eq-3-7)}$$

The coefficient of dynamic viscosity is:

$$C_\mu=\frac{1}{A_o+A_s(kU/\varepsilon)} \quad \textbf{(Eq-3-8)}$$

#### 3.2.2.2 The SST $k-\omega$ model

The utilization of the SST $k-\omega$ turbulence model with the Eddy Dissipation combustion model was presented for the first time in [128]; in the present work, the SST $k-\omega$ model has also been employed for capturing the turbulence in the HVOF flame jet. It was discovered that the SST model improves the predictions in adverse pressure gradients and in separating flows [120], [128], [129]. In the SST $k-\omega$ turbulence model, $k-\omega$ formulation effectively predicts the variations in the viscous sub-layer up to the wall and can be used as a low-

Reynolds turbulence model without extra damping functions. Moreover, the SST $k-\omega$ formulation also switches to $k-\varepsilon$ behaviour in the free-stream, thereby avoiding the common $k-\omega$ problem that the model is too sensitive to the inlet free-stream turbulence properties. The SST $k-\omega$ model does produce rather too large turbulence levels in regions with large normal strain, such as stagnation regions and regions with strong acceleration. This tendency is much less pronounced than with a normal $k-\varepsilon$ model, though. The transport equations of the SST $k-\omega$ model are given as [120]:

$$\frac{\partial}{\partial t}(\rho k)+\frac{\partial}{\partial x_i}(\rho k u_i)=\frac{\partial}{\partial x_j}\left[\left(\mu+\frac{\mu_t}{\sigma_k}\right)\frac{\partial k}{\partial x_j}\right]+G_k-Y_k+S_k \quad \textbf{(Eq-3-9)}$$

$$\frac{\partial}{\partial t}(\rho\omega)+\frac{\partial}{\partial x_i}(\rho\omega u_j)=\frac{\partial}{\partial x_j}\left[\left(\mu+\frac{\mu_t}{\sigma_\omega}\right)\frac{\partial k}{\partial x_j}\right]+G_\omega-Y_\omega+D_\omega+S_\omega \quad \textbf{(Eq-3-10)}$$

$G_k$ denotes the generation of turbulence kinetic energy due to mean velocity gradients. $G_\omega$ represents the generation of $\omega$; $Y_k$ and $Y_\omega$ denote the turbulence dissipation of $k$ and $\omega$; $D_\omega$ represents the cross-diffusion term; and $S_k$ and $S_\omega$ are user-defined source terms.

Some of the conclusion on the basis of the results obtained by using these two turbulence models for different cases are as follows:

- For predicting flame temperature, the Realizable $k-\varepsilon$ turbulence model is the best. Whereas, the SST $k-\omega$ turbulence model can predict the flame temperature at an acceptable level [128].
- The dispersion of droplets in the HVOF flame is captured appropriately by the SST $k-\omega$ turbulence model; however, the Realizable $k-\varepsilon$ turbulence model fails to predict the droplet dispersion in the CC of the HVOF torch.

### 3.2.3 Combustion Modelling

The numerical model computes the temperature and velocity fields of the HVSFS and SP-HVOFS flame jet in an industrial DJ2700 and CH-2000 HVOF torches. Usually in the HVOF torch, the combustion process of premixed O/F reaction is modelled, whereas, in the HVSFS and SP-HVOFS processes two different combustion mechanisms are modelled. The primary premixed

combustion of oxygen and propane is the main heat providing for the reactions in the torch. Then a secondary combustion of non-premixed oxygen and ethanol can improve the heating values of the HVOF torch when the heat is lost during the solvent evaporation process. In the present analysis, the thermal flow fields of the combustion gas are solved by the Eulerian approach. An ideal reaction at stoichiometric ratio is:

$C_3H_8+5O_2 \rightarrow 3CO_2+4H_2O$

However, for combustion temperature>2000K, the effects of dissociations and intermediate reactions are represented by an equilibrium formulation as follows [20], [21], [130]:

$a_1C_3H_8+a_2O_2 \rightarrow a_3CO_2+a_4H_2O+a_5CO+a_6OH+a_7O_2+a_8O+a_9H_2+a_{10}H$

The combustion products considered in our simulation are $CO_2$, $H_2O$, CO, OH, $O_2$, O, $H_2$ and H to account for the dissociation of the gaseous products. For oxygen-ethanol combustion, an ideal reaction at stoichiometric ratio is:

$C_2H_5OH+3O_2 \rightarrow 2CO_2+3H_2O$

Similarly, for equilibrium formulation:

$b_1C_2H_5OH+b_2O_2 \rightarrow b_3CO_2+b_4H_2O+b_5CO+b_6OH+b_7O_2+b_8O+b_9H_2+b_{10}H$

The values for the equilibrium number of moles $a_i$ and $b_i$ are calculated by the Gordon and McBride, STANJAN computer programs [20], [21], [130], [131]. In the present work, propane and ethanol combustion equilibrium coefficients are calculated at reference conditions of 5atm. and 3000K, and represented as follows:

$C_3H_8+5O_2 \rightarrow$

$1.276CO_2+2.89H_2O+1.72CO+0.85OH+0.812O_2+0.356O+0.505H_2+0.354H$

$C_2H_5OH+3O_2 \rightarrow 1.042CO_2+2.397H_2O+0.958CO+0.467OH+0.474O_2+0.145O+0.294H_2+0.151H$

For the solution of the convection-diffusion equation for the $i^{th}$, species, **Fluent** solves the conservation equation for chemical species by predicting the local mass fraction of each species $Y_i$. This conservation equation takes the following general form:

$$\frac{\partial}{\partial t}(\rho Y_i) + \nabla \cdot (\rho \vec{v} Y_j) = -\nabla \cdot \vec{J}_i + R_i + S_i \quad \textbf{(Eq-3-11)}$$

where, $\vec{J}_i$ is the diffusion flux of species $i$ calculated by Maxwell-Stefan equations, $R_i$ is the net rate of production of species $i$ by chemical reaction and $S_i$ the rate of creation by addition from the dispersed phase plus any user-defined sources.

The reaction rates that appear as source terms in Eq-3-11 are computed in **Fluent** by the EDM. The reaction rates are assumed to be controlled by the turbulence, so expensive Arrhenius chemical kinetic calculations are avoided. The model is computationally cheap, but, for realistic results, only one- or two-step heat-release mechanisms should be used [120]. The generalized finite-rate formulation is suitable for a broad range of applications including laminar or turbulent reaction systems. In the present work, EDM is used to simulate combustion in the HVOF torch with premixed and non-premixed flames.

#### 3.2.3.1 The Eddy Dissipation Model

**Fluent** provides a turbulence-chemistry interaction model, based on the work of Magnussen and Hjertager [132], [133], called the EDM. In the present work the EDM is used to simulate the premixed combustion of oxygen and propane, and the non-premixed combustion of liquid ethanol droplets with remnant oxygen left from premixed (oxygen/propane) combustion [120], [132], [134], [135].

The net rate of production of species $i$ due to reaction $r$, $R_{i,r}$ is given by the smaller (i.e., limiting value) of these two expressions:

$$R_{i,r} = \acute{v}_{i,r} M_{w,i} A \rho \frac{\varepsilon}{k} min\left(\frac{Y_R}{\acute{v}_{R,r} M_{w,R}}\right) \quad \textbf{(Eq-3-12)}$$

$$R_{i,r} = \acute{v}_{i,r} M_{w,i} AB \rho \frac{\varepsilon}{k} \frac{\sum_P Y_P}{\sum_j^N v''_{j,r} M_{w,j}} \quad \textbf{(Eq-3-13)}$$

where, $Y_P$ is the mass fraction of product species $P$, and $Y_R$ is the mass fraction of a particular reactant $R$. $M_{w,i}$ is the molecular weight of species $i$, $N$ is the number of chemical species in the system. $\acute{v}_{i,r}$ is the stoichiometric coefficient for reactant $i$ in reaction $r$, $v''_{j,r}$ is the stoichiometric coefficient for product $i$ in reaction $r$. $k$ is the turbulence kinetic energy, $\varepsilon$ is the turbulence dissipation

rate, $\rho$ is the mixture density, and $A$, $B$ are empirical constants equal to 4.0 and 0.5, respectively.

### 3.2.4 Discrete Phase Modelling

#### 3.2.4.1 Droplet Dynamics

After solving the transport equations for the continuous phase, **Fluent** simulates a discrete second phase in a Lagrangian frame of reference. This second stage consists of spherical particles or droplets dispersed in the continuous phase. **Fluent** computes the trajectories of these discrete phase entities, as well as heat and mass transfer to/from them. The coupling between the phases and its impact both on the discrete phase trajectories and continuous phase flow is included. The Lagrangian DPMs follow the Euler-Lagrange approach. The fluid phase is treated as a continuum by solving the time-averaged Navier-Stokes equations while the dispersed phase is solved by tracking a large number of particles, or droplets through the calculated flow field. The dispersed phase can exchange momentum, mass and energy with the continuous phase. A fundamental assumption made in this model is that the dispersed second phase occupies a low volume fraction, even though high mass loading ($m_{particles} \geq m_{fluid}$) is acceptable. The particle or droplet trajectories are computed individually at specified intervals during the fluid phase calculation [120].

After complete simulation of the gas phase, liquid feedstock carrying nanoparticles are injected into the HVOF flame jet where they undergo several stages. The slow moving droplets are injected into the hot flame and are accelerated by the high-velocity gas stream. The first phase is the aerodynamic breakup of droplets [115]–[117], [120], [136]. Based on the droplet size and thermophysical properties, their interaction with the surrounding gas is different, and the droplets undergo severe deformation and breakup into smaller droplets. The physical breakup process needs to be examined to have a better understanding of the liquid spraying processes.

The history of suspension droplets is computed with Lagrangian formulation where the finite interphase transport rates and effects of turbulence interactions between the droplet and gas phases are considered [10], [14], [115], [116],

[136]. By using this treatment, the evaporation history and temperature change for droplets can be calculated during the second stage of heat exchange between the gaseous and liquid phases. As mentioned above that the EDM is also used to simulate non-premixed combustion of ethanol [132], [134], [135]. The heat and mass transfer of the droplets with the continuous phase are modelled using three laws [137], [138] (see section-***3.2.4.4***).

### 3.2.4.2 Droplets Force Balance

The force balance in the Cartesian coordinates for the *x*-direction is written as [120]:

$$\frac{\partial u_d}{\partial t} = F_D(u - u_d) + \frac{g_x(\rho_d - \rho)}{\rho_d} + F_x \quad \textbf{(Eq-3-14)}$$

where, $F_x$ is an additional acceleration force or droplet mass term; $F_D(u - u_d)$ is the drag force per unit droplet mass:

$$F_D = \frac{18\mu}{\rho_d d_d^2} + \frac{C_D Re}{24} \quad \textbf{(Eq-3-15)}$$

$u$ is the fluid phase velocity, $u_d$ is the droplet velocity, $\mu$ is the molecular viscosity of the fluid, $\rho$ is fluid density, $\rho_d$ is the density of the droplet, and $d_d$ is the droplet diameter. $Re$ is the relative Reynolds number, defined as:

$$Re = \frac{\rho d_d |u_d - u|}{\mu} \quad \textbf{(Eq-3-16)}$$

The drag coefficient, $C_D$, can be taken from [139]:

$$C_D = \frac{24}{Re_d}\left(1 + b_1 Re_d^{b_2}\right) + \frac{b_3 Re_d}{b_4 + Re_d} \quad \textbf{(Eq-3-17)}$$

here,

$$b_1 = \exp(2.3288 - 6.4581\emptyset + 2.4486\emptyset^2 \quad \textbf{(Eq-3-18)}$$
$$b_2 = 0.0964 + 0.5565\emptyset$$
$$b_3 = \exp(4.095 - 13.8944\emptyset + 18.4222\emptyset^2 - 10.2599\emptyset^3$$
$$b_4 = \exp(1.4681 + 12.2584\emptyset - 20.7322\emptyset^2 + 15.8855\emptyset^3$$

The shape factor is defined by Haider and Levenspiel [140]:

$$\emptyset = \frac{s}{S} \quad \textbf{(Eq-3-19)}$$

where, $s$ is the surface area of a sphere having the same volume as a droplet, and $S$ is the actual surface area of droplets.

### 3.2.4.3 Droplet Breakup Models

The secondary breakup of droplets into smaller ones is modelled by the TAB model as $\mathrm{We} < 100$ [115], [120], [136], [141]. Different regimes of the droplets

fragmentation are determined by using the critical value of We. The hydrodynamic force required for the deformation of droplets is related to the surface tension force acting to retain the droplet form by the $\mathrm{We} = \frac{\rho_c v_{rel}^2 d}{\sigma}$. Since the $\mathrm{Oh} = \frac{\mu}{\sqrt{\rho \sigma d}}$ remains much below 0.1 $(\mathrm{Oh} \ll 0.1)$ in the computational domain, the main parameter related to the breakup physics is the We. The TAB model is well adapted to the conditions of spraying and validated in earlier studies; complete details can be seen in [115]–[119], [136] and are not repeated here for brevity.

#### 3.2.4.4 Droplet Heat-up and Vaporization Model

Droplet heat and mass transfer in continuous phase are modelled by considering three laws. The inert heating law 1 is applied when the droplet temperature ( $T_d$) is less than the vaporization temperature ($T_{vap}$ = 271K for liquid ethanol) [116], [120], [137], [138]. A simple heat balance equation (Eq-3-20) is used to relate $T_d$ to the convective heat transfer, and the heat gained or lost by the droplet while moving through the continuous phase.

**Law 1:** For $T_d < T_{vap}$,

$$m_d c_d \frac{dT_d}{dt} = hA_d(T_\infty - T_d) \quad \textbf{(Eq-3-20)}$$

where $m_d$, $c_d$, $T_d$, and $A_d$ are mass, heat capacity, temperature and surface area of the droplet, respectively. Here, $h$ and $T_\infty$ are convective heat transfer coefficient and gas temperature.

The mass transfer law 2 is applied to predict the vaporization from a discrete phase droplet using Eq-3-21. This law is used when droplet temperature reaches the $T_{vap}$ and continues until the droplet reaches boiling point.

**Law 2:** For $T_{vap} \leq T_d < T_{boil}$,

$$N_i = k_c\left(C_{i,s} - C_{i,\infty}\right) \quad \textbf{(Eq-3-21)}$$

where $N_i$, $k_c$, $C_{i,s}$, and $C_{i,\infty}$ are the molar-flux of vapour, mass transfer coefficient, vapour concentration at the droplet surface and vapour concentration in the bulk gas, respectively. $k_c$ in Eq-3-21 is calculated from the Sherwood number (Sh) correlation [142], [143]

The droplet mass is reduced according to Eq-3-22:

$$m_d(t + \Delta t) = m_d(t) - N_i A_d M_w \Delta t \quad \textbf{(Eq-3-22)}$$

where $M_w$ is molecular weight of species $i$. During the activation of law 2, the droplet's temperature is updated using heat balance Eq-3-23. It relates the sensible heat change in the droplet to the convective and latent heat transfer between the droplet and the continuous phase.

$$m_d c_d \frac{dT_d}{dt} = hA_d(T_\infty - T_d) + \frac{dm_d}{dt} L \quad \textbf{(Eq-3-23)}$$

here $\frac{dm_d}{dt}$ is the rate of evaporation and $L$ is the latent heat.

For predicting the convective boiling of droplets, law 3 is applied. It uses the boiling rate Eq-3-24 and is activated when droplets reach boiling point, ($T_{boil}$ = 351K for liquid ethanol) [116], [134].

**Law 3:** For $T_d \geq T_{boil}$,

$$\frac{d(d_d)}{dt} = \frac{4K_\infty}{\rho_d \, c_\infty \, d_d}\left(1 + 0.23\sqrt{Re_d}\right) ln\left[1 + \frac{c_\infty(T_\infty - T_d)}{L}\right] \quad \textbf{(Eq-3-24)}$$

where $K_\infty$, $c_\infty$, and $\rho_d$ are the thermal conductivity, heat capacity of the gas and droplet density, respectively.

The droplet with an injection temperature of 300K enters into the hot CC for gradual evaporation and combustion with remnant oxygen left after premixed oxygen/propane burning. Since the Knudsen number ($Kn = \lambda/d_d$), the ratio of gas mean free path ($\lambda$) to droplet diameter ($d_d$), is far less than the transition number 0.01, the discontinuous effects are neglected [41], [144]. It is also stated that the dependence of drag coefficient ($C_D$) on the Kn can be neglected in the case of HVOF spraying, as shown by Sobolev et al. [145]. The Reynolds number ($Re$) varies from $2.09 \times 10^5$ to $1.18 \times 10^5$ in the computation domain based on the characteristics of the gas dynamics.

## 3.3 Summary

Most of the common models used to solve the present problems are listed above, and only a few remaining models will be discussed in the following chapters for a clear understanding of the model applications. For brevity, not all details of each model are presented in the above discussion; for further clarity see references stated in each section.

# 4 EXPERIMENTAL STUDY ON USING DIFFERENT PRECURSOR CONCENTRATIONS, SOLVENT TYPES AND INJECTION TYPES FOR NANOPARTICLES SYNTHESIS

## 4.1 Introduction

In the SP-HVOFS process, fuel and oxygen burn in a chamber at pressures between 0.24 and 0.82MPa. A convergent–divergent Laval nozzle (C-D) is fitted for attaining very high gas velocities (up to 2000m/s). Powders are injected into the torch axially or radially, depending on the gun design. Recently liquid feedstock injection techniques have been developed for improved nanostructured coatings [41]. In the thermal spraying process, the fuel and oxygen are fed into the HVOF torch for the generation of energetic combustion gas flame. Then the coating material is injected in the form of powders, suspensions or solutions precursor. After the interaction of the hot gas with the suspensions or solution precursor, droplets' breakup starts immediately after the material injection. The dynamic gas-to-droplet or gas-to-particle interaction involves droplet's breakup and evaporation with particle's acceleration, heating, melting, oxidation, or modification of surface chemistry. Lastly, the coating formation depends on the particles' impact, flattening, splat formation, cooling, and splat layering first on the prepared substrate and then on already deposited layers [41].

Deposition of coatings with nanometric size structure is performed by injecting a homogeneous solution into the hot gases of the SP-HVOFS process. During the interactions between gas and droplet, the droplets' breakup is caused by the high drag forces and high relative velocities between the droplets and gases. The continuous heating of solution precursor in the HVOF flame led to the evaporation, precursor decomposition and formation of the required species. This is known as the in situ formation of coating particles. Throughout this process the hot gases are cooled by evaporation of the solution and heating of vapours; hence, the gases must have sufficient enthalpy for successful

coatings, such as in HVOF and plasma spraying. The solution can be injected either by atomization with a gas or by mechanical injection.

It is proven that the homogeneity of the solution precursor is good in comparison to suspensions [41], [42]. The study of the SP-HVOFS process experimentally and numerically is performed by a few researchers, (see Chapter 2, section-***2.1.2***). Due to the presence of very few studies related to the SP-HVOFS process, more work is required in this area.

Towards the usage of different solution precursors for nanoparticles' coating formation, the use of metal-nitrate as a precursor has some advantages over others. Firstly it is not expensive and easily available in the market. Secondly, the metal nitrate salts dissolve easily in water and alcohol; hence, the homogeneous precursor solution can be formed by continuous stirring. Moreover, the nitrates act as an oxidizer for fuel during the combustion reaction that will increase the HVOF flame enthalpy. The disadvantage of using metal nitrates as reported by Marchal et al. [146], is that larger (200–2000nm) hollow particles are obtained by the liquid feed flame spray pyrolysis process, whereas, a significant portion of particles has a size below 100nm. For a nitrate-based precursor, two mechanisms of synthesis are explained in the literature. Firstly, the nitrates partially melt and then decompose (rather than combust) on heat-up just after exiting the spray nozzle. This produces large, sometimes hollow, particles (typical of flame spray pyrolysis). In the second process, direct combustion of the spray droplets occurs without melting which forms fine particles [87], [146]–[149]. It may be assumed that the second process is more dominant in HVOF flame spray pyrolysis because the fast moving HVOF flame would hinder the melting of nitrate precursor before decomposition due to the short residence time available for precursor droplets inside the combustion chamber (CC). Hence, it can generate fine, solid nanoparticles before deposition.

As pointed out the studies related to SP-HVOFS process are scarce and more research is required in this area. To date, no work has been reported to study the effects of different feedstock injection parameters on the formation and

growth of nanoparticles' coating by the SP-HVOFS process. The size of nanoparticles needs to be controlled for the specific coating requirement, and it can be regulated by using proper atomization of precursor while injecting into the thermal spraying torch [33], [50], [69]. The SP-HVOFS process includes complex stages of precursor injection, droplet fragmentation, precursor/solvent evaporation, chemical reactions, decomposition, particle formation, heating and melting of nanoparticles while transferring heat, mass and momentum with the surrounding hot gas [33], [34]. This chapter contributes to obtaining more insight to understand the effects of solution precursor fragmentation, advanced evaporation and its consequence on the nanoparticles formation in the SP-HVOFS process.

In the present chapter, experiments are performed to analyse the nanoparticles growth and size distribution by using varied concentrations of solution, different solvent types and injection nozzles. The Zirconium Nitrate (ZrN) pentahydrate [$Zr(NO_3)_4.5H_2O$] precursor is used which is injected into the HVOF torch for the formation of Zirconia ($ZrO_2$) nanostructured coatings. The homogeneous solution of ZrN with solvent pure water (P-W), pure ethanol (P-E) and water-ethanol (W-E) mixture are made for analysing the formation of $ZrO_2$ nanoparticles in the HVOF flame (section-***2.1.3***). Different solute concentrations are employed to determine the difference in the particle's size and morphology. Moreover, for the first time, various injection nozzles with plain-orifice injection (N1), angular injection (N2) and effervescent atomization (N3) are used to examine the effects on nanoparticles formation in the SP-HVOFS process. In the present chapter results for different experiments using N1, N2 and N3 nozzles are discussed. Also, similar nozzles are numerically simulated in the next Chapter ***5***.

## 4.2 Experimental Setup

### 4.2.1 Design and Manufacturing of Liquid Feedstock Injection Nozzles

The experiments are performed using three different nozzles: plain-orifice nozzle N1, angular injection nozzle N2, and effervescent atomization nozzle N3 (**Figure 4-1**a–d and Appendix ***A.1***). The effects of varied nozzle types on the

nanoparticles' morphology and size distribution are analysed. Three kinds of liquid feedstock injection nozzle are designed according to the structural requirements of the CH-2000 HVOF torch. The old injection nozzle N1 head (having an exit diameter of 0.5 mm) is modified to an angular injection nozzle N2, to improve the droplets disintegration by injecting the droplets into the core of the combustion zone (**Figure 4-1**a, b, **Figure A-1** and **Figure A-2**). The nozzle N2 is designed to inject the precursor into the CC of the CH-2000 torch with 60° angle of injection; it has six holes with a diameter of 0.3 mm (**Figure 4-1**b and **Figure A-2**). The results for the old nozzle N1 are analysed and compared with the modified new nozzle N2 in the results section. Furthermore, a new effervescent atomization nozzle N3 with an exit diameter of 1.5mm has been designed for solution precursor atomization based on outside-in design (**Figure 4-1**c–d and **Figure A-3**) [92]–[94], [97]–[102]. The effervescent atomization technique is used to create a bubbly flow inside the nozzle section and then spray it into the CC to obtain a finer disintegration of precursor's droplets. In this technique, the liquid ejects from the orifice with the internal cavity of gas. Due to the pressure difference, gases expand and shatter the liquid into ligaments and fine droplets [93], [94], [102]. Some of the preliminary atomization in the CC of the CH-2000 torch are shown schematically in **Figure 4-1**a–c to compare the old single-fluid (without atomization) and the new twin-fluid (with atomization) precursor spraying phenomena; the detailed results are analysed and discussed in the result section.

### 4.2.2 Torch Geometry and Operating Conditions

The HVOF torch used for the experiments is the CH-2000 type, designed and made in Xi'an Jiaotong University, China (**Figure 4-2**) [121]–[123]. The total inlet radius of the CC is $R_{CC}$=15.5mm, with length $L_{CC}$=19mm. The radius at nozzle throat is $R_T$= 4.0mm, with the extended gun barrel with a constant radius of $R_B$=4.0mm and length $L_B$= 168mm. O/F gases flowed into the CC through several holes distributed evenly around the precursor injection port at the centre of the torch. Propane gas is used as fuel [150] (**Figure A-4** and **Figure A-5**). Firstly the operating conditions for the CH-2000 HVOF torch are set as displayed in **Table 4-1** using flow controllers (**Figure A-6**). The flame at these

conditions reached a supersonic state, and visible shock diamonds are observed in the flame jet. The temperature of the flame is measured by thermocouples, and it is compared with the numerical temperature profile to validate the combustion and turbulence models used in the present research work. Then, precursor gas (nitrogen) is replaced by solution precursor injection using a pump (**Figure A-7**) and nozzle N1 with a feed rate of 50ml/min. After solution injection, the flame brightness is increased, and the shock diamonds disappeared, showing that the temperature is reduced inside the HVOF torch because of heat absorbed by solution droplets for evaporation and in situ formation of $ZrO_2$ particles.

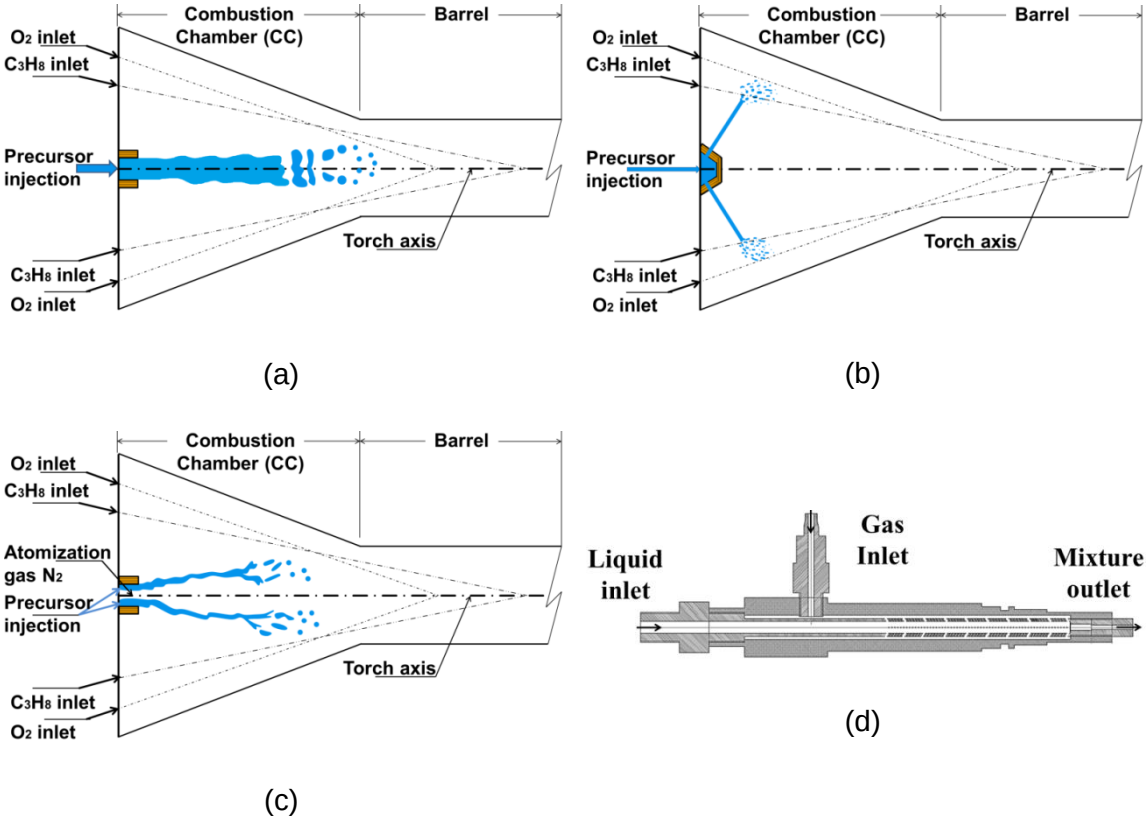


**Figure 4-1** Schematic representation of precursor injection into the CH-2000 HVOF torch, (a) old plain-orifice nozzle N1, (b) modified new angular injection nozzle N2 and (c) new effervescent atomization nozzle N3, (d) cross-section view of effervescent-type nozzle (N3)

### 4.2.3 Precursor Formation and Deposition

In this study, Zirconium (IV) Nitrate (ZrN) pentahydrate, [chemical formula=$Zr(NO_3)_4.5H_2O$] salt produced from Sinopharm Chemical Reagent Co. Ltd, China is used. The ZrN precursor solutions with varied molar concentrations of 0.05M,

0.075M and 0.1M are formed. The salt is dissolved into three different solvent types P-W, W-E mixture carrying 50% water and 50% ethanol by volume, and P-E. Nine sets of precursor solutions are prepared by using the above solvent types and salt concentrations, (see **Table 4-1**).

These precursor solutions are injected sequentially into the HVOF torch, and the generated particles are sprayed over finished Yttria Stabilized Zirconia (YSZ) substrates (**Figure A-8**). The HVOF torch is mounted on the automatic controller Moto-man for spraying purposes (**Figure A-9**). Scanning Electron Microscopy (SEM) is performed on a TESCON MIRA3 (FEG-SEM) with an operating voltage of 15kV (**Figure A-10**). Before SEM, sample substrates are sputter-coated with Platinum to reduce the charging effects (Pt with a coating rate of 8nm/min for 2mins, **Figure A-11**). Different morphologies and nanoparticles size distribution are analysed for different salt concentrations and solvent types (section-***4.3***).

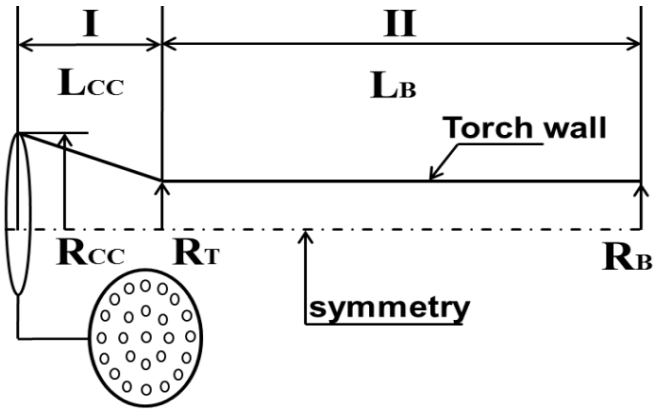


**Figure 4-2** Schematic diagram of CH-2000 HVOF torch

## 4.3 Results and Discussions

The experiments are organized to analyse the effect of varied solvent types and different salt concentrations on size and morphology of nanoparticles formed during the SP-HVOFS process. The HVOF flame is set up according to the flow parameters described in **Table 4-1**. Moreover, with this GFR set up nine cases are experimentally performed. ZrN dissolved in P-W injected with nozzle N1 is named as Cases A, B, C with salt concentration 0.05M, 0.075M and 0.1M, respectively (**Table 4-1**). Similarly, ZrN precursor solutions with varied salt concentrations made in the W-E mixture are designated as Cases D, E, F, those made in P-E are designated as Cases G, H, I (**Table 4-1**). The ZrN

precursor is injected (50ml/min) at the centre of the torch and fed into the CH-2000 HVOF torch with nozzle N1 (**Figure 4-1**a). No atomization technique is applied at this stage. The formed nanoparticles are deposited on the finished surface of YSZ, and SEM micrographs are analysed for various precursor solution concentration and different solvent mixtures. Similar steps are repeated for nozzle N2 (**Figure 4-1**b) (Cases J, K, L, M, N, and O). For brevity, these cases are not mentioned in **Table 4-1**.

**Table 4-1 Operating conditions of CH-2000 HVOF torch, solute concentration (M) and solvent types used in solution precursor formation**

| **Gas flow rates** | **(kg/s)** | | |
|---|---|---|---|
| Oxygen flow rate | 0.007368 | Case1-Without droplet injection | |
| Propane flow rate | 0.001581 | | |
| Nitrogen flow rate | 0.001349 | | |
| Solution precursor flow rate | 50ml/min | Case2-With droplet injection (nozzles N1 and N2) | |
| Solution precursor flow rate | 50ml/min | Case3-With droplet injection nozzle N3 | |
| Nitrogen flow rate | 6l/min | | |
| Solute concentration (M) | Sample/Case name: Solvent Type (N1) | | |
| 0.05M | A: P-W | D: W-E | G: P-E |
| 0.075M | B: P-W | E: W-E | H: P-E |
| 0.1M | C: P-W | F: W-E | I: P-E |

Experiments are then performed by using the new nozzle N3 (**Figure 4-1**c). The precursor and atomizing gas are injected into the nozzle N3 from separate inlets (**Figure 4-1**d). This mixture of fluids is then fed into the CH-2000 torch's CC as shown in **Figure 4-1**c. In these experiments the formed nanoparticles deposited and SEM micrographs are analysed for various precursor solution concentrations, and varied solvent mixtures for the injection with nozzle N3 (Cases P, Q, R, S, T, U, V, W, and X). Again for brevity, these cases are not mentioned in **Table 4-1**.

### 4.3.1 Comparison of the HVOF Flame Temperature: Experimental vs Numerical

High flame temperatures are required for the evaporation of the precursor solution and nanoparticles formation in the HVOF torch [121]–[123]. The GFR are selected according to the previous work to obtain high-temperature flames

with supersonic jet outlet velocities. For Case1, the O/F gases are injected into the CH-2000 torch's CC, and shock diamonds are observed at the torch exit (**Table 4-1**). Temperature sensing is performed by using thermocouples. In Case2, the O/F flow rates remain the same while the nitrogen gas injection is replaced by the liquid injection (**Table 4-1**). For Case2, temperature measurements are repeated by thermocouples. Moreover, three different liquid solvents are fed into the CH-2000 torch successively. P-W injection is named as Case2a, P-E injection Case2b and W-E mixture injection Case2c in **Figure 4-3**. For all the cases the data are gathered and plotted here for model validation (**Figure 4-3**). The temperature sensing performed by the thermocouple has significant errors involved due to radiation, convection and conduction heat losses [151]. So it is assumed that the actual flame temperature could be 200°C higher than the temperature measured by these thermocouples.

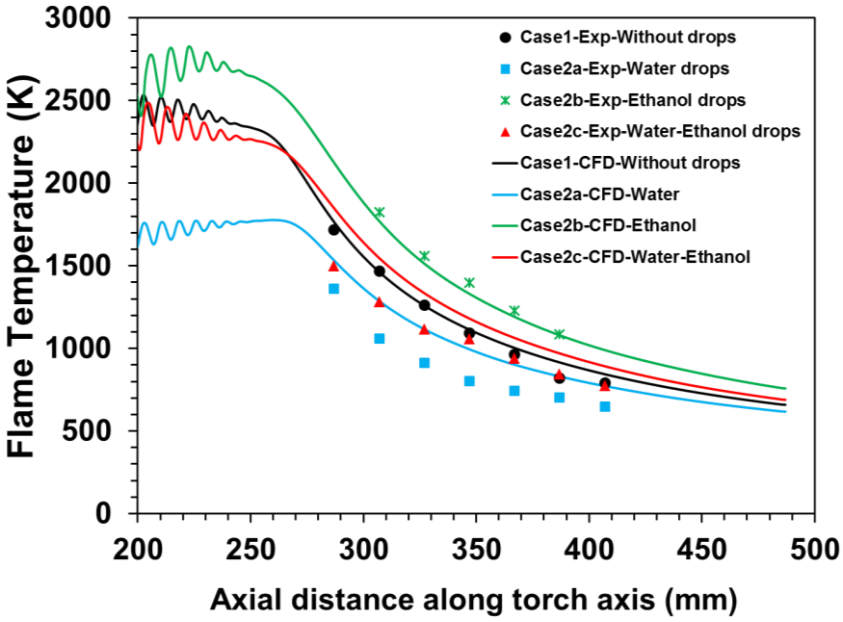


**Figure 4-3** Thermocouple and CFD temperature measurement of the CH-2000 flame (all cases with N1)

Similarly, for numerical validations of the gas flow dynamics, two cases are simulated Case1 and Case2 with and without droplets injection. Temperature profiles from numerical simulations of Case1 and Case2 compare with the experimental measurements (**Figure 4-3**). The temperature profiles measured by CFD in the far field are in good agreement with the experimental results in Case1 and Case2b. For Case2a and Case2c when P-W and W-E mixture

droplets are fed into the CH-2000 torch, the CFD temperature is higher than that measured by the thermocouple, while it has already been discussed that the thermocouple could not measure the gas temperature accurately [151]. Hence, the flame temperature predicted by CFD is in the correct range as the measurements overlap completely with the high-temperature flame. On the other hand, for lower flame temperatures the readings are a little higher when compared with the thermocouples. Thus, it can be said that Case2a and Case2c CFD measurements are more accurate, compared to the other cases. It is observed from **Figure 4-3** that by adding the liquid droplets in Case2, the flame temperature is significantly reduced. The highest peak flame temperature is detected in P-E Case2b (2828.38K), and the lowest peak flame temperature is perceived in P-W Case2a (1777.12K). The maximum temperature observed for Case1 is 2639.58K and for Case2b, 2616.73K. Therefore, for all prescribed cases the flame temperature is high enough to accomplish the in situ nanoparticles formation in the SP-HVOFS torch.

### 4.3.2 The SP-HVOFS process physics

The process physics for the nanoparticles nucleation is explained schematically in **Figure 4-4**. In the SP-HVOFS process, the solution precursor is fed into the HVOF torch through a central opening. The O/F mixture combusts inside the CC and provides the heat required for the precursor droplets' evaporation and in situ particle formation (**Figure 4-4**). The chemical reaction started immediately as the precursor droplets absorbed heat from the surrounding hot gas and converted into vapours (CC-section-**I**). The evaporation of the precursor liquid is dependent on the combustion temperature, and under high GFR, the liquid boils rapidly and evaporation rate increases. It is generally mentioned that a high evaporation rate will eventually increase the average particle growth rate [152].

Particles formation starts where the O/F combustion streams and precursor vapour streams are mixed inside the CC, while the turbulence mixing occurs near the centreline axis of the torch as the precursor droplets are injected axially into the CC (from a central hole/opening, **Figure 4-4**). It is stated that particle formation occurring directly from the vapours takes place via

homogeneous nucleation [152]. The local cooling rate, residence time distribution, and number density in the nucleation and growth zones are the primary factors which affect the nucleation and growth of nanoparticles in the SP-HVOFS process (**Figure 4-4**). Furthermore, the physical and chemical properties of nanoparticles are dependent on a large number of parameters, such as combustion gas temperature, pressure, velocity, C-D nozzle design, O/F injection flow rates and feeding ratio, fuel and precursor properties and their concentration [33], [34], [78]. Firstly, the droplets of the solution precursor, after being injected into the HVOF flame jet, undergo several physical processes taking place simultaneously. The first stage is the aerodynamic breakup, as the slow moving droplets are entrained into the high-velocity jet and accelerated in the high-velocity gas stream (**Figure 4-4**). Depending on the droplet initial size, thermophysical properties of the solution precursor and surrounding gas conditions, droplets can undergo severe deformation and eventually breakup into smaller droplets.

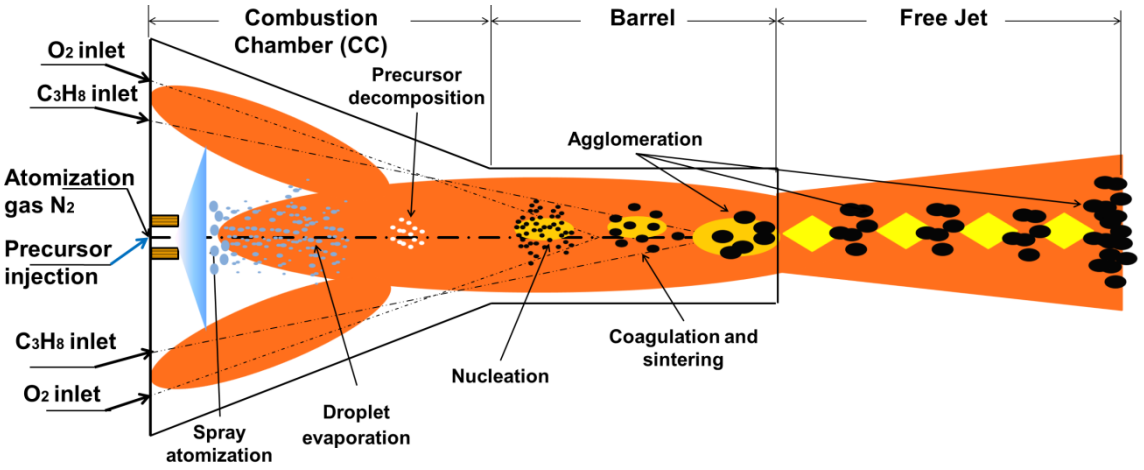


**Figure 4-4** Schematic representation of the SP-HVOFS process for nanoparticles formation

The second stage is the evaporation of micron-sized precursor droplets after which the formation of particles begins when the precursor gas is going through a chemical reaction (**Figure 4-4**). The high-temperature is required to evaporate the precursor and to provide the conditions for the chemical decomposition. The temperature of high-velocity flames varies from 3000–4000K depending on the type of oxidizer and operating conditions [18], [26], [153], [154]. At the early stage, the particles are formed by gas-phase nucleation and grow by

coagulation (particles collide with each other and stick to form agglomerates); later, they coalesce into larger particles. The shape of the final product is determined by the rates of coalescence and coagulation. If the rate of sintering is faster than that of coagulation, the particles formed are spherical. Otherwise, irregularly shaped agglomerates are developed [152], [155].

### 4.3.3 Effect of Increasing Precursor Concentration on Nanoparticles Size and Morphology

Experiments are performed with operating conditions defined in **Table 4-1** (Case 2a), and ZrN dissolved in P-W is deposited on the YSZ substrate. Three varied salt concentrations are utilized to determine the effects of concentration variation on the nanoparticles size and morphology. The solution samples are named A, B and C carrying a solute concentration of 0.05M, 0.075M and 0.1M, respectively. **Figure 4-5** shows the morphology and size variation of the as-sprayed particles at varying salt concentrations. For a low concentration of 0.05M, fewer numbers of particles are observed, as compared to high concentration (**Figure 4-5**a, b, c). In Case-A-0.05M, more numbers of particles are spherical, and a few are fused together (agglomerated and aggregated) with a mean diameter of nanoparticles is $d_{p)mean}$=104nm. The range of particle size distribution observed for the Case-A is 20–340nm.

The solution precursor density is increased from 1007–1018kg/m$^3$ and $ZrO_2$ production rate is augmented from $5.134\times10^{-6}$–$10.2683\times10^{-6}$kg/s (18.483–36.966g/h) with the increment in the solution concentration from 0.05M–0.1M. Hence, with salt concentrations in Case-B-0.075M and Case-C-0.1M, the SEM micrographs showed the presence of numerous agglomerated and aggregated nanoparticles with a mean diameter of 119nm and 143nm, respectively (**Figure 4-5**b, c). It was observed that in comparison to Case-B-0.075M, the range of particle distribution (20–340nm) is also extended in Case-C-0.1M solution (20–440nm). This increase in the diameter of nanoparticles was expected as the higher precursor concentration will result in a higher particle density. It increases the frequency of particle collision, hence, augmented the coalescence and sintering processes that enhance the growth rate of nanoparticles. Also, this increase in the concentration showed the bulk of agglomerated $ZrO_2$

particles with semi-melted and aggregated large size particles. Therefore, it is observed that the increment in the solution concentration reduced the process efficiency, and non-spherical, non-homogeneous nanoparticles are deposited. The effectiveness of this process can be increased by using droplets atomization techniques. The next section used and analysed the techniques to disintegrate precursor droplets into a fine mist to obtain the desired nanosized spherical particles having a homogeneous morphology.

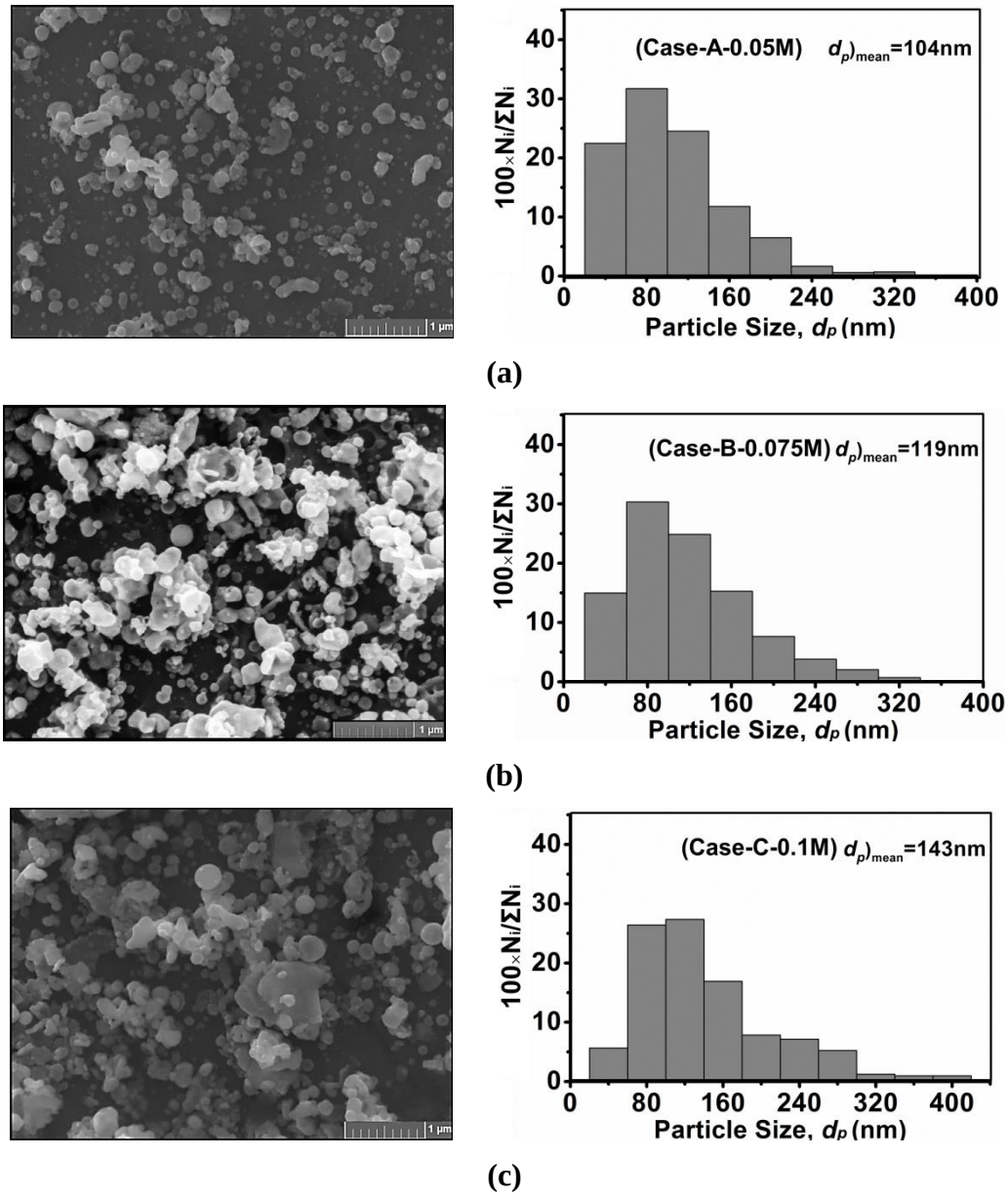


**Figure 4-5** SEM images and nanoparticle size distribution of $ZrO_2$ particles produced from ZrN dissolved in P-W solvent with varied salt concentrations (a) Case-A-0.05M, (b) Case-B-0.075M, (c) Case-C-0.1M

**Error! Reference source not found.** shows the average diameter of nanoparticles as a function of increasing precursor concentration at constant GFR (6l/min), solution feed rates (50ml/min) and injection pressure (0.7MPa) for cases A, B and C. It is observed that, keeping all parameters constant and increasing the precursor concentration from 0.05–0.1M led to an increase in the mean diameter size from 104nm–143nm (**Error! Reference source not found.**). The reason for increasing particle size is the increment in the density of ZrN precursor in the HVOF torch; thus, an increase in particle size is also due to variations in the solution precursor transport properties. Increase in precursor concentration from 0.05M–0.1M would also increase the density, surface tension and viscosity of solution droplets. This may decrease the droplet disintegration process in the HVOF torch, and bigger droplets lead to the formation of larger nanoparticles. The increment in droplet size delays the droplet evaporation rate, and precursor decomposition [119], while the augmentation in the droplets residence time in the HVOF torch will lead to increase the sintering rate of nucleated seed particles, and particles grow bigger [30]. In many applications high solute concentration is required as Chen et al. [65] found that low concentration precursors generally experience surface precipitation and lead to shell formation. The deposits consist of semi-pyrolized material and resulted in a soft, porous coating; while, the high concentration precursors resulted in the ultra-fine splats, and dense, hard coatings.

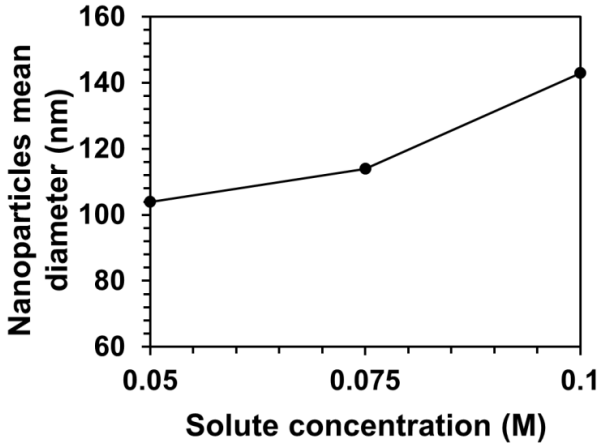


**Figure 4-6** Nanoparticles mean diameter for varied solute (ZrN) concentrations in P-W solvent (using N1)

### 4.3.4 Effect of Different Solvent Types on Nanoparticles Size and Morphology

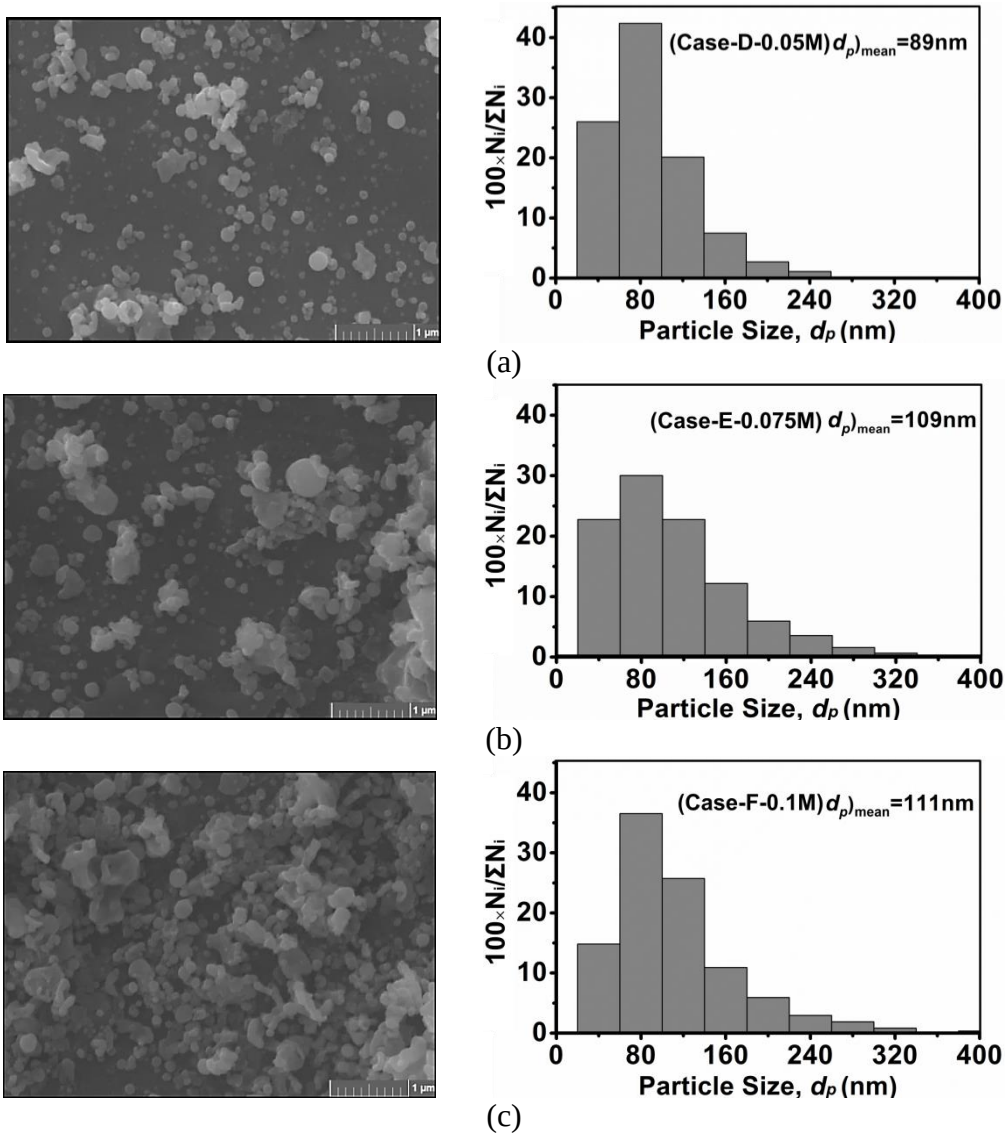


**Figure 4-7** SEM images and nanoparticles size distribution of $ZrO_2$ particles produced from ZrN dissolved in W-E mixture with varied salt concentrations of (a) Case-D-0.05M, (b) Case-E-0.075M, (c) Case-F-0.1M, (W-E mixture solvent carrying 50% water and 50% ethanol)

This section examines the impact of various solvent types on the nanoparticles size and morphology. Three types of solvents are used, including P-W, P-E and W-E mixture. It is observed that the nanoparticles size distribution is changed with varied solvent types. In the **Figure 4-7**a–c and **Figure 4-8**a–c the SEM micrographs and nanoparticles size distributions for W-E mixture (Case-D-0.05M, Case-E-0.075M, and Case-F-0.1 M) and P-E (Case-G-0.05M, Case-H-0.075M, and Case-I-0.1M) Cases are presented. When P-W Case-A-0.05M is

compared to the W-E mixture Case-D-0.05M, and P-E Case-G-0.05M, the average diameter of nanoparticles, observed are 104nm, 89nm and 111nm, respectively (**Figure 4-5**a, **Figure 4-7**a, **Figure 4-8**a).

During flame synthesis of nanoparticles the water cools down the flame and due to its quenching effect the particle size is reduced (**Figure 4-5**a). The best results are obtained for the W-E mixture case, and smallest nanoparticles size are observed with a weak solution concentration of 0.05M (**Figure 4-7**a). However, the addition of P-E increases the flame temperature, and increment in the gas temperature augmented the sintering rate, and large size particles are obtained (**Figure 4-8**a). **Figure 4-7**b, c show the SEM images with particle distribution curves for W-E mixture, carrying salt concentration of 0.075M (Case-E) and 0.1M (Case-F) respectively. For the solution of 50wt.% added ethanol, the particle size and distribution varies little with increasing concentrations, while they both changed in the P-W case (**Figure 4-5**a–c). In W-E mixture cases, the particle size distribution range also narrowed (**Figure 4-7**a–c), and the biggest particle is 360nm (Case-F-0.1M). On the other hand, in the P-W case, the largest diameter is observed as 420nm for Case-C-0.1M concentrated solution. The reason is that the P-W droplets had high surface tension and required high heat for vaporization; hence, an increase in solution concentration further augments these properties. Therefore, the droplets' evaporation process and decomposition of ZrN is delayed, and led to the formation of large nanoparticles compared to that of W-E mixture cases. Moreover, under the adverse conditions non-pyrolized precursor may appear on the substrate. Hence, a small spray distance may help to reduce the presence of the non-pyrolized material by heat transfer and may improve bonding mechanism and decreased porosity [42], [73], [77], [156]

Furthermore, it is known that the value of the surface tension of water ($\sigma_{P-W}=72x10^{-3}$N/m) is three times that of ethanol ($\sigma_{P-E}=22x10^{-3}$N/m). A small increase in salt concentration will cause an increment in P-W surface tension. Hence, at high concentrations of 0.1M, P-W shows a large particle size of 143nm (Case-C-0.1M, **Figure 4-5**c) while W-E mixture shows a mean diameter of 111nm (Case-F-0.1M, **Figure 4-7**c), and P-E solvent gives out particles with

an average diameter of 101nm (Case-I-0.1M, **Figure 4-8**c). Thus increasing the precursor concentrations has less effect on the organic solvents, compared to water. Therefore, organic solvents are more resistant to show a change in their surface tension by an increment in solute concentration.

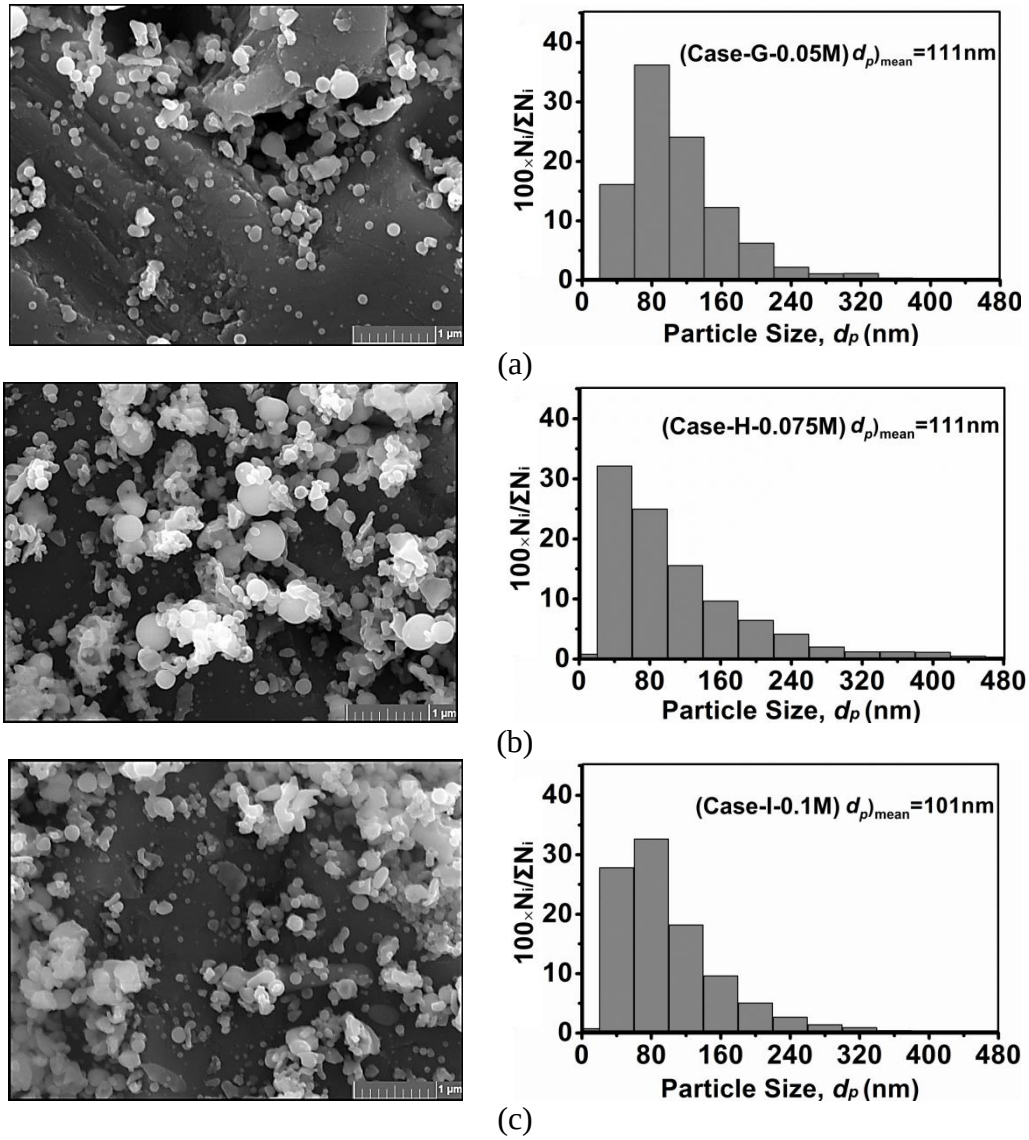


**Figure 4-8** SEM images and nanoparticles size distribution of $ZrO_2$ particles produced from ZrN dissolved in P-E solvent with varied salt concentrations of (a) Case-G-0.05M, (b) Case-H-0.075M, (c) Case-I-0.1M

Moreover, when P-E is used as the solvent, the individual particle shape is more spherical, and an increase in agglomeration is also detected (**Figure 4-8**a–c). The organic solvents and their mixtures have fast evaporation and subsequent early salt decomposition [115]. Thus, these early evaporations allow the $ZrO_2$ seed particles to remain in the higher flame temperature regions

for a longer time, compared to the P-W-based solvents cases. Hence, it increases the particle sintering and growth rate [152]. The particle size distribution is widened for the P-E case, and the largest particle size $d_p$=496nm is observed for Case-H-0.075M concentration. Besides, the particle temperature may also increase during the flight, which is suitable for making a strong bond between the coating and substrate. The P-E can be used to have more spherical particulate matter, and it helps to control the particle size variation and distribution range.

**Figure 4-9** shows the variations in mean particle diameter by using different solvent types. As mentioned above, P-W solvents are highly sensitive to variation in the concentrations of the solution. Thus, their thermophysical properties, i.e. surface tension, viscosity and specific heat capacity, are augmented by the increment in the solution concentrations, while the organic solvents and their mixture show no significant change in their properties [35], [65]. It is studied by Chen et al. [35] that droplet with a high surface tension and high boiling point solvent experiences incomplete solvent evaporation process in the jet leading to a porous coating. Droplet created from a low surface tension and low boiling point solvent undergoes rapid solvent evaporation, solute precipitation, pyrolysis, melting process during the flight, and forms splat upon impacting on the substrate; the build-up of splats results in a dense coating. Thus it can be said that organic solvents can be beneficially used for the generation of dense pore free coating.

Similar kinds of observation are made during the present experimental work. The particle size is increased for P-W solvents with a rise in the solution concentrations, whereas, the particle size shows fewer variations for the W-E mixture. Moreover, for P-E the particle size is decreased with the increase in solute concentration (**Figure 4-9**). Thus, it is proved that the nanoparticles size distribution and morphology are mainly dependent on the (i) solution concentrations, and (ii) type of solvent. Because the increment in the solution precursors' surface tension and heat of vaporization are also reliant on the kind of solvent and solute concentrations. Solution precursor with higher surface tension required higher energy for droplets breakup and also need high heat for

vaporization; thus, it delays the overall process of nanoparticles synthesis inside the SP-HVOFS torch.

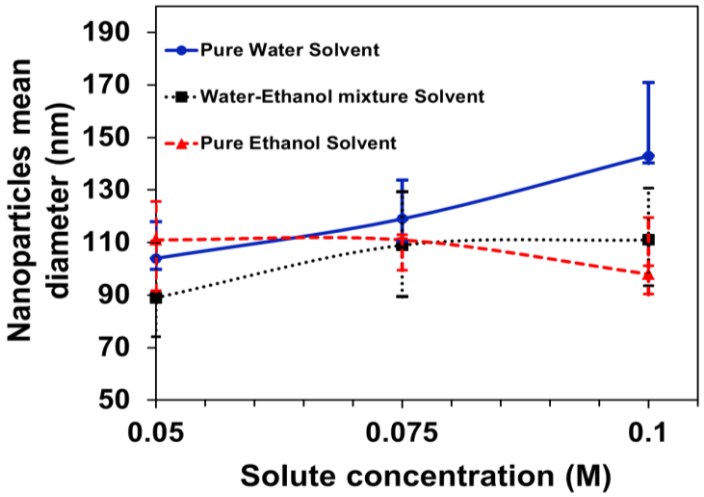


**Figure 4-9** Nanoparticles mean diameter for varied ZrN solute concentrations dissolved in different solvent types (using N1)

### 4.3.5 Effect of Different Injection Types on the Nanoparticles Size and Morphology

For P-W-based precursor carrying high solute concentrations, the atomization becomes compulsory to improve the overall process efficiency. A new atomization technique is applied to obtain small nanosized particles (<100nm) with improved morphology. The ETI uses the twin-fluid flow through a nozzle and at the point of ejection the gas core is confined to a liquid layer; hence, due to the pressure difference between the two fluids, the liquid sheet is shattered by the high-pressure gases. This causes disintegration of the liquid feedstock [93], [94]. However, the plain-orifice N1 and angular injection N2 nozzles use only one fluid which is the solution precursor without any atomizing gas.

The N1 injected the liquid feedstock into the CC of the CH-2000 HVOF torch at a 0º angle of injection. All the droplets travelled along the torch's central axis. It is assumed that from N1 injection, the initial droplet size is equal to the nozzle orifice exit diameter=500µm. The droplet breakup starts inside the HVOF torch due to the velocity differences between the injected droplets and combustion gas. These high relative velocities exert an aerodynamic force onto the injected droplets, thus, the droplet breakup started and continued. The droplets start

heating once they are fed into the CC. By gradual heating inside the torch, they are evaporated and then decomposed to form $ZrO_2$ particles. It is assumed that residence time of the droplets or the formed $ZrO_2$ particles is very small in the case of N1. Due to the lower residence time, the heat transfer between the hot gas-to-droplets or hot gas-to-formed particles is reduced.

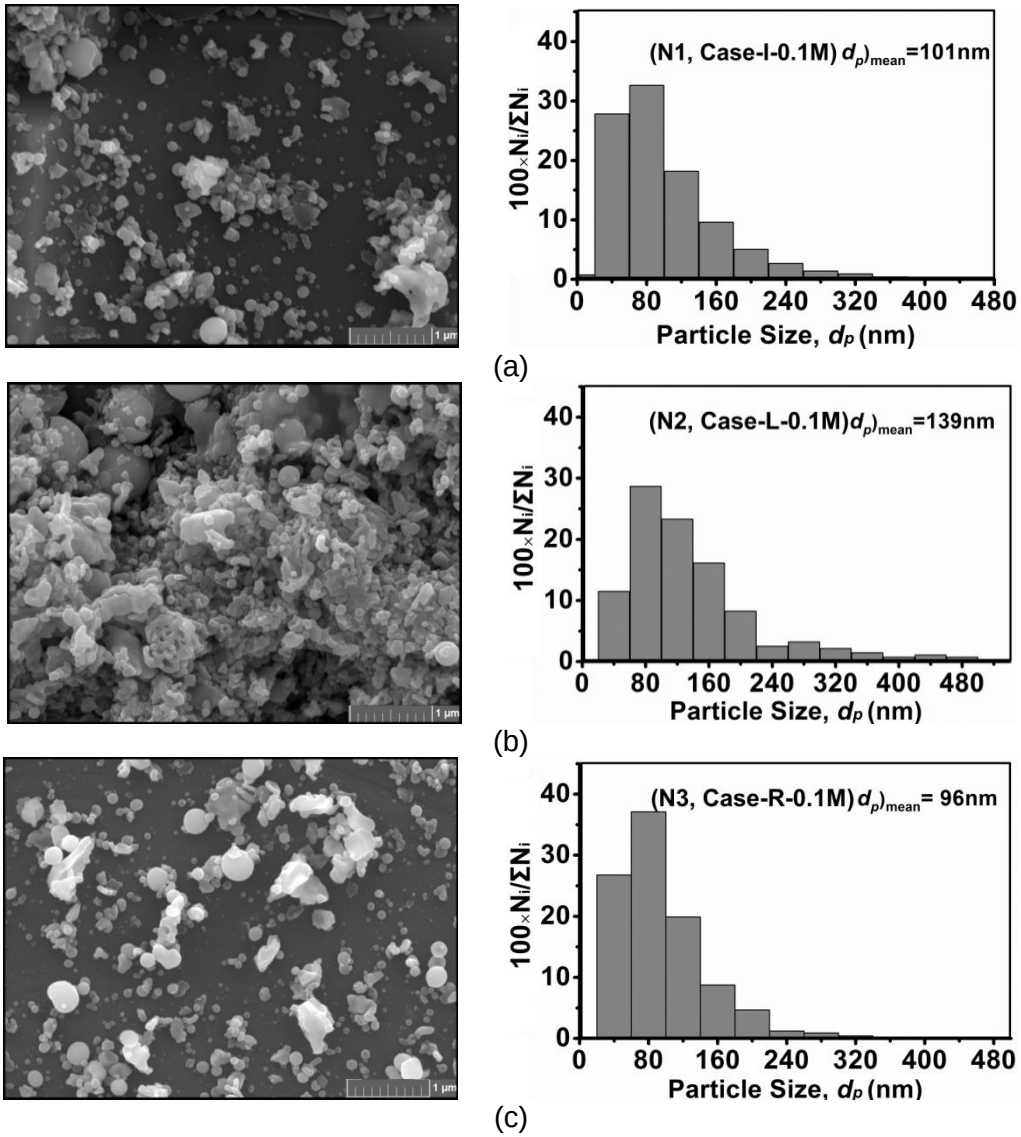


**Figure 4-10** SEM images and nanoparticles size distribution of $ZrO_2$ particles produced from ZrN with 0.1M salt concentrations dissolved in P-E solvent (a) N1, Case-I-0.1M, (b) N2, Case-L-0.1M (c) N3, Case-R-0.1M

**Figure 4-10**a shows the SEM micrograph of nanoparticles generated by using N1 injection scheme. The figure shows very few solid spherical nanoparticles and more non-uniform aggregates of $ZrO_2$, demonstrating that less sintering

time means the particles remain in the form of agglomerates, and small numbers of spherical particles are observed [152]. The average diameter calculations for this type of nozzle show that $d_{p)mean} \leq 100nm$. In angular injection, the liquid feedstock is fed into the CC of the HVOF torch at an angle of 60º. It is assumed that the maximum amount of the solution droplets are evaporated inside the torch CC, and the vapours start converting into $ZrO_2$ particles by the chemical reaction in the barrel section. Thus, these particles remain in the hot flame for a longer time, compared to the injection cases of nozzle N1 and N3. Thus, the $ZrO_2$ particles are melted and form bigger agglomerated clusters of non-homogeneous morphology, as shown in **Figure 4-10**b. The mean diameter observed for the nanoparticles formed by N2 is $d_{p)mean} > 100nm$. In the case of ETI nozzle N3, most of the nanoparticles are solid and spherical, while the size distribution is varied throughout the sample substrate and very few agglomerated particles are observed (**Figure 4-10**c). It is due to the atomization of the precursor droplets, and thus, the smaller droplets generate small solid nanoparticles.

**Table 4-2 Nanoparticles range and mean diameter for different injection nozzles at 0.1M solute concentration with P-E solvent**

| Nozzle type | Nanoparticles diameter range | Mean diameter (nm) |
|---|---|---|
| N1 | 11–457nm | 101 |
| N2 | 30–549nm | 139 |
| N3 | 20–400nm | 96 |

For nozzle N1, the highest nanoparticles size observed in 0.1M concentrations with P-E as the solvent is $d_p=457nm$ (**Table 4-2**). The range of particle size is found to be 11–457nm, whereas, the mean diameter of nanoparticles generated by N1 is $d_p=101nm$. The average diameter of particles generated by using the nozzle N2 is $d_p=139nm$ while the range of nanoparticles size distribution has widened up to 549nm. It can be said that in nozzle N2 the size of nanoparticles is increased due to the increment in the nanoparticles resident time inside the torch. The 60° angle of injection can be reduced to decrease the particles residence time in the torch and to avoid the collision with the walls of torch's

CC. For nozzle N3 the mean diameter is observed as 96nm and the lowest range observed for this kind of nozzle is 20–400nm, (**Table 4-2**). Hence, it can be said that the best results are obtained from nozzle N3 and the worst results from nozzle N2. Therefore, the atomizing nozzle N3 can work efficiently to increase the effectiveness of the SP-HVOFS process.

In all cases, the mean diameter of all nanoparticles remains below $d_p)_{mean}$<150nm, whereas the diameter distribution varies significantly (**Figure 4-11**, **Table 4-2**). In nozzle N1, there is a very different kind of effect and by increasing the solute concentration, the average diameter of nanoparticles reduces. The consequence of this decrement in particle size is not clear and more experiments are required to clarify the effect of increasing nanoparticles concentration on the as sprayed nanoparticles' size and morphology for nozzle N1. The effect of increasing concentrations on nanoparticles size is significant for nozzle N2 in comparison to other cases, and with increasing concentration the particle size is increased. The performance of nozzle N3 is better than all other injection types, where for a higher concentrated solution the mean particle size remains constant (**Figure 4-11**).

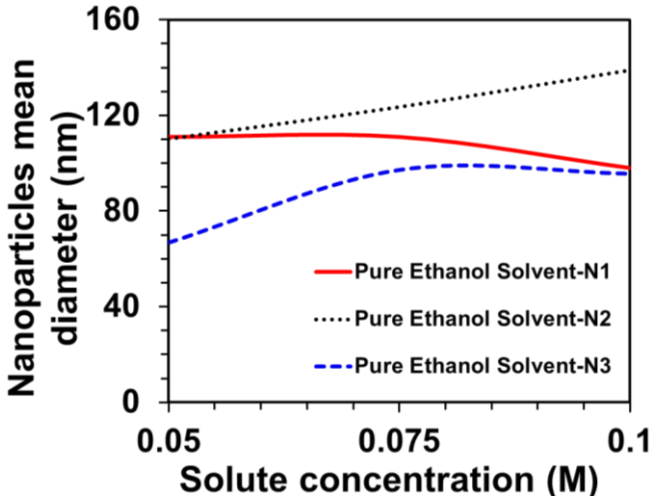


**Figure 4-11** Nanoparticles mean diameter for varied ZrN solute concentrations using nozzles N1, N2 and N3 (solvent type P-E)

It must be noted that the detail analysis of the steps including in the ZrN salt decomposition, species chemical reaction/oxidation and seed particles

nucleation /growth are out of scope of this study and not included in the present research work.

## 4.4 Summary

The SP-HVOFS process is used for the deposition of the $ZrO_2$ particles on the YSZ substrate. The ZrN precursor is prepared in P-W, P-E and W-E mixture solvents. Different solute concentrations, solvents types and nozzles designs are utilized to analyse the variation in nanoparticles deposition. It is determined in this study that the size of nanoparticles and morphology are dependent on the precursor solution concentration and solvents types; thus using pure organic solvent or its mixtures with low solute concentrations can generate smaller size particles with homogeneous morphology. From the above study following conclusions are made:

- The particles at low salt concentration showed spherical morphology with small size distribution while at a higher solution concentration irregular shape, agglomerated and large particles with various size distributions are observed. The higher precursor concentration results in a higher particle density, which increases the frequency of particle collision. Therefore, the growth of nanoparticles is enhanced which widened nanoparticles' diameter and size distribution range.
- Higher heat of vaporization and high surface tension values for P-W limits its use as a solvent. The overall process efficiency decreases with increment in the salt concentration in the P-W-based precursor. The addition of ethanol reduces this deficiency to some extent, and it is proved that the use of P-E improves the nanoparticles morphology and size distribution.
- The efficiency of the SP-HVOFS process is also increased by using precursor droplets atomization techniques. The atomization of the solution precursor decreased the droplet size for both organic and inorganic solvents and improved the overall results.
- From the present study, it is analysed that the best type of injection is the effervescent atomization nozzle. This injection type reduces the average

diameter of nanoparticles, and decreases the overall size distribution and improves the particle morphology.

- The present angular injection nozzle design has an opposite effect on the nanoparticles size and morphology. It generated bigger sized particles with irregular shapes and widened the size distribution due to the increased residence time. It can be modified further, and new design with the optimal angle of injection can increase its efficiency of nanoparticles depositions.

# 5 NUMERICAL ANALYSIS OF AN EFFERVESCENT ATOMIZATION IN SOLUTION PRECURSOR THERMAL SPRAYING PROCESS

## 5.1 Introduction

The solution precursor thermal spraying process (SPTS) is used for the production of the nanosize dense coating to form a TBC layer. Inside the thermal spraying torch, the in situ formation of nanometric-sized particles is mainly dependent on the precursor droplets fragmentation. Droplets disintegration can be achieved by using atomization techniques when injecting solution precursor into the thermal spraying torch. This chapter focuses on the atomization of precursor streams into fine droplets using an effervescent twin-fluid atomizer. As studied in Chapter-4 that the atomization of droplets is necessarily required for water-based precursor solution carrying high solute concentrations to improve process efficiency for generating dense nanosized coating [115]. Thus, the atomization of liquid feedstock can be controlled by the atomizer nozzle design and its injection parameters [92]–[94].

A detailed literature review is added and from previous studies, the best possible techniques are applied to atomize the liquid (Chapter ***2***, section-***2.1.4***). It is highlighted in Chapter-2 that the droplets' SMD is dependent on the operating conditions of the injection nozzle including injection pressure, GLR, injector exit diameter, and liquid physical properties including viscosity, and surface tension [93]. Liquid viscosity has small effects on droplets size and their distribution, and an effervescent atomizer can work efficiently even with highly viscous fluids [106]. Also, smaller liquid density and surface tension will give finer droplet atomization. Furthermore, the atomization phenomena can easily be studied using droplet's Weber and Ohnesorge numbers [104]. Fung et al. [114] numerically analysed the spray atomization under low pressure using LISA model (Chapter ***2***, section-***2.1.4***). It is stated in Chapter ***4*** that atomization of precursor droplets inside the HVOF torch is necessary for successful nanostructured dense coatings and the injection of solution precursor without atomization resulted in large size nanoparticles and may produce porous

coatings. In the present chapter, the solution precursor is atomise into fine droplets inside the CC of the CH-2000 HVOF torch using an ETI nozzle [93], [94], [102].

## 5.2 Methodology

### 5.2.1 Nozzle Design and Manufacturing

The effervescent nozzle is designed according to the structural requirements of the CH-2000 HVOF torch (Chapter ***4***, section-***4.2.1***).

### 5.2.2 Numerical Modelling and Setup

#### 5.2.2.1 Numerical Setup

Firstly, the axisymmetric, two-dimensional grid with a size of 48208 cells is generated (**Figure 5-1**a) for the model validation. The time step size required for this size of mesh is $\Delta t=1x10^{-5}$. The mesh is fine near the spray nozzle exit area for capturing the atomization details. Different cases are simulated for the effervescent nozzle with varied Gas-to-Liquid flow rates ratios (GLRs). The operating conditions of Liu et al. [92], Qian et al. [101], [104] and the present numerical work are $P_{inj}$=0.6MPa, $D_{inj}$=4mm, $m_w$=1.6kg/min and the GLR is varied from 0.067, 0.090, 0.132, 0.176. **Fluent** is used to model the atomization for the effervescent nozzle spray. All numerical equations are discretized by using a second order upwind scheme while the pressure-velocity coupling is solved by SIMPLE scheme. Further cases are simulated for the effervescent nozzle with varied GLR, nozzle exit diameters ($D_{inj}$), injection pressures ($P_{inj}$) and varied types of liquids. Some common injection properties are defined in **Table 5-1**.

Secondly, the axisymmetric, two-dimensional grid for the CH-2000 HVOF torch (Chapter 4, section ***4.2.2***) is considered for the numerical simulations of effervescent atomization in the CH-2000 HVOF torch (grid size=144300 cells, **Figure 5-1**b) [121]–[123]. The time step size required for these simulations is $\Delta t=1x10^{-6}$. The premixed oxy-fuel (O/F) is injected into the CH-2000 torch (**Figure 5-1**b); the resulting hot combustion gases are accelerated inside the CC convergent nozzle and flow through the barrel section towards the exit of the gun. The O/F and droplet injection mass flow rates are selected on the basis of

[121]–[123] (**Table 5-1**). After the numerical simulations of combustion and turbulence of gaseous flow inside the torch, precursor droplets carrying P-W, P-E, and W-E mixture are injected axially into the CC through a central opening (**Table 5-1, Figure 5-1**b). The DPM from Fluent is used to model the droplet breakup and evaporation in the torch for all numerical simulations. The numerical equations are discretized by using a second order upwind scheme while the pressure-velocity coupling is solved by Coupled scheme. The operating conditions and injection properties for the CH-2000 HVOF torch are defined in **Table 5-1**. Also different injection nozzles (**Figure 4-1**a-c) are compared to observe the droplets breakup inside the torch. For all numerical results, the mesh independence studies are considered while the results are not included here for brevity.

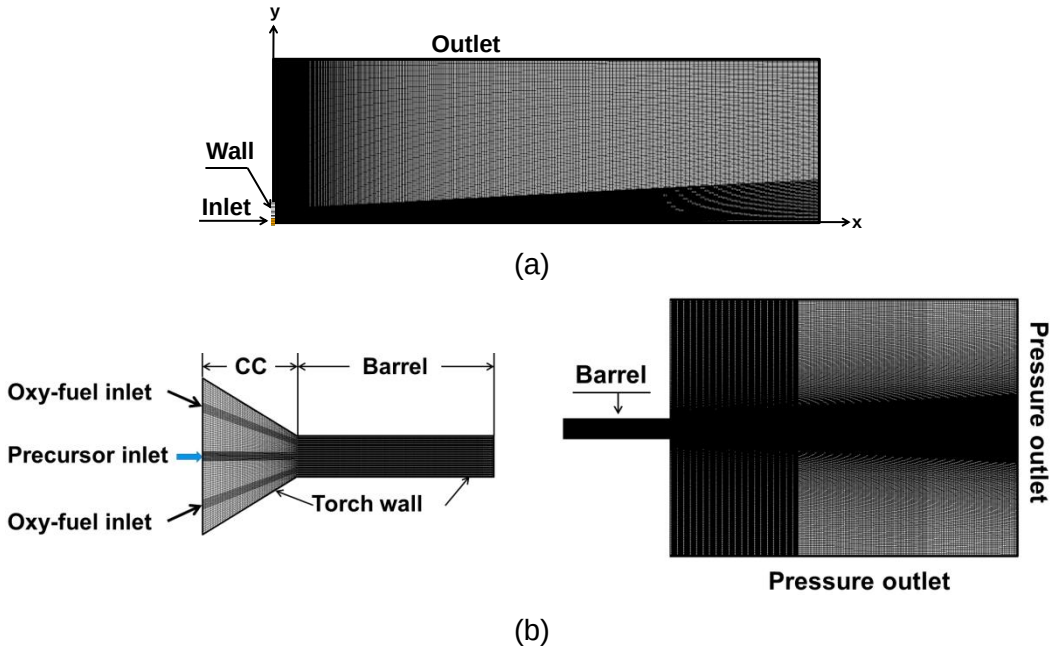


**Figure 5-1** Axisymmetric, two-dimensional grids for (a) spray atomization in atmosphere for model validation (b) spray atomization in CH-2000 HVOF torch application

The numerical modelling of the combustion process in the HVOF torch has been performed by many researchers [20], [22], [24], [157]. Here the droplets of solution precursor, after being injected into the HVOF flame-jet, undergo several physical processes taking place simultaneously. The first stage is the aerodynamic breakup. The secondary breakup of droplets to smaller ones is modeled by the TAB model as the We<100 [115], [118], [136], [158].For the

supersonic combustion of propane inside the CH-2000 torch, a two-dimensional CFD model is employed using the Eulerian continuum approach. The eddy-dissipation model [132], [134], [135] is used to express the reaction rate and to consider the interaction between eddy motion and chemical reaction. Then to capture the droplet dynamics in the domain, the Lagrangian model is coupled with the Eulerian continuum model for the description of multicomponent spray droplet breakup, atomization, transport, and evaporation. The employed mathematical models have been strongly tested against experimental, and numerical data [10], [20], [24], [119] and are not repeated here for brevity (see models detail in Chapter ***3***).

**Table 5-1 Properties of fluids and injection parameters of the atomization nozzle**

| **Injection parameters for the spray in the atmosphere** | |
|---|---|
| Water Density | $\rho_w$=998.2kg/m$^3$ |
| Water Viscosity | $\mu_w$=0.001003kg/m-s (kg m$^{-1}$ s$^{-1}$) |
| Water Surface tension | $\sigma_w$=0.0719N/m |
| Water Mass flow rate | $m_w$=0.00083183kg/s |
| Nozzle-Injection pressure | $P_{inj}$=0.6, 0.7, 0.8MPa |
| Nozzle-Injection diameters | $D_{inj}$=0.5, 1.0, 1.5, 2.0mm |
| Nitrogen flows rates | $Q_{gas}$=6, 8 and 10l/min |
| Gas-to-Liquid mass flow rate Ratio | GLR=0.0456, 0.0912, 0.137, 0.182, 0.228 |
| **Operating conditions and injection parameters for spray in CH-2000 HVOF torch** | |
| Oxygen flow rate | 0.007368kg/s |
| Propane flow rate | 0.001581kg/s |
| Nitrogen flow rate | 0.001349kg/s (Case1-Without droplet injection) |
| Solution precursor flow rate | $Q_{P-W}$=50ml/min ($m_{P-W}$=0.000831833kg/s) |
| Solution precursor flow rate | $Q_{P-E}$=50ml/min ($m_{P-E}$=0.000658333kg/s) |
| Solution precursor flow rate | $Q_{W-E}$=50ml/min ($m_{W-E}$=0.000745083kg/s) |
| Solution precursor flow rate | $Q_{liquid}$=50, 100, and 200ml/min |
| Nitrogen flow rates (N3) | $Q_{gas}$=8l/min |
| Gas-to-Liquid mass flow rate Ratio (N3) | GLR= 0.0456, 0.0912, 0.182 |
| Nozzle-Injection diameters (N3) | $D_{inj}$=0.5, 1.5, 2.0mm |
| Nozzle-Injection pressure | $P_{inj}$=0.7, 0.8, 0.9, 1.0MPa |

### 5.2.2.2 The Governing Equations

Chapter ***3*** provides details for the governing equations in two-dimensional Cartesian tensor form and the Realizable $k-\varepsilon$ turbulence model.

### 5.2.2.3 Primary Breakup Model

The LISA model is applied to capture the primary breakup of ligaments [120]. The motion of the liquid in the injector creates an air core surrounded by the liquid film; the thickness of this film $t$ is related to the mass flow rate $\dot{m}_{eff}$, nozzle exit diameter $D_{inj}$, liquid density $\rho_l$ and axial velocity of liquid film $u = Ucos\theta$ as follows:

$$\dot{m}_{eff} = \pi\rho_l ut(D_{inj} - t) \quad \textbf{(Eq-5-1)}$$

The total velocity is assumed to be related to the injector pressure by:

$$U = k_v\sqrt{\frac{2\Delta P}{\rho_l}} \quad \textbf{(Eq-5-2)}$$

To ensure that the size of the air core is non-negative, the velocity coefficient $k_v$ is given by:

$$k_v = \max\left[0.7, \frac{4\dot{m}_{eff}}{d_o^2\rho_l cos\theta}\sqrt{\frac{\rho_l}{2\Delta P}}\right] \quad \textbf{(Eq-5-3)}$$

Where spray angle $\theta$, and injection pressure $\Delta P$ are assumed to be known.

The pressure-swirl atomizer model includes the effects of the surrounding gas, liquid viscosity, and surface tension on the breakup of the liquid sheet. The model assumes that a two-dimensional, viscous, incompressible liquid sheet of thickness $2h$ moves with velocity $U$ through a quiescent, inviscid, incompressible gas medium. The liquid and gas have densities of $\rho_l$ and $\rho_g$, respectively, and liquid viscosity of $\mu_l$. The infinitesimal wavy disturbance imposed on the initial steady motion has the form of:

$$\eta = \eta_o e^{-ikx+\omega t} \quad \textbf{(Eq-5-4)}$$

Where $\eta_o$ is the initial wave amplitude, $k = \frac{2\pi}{\lambda}$ is the wave number, and $\omega = \omega_r + i\omega_i$ is the complex growth rate. The most unstable disturbance can be calculated from the dispersion relation as a function of wave number $\omega = \omega(k)$ [159].

The sheet breaks up and the ligaments formed with length given by:

$$L_b = \frac{U}{\Omega}\ln\left(\frac{\eta_b}{\eta_o}\right) \quad \textbf{(Eq-5-5)}$$

Where $\ln\left(\frac{\eta_b}{\eta_o}\right)$ is an empirical sheet constant, Dombrowski and Hooper [160] showed that a value of 12 for the sheet constant agreed favourably with

experimental sheet breakup lengths over a range of We from 2–200. The breakup from ligaments to droplets is assumed to behave according to Weber's analysis [161]:

$$d_o = 1.88 d_L (1 + 3Oh)^{1/6} \quad \textbf{(Eq-5-6)}$$

Once $d_o$ is determined this droplet diameter is assumed to be the most probable droplet size of a Rozin-Rammler distribution with a spread parameter of 3.5 and dispersion angle of 6°.

Additional details of the model are in [159].

#### 5.2.2.4 Secondary Breakup Model

The secondary breakup of droplets is modelled by the TAB model (see section-***3.2.4.3***).

#### 5.2.2.5 Droplets Collision and Coalescence Model

In **Fluent**, the collision model assumes that the frequency of collisions is much less than the particle time step. This model is most applicable for low We collisions where collision results in bouncing and coalescence. If the droplets collide head-on, then the outcome tends to be coalescence, whereas, in bouncing collision the outcome is more oblique. The probability of coalescence can be related to the offset of the collector droplet centre and the trajectory of the smaller droplet. The critical offset is a function of the collision We and the relative radii of the collector and smaller droplet.

The critical offset is calculated by O'Rourke [162] using the expression:

$$b_{crit} = (r_1 + r_2)\sqrt{min\left(1.0, \frac{2.4f}{We}\right)} \quad \textbf{(Eq-5-7)}$$

Where $f$ is a function of $\left(\frac{r_1}{r_2}\right)$, defined as:

$$f\left(\frac{r_1}{r_2}\right) = \left(\frac{r_1}{r_2}\right)^3 - 2.4\left(\frac{r_1}{r_2}\right)^2 + 2.7\left(\frac{r_1}{r_2}\right) \quad \textbf{(Eq-5-8)}$$

$r_1$ and $r_2$ are the radii of colliding larger and smaller droplets respectively.

## 5.3 Results and Discussions

### 5.3.1 Model Validation

The validation of the LISA model used in the present work is demonstrated in **Figure 5-2**. Here, the experiments using an effervescent atomizer nozzle by Liu et al. [92] and numerical work of Qian et al. [101], [104] are used for the validation. The LISA model and the numerical and experimental work considered here for validations use the effervescent nozzle spraying the water into the atmosphere.

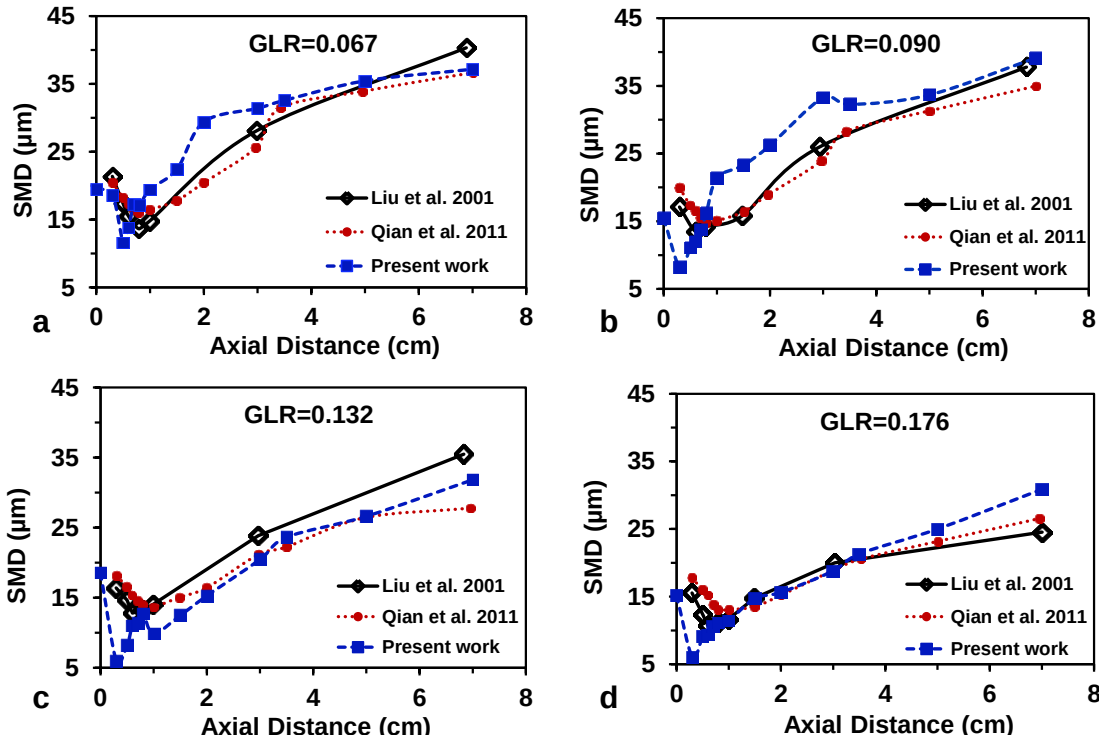


**Figure 5-2** Comparison of the predicted results at different GLRs with the work of Liu et al., 2001 (experimental) [92] and Qian et al., 2011 (numerical) [101], [104], (a) GLR=0.067, (b) GLR=0.090, (c) GLR=0.132, and (d) GLR=0.176

The operating conditions of [92], [101], [104] and the present numerical work are $P_{inj}$=0.6MPa, $D_{inj}$=4mm, $m_w$=1.6kg/min and GLR is varied from 0.067, 0.090, 0.132, 0.176. **Figure 5-2** depicts that the present numerical model can correctly predict the value of SMD for the spray droplets along the axial direction. Also, the LISA model performs better for higher GLRs (0.132 and 0.176) while it shows some deviation along the axial direction (from 1–3cm) for lower GLRs of 0.067 and 0.090. Overall analysis shows that droplets diameter first decreases and then increases along the axial direction [92], [93], [101], [104]. This

happens due to the presence of higher relative velocities between atomization gas and droplets near the nozzle exit region. However, in the downstream region, the droplets with lower velocities collide with each other, and coalescence takes place, causing an increment in the droplet diameter [101], [104]. Moreover, these results indicate that the increment in the GLR from 0.067–0.176 decreases the size of the droplets and increases the atomizer efficiency.

### 5.3.2 Effect of Varied Injection Parameters on Sauter Mean Diameter

#### 5.3.2.1 Effect of varied GLR

In SPTS applications, it is desired that a small amount of atomization gas is injected to achieve good atomization with small droplet size, as the higher GFR will cool the HVOF flame jet, and decreases its energy. The effervescent atomizer is used to be optimized by controlling the GLR and can operate well at lower GLR [103]. **Figure 5-3**a illustrates the graphical comparison of SMD with varied GLR. The nozzle exit diameter is 1.5mm, and the operating pressure is set at 0.7MPa while the liquid flow rates (LFRs) are changed. As mentioned in the captions, **Figure 5-3**a have a constant GFR ($Q_{gas}$) of 8l/min while LFR ($Q_{P\text{-}W}$) vary from 50–200ml/min. Increase in the SMD is observed by an increment in the water injection flow rate from 50–200ml/min, and larger size droplets are observed for lower GLR values [94]. The reason is that less gas quantity is supplied to disintegrate a large amount of liquid, so less energy is transferred to the liquid which generates bigger diameter droplets. **Figure 5-3**a also demonstrates that this effervescent atomizer is capable of producing a spray with the initial droplet size of less than 20µm up to a spray distance of 3cm. Also, the droplet size remains well below 50µm till it reaches a spray distance of 10cm from the nozzle exit. Hence, the spray nozzle is capable of producing high atomization energy that keeps the size of droplets below 50µm.

When this ETI nozzle is used for the injection of P-E in the CH-2000 HVOF torch, the reduction in the SMD has been enormously increased (**Figure 5-3**b). As the HVOF combustion flames have higher amount of kinetic energies that supports the droplets disintegration inside the HVOF torch. Moreover, in the flame jet, P-E droplets are evaporated and the droplets completely converted

into the ethanol vapours which then burn inside the torch and improved its thermal and kinetic energies. However, the increment in the P-E's LFR ($Q_{P-E}$) has an adverse effect on the droplet breakup, and at higher LFR the reduction in SMD is small as compared to lower LFR. Nevertheless, for all cases droplet size remains well below 25µm. Thus, it can be said that this type of atomizer can work well for precursor injection in the HVOF torches for the production of nanosize particles that lead to the generation of dense coatings.

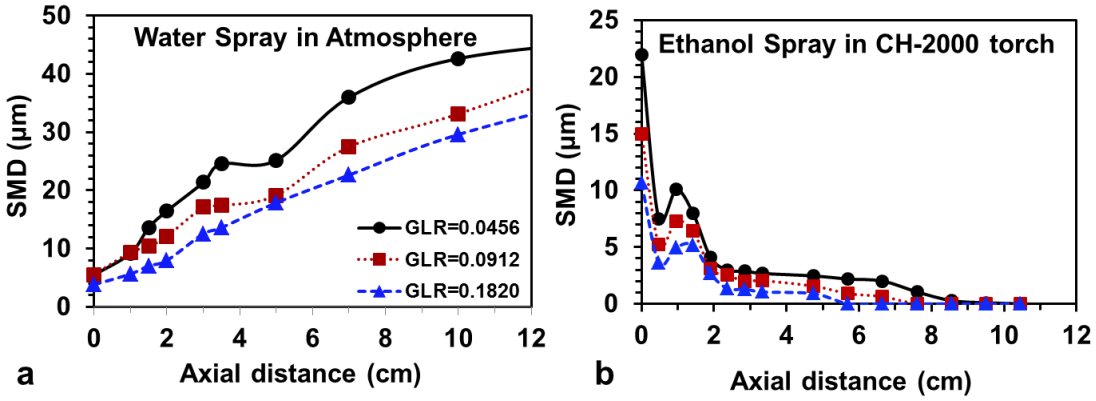


**Figure 5-3** Comparison of SMD at varying GLR with $Q_{gas}$=8l/min (●) $Q_{liquid}$=200ml/min, (■) 100ml/min, and (▲) 50ml/min for (a) Water spray in atmosphere and (b) Ethanol spray in CH-2000 torch

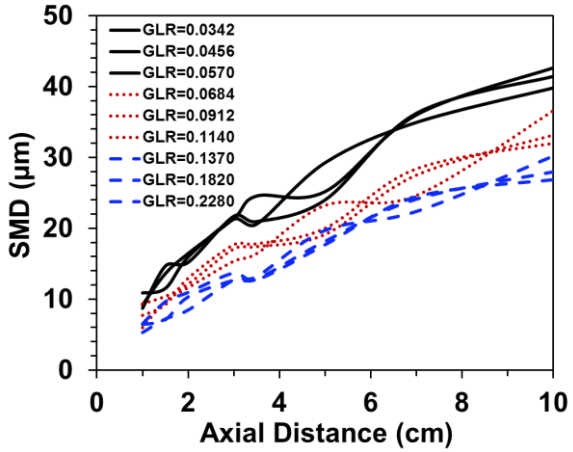


**Figure 5-4** Variations in SMD with different GLR along the axial direction [The blue dashed lines LFR=50ml/min, the red dotted lines LFR=100ml/min, and the solid black lines are for the LFR=200ml/min]

Different cases are simulated for the P-W spray into the atmosphere with varied GLR. It is observed that when the GFR is increased while keeping the LFR constant, a small effect on SMD is detected (**Figure 5-4**). The GFR are 6, 8 and 10l/min.; the blue dashed lines are for the smallest LFR of 50ml/min, and the

droplet size remains below 30µm (d<30µm) throughout the spray region. No significant effects of increasing GFR from 6–10l/min over the SMD are observed. For 100ml/min LFR, the largest droplet sizes are in the range of 30–38µm (red dotted lines in **Figure 5-4**). The solid black lines are for the LFR of 200ml/min and the droplet size increases up to 40–42µm when the GFR changes from 10–6l/min. Bigger droplet diameters are detected for high LFR when compared to low LFR throughout the axial distance of spray region from 1–10cm. Hence, the smallest values are observed when the small LFR are sprayed out, and it improves the efficiency of the effervescent type nozzle. Thus, it can be said that higher GLR increases the efficiency of the droplets breakup.

#### 5.3.2.2 Effects of different nozzle exit diameters ($D_{inj}$)

Lefebvre et al. [97] found that by using a small diameter orifice the smallest droplet size can only be produced with lowest GLR and low operating pressures. While for GLR>0.08 and pressure $P_{inj}$>138kPa they concluded that atomization is insensitive to the diameter of the discharge orifice [97], [163]. Moreover, it is understood that the advantage of using a bigger diameter orifice can eliminate the problems of contamination. In the present work some cases are simulated with a constant value of $P_{inj}$=0.7MPa and GLR=0.182, and varied injector orifice diameters of 0.5, 1.0, 1.5 and 2mm, to analyse the effect over spray atomization. **Figure 5-5**a, illustrate that nozzle exit diameter has some impact on the SMD in the far field region of spray at *x*>3cm while no significant difference is observed in the near-nozzle exit region. Moreover, the lowest droplet size is observed for the biggest nozzle exit diameter of $D_{inj}$=1.5mm while larger droplet sizes are seen at the smallest diameter orifice of D=1.0mm; the reason could be the insensitiveness of model with respect to $D_{inj}$, as the dependence of SMD is more visible when the values of model inputs such as spray half angle, liquid sheet constant and atomizer dispersion angle are varied. In the present LISA model, all injection parameters remain constant, and only $D_{inj}$ is varied, and it is one of the reasons that insignificant effects over the SMD are observed.

The increase in the effervescent nozzle exit diameter has minor effects over the SMD when P-E is sprayed into the CH-2000 torch (**Figure 5-5**b). Near the nozzle exit region, it is observed that the initial droplets size observed for the smallest $D_{inj}$=0.5mm is $d_i$=18µm compared to $d_i$=12µm and 11µm for $D_{inj}$=1.5mm and 2.0mm respectively. However, the droplet fragmentation is greater for $D_{inj}$=0.5mm compared to that of $D_{inj}$=1.5mm and 2.0mm. Overall it is observed that the effervescent nozzle work efficiently even with the bigger $D_{inj}$. Thus, this type of injection nozzle can be beneficially used in the suspension and solution precursor thermal spraying with diminishing clogging.

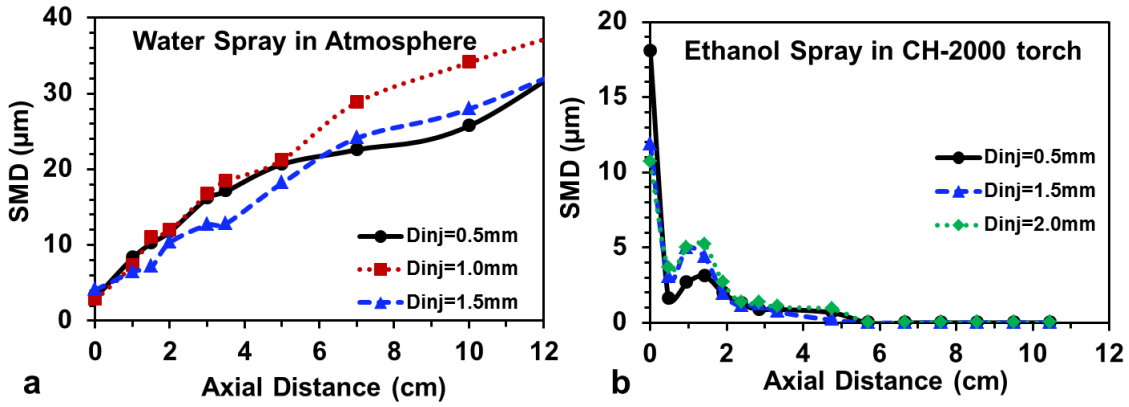


**Figure 5-5** Comparison of SMD at constant GLR=0.182 and Pinj=0.7MPa with various nozzle exit diameters (Dinj) at different operating pressures (a) Water spray in atmosphere and (b) Ethanol spray in CH-2000 torch

### 5.3.2.3 Effects of different injection pressures ($P_{inj}$)

It is shown that droplet size may decrease with an increase in operating pressure of the effervescent nozzle working with low mass flow rates [94], [103] and that the atomization quality increases effectively at higher injection pressures [97], [163]. Here, the spray atomization is analysed with different injection pressure ($P_{inj}$) at constant GLR of 0.182 and nozzle exit diameter of $D_{inj}$=1.5mm. Experimentally keeping the GLR constant while increasing or decreasing the value of injection pressure is not possible until the GFR or LFR are altered. However, in these numerical simulations, all parameters remain constant, only the injection pressure is increased. Therefore, it is observed (**Figure 5-6**a) that increments in injection pressure have small effects on the SMD in the downstream region while the SMD at the near-nozzle exit region has no variations. Overall, increasing the delivery pressure has no significant

impact on the SMD while keeping GLR and all other parameters constant. Again the reason could be the LISA model input parameters, and it is required to select appropriate input values to predict the variations in the SMD for increased injection pressures.

In **Figure 5-6**b, the SMD is plotted against different $P_{inj}$ for the spray in the CH-2000 torch. At varied $P_{inj}$ of 0.7–1.0MPa the initial droplet size is reduced from 10.57–to–7µm while near the exit of the torch's CC the droplet size varied from 4–to–3µm for 0.7–1.0MPa $P_{inj}$ variations. Thus, it can be said that no significant variations are observed even at higher $P_{inj}$=1.0MPa, and droplets size remains <12µm for all cases. Thus, it can be said that variation in delivery pressure has no significant effects on the SMD for this type of effervescent atomizer used in the CH-2000 torch.

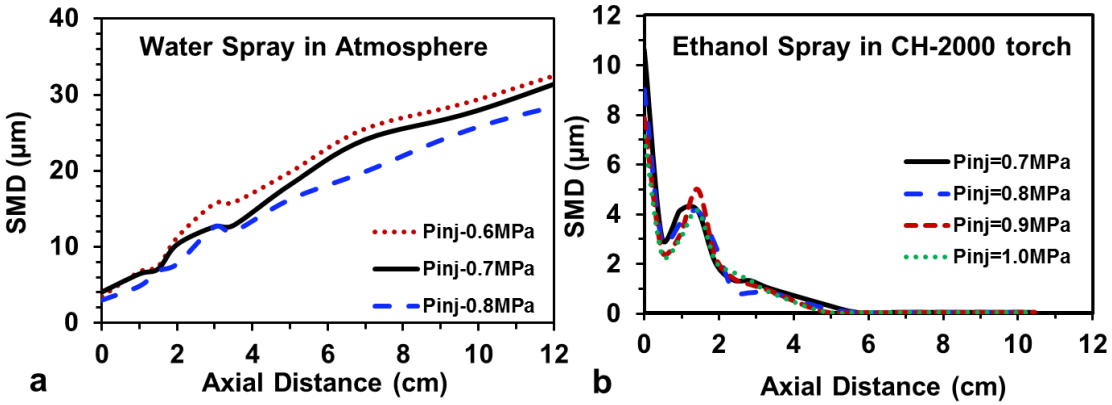


**Figure 5-6** Comparison of SMD at constant $D_{inj}$=1.5mm and GLR=0.182 with various injection pressures ($P_{inj}$) (a) Water spray in atmosphere and (b) Ethanol spray in CH-2000 torch

### 5.3.2.4 Effects of different liquid/ solvent

The effervescent atomizer is tested to atomize various liquids including P-W, P-E and W-E mixture with different viscosities and surface tensions. The physical properties of these liquids are given in **Table 5-2**. It is stated in [93], [106] that liquid viscosity has small effects on droplet size and its distribution and effervescent atomizer can work efficiently even with highly viscous fluids. Also, smaller liquid density and surface tension will give finer droplet atomization. Moreover, the We plays a significant role in the analysis of droplet disintegration phenomena [104], [105]. The definitions of the $We = \frac{\rho_c v_{rel}^2 d}{\sigma}$ and $\mathrm{Oh} = \frac{\mu}{\sqrt{\rho \sigma d}}$

containing the thermophysical properties of fluid like density ρ, surface tension σ and droplet viscosity μ, and hence the atomization phenomena can easily be studied by the droplet Weber and Ohnesorge number [104], [105]. **Figure 5-7**a shows the comparison of the We for two different liquids P-W and P-E spray in the atmosphere. It is seen in this graph that P-E has the higher values of We in comparison to P-W. We know from the property data in **Table 5-2** that the value of the surface tension of P-W ($\sigma_{P\text{-}W}$=71.940×10$^{-3}$N/m) is three times that of P-E ($\sigma_{P\text{-}E}$=22.348×10$^{-3}$N/m) and therefore, higher surface tension declines fragmentation and higher gas kinetic energies are required to disintegrate the P-W droplet, as compared to that for P-E. Furthermore, the value of We is higher in the near-nozzle exit regions for both fluids. It decreases gradually along the length of spray, and then in the far field regions of spray, x>10cm the value of We again increases. So the main fragmentation is occurring in near exit regions and far field regions of an effervescent spray into the atmosphere (**Figure 5-7**a).

**Table 5-2 The thermophysical properties of various liquids**

| Name | Density kg/m$^3$ | Viscosity kg/m-s | Surface tension N/m (dyne/cm) |
|---|---|---|---|
| P-W | 998.2 | 0.001003 | 0.0719404 (71.9404) |
| P-E | 790 | 0.0012 | 0.022348 (22.348) |
| W-E | 894 | 0.0011015 | 0.047144 (47.144) |

In analysing the effects of various liquid properties on the effervescent atomization in the CH-2000 torch, different simulations are performed based on **Table 5-2** data and the results are shown in **Figure 5-7**b–c. **Figure 5-7**b demonstrates the variations in the droplet diameter for liquids with different thermophysical properties. It is determined that the droplet diameter is increased by a rise in the liquid density, viscosity and surface tension. The initial values of SMD at *x*=0cm is highest for P-W case (19μm) and lowest for P-E case (11μm). It is according to previous findings that the droplet size increases with increment in the surface tension of liquids [101]. Here, the P-W has the maximum surface tension of 0.071904N/m and higher values of SMD in the near-nozzle exit regions (from x=0–10cm) are observed. Moreover, for P-W and W-E mixture cases, the droplet size is further increased in the axial distance due to the coalescence. The P-E droplets observed a reduction in diameter with

slight coalescence occurred in the mid-section of torch CC, and then they evaporated completely at x=5.8cm in the barrel section. Finally, it is predicted that even with high surface tension liquid such as P-W, the droplet SMD remain below 20µm; and this ETI nozzle can efficiently work as a good atomizer.

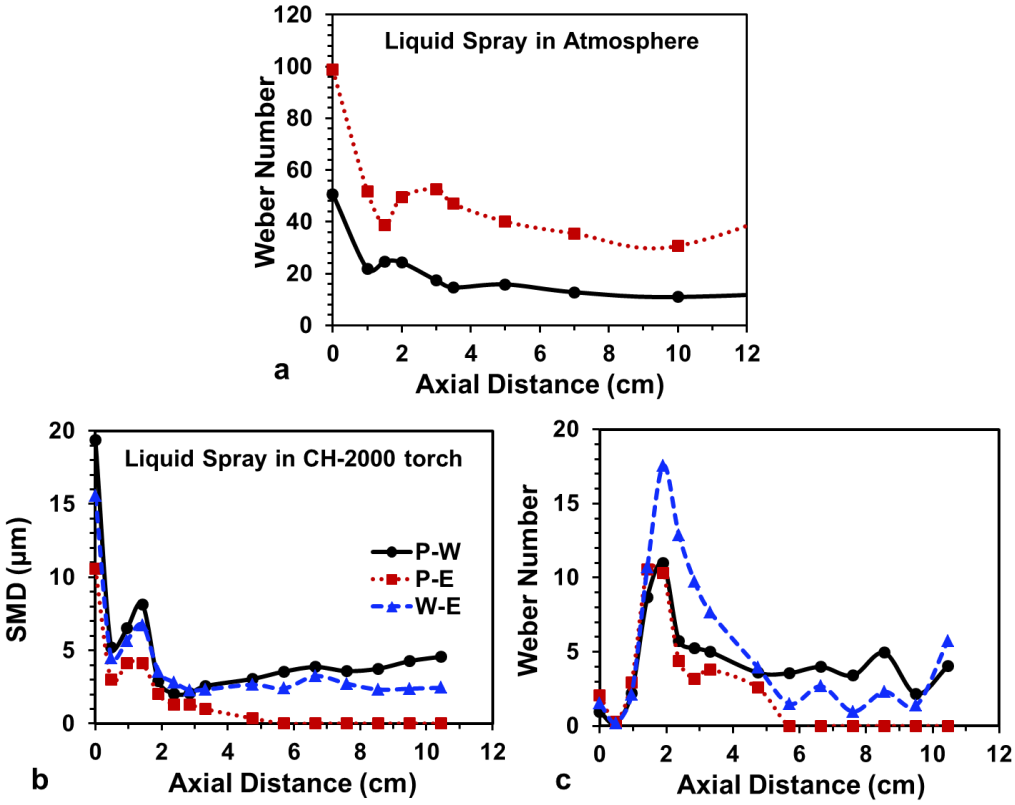


**Figure 5-7** Comparison of SMD, at constant $P_{inj}$=0.7MPa, GLR=0.182, and $D_{inj}$=1.5mm, for various liquid spray in (a) atmosphere, (b) CH-2000 torch, and (c) the Weber number of various liquid sprayed in CH-2000 torch

Comparison of We variations for droplets in the computational domain is depicted in **Figure 5-7**c. In the case of P-W, the We reached a peak value of about 12 near the exit of CC; whereas, the primary atomization occurs due to relative velocities between the droplets and the gas phase in the CC. However, the value of We remains below 14 for P-W and P-E cases, while for W-E multicomponent droplet mixture We=18. As mentioned above that value of the surface tension of P-W is three times of P-E; thus, in the CH-2000 torch, the increment in surface tension also deteriorates the precursor's droplets fragmentation (**Table 5-2**).Overall, it can be said that this type of ETI nozzle can

perform efficiently even with higher values of surface tension, viscosities and densities [101], [106].

#### 5.3.2.5 Effects of different nozzles types

The three different types of nozzle designed and used in Chapter 4 (section-***4.2.1***) are tested numerically to observe clearly the impact over the droplets disintegration. As mentioned previously that plain-orifice nozzle N1 and angular injection nozzle N2 use only single fluid solution precursor without any atomizing gas. The N1 injected the liquid into the CC of the CH-2000 HVOF torch at a 0º angle of injection, and all the droplets travelled along the torch's central axis (**Figure 5-8**a). As stated earlier that the nozzle N1 exit diameter is 0.5mm and the initial diameter of droplets ejecting out from the nozzle is $d_{i)N1}$=500µm. The droplet breakup starts in the CH-2000 HVOF torch due to high relative velocities. These velocities exert an aerodynamic force onto the injected droplets, and the droplet breakup started and continued. A comparison of droplets diameter reduction is shown in **Figure 5-8**b for various nozzles N1, N2 and N3. The graph of N1 demonstrates the secondary breakup and a decrease in the diameter of 500µm droplets; it can be seen that droplets experience a sharp decrease in diameter from 500µm–125µm, and 125µm–35µm in the torch's CC and at x=4.75cm, the droplets disappeared due to the complete evaporation in the barrel section.

In angular injection, the liquid feedstock is fed into the HVOF torch at an angle of 60º (**Figure 5-8**a). Here, the initial droplet size is equal to the nozzle exit diameter $d_{i)N2}$=300µm. In case of nozzle N2, the 60º angle of injection is very high, and it causes the droplets to collide with the torch's CC walls and then converges back to the centreline axis of the torch as seen in **Figure 5-8**a. As the size of exit orifice diameter is smaller, ($d_{i)N2}$=300µm) the droplet reduction increases for the N2 injection nozzle. Thus, due to the reduced injection diameter N2 shows a faster reduction in droplet diameter as compared to N1. For N2, a sharp decrease in the droplet diameter is also detected in the torch's CC from 300µm–75µm and then from 75µm–25µm and at x=10.5cm the droplet diameter is reduced to 1µm and are completely evaporated at x=15cm.

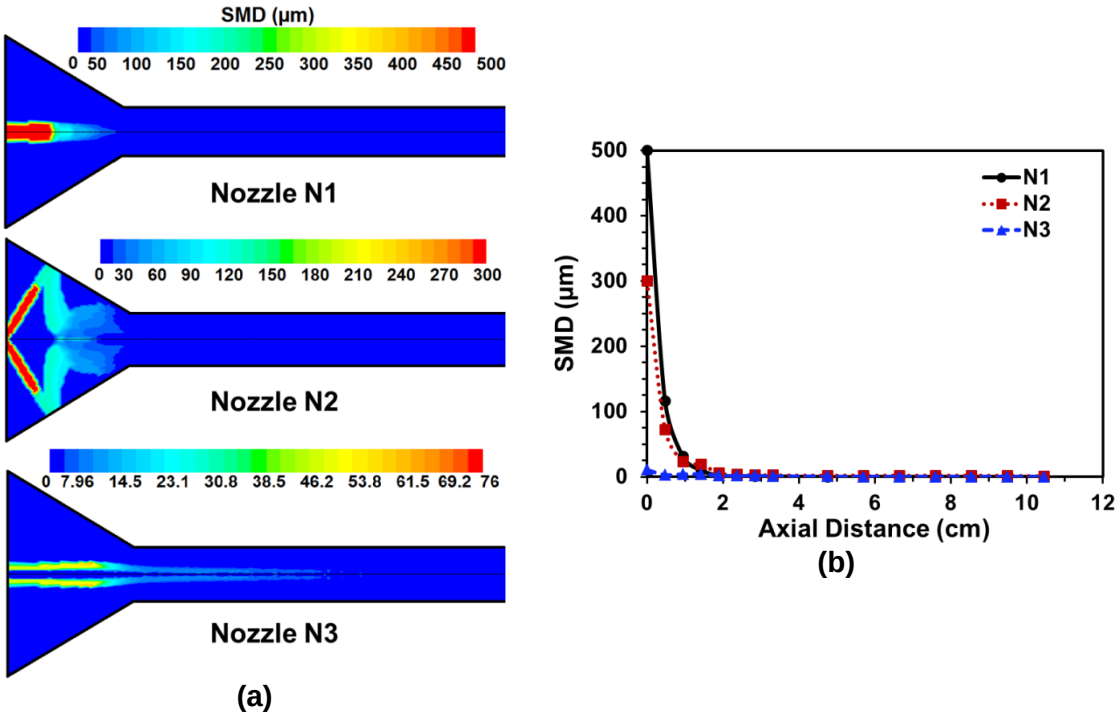


**Figure 5-8** Comparison of SMD using P-E solvent injected at constant $P_{inj}$=0.7MPa, GLR=0.182, and with varied nozzle types (a) Contours plot, and (b) graphical representation

The new ETI technique is applied to disintegrate the precursor droplets to smaller size<20μm that resulted in the formation of nanoparticles' sized<100nm with improved morphology (as mentioned in Chapter 4, section-4.3.5). The ETI nozzle N3 uses the twin-fluid flow through a nozzle and at the point of ejection the gas core is confined to a liquid layer; hence, due to the pressure difference between the two fluids, the liquid sheet is shattered by the high-pressure gases (**Figure 5-8**a). This causes disintegration of the liquid feedstock [93], [94]. In case of nozzle N3, due to the atomization of the precursor droplets the smaller size droplets d=11μm are formed at the point of initial injection x=0cm (**Figure 5-7**b (case P-E), **Figure 5-8**b). These droplets further fragmented into d=3μm inside the CH-2000 torch's CC. Small coalescence is observed in the middle of CC, and the droplet size becomes d=4μm, but due to higher relatives velocities, these droplets shattered into the smaller size and got evaporated completely in the barrel section at x=5.7cm. In numerical simulations it is needed to have a sufficiently fine mesh to adequately capture regions where the flow will experience rapid change in key variables such as pressure, velocity or

temperature. As seen in **Figure 5-1**b, the similar mesh size has been utilized for all types of the solution precursor injection nozzles. Hence, it could be said that for different types of injection nozzles an optimization of the mesh near injection regions would further improve the results. And droplets breakup and dispersion can be captured more accurately in these regions.

Overall, the best performance is observed for nozzle N3 compared to all other injection types (**Figure 5-8**a–b). The effervescent atomization can improve the droplets' fragmentation that leads to complete evaporation of the solution or suspension carrying the nanoparticles. Thus, the in-situ heating process of reduced sized solution or suspension droplets can result in the formation of smaller size nanoparticles with the improved morphology (as demonstrated in Chapter 4 result section-***4.3.5***). Moreover, the thermophysical properties of liquid solution or suspension have no significant effects on the performance of the effervescent atomizer, and even with the higher density, viscosity or surface tension the mean droplets size remains well below 20µm (**Figure 5-7**).

## 5.4 Summary

The phenomenon of effervescent atomization is analysed numerically for precursor droplets disintegration. The droplet size distribution is measured for different GLR, $D_{inj}$, $P_{inj}$, various types of solvent and injection nozzles. CFD modelling is performed using the LISA model and validated by the previous work. Different injection parameters are numerically tested, and results are compared to observe the effects on droplet disintegration. Furthermore, the impact of liquid properties on droplet fragmentation is analysed by using various liquids P-W, P-E and W-E mixture. Finally, the ETI nozzle is compared with other injection nozzle types. Following are the conclusions made out of the present work:

- The LISA model can predict variations in spray atomization with respect to changing injection parameters, and is in good agreement with the experimental results.
- In overall comparison, it is analysed that the droplets size is significantly varied with the external spray conditions. The spray in the atmosphere has droplet size ranged from 10–44µm, and due to the droplet's

coalescence SMD increased in the axial direction. Whereas, in case of spray in the CH-2000 HVOF torch, the droplet size reduced from 20–3µm, and coalescence is insignificant. The reason is the evaporation of the droplets in the high-temperature zones of the HVOF torch.

- It is concluded that effervescent atomization is significantly dependent on GLR variations. An increase in the GLR will increase the efficiency of atomization hence generate smaller size droplets. The present effervescent nozzle design works efficiently with GLR 0.034–0.228.
- Moreover, the effects of nozzle exit diameter and injection pressure observed by the LISA model are not very significant. The reason could be the use of constant input values of spray half angle, liquid sheet constant and atomizer dispersion angle.
- For the spray in the atmosphere, the Weber number demonstrates that liquids having higher surface tension require more energy to disintegrate at the first point as compared to lower surface tension fluids. While the effect of various fluid properties such as density, viscosity and surface tension has no significant impact on the performance of the effervescent atomization inside the CH-2000 torch and the droplet size remains below 20µm even for P-W case.
- It is concluded that droplets breakup and dispersion has been enormously improved by using the effervescent type nozzle. Because the best atomization is observed for the effervescent type nozzle N3 when compared to plain orifice type nozzle N1 and angular injection type nozzle N2.

# 6 MODELLING OF MULTICOMPONENT DROPLET INJECTION IN HIGH-VELOCITY OXYGEN FUEL THERMAL SPRAYING TORCH

## 6.1 Introduction

Classic methods of powder spraying are difficult to use for nanosize particles spraying. To overcome this problem suspension and solution precursor thermal spraying has been introduced which easily handle flowability of nanosize particles [125]. For this purpose, ethanol, water and their mixture have been used as a solvent in suspension thermal spraying. The effect of a liquid feedstock over combustion gases, droplet disintegration, and evaporation is modelled by Dongmo et al. [10], [14], Taleby & Hossainpour [130] and Gozali et al. [116]. Different injection parameters are varied, including injection velocity, injection position, droplet sizes, and their effects on the process gas dynamics, and droplet evaporation are analysed.

In this chapter, a CFD model is used for analysing the effect of droplet fragmentation and the vaporization process on the combustion gases while injecting varied W-E mixtures in the HVOF torch. It is detected that the W-E mixture takes more heat to vaporize than P-E; this is because the latent heat of vaporization for P-E is 846kJ/kg, whereas the latent heat of vaporization is 2257kJ/kg for P-W [164]. Furthermore, for reasons stated above the time required for P-W and W-E mixture droplet to vaporize is significantly greater than the vaporization time of P-E. It is found that P-E is preferable to P-W as a solvent because it has better droplet fragmentation ability, consumes less time for complete evaporation and vaporizes completely long before reaching the spray gun exit [43]. Also, we know from the property data of P-W and P-E that the value of surface tension of water ($\sigma_w$= $72\times10^{-3}$N/m) is three times that of ethanol ($\sigma_{eth}$= $22\times10^{-3}$N/m). Therefore, higher surface tension declines fragmentation and water and its mixtures usually consume more hot gas energy to become fully vaporized [165].

## 6.2 Problem Description

The modelling and simulation of HVOF thermal spraying are performed by using **Fluent** code. In this chapter, details of a numerical study are presented for understanding the phenomenon of multicomponent droplet fragmentation and evaporation. Here the multicomponent droplets of W-E mixture with different sets of mass fractions are used. The mass fractions of ethanol are varied from 1.0–0; whereas the mass fractions of water are varied from 0–1.0 respectively. The HVOF gun geometry used in this study is the DJ2700 torch with $L_{FJ}$=200mm (**Figure 3-1**, **Table 3-1**). The operational details are mentioned in **Table 6-1**, and the axisymmetric mesh is illustrated in **Figure 6-1**. The droplets are injected into the CC with an initial speed of 30m/s, and mass flow rate of $1\times10^{-4}$kg/s while the diameter of droplets is 300μm with the initial temperature of 300K (**Table 6-1**). The thermophysical properties of ethanol and water are a function of the temperature and are inserted into the solver by utilizing properties of pure liquid taken from [89] and curve-fitted in their temperature range (**Table 6-2**).

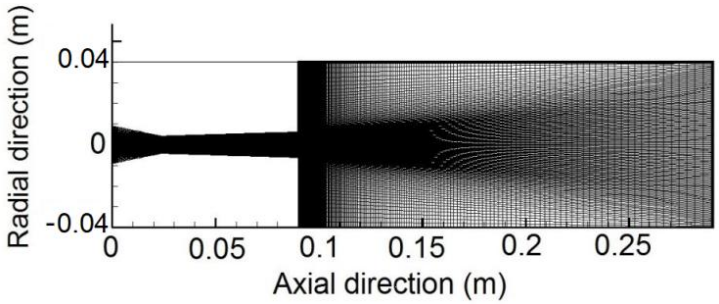


**Figure 6-1** The mesh of DJ2700 HVOF torch

**Table 6-1 The Working conditions of DJ2700 HVOF torch**

| Working Conditions | | |
|---|---|---|
| Fuel Flow rate | 0.004kg/s | Temp. 300K |
| Oxygen Flow rate | 0.014kg/s | |
| Air Flow rate | 0.002kg/s | |
| Atm. Pressure, Temp. | 101325Pa | |
| Wall boundary Temp. | Non-slip | |
| Droplet diameter & initial Temp. | 300μm | |
| Droplet flow rate, & initial velocity | $1\times10^{-4}$kg/s, 30m/s | |

## Table 6-2 Thermophysical properties of pure liquid ethanol and water

| Property | Liquid | |
|---|---|---|
| | **Ethanol** | **Water** |
| Density kg/m³ | $\rho_{C2H5OH} = aT^4 + bT^3 + cT^2 + dT + e$<br>$a = -3.35084 \times 10^{-8}$<br>$b = 3.62174 \times 10^{-5}$<br>$c = -1.51788 \times 10^{-2}$<br>$d = 2.06108$<br>$e = 824.718$<br>Tmin.=159.055K, Tmax.=489.05K | $\rho_{H2O} = aT^3 + bT^2 + cT + d$<br>$a = -5.67516 \times 10^{-7}$<br>$b = 1.97888 \times 10^{-4}$<br>$c = -0.2272$<br>$d = -1060.20$<br>Tmin.=273.16K, Tmax.=333.15K |
| | | $\rho_{H2O} = aT^2 + bT + c$<br>$a = -8.0 \times 10^{-4}$<br>$b = -0.136$<br>$c = 1116.7$<br>Tmin.=333.15K, Tmax.=403.15K |
| | | $\rho_{H2O} = aT^2 + bT + c$<br>$a = -4.1 \times 10^{-3}$<br>$b = 2.6561$<br>$c = 531.79$<br>Tmin.=403.15K, Tmax.=631.15K |
| Viscosity kg/m-s | $\mu_{C2H5OH} = aT^4 + bT^3 + cT^2 + dT + e$<br>$a = 7.39080 \times 10^{-10}$<br>$b = -7.10108 \times 10^{-7}$<br>$c = 2.57861 \times 10^{-4}$<br>$d = -4.20366 \times 10^{-2}$<br>$e = 2.60436$<br>Tmin.=200K, Tmax.=250K | $\mu_{H2O} = aT^6 + bT^5 + cT^4 + dT^3 + eT^2 + fT + g$<br>$a = 2.90968 \times 10^{-15}$<br>$b = -5.70368 \times 10^{-12}$<br>$c = 4.67166 \times 10^{-9}$<br>$d = -2.0477 \times 10^{-6}$<br>$e = 5.06996 \times 10^{-4}$<br>$f = -6.73010 \times 10^{-2}$<br>$g = 3.74777$ Tmin.=273.16K, Tmax.=353.16K |
| | $\mu_{C2H5OH} = aT^6 + bT^5 + cT^4 + dT^3 + eT^2 + fT + g$<br>$a = 2.44178 \times 10^{-16}$<br>$b = -5.46743 \times 10^{-13}$<br>$c = 5.10455 \times 10^{-10}$<br>$d = -2.54691 \times 10^{-7}$<br>$e = 7.717612 \times 10^{-5}$<br>$f = -1.08558 \times 10^{-2}$<br>$g = 0.691817$<br>Tmin.=250K, Tmax.=440K | $\mu_{H2O} = aT^5 + bT^4 + cT^3 + dT^2 + eT + f$<br>$a = -4.44111 \times 10^{-15}$<br>$b = 9.78944 \times 10^{-12}$<br>$c = -8.68042 \times 10^{-9}$<br>$d = 3.87701 \times 10^{-6}$<br>$e = -8.74494 \times 10^{-4}$<br>$f = 0.0801061$,Tmin.=353.16K, Tmax.=473.16K |
| | | $\mu_{H2O} = aT^6 + bT^5 + cT^4 + dT^3 + eT^2 + fT + g$<br>$a = 7.104798 \times 10^{-19}$<br>$b = -2.319136 \times 10^{-15}$<br>$c = 3.18090 \times 10^{-12}$<br>$d = -2.357152 \times 10^{-9}$<br>$e = 9.991820 \times 10^{-7}$<br>$f = -2.307573 \times 10^{-4}$<br>$g = 0.0229112$.=473.16K, Tmax.=646.15K |
| Specific heat J/kg-K | $C_{C2H5OH} = aT^3 + bT^2 + cT + d$<br>$a = 4.42516 \times 10^{-5}$<br>$b = -6.58607 \times 10^{-4}$<br>$c = -3.03093$<br>$d = 2227.99$<br>Tmin.=159.05K, Tmax.=390.0K | $C_{H2O} = aT^4 + bT^3 + cT^2 + dT + e$<br>$a = 5.2012 \times 10^{-7}$<br>$b = -7.83557 \times 10^{-4}$<br>$c = 0.451006$<br>$d = -116.018$<br>$e = 15340.9$<br>Tmin.=273.16K, Tmax.=533.15K |
| Thermal conductivity W/m-K | $k_{C2H5OH} = aT + b$<br>$a = -2.640 \times 10^{-4}$<br>$b = 2.468 \times 10^{-1}$<br>Tmin.= 159.05K , Tmax.=353.15K | $k_{H2O} = aT^3 + bT^2 + cT + d$<br>$a = -1.861 \times 10^{-9}$<br>$b = -8.078 \times 10^{-6}$<br>$c = 5.7255 \times 10^{-3}$<br>$d = -0.432$<br>Tmin.=273.16K, Tmax.=633.15K |
| Surface tension N/m | $\sigma_{C2H5OH} = aT^4 + bT^3 + cT^2 + dT + e$<br>$a = -1.07587 \times 10^{-11}$<br>$b = -1.68173 \times 10^{-8}$<br>$c = 9.63852 \times 10^{-6}$<br>$d = -2.50097 \times 10^{-3}$<br>$e = 2.71626 \times 10^{-2}$<br>Tmin.=313.1 5K, Tmax.=493.17K | $\sigma_{H2O} = aT^4 + bT^3 + cT^2 + dT + e$<br>$a = -1.16550 \times 10^{-11}$<br>$b = 1.54149 \times 10^{-8}$<br>$c = -7.87691 \times 10^{-6}$<br>$d = 1.66546 \times 10^{-3}$<br>$e = -4.0814 \times 10^{-2}$<br>Tmin.=273.16K, Tmax.=373.15K |

## 6.3 Numerical Scheme and Governing Equations

Numerical modelling of the combustion process in the HVOF thermal spraying torch has been done by many researchers [20], [22], [24], [157]. In this work, the premixed oxygen and propane with some excess air were axially injected into the DJ2700 gun. The resulting hot combustion gases are accelerated inside the C-D nozzle and flow through the barrel section towards the exit of the torch (**Figure 3-1**). After the numerical simulations of combustion and turbulence of gaseous flow inside the torch, multicomponent droplets carrying P-W, P-E, and W-E mixture are injected axially into the CC through a central opening.

The premixed and non-premixed combustion, droplets fragmentation and evaporation are modelled by **Fluent**. The solver can model the mixing and transport of chemical species by solving conservation equations describing convection, diffusion, and reaction sources for each component species. Multiple simultaneous chemical reactions can be modelled by using EDM built-in combustion models. In this work turbulence inside the gaseous flow is modelled by the Realizable $k-\varepsilon$ model; for the analysis of droplets disintegration the TAB model is activated in the solver [166]. **Fluent** simulates the droplet dispersion in gas as a discrete phase in the Lagrangian frame of reference. Furthermore, droplets trajectory and heat-mass transfer are simulated during their flow through the gas, whereas droplet evaporation and momentum transfer also affect the gas dynamics through the two-way coupling. The multicomponent droplets contain a mixture of several components or species. The mass and momentum conservation equations of all components, energy equation, and vapour-liquid equilibrium at the multicomponent droplet surface form a coupled system of differential equations. Multicomponent Law is used for solving this system of differential equations [120]. Details of the combustion, turbulence and DPM models are presented in Chapter 3.

### 6.3.1 Multicomponent Law

The volume weighted mixing law is used to define the mixture droplet density [120]. Droplet mass $m$ is the sum of the masses of the components, (Eq-6-1):

$$m = \sum_i m_i \quad \textbf{(Eq-6-1)}$$

The density of the droplet $\rho_d$ is volume-averaged, (Eq-6-2):

$$\rho_d = \left( \sum_i \frac{m_i}{m\rho_i} \right)^{-1} \quad \textbf{(Eq-6-2)}$$

The multicomponent droplet vaporization rate is calculated as the sum of the vaporization rates of the individual components. For the convection/diffusion controlled vaporization model, the vaporization rate of component $i$ is given by (Eq-6-3):

$$\frac{dm_i}{dt} = A_d k_{c,i} \rho_\infty ln(1 + B_{m,i}) \quad \textbf{(Eq-6-3)}$$

where $m_i$ is mass of component $i$ in the droplet, $A_d$ droplet surface area, $\rho_\infty$ density of bulk gas, and $B_{m,i}$ is the Spalding mass number for species $i$ and is given by (Eq-6-4):

$$B_{m,i} = \frac{\left(Y_{i,s} - Y_{i,\infty}\right)}{1 - Y_{i,s}} \quad \textbf{(Eq-6-4)}$$

Here,

$Y_{i,s}$ = vapour mass fraction at the surface

$Y_{i,\infty}$ = vapour mass fraction in bulk gas,

and in (Eq-6-3) $k_{c,i}$ is the mass transfer coefficient of component $i$ and is calculated from the Sh correlation as [142], [143], (Eq-6-5)

$$Sh_{AB} = \frac{k_{c,i} d_d}{D_{i,m}} \left(2 + 0.6 Re_r^{0.5} Sc^{1/3}\right) \quad \textbf{(Eq-6-5)}$$

$D_{i,m}$= diffusion coefficient of vapour in the bulk gas, ($m^2$/s)

$Sc$ = the Schmidt number, $\frac{\mu}{\rho D_{i,m}}$

$d_d$ = the droplet diameter, (m)

Where $Re_r$is the relative Reynolds number, and given as $Re_r = \frac{\rho_\infty d_d |\overrightarrow{u_p} - \vec{u}|}{\mu}$

here, $\vec{u}$ is the fluid phase velocity, $\overrightarrow{u_d}$ is the particle/droplet velocity, μ is the molecular viscosity of the fluid, and $\rho_\infty$ is the continuous gas density.

When the total vapour pressure at the droplet surface exceeds the cell pressure, the multicomponent droplet is in the boiling regime and the solver

applies the boiling rate equation (Eq-6-6). The total vapour pressure is computed as $P_t = \sum P_i$ where $P_i$ is the partial pressure of component $i$.

The boiling rate equation is

$$\frac{dm_i}{dt} = x_i \frac{\pi k_\infty d_d}{C_{p,c}} \left(2 + 0.6 Re_r^{0.5} Pr^{1/3}\right) ln(1 + B_{T,i}) \quad \textbf{(Eq-6-6)}$$

where,

$x_i$ = volume fraction of component $i$ in the droplet

$k_\infty$ = thermal conductivity of the continuous phase (W/m-K)

$C_{p,c}$ = specific heat of the continuous phase (J/kg-K)

$Pr = \frac{c_p \mu}{k_\infty}$ = Prandtl number of continuous phase

$B_{T,i}$= Spalding heat transfer number for component $i$ computed by (Eq-6-7)

$$B_{T,i} = \frac{C_{p,c}(T_\infty - T_d)}{h_{vap,i}} \quad \textbf{(Eq-6-7)}$$

The energy equation for the multicomponent droplet is written thus: (Eq-6-8)

$$m_d c_d \frac{dT_d}{dt} = hA_d(T_\infty - T_d) + \sum_i \frac{m_i}{dt}(h_{vap,i}) \quad \textbf{(Eq-6-8)}$$

where $\frac{dm_i}{dt}$ is computed from Eq-6-3 or Eq-6-6 and $h_{vap,i}$ is the latent heat of vaporization for component $i$. The heat transfer coefficient $h$ is computed from (Eq-6-9) for the diffusion-controlled vaporization model: [167]

$$Nu = \frac{hd_d}{k_\infty} = \frac{ln(1 + B_{T,i})}{B_T} \left(2 + 0.6 Re_r^{0.5} Pr^{1/3}\right) \quad \textbf{(Eq-6-9)}$$

Raoult's law is the default vapour-liquid equilibrium expression used for the multicomponent droplet model. The correlation between the vapour concentration of a species $C_{i,s}$ over the surface and its mole fraction in the condensed phase $x_i^L$ is described by Raoult's law, (Eq-6-10)

$$C_{i,s} = \frac{p_i}{RT} = \frac{x_i^L P_{sat,i}}{RT} \quad \textbf{(Eq-6-10)}$$

In the Peng-Robinson Real Gas Model, the vapour concentration of each species at the surface is deduced from the calculations of vapour mole fraction and compressibility: (Eq-6-11)

$$C_{i,s} = x_i^V \frac{p}{Z^V RT} \quad \textbf{(Eq-6-11)}$$

The vapour-liquid equilibrium is deduced from the inputs for the Peng-Robinson model in the evaporating vapour species, so it is not necessary to specify vapour pressure separately.

## 6.4 Results and Discussions

The results section includes the analysis related to the effect of increasing the water percentage in the mixture and its consequences on gas dynamics, droplets fragmentation and the evaporation process. The effect of solvent evaporation and corresponding cooling is shown in the **Figure 6-2**a. The Without Droplets case has the highest temperature values in the CC, as it only displays the combustion gas temperature without any droplet injection, whereas, the cases with W-E mixed fractions show the decreasing temperature values due to heat extraction for the evaporation of droplets. The increase in the water mass fraction of the suspension droplets increases the amount of heat required for the vaporization and thus the gas cooling is augmented.

The maximum evaporation of the P-E and its mixture with water occurred in the torch CC (section-**I**) and at the nozzle throat. Moreover, as a result, of this evaporation, an enormous amount of gas cooling is observed in these sections. In the barrel section-**II**, a slight recovery in the gas temperature is detected. Furthermore, ethanol droplets are evaporated and then the gaseous ethanol burns with the remnant oxygen, which increases the flame temperature after the torch exit (**Figure 6-2**a). Even with the high water mass fractions, the flame temperature increased in free jet section-**III**. The heating in the free jet region is more in the P-E droplets injection and droplets carrying higher mass fractions of ethanol. Whereas, **Figure 6-2a** shows that the flame temperature is lower for higher water mass fractions.

From **Figure 6-2**b the variation in gas velocity is analysed by the addition of solvent droplets; on the percentage increments of water content inside the droplets, the gas velocity is reduced. However, the loss of kinetic energy is insignificant compared to the loss in enthalpy. Further, a slight increment in the flame velocity is also observed after the hot gas ejection from the thermal spray torch. The energy is added from the combustion of the ethanol vapours with the

excess air. An overall analysis suggests that the use of organic solvents will improve the torch gas dynamics in the free jet regions and help to improve the heating and melting of the solid nanoparticles. The addition of water to the suspension could reduce the extra heating of the suspension droplets and also minimize the heating of the solid nanoparticles. Hence, depending on the application requirement, it is necessary to control the water content in the suspension to regulate the gas temperature and gas velocity of the HVOF flame. For the spraying of nanoparticles material having a high-melting-point, P-E can be used. However, for lower melting point materials, the ethanol-water mixture can be used efficiently to control the flame temperature throughout the spraying process.

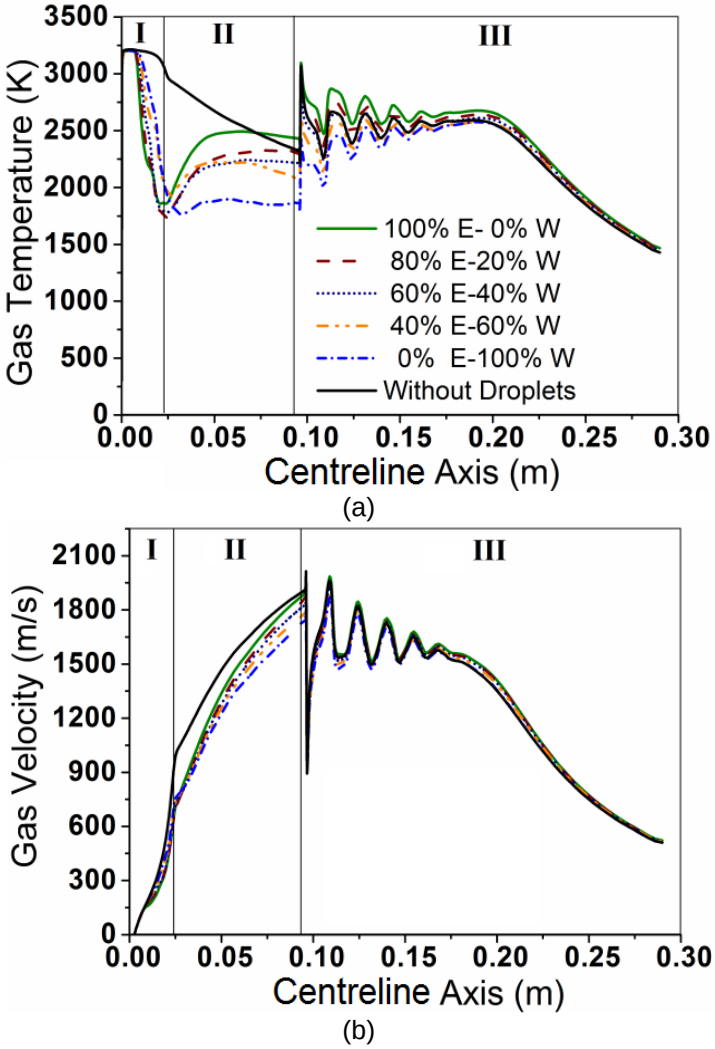


**Figure 6-2** Comparison graph of (a) gas temperature and (b) gas velocity Without Droplets injection and with the injection of P-E, W-E mixtures and P-W

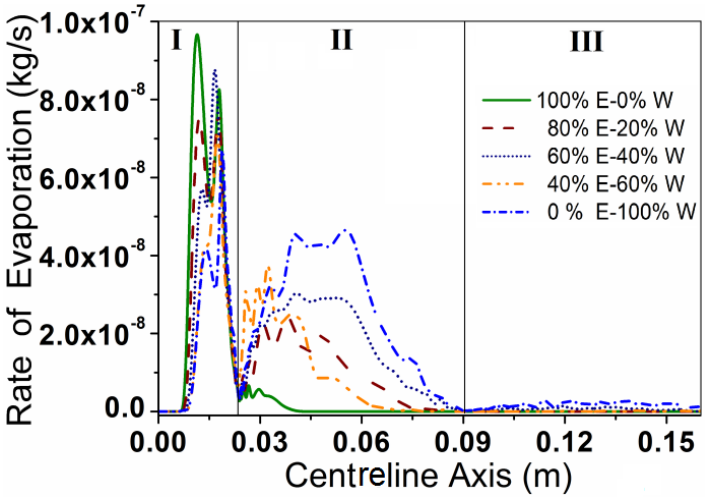


**Figure 6-3** Rate of evaporation of multicomponent droplets

The graphs for the evaporating droplets of the ethanol-water mixture are shown in **Figure 6-3**; a gradual increment in the mass fraction of water causes delays in the evaporation of the suspension droplets. It can be seen that maximum evaporation occurs inside the CC for the cases with high ethanol content in the suspension, and all droplets evaporate well before the gun exit. However, with a solvent having a greater percentage of water, half of the evaporation takes place in the CC and the remaining part of droplets are evaporated in the barrel. Also, the droplets cover more distance in the free jet region before complete evaporation. The reason, stated above, is the increase in the value of the latent heat of vaporization for the W-E mixture with increasing percentage of water content [43].

Overall the rate of evaporation decreases for the droplets with greater amounts of water. Furthermore, the droplet evaporation for a mixed mass fraction of W-E droplets is shown in **Figure 6-4**a–e. It can be seen clearly that as the percentage mass of water increases the rate of evaporation of droplets decreases. Moreover, droplets carrying 40%, 60% and 100% of water are exiting the torch without complete evaporation. This incomplete evaporation of droplets causes defects in the final coatings. The left-over nanoparticles required to be heated enough to remain in a state of semi-melted or entirely melted before the deposition. If the nanoparticles remain un-melted, this will create porous coating [11], [12]. It is also necessary for the HVSFS coating process to set at a shorter spraying distance so that continuous heat is transferred to the substrate from

the HVOF flame to make a pore-free dense coating [11], [12]. Hence, the use of P-W as a suspension carrier is not beneficial, and the addition of organic compound is necessarily required for improving the heating of the solid content in the HVSFS process.

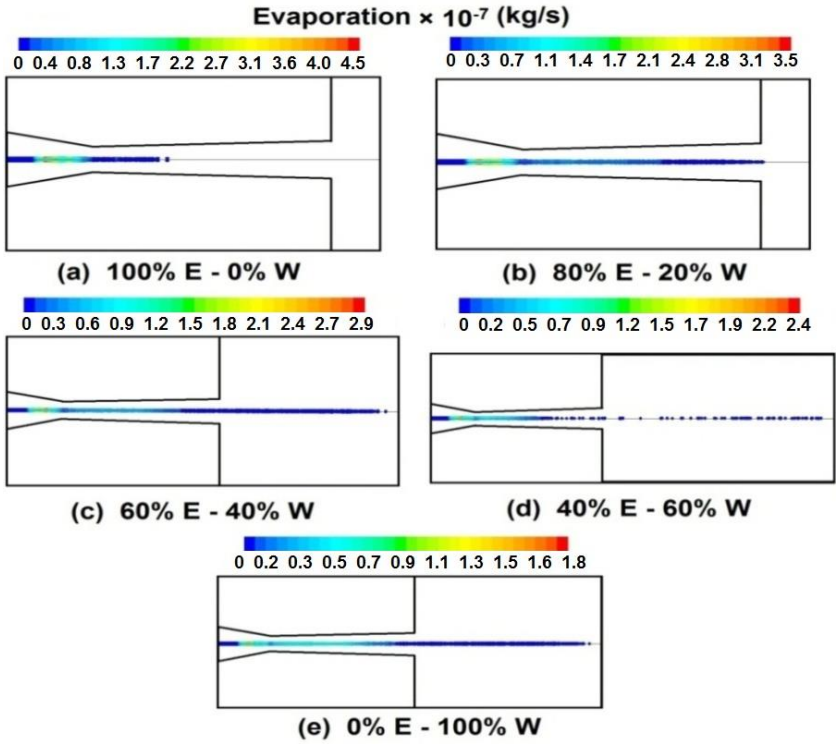


**Figure 6-4** Rate of Evaporation of multicomponent droplets carrying (a) 100%E and 0%W, (b) 80%E and 20%W, (c) 60%E and 40%W, (d) 40%E and 60%W, (e) 0%E and 100%W

Finally, the We of droplets injected into the torch with varied W-E percentage is illustrated in **Figure 6-5**. The value of a maximum We of about 46 is observed for the solvent with P-E, and intense fragmentation occurred inside the CC. When the droplets contain 20%W and 80%E, then We is reduced to 40. Further increments in the percentage of water in the solvent decrease the value of the We, and for 40%W, We is 32, whereas, for 60%W, it is approximately 28, and the value of the We with P-W is 24. This confirms that the increasing water content in droplets would result in an increment in surface tension and hence the value of the We is decreased which means less fragmentation of droplets. In all cases, the maximum breakup occurred in the combustion area and all the time the value of the We remains well above 14, which indicates that the fragmentation process is dominant. It is clearly seen from these graphs that

increasing the water percentage in the solvent will decrease the We, and this is due to the influence of greater surface tension forces for droplets carrying a greater percentage of water. As stated earlier P-W and P-E have the value of surface tension $\sigma_{P\text{-}W}=72\times10^{-3}$N/m, and $\sigma_{P\text{-}E}=22\times10^{-3}$N/m respectively, and higher surface tension declines fragmentation and usually consumes more hot gas energy for vaporization [165].

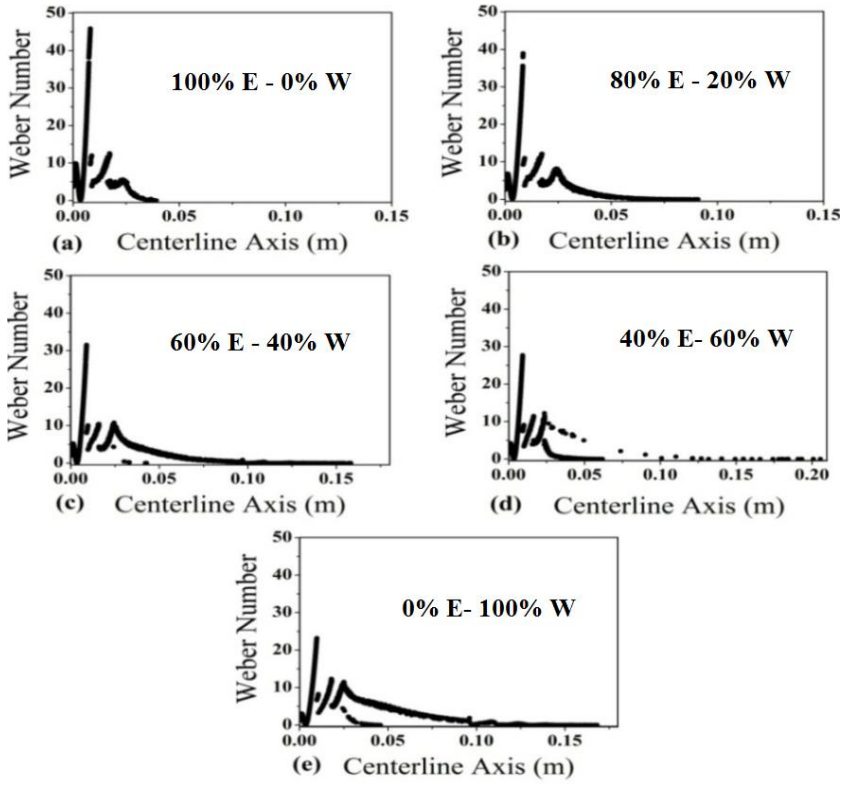


**Figure 6-5** Weber number of droplets for mixed water-ethanol mass fractions

## 6.5 Summary

The modelling of multicomponent droplets injection in the HVSFS torch is presented in this chapter. It includes the effect of a liquid feedstock on the gas temperature and velocity, and the effects of hot gas onto the droplets breakup, fragmentation and evaporation process. Three solvents including P-W, P-E, and W-E mixture are injected into the HVOF torch to observe the variation in gas dynamics and droplet dynamics. Following is the summary of the work:

- The increasing mass fraction of water in suspension droplets will cause the droplets to eject from the gun without complete evaporation.

- The incomplete evaporation of suspension droplets may cause insufficient heating of the solid nanoparticles, and un-melted particles can generate porous coating.
- It is necessary to decrease the surface tension of water droplets for increasing the fragmentation of droplets. Therefore, the surfactant must be added.
- The controlling mass fractions of water content can help to regulate the HVOF flame temperature and velocity for the specified application.
- The ethanol solvent can contribute to improving the heating and melting of materials having high melting points while the addition of water will be suitable for the lower melting point material.
- This study only considers the constant diameter droplets injection i.e. the effects of size variation are not included; however, the real process may consist of various sizes of droplets at the point of injection.

# 7 MODELLING OF LIQUID FEEDSTOCK INJECTION CARRYING NANOPARTICLES IN HIGH-VELOCITY SUSPENSION FLAME SPRAYING

## 7.1 Introduction

The technology of dense nanostructured coating uses liquid feedstock to inject the nanosized powder materials into the thermal spraying torch.The increasing trends of nanoparticles coating have intensified the interest in modelling the process of thermal spraying. Nowadays, nanoparticles are injected into different torches including the HVOF flame with the help of liquid precursors and suspension mechanisms. The injection of liquid suspension into the HVOF thermal spray gun is called HVSFS [10], [14], [15], [17], [116]. Rauch et al. [17] and Bolelli et al. [15] experimentally worked out the effect of suspension flame spraying with different suspension compositions on the characteristics of coating microstructures, whereas, Dongmo et al. [10], [14] numerically studied the parametric optimization of the process to analyse the effects on combustion and gas dynamics by the injection of liquid feedstock droplets and nanoparticles separately. Gozali et al. [116] analysed the effect of P-E droplet evaporation and its effect on the gas dynamics in the HVSFS torch by varied injection parameters (Chapter 2, section-***2.1.2***).

This chapter deals with nanoparticles suspended in pure liquid ethanol which are injected into the HVSFS thermal spraying torch DJ2700. The effects of the increasing concentration of solid nanoparticles in the liquid feedstock injection on the HVSFS process are analysed. Four different concentrations of solid nanoparticles in suspension droplets with various droplet diameters are considered, and their effects on gas dynamics, vaporization rate, and secondary breakup investigated. Moreover, two injection types Surface and Group are modelled to analyse the impact on the HVSFS process. The main objective of this work is to consider the suspension droplets disintegration and evaporation processes inside the HVOF torch. Due to the vaporization of suspension liquid there is a loss of HVOF flame enthalpy and kinetic energy and to reduce these losses a new angular injection technique is applied to increase the efficiency of

the present process. This study assumes that the completion of liquid phase evaporation and proper heating/melting of solid nanoparticles is essential for obtaining a defect-free coating. The improper heating of suspended nanoparticles would lead to the coating comprising of un-melted particles that result in porous coatings [11], [12].

## 7.2 Model Description

The numerical model used is an extension of the numerical analysis of the conventional HVOF thermal spray process [115]–[117]. The turbulent, combustion, discrete phase, flow and spray models employed are validated against experimental data, and demonstrate satisfactory predictions [20], [21], [23], [29], [115]–[119]. These models detail are presented in Chapter 3.

The schematic representation of the computational domain of an industrial DJ2700 torch with $L_{FJ}$=200mm is similar to **Figure 3-1**. The working conditions used in these simulations are summarised in **Table 7-1** [115], [117], [119]. The schematic of the two injection methods Surface-Type Injection (STI) and Group-Type Injection (GTI) are presented in **Figure 7-1**a–b. In all constant diameter cases, the droplet mass flow rate is $1\times10^{-4}$kg/s, whereas, the mass fraction is varied for different diameter droplets in the Rosin-Rammler diameter distribution (section-***7.2.2***). Initial droplet velocities are 15m/s and 30m/s (based on the droplets' diameter). The injection velocity increases for larger diameter droplets, due to the higher injection force required to penetrate into the HVOF jet. In the present study, the droplets are injected into the core of the combustion zone at an angle of 45°, and the horizontal and vertical components of injection velocities are equal to 30m/s, and from that the mean droplet velocity becomes 42.426m/s (**Table 7-1**). The droplets mass flow rate and velocity are specified based on previous parametric investigations aimed at exploring optimum operating parameters for the HVSFS spraying process [115]–[117].

Firstly, the numerical model computes the temperature and velocity fields of the HVSFS flame jet. The Realizable $k-\varepsilon$ model is used for modelling the turbulence in the jet, including compressibility effects. The thermal and flow fields of the gas are solved by the Eulerian approach. The EDM is used to

simulate the premixed combustion of oxygen and propane [132], [134], [135] (section-***3.2.3***). After complete simulations of the gas phase, ethanol droplets carrying suspended nanoparticles are injected into the HVSFS flame jet where they undergo several stages (section-***3.2.4***). The history of suspension droplets is computed with Lagrangian formulation where the finite interphase transport rates and effects of turbulence interactions between the droplet and gas phases are considered [10], [14], [115], [116], [136]. The heat and mass transfer of the droplets within the continuous phase is modelled using three laws [137], [138], as described in Chapter 3, section-***3.2.4.4***.

**Table 7-1 The working conditions of DJ2700 HVSFS torch**

| Working Conditions | | |
|---|---|---|
| Oxygen flow rate | 0.01197kg/s | Initial temperature, 300K |
| Fuel flow rate | 0.003526kg/s | |
| Droplet constant diameter | 50μm | |
| Droplet flow rate | $1\times10^{-4}$kg/s, | |
| Mean velocity Surface-type Injection (STI) | 15m/s and 30m/s | |
| Mean velocity Group-type Injection (GTI) | 42.426m/s | |

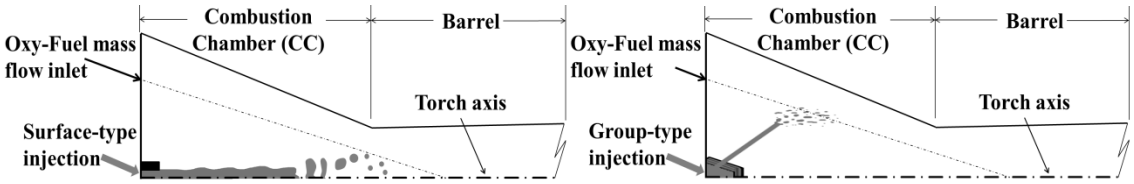


(a) (b)

**Figure 7-1** Schematic diagram of the (a) Surface-type injection, and (b) Group-type injection in the DJ2700 torch

The conditions under which each droplet has a set of governing equations are:

1. The liquid droplets and gas phases have initial continuous velocities and temperature that co-exist at each location.
2. The liquid phase has turbulent fluctuations resulting in droplet transport of mass, momentum and energy. The random effects of turbulence on the particle motion are considered by integrating the individual particle trajectory with the instantaneous fluid velocity.
3. The suspension properties are functions of temperature and used in the solver by applying nanofluids models, with thermophysical properties of pure liquid and solid particles (**Figure 7-2**, **Table 7-2**).

Detailed descriptions of the gas phase, discrete phase, droplets breakup and combustion models are reported in Chapter 3.

### 7.2.1 Nanoparticles' Suspension Theoretical Model

The thermophysical and transport properties of nanoparticles are quite different from their original solid substance (in bulk) [168]. In the present work the nanofluids are the liquid feedstock prepared by the nanoparticles suspended in the base solvent P-W, P-E or W-E mixture and named as 'nanoparticles suspension' or simply 'suspension'.

The necessary thermophysical properties of nanoparticles suspension are calculated from nanofluids models, as described below. The density of nanofluids is calculated by using the mixture rule (Eq-7-1) [169]:

$$\rho_{\mathrm{susp}} = (1 - C)\rho_{\mathrm{l}} + C\rho_{\mathrm{p}} \qquad \textbf{(Eq-7-1)}$$

where $C$ is the volume concentration of solid particles in suspension, $\rho_{\mathrm{l}}$ the density of liquid ethanol and $\rho_{\mathrm{p}} = 4230\mathrm{kg/m^3}$ the density of solid $TiO_2$ particles. The value of suspension density $\rho_{\mathrm{susp}}$ is increased by the increment in percentage concentrations of nanoparticles from 0wt.% to 25wt.%. The analysis shows that an increase in temperature will gradually decrease the overall value of suspension density because of a reduction in the base fluid density (**Table 7-2**, **Figure 7-2**).

For the viscosity of suspension ($\mu_{\mathrm{susp}}$), Einstein's formula is restricted to the low volume concentration $\{\mu_{\mathrm{susp}} = \mu_{\mathrm{l}}(1 + 2.5\mathrm{C})\}$ and is modified by Brinkman for higher concentration of nanoparticles (Eq-7.2) [168], [170] as under:

$$\mu_{\mathrm{susp}} = \frac{\mu_{\mathrm{l}}}{(1 - C)^{2.5}} \qquad \textbf{(Eq-7-2)}$$

where $\mu_{\mathrm{l}}$ is the viscosity of liquid ethanol. The consequence of temperature variation on the viscosity of the suspension is similar to that of the density; i.e., a gradual increase in temperature will decrease the viscosity (**Table 7-2**, **Figure 7-2**) [171].

The specific heat also increases with increasing the percentage concentration of nanoparticles in the suspension; furthermore, it has a direct relation to temperature increment (**Table 7-2**, **Figure 7-2**) [168], [172].

$$c_{\mathrm{susp}} = C c_{\mathrm{p}} + (1 - C) c_{\mathrm{l}} \quad \textbf{(Eq-7-3)}$$

where $c_p = 3780 \frac{J}{kg \cdot K}$ is the specific heat capacity of $TiO_2$ powder, and $c_{\mathrm{l}}$ is the specific heat capacity of liquid ethanol.

From experimental work, researchers have proved that thermal conductivity ($k_{\mathrm{susp}}$) of nanofluids increases with the increment of nanoparticles concentration; however, it also depends on the size, shape and temperature of suspended particles [171], [173], [174]. For thermal conductivity of spherical nanoparticles, the Bruggeman model gives better predictions [172], [175], [176] than other models with no limitation on the volume concentration of solid particles in suspension.

$$k_{\mathrm{susp}} = \frac{1}{4}\left[(3C - 1)k_{\mathrm{p}} + (2 - 3C)k_{\mathrm{l}}\right] + \frac{k_{\mathrm{l}}}{4}\sqrt{\Delta} \quad \textbf{(Eq-7-4)}$$

$$\Delta = \left[(3C - 1)^2 \left(\frac{k_{\mathrm{p}}}{k_{\mathrm{l}}}\right)^2 + (2 - 3C)^2 + 2(2 + 9C + 9C^2)\left(\frac{k_{\mathrm{p}}}{k_{\mathrm{l}}}\right)\right] \quad \textbf{(Eq-7-5)}$$

where $k_{\mathrm{p}} = 10.4 \frac{\mathrm{W}}{\mathrm{m \cdot K}}$ is the thermal conductivity of $TiO_2$ powder and $k_{\mathrm{l}}$ is the thermal conductivity of the base fluid (**Table 7-2**, **Figure 7-2**).

It is reported that the surface tension of ethanol-based suspension deviates little from P-E for low particle concentrations (up to 3wt.%) [168], [173]; after which the surface tension increases with increasing nanoparticles concentration [88], [171]. A 10% increase is noticed for nanoparticles concentration of 10wt.%. This is because of the rise in the Van der Waals forces between nanoparticles at the interface between liquid and gas, which causes an increase in surface tension. Furthermore, latent heat of vaporization has a direct relation to the cohesive forces. Hence, the rise in surface tension will increase the value of heat required to evaporate the base liquid carrying nanoparticles [177].

In the present work, four different solid nanoparticles concentrations (0, 5, 15 and 25wt.%) suspended in P-E are studied. The surface tension of the suspension is calculated by a 10% increase in the two latter concentrations (Eq-7-6):

$$\sigma_{15,25\%\mathrm{susp}} = \sigma_{0\%\mathrm{susp}} + \left(10\%(\sigma_{0\%\mathrm{susp}})\right) \quad \textbf{(Eq-7-6)}$$

It should be noted that the non-homogeneous effect of suspended nanoparticles ($TiO_2$) in a solvent (ethanol) are considered for numerical modelling of droplets flow inside the torch. The solid powders are not charged into droplets, as the main aim of this work is to track the effect of solid loading on droplet breakup and evaporation numerically. The addition of nanoparticles in the suspension is incorporated by modifying pure liquid properties using the correlations mentioned in Eqs. 7-1–to–7-6. The suspension properties are calculated from commonly used theoretical models as stated above, and details can be found in [168], [170], [172], [173], [175], [176]. The curve-fitted procedure calculated the temperature-dependent pure liquid properties in the required temperature range, (see **Table 7-2**, **Figure 7-2**) [89].

**Table 7-2 Thermophysical properties of pure liquid (0wt.%) ‡ and suspension (5–25wt.%) ‖**

| Property | Mass Fractions | | | | Temperature (K) |
|---|---|---|---|---|---|
| | 0wt.% | 5wt.% | 15wt.% | 25wt.% | |
| Density kg/m³ | $\rho_{susp} = aT^3 + bT^2 - cT + d$<br>$a = -3.76345 \times 10^{-6}$<br>$b = 2.27199 \times 10^{-3}$<br>$c = -1.2412$<br>$d = 1053.73$ | $\rho_{susp} = aT^3 + bT^2 - cT + d$<br>$a = -3.57527 \times 10^{-6}$<br>$b = 2.15839 \times 10^{-3}$<br>$c = -1.17914$<br>$d = 1212.55$ | $\rho_{susp} = aT^3 + bT^2 - cT + d$<br>$a = -3.1989 \times 10^{-6}$<br>$b = 1.93119 \times 10^{-3}$<br>$c = -1.05502$<br>$d = 1530.17$ | $\rho_{susp} = aT^3 + bT^2 - cT + d$<br>$a = -2.82258 \times 10^{-6}$<br>$b = 1.70399 \times 10^{-3}$<br>$c = -0.930898$<br>$d = 1847.799$ | 250-385 |
| Viscosity kg/m-s | $\mu_{susp} = aT^6 + bT^5 + cT^4 + dT^3 + eT^2 + fT + g$<br>$a = 5.3947 \times 10^{-16}$<br>$b = -1.11875 \times 10^{-12}$<br>$c = 9.6983 \times 10^{-10}$<br>$d = -4.50443 \times 10^{-7}$<br>$e = 1.18439 \times 10^{-4}$<br>$f = -1.67608 \times 10^{-2}$<br>$g = 1.00143$ | $\mu_{susp} = aT^6 + bT^5 + cT^4 + dT^3 + eT^2 + fT + g$<br>$a = 6.13279 \times 10^{-16}$<br>$b = -1.27182 \times 10^{-12}$<br>$c = 1.10252 \times 10^{-9}$<br>$d = -5.12071 \times 10^{-7}$<br>$e = 1.34643 \times 10^{-4}$<br>$f = -1.9054 \times 10^{-2}$<br>$g = 1.13845$ | $\mu_{susp} = aT^5 + bT^4 + cT^3 + dT^2 + eT + f$<br>$a = -1.84601 \times 10^{-13}$<br>$b = 3.19998 \times 10^{-10}$<br>$c = -2.22806 \times 10^{-7}$<br>$d = 7.8043 \times 10^{-7}$<br>$e = -1.37915 \times 10^{-2}$<br>$f = 9.88072 \times 10^{-1}$ | $\mu_{susp} = aT^5 + bT^4 + cT^3 + dT^2 + eT + f$<br>$a = -1.84601 \times 10^{-13}$<br>$b = 3.19998 \times 10^{-10}$<br>$c = -2.22806 \times 10^{-7}$<br>$d = 7.8043 \times 10^{-7}$<br>$e = -1.37915 \times 10^{-2}$<br>$f = 9.88072 \times 10^{-1}$ | 250-385 |
| Specific heat J/kg-K | $c_{susp} = aT^3 + bT^2 - cT + d$<br>$a = 4.42516 \times 10^{-5}$<br>$b = -6.58607 \times 10^{-4}$<br>$c = -3.03093$<br>$d = 2227.99$ | $c_{susp} = aT^3 + bT^2 - cT + d$<br>$a = 4.20390 \times 10^{-5}$<br>$b = -6.25677 \times 10^{-4}$<br>$c = -2.87938$<br>$d = 2305.59$ | $c_{susp} = aT^3 + bT^2 - cT + d$<br>$a = 3.76138 \times 10^{-5}$<br>$b = -5.59816 \times 10^{-4}$<br>$c = -2.57629$<br>$d = 2460.79$ | $c_{susp} = aT^3 + bT^2 - cT + d$<br>$a = 3.3189 \times 10^{-5}$<br>$b = -4.939 \times 10^{-4}$<br>$c = -2.2732$<br>$d = 2616.0$ | 250-385 |
| Thermal conductivity W/m-K | $k_{susp} = aT + b$<br>$a = -2.640 \times 10^{-4}$<br>$b = 2.468 \times 10^{-1}$ | $k_{susp} = aT^2 + bT + c$<br>$a = -4.25685 \times 10^{-9}$<br>$b = -3.05705 \times 10^{-4}$<br>$c = 2.89592 \times 10^{-1}$ | $k_{susp} = aT^3 + bT^2 + cT + d$<br>$a = -8.21754 \times 10^{-12}$<br>$b = -2.95254 \times 10^{-8}$<br>$c = -4.49135 \times 10^{-4}$<br>$d = 4.52780 \times 10^{-1}$ | $k_{susp} = aT^2 + bT + c$<br>$a = -1.96341 \times 10^{-7}$<br>$b = -6.48697 \times 10^{-4}$<br>$c = 8.2865 \times 10^{-1}$ | 250-385 |

| | | | | | |
|---|---|---|---|---|---|
| Surface tension N/m | $\sigma_{susp} = aT^6 + bT^5 + cT^4 + dT^3 + eT^2 + fT + g$<br>$a = -7.24434 \times 10^{-16}$<br>$b = 1.74074 \times 10^{-12}$<br>$c = -1.7235 \times 10^{-9}$<br>$d = 9.00117 \times 10^{-7}$<br>$e = -2.61702 \times 10^{-4}$<br>$f = 4.01095 \times 10^{-2}$<br>$g = -2.50259$ | $\sigma_{susp} = aT^6 + bT^5 + cT^4 + dT^3 + eT^2 + fT + g$<br>$a = -7.24434 \times 10^{-16}$<br>$b = 1.74074 \times 10^{-12}$<br>$c = -1.7235 \times 10^{-9}$<br>$d = 9.00117 \times 10^{-7}$<br>$e = -2.61702 \times 10^{-4}$<br>$f = 4.01095 \times 10^{-2}$<br>$g = -2.50259$ | $\sigma_{susp} = aT^6 + bT^5 + cT^4 + dT^3 + eT^2 + fT + g$<br>$a = -7.96877 \times 10^{-16}$<br>$b = 1.91481 \times 10^{-12}$<br>$c = -1.89586 \times 10^{-9}$<br>$d = 9.90129 \times 10^{-7}$<br>$e = -2.87872 \times 10^{-4}$<br>$f = 4.4120 \times 10^{-2}$<br>$g = -2.75285$ | $\sigma_{susp} = aT^6 + bT^5 + cT^4 + dT^3 + eT^2 + fT + g$<br>$a = -7.96877 \times 10^{-16}$<br>$b = 1.91481 \times 10^{-12}$<br>$c = -1.89586 \times 10^{-9}$<br>$d = 9.90129 \times 10^{-7}$<br>$e = -2.87872 \times 10^{-4}$<br>$f = 4.4120 \times 10^{-2}$<br>$g = -2.75285$ | 270-490 |

‡ Pure liquid properties are taken from [89] and curve-fitted in their temperature range. ‖ Suspension properties are then calculated from theoretical models [168]–[170], [172], [175], [176] in which temperature-dependent pure liquid properties are incorporated.

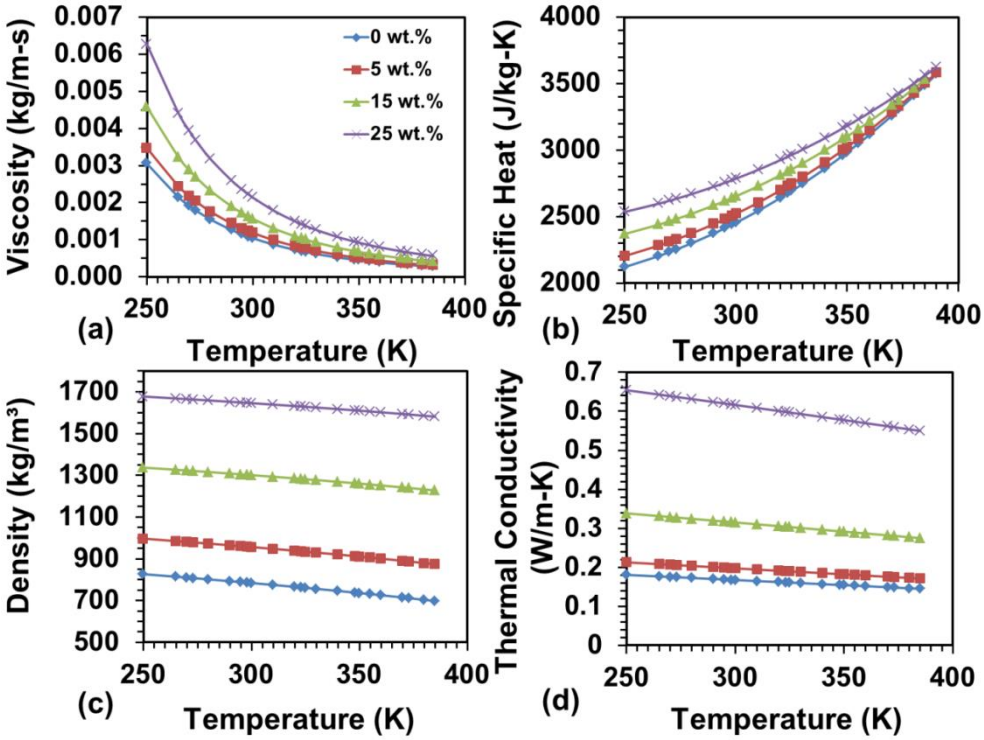


**Figure 7-2** Variations in the thermophysical properties of liquid feedstock droplets with increasing nanoparticles concentration and temperature

It can be seen clearly from the **Figure 7-2** that by increasing the concentration of nanoparticles in the suspension will significantly affect their thermophysical properties. Moreover, the increments in the temperature of the droplets also have a significant effect on the properties of suspension (**Figure 7-2**).

### 7.2.2 Injection Properties

The cases are solved by analysing different injection schemes related to the droplets' atomization in the CC of the thermal spray gun; details are given **Figure 7-3**. The two main injection schemes; STI Case-2 and GTI Case-3 are

employed to see the effects of varied injection types on gas dynamics and droplet dynamics. In the STI method, streams of droplets are released axially at an angle of 0° from each facet of the inlet surface (**Figure 7-1**a). As the droplets move along the axis, the solver simulates the interaction of droplets with the combustion gas along the central axis of the torch. For GTI, droplets are injected at an angle of 45° into the core of the combustion zone (**Figure 7-1**b). For these two injection types, different sizes of droplets with constant and Rosin-Rammler diameter distribution are considered. Firstly, torch flow dynamics are studied for constant diameter droplets of 50, 150 and 300μm having a nanoparticles concentration of 0, 5, 15, and 25wt.%. In the second type, a similar study is repeated for Rosin-Rammler diameter distribution of droplets having size variations of 30−70μm, 130−170μm and 280−320μm (**Figure 7-3**).

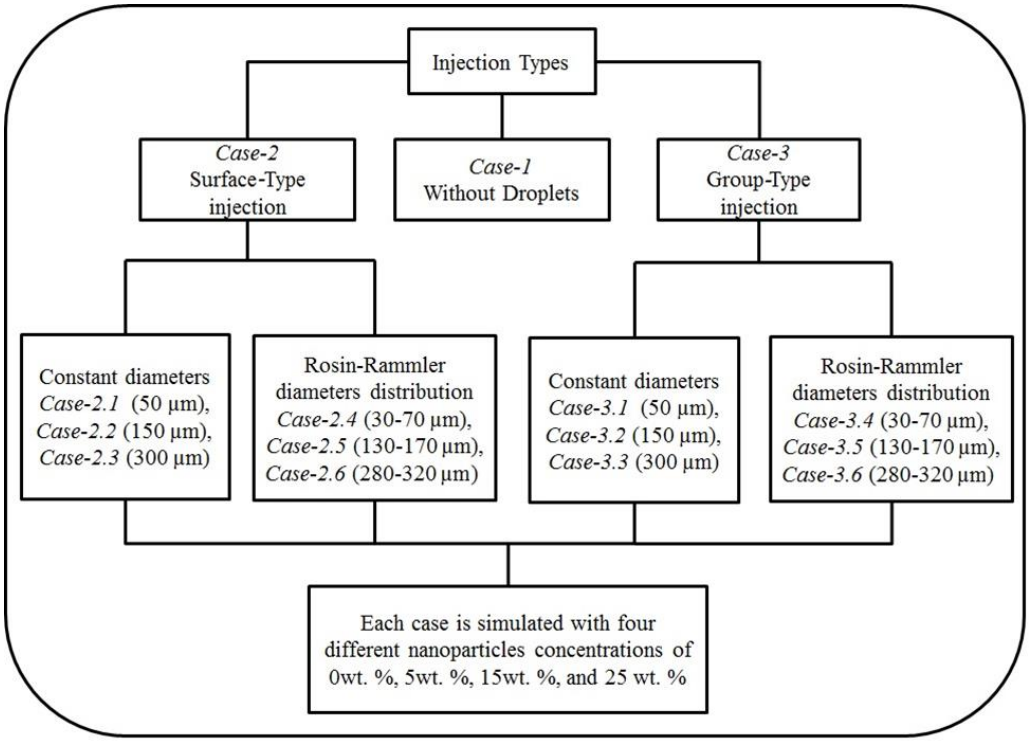


**Figure 7-3** Droplets injection types, and Cases division

The Rosin-Rammler diameter distribution is applied that allows the range of diameters to be divided into an adequate number of discrete intervals; this distribution function is based on the assumption that an exponential relationship

exists between the droplet diameter, $d$ and the mass fraction of droplets $Y_d$ with a diameter greater than $d$ and is given as [178]–[180]:

$$Y_d = e^{-(d/\bar{d})^n} \quad \textbf{(Eq-7-7)}$$

where $\bar{d}$ is the size constant 'Mean Diameter', and $n$ is the size distribution parameter 'Spread Parameter'. The mass fraction of these droplets is dependent on diameter. The mass fraction for larger diameter droplets is lower than the smaller diameter droplets (**Table 7-3**). **Table 7-3** shows the Rosin-Rammler diameter distribution with the varied mass fraction of the suspension droplets.

For each type of droplet injection, different rates of evaporation and fragmentation are detected. Also, the effect of droplets breakup and evaporation on gas dynamics changes with varying injection parameters due to the variation in droplet interaction with the continuous combustion gas inside the HVSFS torch. The results and discussion section addresses how gas dynamics, rate of evaporation and secondary breakup of liquid droplets are influenced by varying the concentration of solid nanoparticles in the liquid feedstock droplets. In the results, Without Droplets (Case-1) refers to a case in which only combustion gas flow characteristics in the HVSFS process are analysed. The domain sections in the figures are marked as (**I**) Combustion Chamber (CC), (**II**) Barrel and (**III**) Free jet. Furthermore, the vertical line separating the CC and Barrel sections is the C-D nozzle throat region (**Figure 3-1**). For clarity, the effects of different nanoparticles loading with varied injection parameters on the droplets dynamics and gas dynamics are presented in different sections. For brevity, not all cases mentioned in **Figure 7-3** are discussed in detail; however, the main analysis is included.

**Table 7-3 The Rosin-Rammler diameter distribution with varied mass fractions**

| Diameter, (30−70μm) | Mass fraction | Diameter, (130−170μm) | Mass fraction | Diameter, (280−320μm) | Mass fraction |
|---|---|---|---|---|---|
| 30 | 0.844 | 130 | 0.548 | 280 | 0.461 |
| 40 | 0.631 | 140 | 0.457 | 290 | 0.414 |
| 50 | 0.368 | 150 | 0.368 | 300 | 0.368 |
| 60 | 0.152 | 160 | 0.284 | 310 | 0.323 |
| 70 | 0.040 | 170 | 0.210 | 320 | 0.280 |

## 7.3 Numerical Results and Discussions

### 7.3.1 Effects of the Nanoparticles Suspension on Gas Dynamics and Rate of Droplet Vaporizations in the HVSFS Process

#### 7.3.1.1 Surface-type injection

The first sets of simulations are performed for the axial injection of droplets from a centralized inlet surface into the torch. The STI is used for injecting (A) constant diameter droplets and (B) varied diameter droplets. For each case four nanoparticles concentration loadings are used, 0, 5, 15, and 25wt.%. The effects of increasing nanoparticles loading inside the liquid feedstock, on the torch's flow dynamics, and droplets' rate of evaporation are discussed below.

***(A) Constant diameter droplet injection***

Case-2.1 is simulated for analysing the injection of droplets from the surface having a constant diameter of 50µm with a velocity of 15m/s, and mass flow rate of $1\times10^{-4}$kg/s, using different solid nanoparticles concentrations (**Table 7-1**). When these droplets are added to the gun, cooling effects are detected over the hot gas near the CC back wall, as compared to Without Droplet Case-1 (**Figure 7-4**a). The temperature drop for two extreme nanoparticles concentrations, 0wt.% and 25wt.% is 440K and 120K, respectively (at x=0.0033m away from the point of injection, **Figure 7-4**a). Moreover, the gases experience more cooling after the C-D nozzle for droplets having high-concentration 25wt.% with the temperature difference of 390K as compared to 250K for 0wt.% droplets (at x=0.04042m away from the point of injection, **Figure 7-4**a). The result shows that temperature fluctuations in the HVSFS process are a direct function of the energy required for droplet vaporization. In particular, less cooling of gas is observed with lower heat requirement for evaporation and vice versa.

It is also reflected in the velocity field of the HVSFS process; the variation in velocity is 114m/s between the Without Droplet Case-1 when compared to a case with 0wt.% nanoparticles concentration droplet injection (at x=0.04042m away from the point of injection, **Figure 7-4**b). Moreover, this difference increases to 161m/s when compared to 25wt.% nanoparticles concentration (**Figure 7-4**b); therefore, lower velocities are predicted for high-concentration

droplets. The reason can be the cooling of combustion gas which led to the small pressure decrement that causes small velocity-drop; however, the difference in gas velocities for increasing nanoparticles concentration is insignificant.

The rate of evaporation of droplets with different solid nanoparticles concentrations is compared in **Figure 7-4**c. The highest value of the rate of evaporation is detected for homogeneous droplets ($1.83\times10^{-4}$kg/s for 0wt.% nanoparticles loading), while by adding 25wt.% nanoparticles into the base fluid the rate of evaporation is reduced by 20%. Downstream of the C-D nozzle, higher cooling and vaporization rates are identified for high concentration droplets. The maximum rate of evaporation occurs inside the CC for all droplets, while the final location of evaporation stretches to the gun exit when droplets are loaded with higher concentrations, proving that the heat of vaporization required for non-homogeneous droplets is much greater than for homogeneous droplets.

The overall data show that P-E droplets are entirely vaporized in the CC section, resulting in the highest gas cooling and temperature reduction in section-**I**. However, solid-loaded droplets are not completely vaporized, resulting in less gas cooling in the CC, but greater cooling in the expansion nozzle where vaporization continues. This heat imbalance is due to the increase in the heat capacity of the high concentration droplets that takes a longer time to reach the boiling point and, in turn, delays the evaporation process. As stated in section-***7.2.1***, the specific heat of suspension droplets increases with the increase in percentage concentration of nanoparticles. Thus, the heat required to raise the temperature of the high concentration suspension droplets is much greater than that for less concentrated or 0wt.% suspension droplets. Hence, more cooling is observed in the barrel for higher concentration suspension cases.

In Case-2.2 droplets are injected with the mass flow rate, velocity and constant diameter of $1\times10^{-4}$kg/s, 30m/s and 150µm, respectively. Comparison of the variation in the HVSFS process temperatures, velocities and rate of evaporation

experienced by these droplets along the centreline is shown in **Figure 7-4**(d-f). First cooling is detected before the C-D nozzle with a temperature difference of about 730K between two extreme cases (25wt.% and 0wt.%). This is much larger than the 390K temperature difference observed in the case of droplets injected with a 50µm diameter (Case-2.1) which confirms that larger size droplets cause more cooling inside the HVSFS torch. The second most significant temperature difference in Case-2.2 is just after the C-D nozzle, at about 150K. It reduces to 85K in the middle of the barrel and reaches a negligible amount at the gun exit (**Figure 7-4**d).

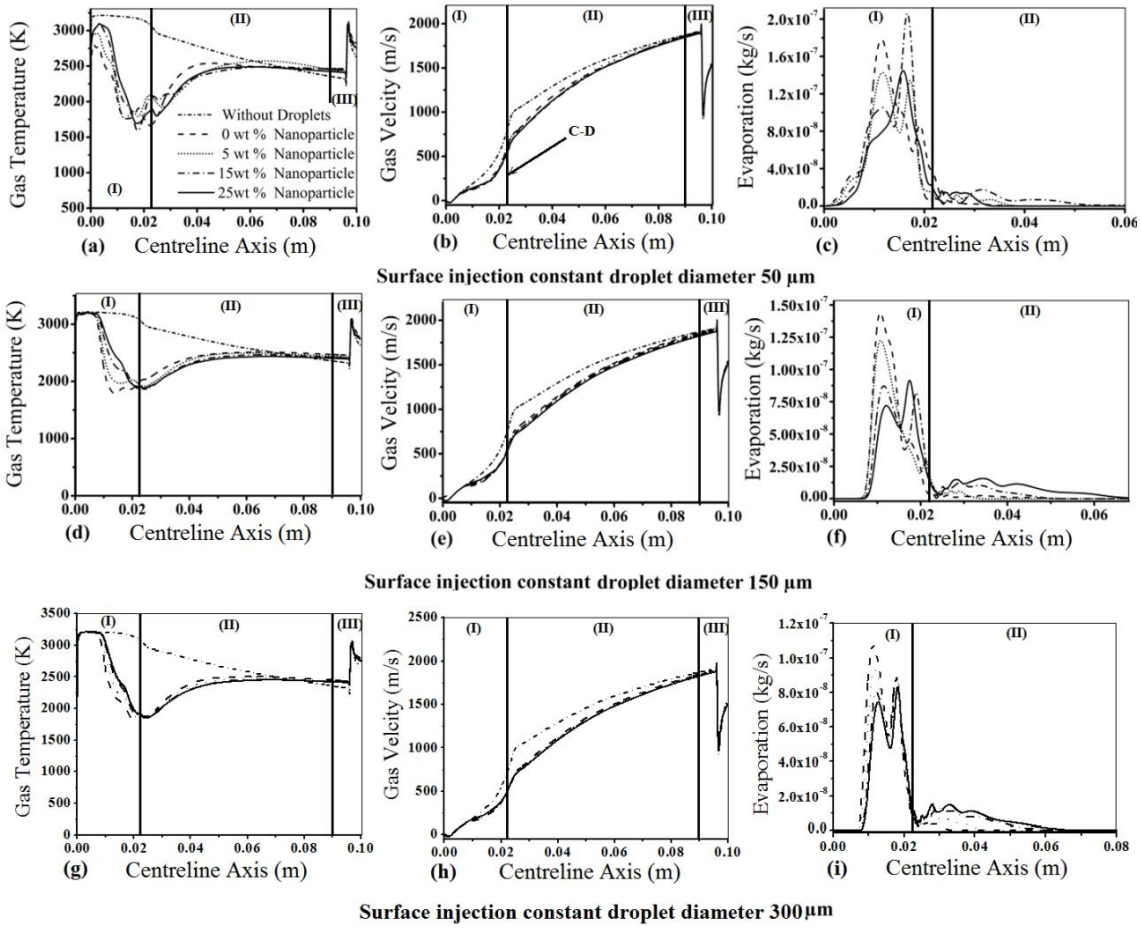


**Figure 7-4** Comparison of gas temperature, velocity fields, and rate of evaporation experienced by droplets injected from the surface with constant diameters of (a-c) 50µm and (d-f) 150µm, (g-i) 300µm, having different solid nanoparticles concentrations

The velocity field in Case-2.2 experiences small changes and this difference reaches 45m/s just after the C-D nozzle (**Figure 7-4**e). Moreover, a significant difference in evaporation of droplets with different concentrations is noticed inside the CC. The highest and lowest evaporation rates of $1.54\times10^{-7}$kg/s and

$9.52\times10^{-8}$kg/s are observed for droplets with 0wt.% and 25wt.% concentrations, respectively. When these values of Case-2.2 are compared with Case-2.1, a 15% decrease in evaporation is noticed, suggesting that the increasing size of the injection droplet could reduce the vaporization of the liquid feedstock.

In contrast, as the droplet diameter is further increased to 300µm (Case-2.3), the maximum gas temperature difference along the centreline between two cases (0wt.% and 25wt.%) reaches 460K in the CC (**Figure 7-4**g). In the barrel, it remains below 100K, and at the gun exit, the temperature difference between all nanoparticle concentrations is negligible. The velocity variations for different concentrations are not considerable (**Figure 7-4**h). A similar trend is observed in the droplet vaporization rate compared to the earlier analysis (Case-2.2 with 150µm droplet size) and the difference in the rate of evaporation for different nanoparticle loadings is further reduced (**Figure 7-4**i). **Figure 7-4**f–i show that the droplet evaporation is delayed for the bigger diameter droplets, and starts evaporating at $x$=0.00747m away from the point of injection, while for the smaller droplet diameter of 50µm, evaporation starts immediately after the injection into the CC (**Figure 7-4**c). Firstly, there is a reduction in the diameter of 150µm and 300µm droplets and an increase in We, droplet deformation and atomization is observed inside the torch CC (*section-**7.3.2*** gives details of droplets fragmentation). Also, after certain deformation, these droplets start evaporating. The timescale of droplet breakup is typically microseconds, which is almost instantaneous compared to the timescale of vaporization [34].

**Figure 7-5** (a-h) compares droplet evaporation for STI of 50µm and 150µm with 0, 5, 15, and 25wt.% nanoparticles concentrations. The significance of droplet evaporation in the HVSFS torch's CC is evident. **Figure 7-5** shows that the maximum rate of evaporation occurs inside the CC while the final location of droplet evaporation stretches to the gun exit for the droplets carrying higher concentrations. The possible reason for this is the increase in heat capacity of the higher concentration droplets (required high heat of vaporization). It takes longer to reach boiling point, which led to a lower vaporization in the CC. Moreover, larger droplets (150µm) with a high concentration (25wt.%) leave the gun without complete vaporization (**Figure 7-5**e-h); this can lead to serious

consequences in real applications and create defects in the final coating. Delay in evaporation of the suspension droplets causes insufficient heating of suspended nanoparticles that may deposit without prior melting. It can cause the inclusion of un-melted particles that lead to porosity [12], [74], [156]. It is inferred that by increasing percentage concentrations of nanoparticles in the base fluid, the rate of evaporation decreases, which causes a delay in the complete vaporization of droplets; however, small droplets are completely evaporated in the middle of the barrel. The implication is that small droplet can be effectively used in applications where the suspension contains nanoparticles with a high melting point, e.g., coating applications with high melting point materials.

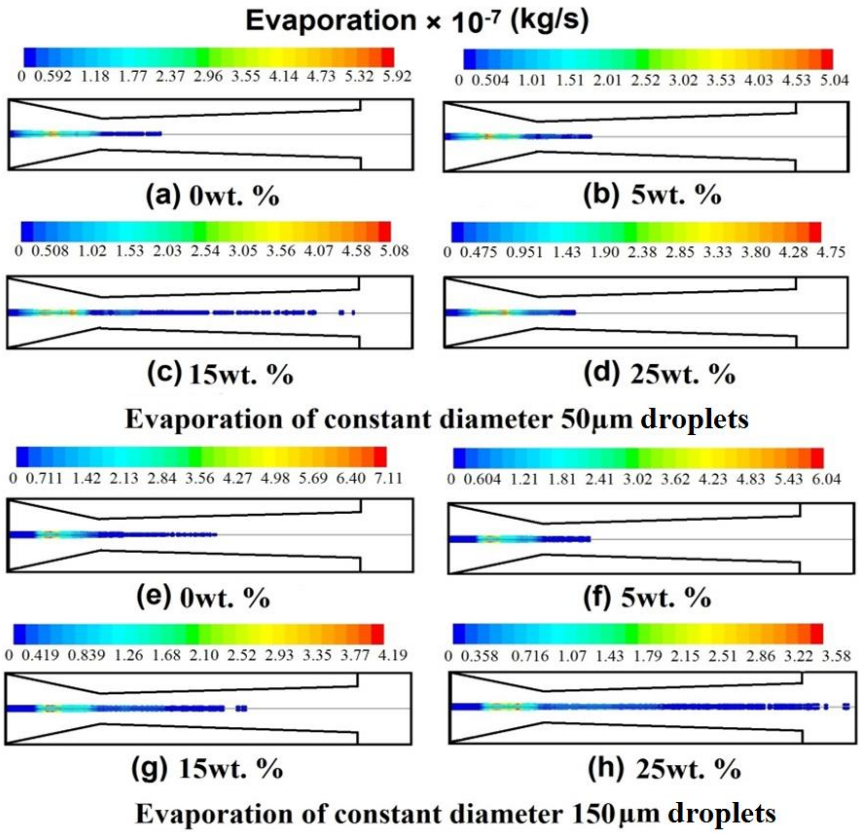


**Figure 7-5** Evaporation rates of droplets inside the domain for STI with constant diameters of (a-d) 50µm and (e-h) 150µm having different solid nanoparticles concentrations

### *(B) Varied diameter droplet injection*

The effect of injecting different diameter droplets from a surface is studied by using three sets of Rosin-Rammler diameter distributions (**Figure 7-3**). In Case-

2.4, five streams with varied diameters of 30, 40, 50, 60, and 70µm are injected simultaneously from a surface having Rosin-Rammler diameter distribution (**Figure 7-6**a).

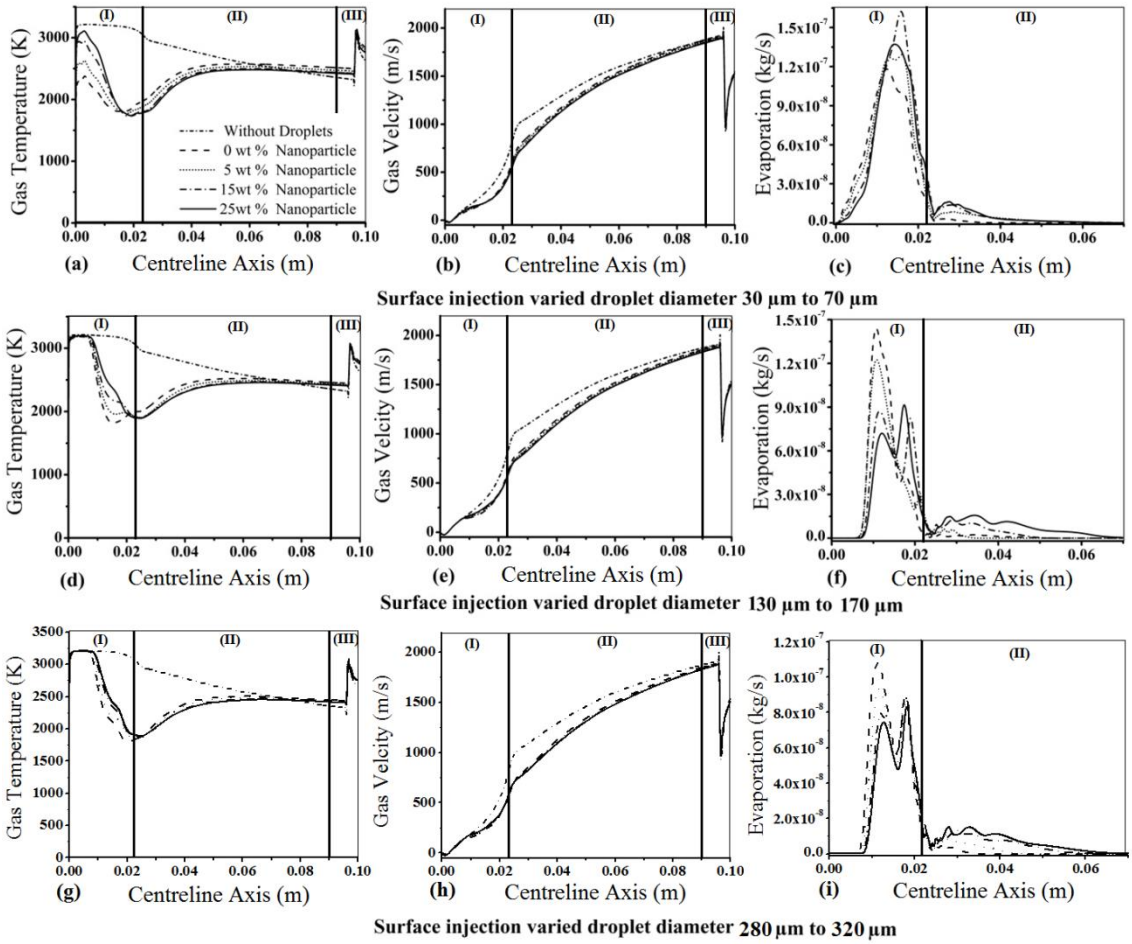


**Figure 7-6** Comparison of gas temperature, gas velocity fields, and rate of evaporation experienced by droplets for STI with varied diameters of (a-c) 30–70µm (d-f) 130–170µm, (g-i) 280–320µm, having different solid nanoparticles concentrations

For these droplet injections the difference in temperature between Without Droplets (Case-1) and droplets with nanoparticles (Case-2.4) increases. For high nanoparticles loading (25wt.%) the temperature difference is 145K while in low nanoparticles loading (0wt.%) it is 850K. The result shows an increase in temperature reduction for lower nanoparticles loading in comparison to Case-2.1, confirming that more evaporation occurs for varied diameter droplets than constant diameter droplets. After the C-D nozzle, massive evaporation of droplets with the high concentration of nanoparticles (25wt.%) affected the gas temperature difference increasing it to 370K while for 0wt.% nanoparticles

loading it is 250K. This increase in temperature difference for varied diameter droplets injection depicts that the rate of vaporization is dependent on the droplet injection diameter. For small diameter droplets (30–40µm) evaporation occurs mainly inside the CC while larger diameter droplets (60–70µm) are evaporated in the barrel.

Compared to the value of velocity in Case-2.1, when five differently sized droplet streams are added, the effect on gas velocity intensifies (**Figure 7-6**b). For 0wt.% concentration, the velocity difference between Case-2.1 (with constant diameter droplets) and Case-2.4 (with varied diameter droplets) becomes 165m/s; while for 25wt.% loading the difference observed is 220m/s (**Figure 7-6**b). This increment in velocity difference is due to the higher cooling effect and the presence of droplets of varying size from 30–70µm. In this case, every droplet has a different evaporation rate and moves with a different velocity inside the torch. Hence, these changing droplets' velocities have different rates of interaction with the combustion gases, which results in larger variations in gas dynamics as compared to constant diameter droplets.

The **Figure 7-6**c illustrates that 0wt.% droplets have a lower evaporation rate ($1.2\times10^{-7}$kg/s) compared to 25wt.% ($1.36\times10^{-7}$kg/s) droplets along the centreline axis. Nevertheless, the overall evaporation rate inside the CC is higher for 0wt.% loaded droplets in comparison to that of 25wt.% loaded droplets. The variation in evaporation rate is because of the different diameters of droplets that have different mass fractions (**Table 7-3**). Small droplets (d≤50µm) carry high mass fractions, but due to their smaller size, the evaporation started earlier and completed at a much faster rate compared to larger droplets. However, the larger diameter droplets (d>50µm) have lower mass fractions and experience high aerodynamics forces that first led to the disintegration of the droplets, and then their evaporation. Hence, for larger droplets a delay in their evaporation process is observed due to the huge amount of heat required to bring the larger droplets to their point of evaporation. Also, a 10-fold increase in the diameter of droplets implies a 1000-fold rise in volume, and hence in heat capacity. The droplet can, therefore, absorb a large amount of heat without being vaporized, at least before the breakup begins. The increase in nanoparticles concentration

also affects the vaporization of these varied diameter droplets, and high concentration droplets show decreased levels of evaporation due to further increase in the heat capacity (**Figure 7-2**).

Similarly, when droplets are injected with the mass flow rate of $1\times10^{-4}$kg/s, the velocity of 30m/s, and different diameters of 130, 140, 150, 160 and 170µm, the trends for gas temperature cooling are changed. Moreover, gas velocity decreases, and reduced evaporation rates for droplets are observed (Case-2.5). Here, the temperature difference in the middle of the CC between 0wt.% and 25wt.% nanoparticles loading is 550K and decreases to 100K along the barrel central axis (**Figure 7-6**d). In **Figure 7-6**e the velocity field does not experience any significant change and shows the same difference as observed for Case-2.2 with constant diameter 150µm droplets injection. This is because the mean diameter of Rosin-Rammler distribution is 150µm and this droplet size carries the high mass fractions of a liquid feedstock, compared to the other sized droplets.

In **Figure 7-6**f, evaporation noticed in Case-2.5 is $1.4\times10^{-7}$kg/s and $7.67\times10^{-8}$kg/s for 0wt.% and 25wt.% nano-loading, respectively. Furthermore, an analysis of Case-2.5 shows a decrease in the overall evaporation along the gun axis by 9% for 0wt.% loading and by 19% for 25wt.% loading when compared to Case-2.2. This is because the large droplets initially absorb a huge amount of heat without evaporation, and start vaporizing once fragmentation has reduced their size significantly. The final location of droplet evaporation moves from the C-D nozzle towards the middle of the barrel for 0 and 5wt.% nanoparticles concentrations. The droplets with 15 and 25wt.% nanoparticles solid loadings leave the HVSFS torch without complete evaporation and are ejected into the atmosphere. As more concentrated droplets have a higher surface tension and require more heat to vaporize, their evaporation process is also delayed. In Case-2.6, when the set of droplet diameters of 280, 290, 300, 310, and 320µm are injected, no significant variations are observed, compared to a constant diameter (300µm) Case-2.3. This confirms that all these droplets have similar trends of gas cooling, gas velocity and rate of evaporation (**Figure 7-6**g–i).

In summary, for STI, the effect on droplets evaporation is dependent on two parameters increase in droplet diameter and nanoparticles concentration. As the droplets size and nanoparticles concentration increases, the rate of evaporation decreases. For STI, the varied diameter set of 30–70µm increases the rate of evaporation in comparison to constant 50µm diameter. Moreover, for the second and third set of varied diameters of 130–170µm and 280–320µm, the effect is reversed due to increased droplet sizes. It is concluded that increasing nanoparticles concentration in liquid feedstock droplets with varied large sizes would decrease the droplets' evaporation process. For many practical applications, injected droplets have different diameters and the trend of change in gas temperature, velocity and droplets' evaporation is very similar to that illustrated in section-***7.3.1.1*** part-B.

#### 7.3.1.2 Group-type injection

Similar to STI, the GTI uses two streams having (A) constant diameter droplets and (B) varied diameter droplet injection (**Figure 7-3**). The GTI is not axial, and its direction is set at an angle of 45° (to the horizontal axis). This is to increase the interaction time of suspension droplets with higher temperature gases, reduce the evaporation length of ethanol droplets and confine the evaporation within the CC and barrel sections of the HVSFS torch [10], [14]. All cases are simulated for four different nanoparticles concentration of 0, 5, 15, and 25wt.%. For brevity, the results related to GTI are presented only for 150µm (constant diameter), and 130–170µm diameter droplets (Rosin-Rammler diameter distributions).

***(A) Constant diameter droplet injection***

In Case-3.2, the droplets are injected in a group with a 45°angle of injection to observe the effects over the gases inside the torch's CC and barrel section-**II**. These droplets are not moving along the centreline axis of the gun. The droplets are injected with a mass flow rate of $1\times10^{-4}$kg/s, the velocity of 42.426m/s and a constant diameter of 150µm into the HVSFS torch. They influence the centreline temperature and velocity of gases when they converge on the torch central axis after striking the CC walls (**Figure 7-7**). In the previous Case-2.2 with STI, the angle of injection is 0°, and the droplets move along the centreline axis of the

torch while in the GTI the angle of injection is varied and the droplets move at a 45° angle with the torch's centreline axis (**Figure 7-7**). Therefore, the droplets are injected into the core of the combustion zone, and come in direct contact with the hot flame. They reach the evaporation point rapidly in comparison to the STI Case-2.2 and evaporate completely within the torch. Furthermore, **Figure 7-7** shows that due to the complete evaporation of droplets inside the torch, the temperature of the flame increases in the free jet region of the GTI case. However, it is observed that greater gas cooling occurred for GTI; the reason is that GTI supports higher evaporation of droplets, and evaporation rate is increased up to 67%. As droplets come into direct contact with the combustion gases in the hottest zones of CC, they receive more thermal energy to heat the suspension and suspended nanoparticles.

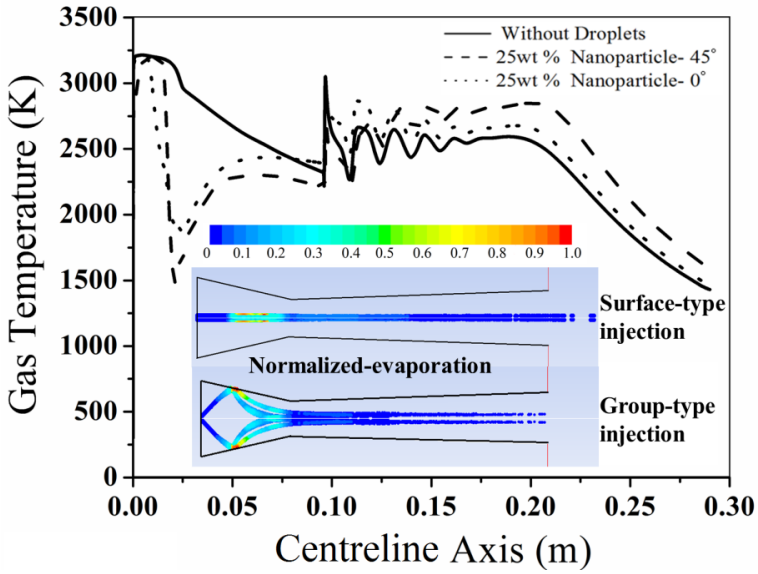


**Figure 7-7** Comparison of gas temperature and normalized droplet evaporation with the STI (angle of injection 0°) and GTI (angle of injection 45°) of constant diameter droplet of 150µm and having 25wt.% nanoparticles concentrations

The effect of droplet evaporation on centreline temperature and velocity for Case-3.2 is shown in **Figure 7-8**(a-b). When droplets converge along the centreline axis after striking the CC walls, they start to influence the gas dynamics along the x-axis. Only the droplets with 25wt.% concentration are converged along the central axis while others evaporated in the vicinity of the combustion zone. The temperature reduction before the C-D nozzle is about 1400K for droplets with 25wt.% concentration in contrast to Without Droplets

Case-1, and downstream of the C-D nozzle it becomes 900K. Other droplets carrying 0, 5, and 15wt.% nanoparticles are evaporated in the CC as they come in direct contact with the flame and leave the nanoparticles that accelerated and were heated in the nozzle and barrel sections.

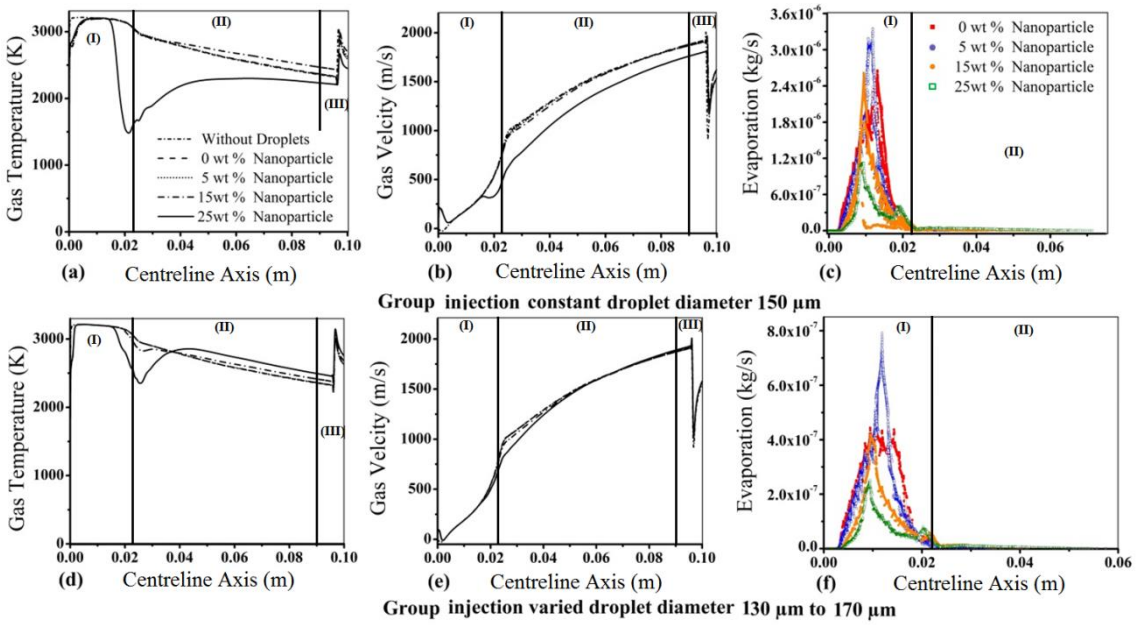


**Figure 7-8** Comparison of gas temperature, gas velocity fields, and rate of evaporation experienced by droplets injected as a group at an angle of 45° with constant diameter of (a-c) 150µm and with varied diameters of (d-f) 130–170µm, having 0, 5, 15, and 25wt.% nanoparticles concentrations

Similarly, the velocity field of combustion gases along the axis is influenced by the droplets carrying 25wt.% nanoparticles concentration the difference is about 220m/s. Furthermore, the rates of evaporation of droplet streams are captured along their actual path in the direction of increasing *x*-position, (**Figure 7-8**c). It can be seen that droplets with 0, 5 and 15wt.% concentration have the value of their peak evaporation rate of $2.59\times10^{-6}$kg/s, $3.30\times10^{-6}$kg/s and $2.62\times10^{-6}$kg/s, respectively, in the middle of the CC, whereas, droplets with 25wt.% concentration have the lowest evaporation rate of $1.11\times10^{-6}$kg/s. It is also shown that the evaporation is lower when the droplets are carrying a higher percentage of nanoparticles concentration for the GTI. However, these rates of evaporation are considerably higher in GTI when compared to the STI; overall the increment in vaporization is 94% and 91% for 0wt.% and 25wt.% nano-loading, respectively.

### *(B) Varied diameter droplet injection*

The droplets with varied diameters of 130, 140, 150, 160 and 170µm are injected into the core of the combustion zone (Case-3.5); the results for gas temperature and velocity along the central axis are in **Figure 7-8**d–e. Except for 25wt.% loading, no considerable change is evident on the centreline temperature and velocity profiles as varied diameter droplets move away from the central axis. For 25wt.% loading there is a significant difference as compared to Case-1, although much lower than Case-3.2 (**Figure 7-8**a, d).

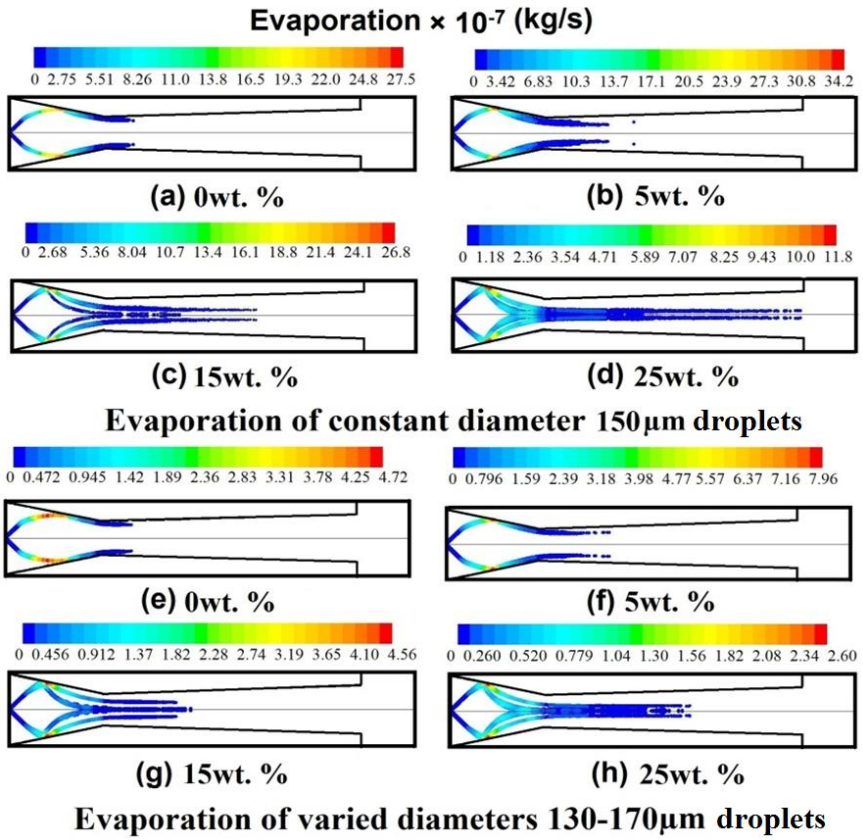


**Figure 7-9** Evaporation rates of droplets inside the domain for GTI with constant diameters of (a-d) 150µm and with the varied diameters of (e-h) 130–170µm having different solid nanoparticles concentration

When differently sized diameters in GTI (Case-3.2) are compared to constant size GTI (Case-3.5), a significant reduction in the rate of evaporation is observed for all concentrations of nanoparticles (**Figure 7-8**c, f). For 0 and 25wt.% nanoparticles loading, the reduction in evaporation is about 83% and 78% respectively. These variations are the result of greater fragmentation of larger droplets, the difference in the relative velocities of droplets, and the

requirement of high heat of vaporization, which in turn reduces the evaporation process. The behaviour of the other GTI with the constant diameter of 50µm and 300µm, and variable droplet sizes of 30–70µm and 280–310µm is more or less similar, and for conciseness figures for these results are excluded.

Evaporation rates for GTI are shown in **Figure 7-9**. These trends indicate that nanoparticle concentration has to be controlled by increasing the efficiency of the evaporation process. Droplets with constant diameters and having lower nanoparticles concentration are evaporated in the barrel section (**Figure 7-9**a-c). When droplets are loaded with 25wt.% nanoparticles they reach the end of the barrel before prior evaporation (**Figure 7-9**d). The highest evaporation rates are observed in all cases with constant diameter droplets delivered through GTI. It can be detected that different size droplets also leave the nanoparticles in the middle of the barrel while the rate of evaporation is reduced (**Figure 7-9**e–f; 78% reduction for 25wt.%). Moreover, the group injection of constant diameter droplets and varied size droplets with an injection angle of 45°, work efficiently for smaller droplets (diameter≤50µm) having small nanoparticles concentration (0–5wt.%). On the other hand, droplets with a diameter>50µm and a high nanoparticles concentration (15–25wt.%) will strike the walls of the CC and move forward along the walls of the torch. This must be avoided by using the proper angle of injection and injection velocities.

It is observed that when suspension droplets are fed into the HVSFS by using the STI at a 0º angle of injection, the gas enthalpy, and kinetic energy are decreased, and the efficiency of the HVSFS flame is reduced significantly (**Figure 7-7**). To reduce this cooling effect and to add more energy to the HVSFS flame GTI is carefully chosen, and it works efficiently. The overall behaviour of GTI is more efficient compared to STI, as low gas cooling is observed along the centreline axis, and a high rate of droplet evaporation is noticed inside the CC. Hence, it will improve the solid particle heating, and improved kinetic energies can generate denser coatings.

### 7.3.2 Effects of the Nanoparticles Suspension on the Secondary Breakup of the Suspension Droplets

The TAB model captured the droplet secondary breakup, and the We detected in all cases remained below 100. Since droplets fragmentation in the HVSFS process is one of the major physical phenomena, a thorough investigation on breakup is carried out in all cases. For the analysis, droplet streams with constant diameter injected in the gun are picked up, and results in diameter reduction and final location of evaporation are highlighted. Furthermore, for the Rosin-Rammler diameter distribution, a set of five streams is analysed for clarity. Since the droplets $Oh$ remains below 0.1, $We$ is the dominating parameter and is analysed here in detail [115], [136].

#### 7.3.2.1 Surface-type injection

***(A) Constant diameter droplet injection***

A comparison of droplets diameter reduction is shown in **Figure 7-10**(a–d) for STI (Case-2.1). This demonstrates the secondary breakup and a decrease in the diameter of 50µm droplets with four different solid nanoparticles concentrations. It can be seen that droplets experience a sharp decrease in diameter from 45µm–20µm, and 20µm–10µm approximately for all nanoparticles concentrations.

Comparison of We variations for droplets in the computational domain is depicted in **Figure 7-10**(e–h). In Case-2.1, the We reached a peak value of about 12 in the CC, where the primary atomization occurs due to relative velocities between the droplets and gas phase in the CC. However, the value of $We$ remains below 14 for all nano-loading; hence, the breakup type is vibrational [118], [136]. Even an increase in solid nanoparticles concentration inside the 50µm droplets does not affect the disintegration process. Therefore, droplet vaporization is dominant and controls the process when solid nanoparticles suspended in the droplets are injected with a small constant diameter of 50µm.

In Case-2.2, as the droplet diameter increases to 150µm the droplets disintegration is reflected by the reduction of droplet diameter from 150–35µm and 35–13µm inside the CC of the spray gun **Figure 7-11**(a-d). The We varies

from 25–30, depending on the nanoparticles concentration in the droplets and led to severe fragmentation in the middle of the CC **Figure 7-11**(e-h). For all concentrations, the droplets are evaporated in the midst of the barrel and release solid nanoparticles, except for the highest concentration (25wt.%). These high concentration droplets face a delay in the evaporation process and reach the exit of the barrel. Similar results are observed for larger droplets diameter reductions (300µm) while the We increased from 50–70 for constant diameter Case-2.3. The above analysis indicates that the fragmentation process is dominant for large droplets (150 and 300µm) while the rate of evaporation is higher for small droplets (50µm). For brevity Case-2.3, figures for droplets diameter reduction and We are not included.

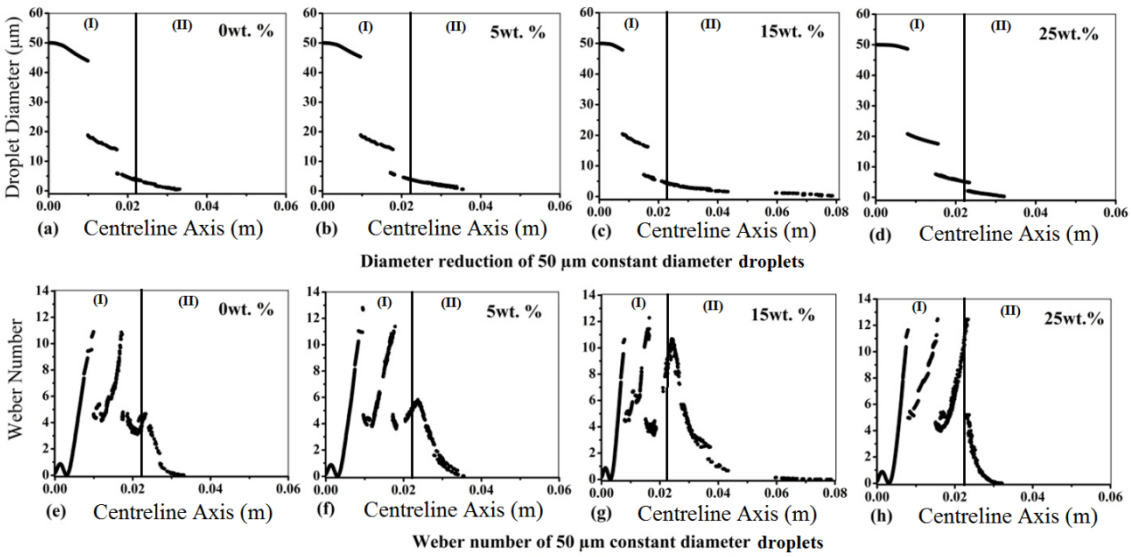


**Figure 7-10** Comparison of (a-d) droplet diameter reduction and (e-h) Weber number for STI with a constant diameter of 50µm having different solid nanoparticles concentrations

### *(B) Varied diameter droplet injection*

Considerable reduction in diameter is observed for Case-2.4 when droplet streams with five different diameters (30, 40, 50, 60 and 70µm) are injected into the gun (**Figure 7-12**a–d). For these cases, the reduction is dependent on the injected size of droplets. For droplets with 30µm diameter the reduction is from 20–14 and 14–7µm; and for 40µm droplets, this reduction is from 30–20 and 20–14µm. Moreover, for larger droplets of 60µm diameter, a sharp decrease from 56–25 and 25–18µm is observed, and for 70µm this reduction is even

greater, from 66–30 and 30–24µm. This scenario of decreasing diameters for different initial droplet sizes illustrates the higher fragmentation for droplets larger than 50µm and lower fragmentation for droplets smaller than 50µm.

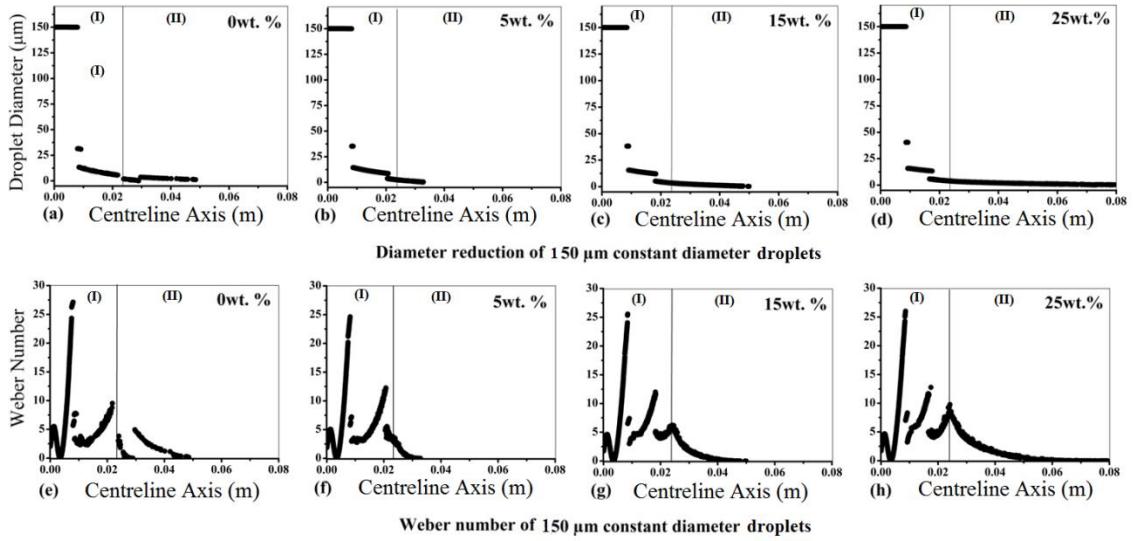


**Figure 7-11** Comparison of (a-d) droplet diameter reduction and (e-h) Weber number for STI with a constant diameter of 150µm having different solid nanoparticles concentrations

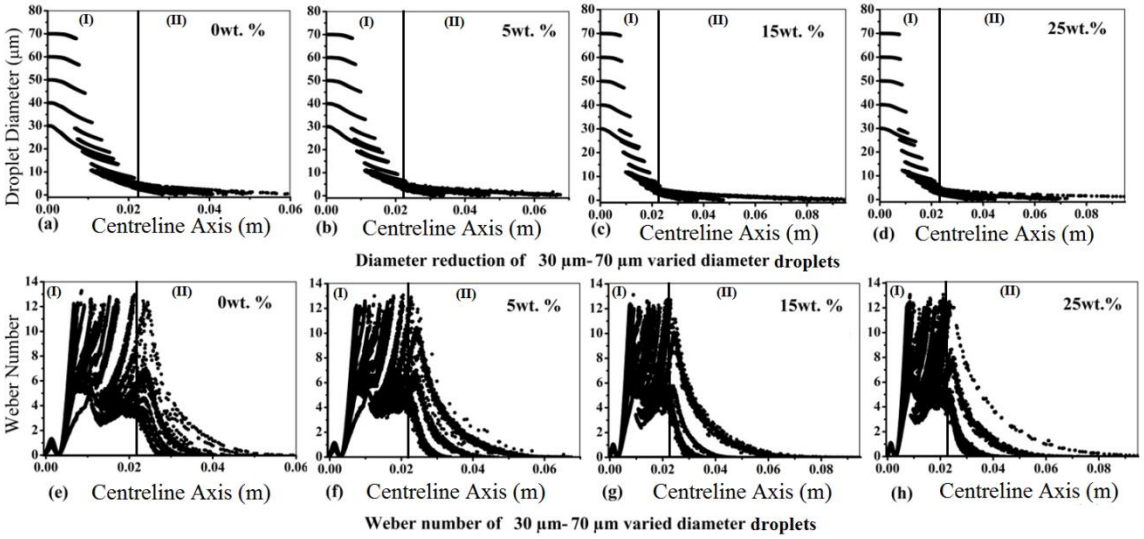


**Figure 7-12** Comparison of (a-d) droplet diameter reduction and (e-h) Weber number for STI with varied diameters of 30–70µm having different solid nanoparticles concentrations

The We for these varied diameter droplets (30–70µm) injection is presented in **Figure 7-12**(e–h). Due to the presence of varied sizes droplets, droplets fragmentation is observed at varying positions along the axis. Varied diameter droplets carrying different nanoparticles concentration have values of We<14,

and similar vibrational type of breakup [118], [136] as observed for constant diameter droplets of 50µm (Case-2.1).

When injected droplets have varied sizes from 130–170µm (Case-2.5) and 280–320µm (Case-2.6) a similar trend in the results is noticed. The figures for these findings are excluded for brevity. In Case-2.5, a 71% reduction is noticed in the droplet size for all four different concentrations. In these cases, the We fluctuates from 26–35, and severe fragmentation is observed inside the CC. Further, an increase in the nanoparticles concentration influences the disintegration and evaporation process of droplets; hence, droplets exit the gun without complete evaporation. The reduction in diameter for the larger droplets, with size varying from 280–320µm (Case-2.6), is 85% the highest in comparison to all other cases. Moreover, We increase from 55–80, proving that large droplets experience severe fragmentation inside the CC. Overall, when the Rosin-Rammler diameter distribution is applied to the ST injection, then more droplets discharge through the torch without prior evaporation. This complication intensifies with an increase in the nanoparticles concentration.

#### 7.3.2.2 Group-type injection

***(A) Constant diameter droplet injection***

The diameter reduction for GTI is also significant, and augmentation in the diameter reduction is detected with increasing injection diameter (Case-3.2). It is further augmented by increasing the nanoparticles concentration from 0–25wt.% (**Figure 7-13**a–b). The reduction in diameters of uniform size droplets (150µm) with 0wt.% nano-loading equals 65% (from 150–52µm) and for 25wt.% nano-loading it is 74% (from 150–40µm). The value of maximum We for Case-3.2 is decreased from 38–32 for 0 and 25wt.% concentrations of nanoparticles, respectively (**Figure 7-13**c, d). When compared with the STI (Case-2.2) higher values of We are observed for GTI (Case-3.2), proving that droplets disintegration is increased up to 34%.

***(B) Varied diameter droplet injection***

The reduction in diameter and the values of We are changed when GTI of varied size droplets is examined in Case-3.5. **Figure 7-13**(e–f) shows the

reduction in diameter of the 0wt.% nanoparticles concentration is 70% (170–47µm); however, diameter reduction of the 25wt.% concentration droplet is 79%. The maximum reduction is witnessed inside the CC and droplets completely evaporate before escaping the gun. The maximum We for these extreme cases, having 0wt.% and 25wt.% concentration, changes from 50–42 (**Figure 7-13**g–h). The droplet deformation detected for the GTI with the various droplet diameters is significantly higher than Case-2.5 with STI (carrying different diameter droplets).

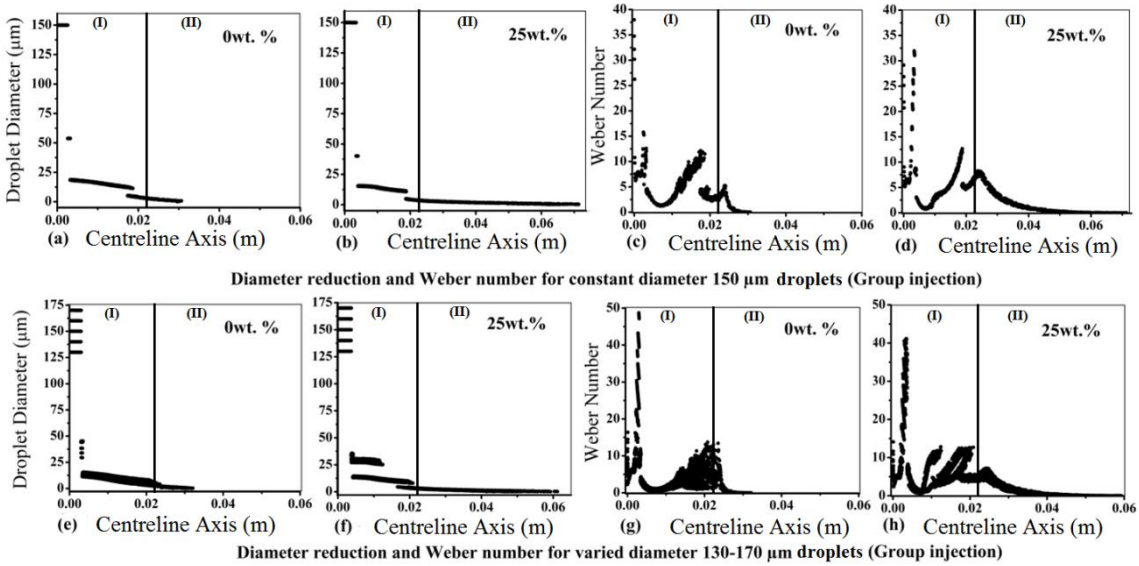


**Figure 7-13** Comparison of droplet diameter reduction and droplet We number for GTI with a constant diameter of (a-d) 150µm and with varied diameters of (e-h) 130–170µm having different solid nanoparticles concentrations

In summary, if the small size droplet (diameter≤50µm) injection is favoured in an application, the extra liquid surfactant should be added to the suspension for reducing the droplets' surface tension and intensifying the fragmentation process. However, regarding the droplets atomization in the HVSFS process, the larger droplets lead to severe breakup with less evaporation when carrying higher nanoparticles concentration. Smaller droplet injection is required with an optimized range of nanoparticles concentration to increase the effectiveness of the HVSFS process as the large sized suspension droplets delay the droplet evaporation rate. This delay in the suspension evaporation would decrease the residence time of the solid particles in the hot flame regions which increases the number of un-melted particles over the substrate. The increase in un-melted

nanoparticles can cause the increment in the coating porosity. Hence, to form a defect-free coating, the smaller size suspension droplets would be used for completing the evaporation process of suspension and better melting of solid nanoparticles before deposition. For GTI, optimization is required for selecting the injection angle and the injection velocity with varying sizes of droplets to obtain the best results for the thermal spraying process.

It should be noted that in the original design of the DJ2700 gun, the gas-carrier-tube is located at the centre of the back wall, and is surrounded by annular O/F inlets. This creates a recirculation zone close to the back wall at the injection area, and the particles start to spread out near the nozzle throat where the flame reaches the axis of the torch and interacts with the droplets. Likewise, when droplets inject at an angle of 45° directed towards the combustion core, they have direct interaction with the flame which makes the evaporation process more efficient in comparison to the axial injection. For this procedure, one has to control the injection parameters and fix them to avoid droplet collision with the CC walls.

Practically, a spray cone with a variety of droplet diameters is injected into a thermal spray gun. This causes velocity oscillations due to the unsteady nature of the HVSFS jet. These oscillations create droplets in any part of the domain from sub-microns to tens of microns in diameter. Due to the fluctuations of the velocity field, droplets with a larger diameter can move towards the low-velocity jet area and may not experience aerodynamic fragmentation. Moreover, a number of large droplets may not be fragmented as efficiently as others, resulting in the existence of bigger droplets tens of microns in size. Particular care must be taken when injecting large droplets into the HVSFS process. In the HVSFS process, the coating efficiency is dependent on both the torch operating parameters and injection parameters. The in-flight behaviour of suspension droplets, including breakup and evaporation, has a strong link with the deposition efficiency. Hence, the complete evaporation of droplets inside the CC will lead to sufficient heating and melting of suspended nanoparticles, and fine coating can be achieved.

## 7.4 Summary

Thermophysical properties of liquid fuel droplet with various solid nanoparticles concentrations (0, 5, 15 and 25wt.%) are calculated and modified based on the proposed models in the literature and then inserted into the models employed in this study. Subsequently, the effects of nanoparticles suspension on the gas dynamics and droplet dynamics (secondary breakup and vaporization rate) inside the HVSFS process are investigated. The main conclusions are as follows:

- The final location of evaporation is significantly changed for P-E and suspension droplets (homogeneous and non-homogeneous droplets). During the simulations, nanoparticles are created in the computational domain as new entities; hence, the final location of evaporation is an important aspect of the numerical analysis of suspension droplets in the HVOF torch.
- Droplets with higher concentration have greater surface tension and require higher heat of vaporization; thus, an increase in the nanoparticles concentration delays the evaporation process of the droplets and adversely affects their disintegration.
- For STI and GTI, the effect on droplets breakup and evaporation is dependent on two parameters: (1) the nanoparticles concentration, (2) and droplet diameter. The rate of evaporation and droplet disintegration is reduced with the increase in droplets size and nanoparticles concentrations.
- Smaller droplets (d≤50μm) show a better trend for high concentration loading, as they experience high evaporation in the mid-section of the nozzle and can be effectively used in applications where the suspension contains nanoparticles having a high melting point. The injection of smaller diameter suspension droplets would improve the evaporation of suspension droplets and heating/melting of solid content.
- For larger droplets (150 and 300μm), fragmentation is the dominant factor that controls the process. Moreover, the larger droplets with high

concentration leave the gun without complete vaporization. This can lead to serious consequences in real applications and can create defects in the final coating.

- The delay in the evaporation of larger droplets carrying higher nanoparticles concentration causes insufficient heating of the suspended nanoparticles, and they may be deposited without prior melting. These un-melted particles create defects and result in the increment of the coating porosity.
- The droplets added using GTI (at an angle of 45°) are inserted into the core of the combustion zone and reach the evaporation point rapidly in comparison to the STI (at an angle of 0°), and evaporate completely inside the torch.
- The GTI increases the efficiency of droplets disintegration and evaporation, and the effects of gas cooling are reduced.
- For increasing the effectiveness of GTI, optimized values of angles of injection, injection diameter and injection velocity are required to avoid droplet collision with the torch’s CC walls.

# 8 EFFECT OF ANGULAR INJECTION, AND EFFERVESCENT ATOMIZATION ON HIGH-VELOCITY SUSPENSION FLAME SPRAYING PROCESS

## 8.1 Introduction

The technology for producing thermal barrier and wear-resistant dense coatings can be modified with nanosize powder injection in order to obtain lower coating thickness. Recently, this technique has been developing a liquid feedstock system for injecting nanometre size to 10µm size powder particles in a thermal spraying torch [13], [16], [68]. The suspension spraying works well for several applications including TBCs, tribofunctional and wear-resistant coatings, biofunctional coatings, fuel cell development, and coatings for catalytically active surfaces [68], [70]–[72] (literature review, Chapter 2).

The HVOF torches are modified, and the liquid feedstock injected with the aid of suspension feeder and suspension injector [64], [68], [181]. The HVOF applications use axial (internal) injections [17], [64], [71], [73], [181]. The suspension liquid is injected into the HVOF flame spray jet and under the action of the combustion gas thermal energy and high-velocity the suspension droplets disintegrate, evaporate and release the nanoparticles inside the torch. These nanoparticles/nano-agglomerates become heated, melt and accelerate towards a prepared surface, and produce a coating. The advantage is that the precursor can be nanosize, and the coatings are thin, smooth and finely structured, even nanostructured [73], which is not possible with standard dry powder feeders. The size of nanoparticles coating depends on a number of parameters, including flame temperature and velocity, solution feed rate, liquid precursor concentration, liquid precursor solvent properties, and the atomization of precursor streams [7], [35], [42], [58], [62]–[64], [90].

Furthermore, to improve the process efficiency of generating the dense nanosized coating, the atomization of droplets is essential for the precursor solution carrying high concentrations of suspended particles. The atomization of liquid feedstock can be controlled by the atomizer nozzle design and its

injection parameters [92]–[94]. Many researchers have studied the phenomenon of atomization and some specific work is highlighted in Chapter 2 section-***2.1.4***. The effervescent atomizing nozzle is based on the twin-fluid atomization, in which a small amount of gas is injected into the liquid before the exit orifice to form a bubbly mixture of gas and liquid. On emerging from the nozzle, due to the pressure difference, gas bubbles rapidly expand and shatter the liquid into ligaments and fine droplets. This method offers the advantage of smaller droplet sizes at low injection pressure and atomizing even high viscosity liquids effectively [92]–[94], [97], [100]–[102], [105].

The effects of varying injection parameters and injection types over the flow physics inside the spray torch have not been studied previously. It must be noted that this analysis needs to be implemented to inspect the effectiveness of the different injection processes. These shortcomings are addressed in this chapter. In the present work, for atomizing the suspension liquid into fine droplets inside the CC of the HVOF torch, a new effervescent atomizer is designed based on previous research studies [93], [94], [102]. A numerical model is used to study the effect of varying injection types on HVOF flow dynamics. For understanding the atomization of the suspension droplet, results are presented and compared for three types of injection: STI, GTI and ETI.

## 8.2 Model Description

The HVOF gun geometry used is similar DJ2700-torch (Chapters 3, **Figure 3-1**) [115], [116]. The operating parameters, along with the schematic representation of the computational domain, are similar (**Figure 3-1**, **Table 3-1** and **Table 7-1**). Similarly, the premixed O/F is injected into the DJ2700 gun; the resulting hot combustion gases are accelerated inside the C-D nozzle and flow through the barrel section towards the exit of the gun. The droplet injection mass flow rate and injection velocity, selected on the basis of previous work [115], [116], [119], (as given in **Table 7-1**). Moreover, similar modelling techniques are applied to simulate the combustion, turbulence and droplet dynamics inside the HVSFS torch (for detail see Chapter 3 & Chapter 7).

The numbers of cases are simulated to analyse the effects of varying injection schemes on the droplet atomization in the CC of the thermal spray gun. A clear case representation is presented in **Table 8-1**. Here, Without Droplets (Case 1) refers to a case in which droplets are not injected, and only combustion gas flow characteristics in the HVSFS process are analysed. Furthermore, different injection types are studied, namely STI, GTI and ETI. The first type of injection is analysed for axial injection of droplets from a centralized inlet opening into the DJ2700 HVSFS torch. For the STI scheme (Case 2.1), the angle of injection is 0°, and the suspension droplets move along the centreline axis of the torch (**Figure 8-1**a, **Table 8-1**). In the GTI, different angles of injection at 5°, 10°, 15°, and 20° are considered for suspension injection and cases are named Cases 2.2, 2.3, 2.4, and 2.5, respectively (**Figure 8-1**b, **Table 8-1**). It is expected that the droplets are injected into the core of the combustion zone and reach the evaporation point rapidly in the GTI compared to the STI, and evaporate completely within the torch (**Figure 8-1**a-b).

The third type of injection uses the twin-fluid phenomenon in which nitrogen gas and liquid feedstock are injected separately into the effervescent-type nozzle. This creates a bubbly flow inside the injection nozzle and then sprays it into the torch's CC to obtain a finer disintegration of the suspension's droplets (**Figure 8-1**c-d). With this technique, the liquid discharged from the orifice with the internal cavity of gas (**Figure 8-1**c). The motion of the liquid at the exit of the injector creates a gas-core surrounded by the liquid film, and due to the pressure differences, the gases expand and shatter the liquid film into ligaments and fine droplets [92]–[94], [97], [100]–[102] (Chapter 2, section-***2.1.4***). For the ETI, different spray half angles of 4°, 6° and 8° are selected based on various GLRs of 0.095, 0.190 and 0.285, respectively (**Table 8-1**). These studies are named Cases 3.1, 3.2 and 3.3, respectively, (see **Table 8-1**). It should be noted that increasing the GLR will eventually increase the spray-half-angle which can further improve the atomization. The LISA model is applied to capture the primary breakup of ligaments ejecting out from the ETI nozzle (Chapter 5, section-***5.2.2***).

**Table 8-1 Cases description with injection types and injection parameters for HVSFS process**

| Injection Types | | | | |
|---|---|---|---|---|
| Case 1→ Without Droplets, only combustion gas flow characteristics | | | | |
| Case 2.1→ **Surface-Type Injection**, Angle of injection 0° | | | | |
| **Group-Type Injection** | | **Effervescent-Type Injection** | | |
| Cases | Angle of injection | Cases | Spray-half-angle | GLR |
| Case 2.2 | 5° | Case 3.1 | 4° | 0.095 |
| Case 2.3 | 10° | Case 3.2 | 6° | 0.190 |
| Case 2.4 | 15° | Case 3.3 | 8° | 0.285 |
| Case 2.5 | 20° | | | |

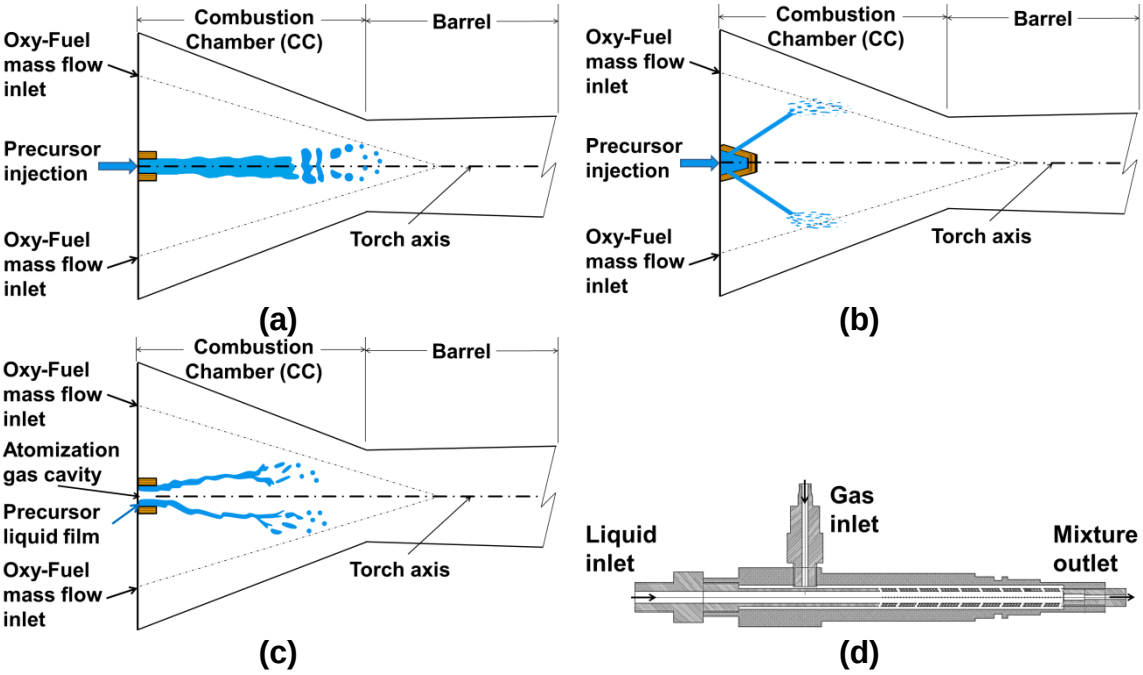


**Figure 8-1** Schematic of liquid feedstock injection inside the DJ2700 HVSFS torch (a) STI (b) GTI (c) ETI, and (d) cross-section of ETI nozzle

Detailed descriptions of the gas phase, discrete phase, droplets' breakup and combustion models are reported in Chapter 3, sections-***3.2.3***, and ***3.2.4***. For each type of droplet injection (axial, angular and effervescent), different rates of evaporation and fragmentation have been detected. Also, the effect of droplets' breakup and evaporation on gas dynamics is changed with varying injection parameters (**Table 8-1**). This is due to the variation in droplet interface with the continuous combustion gases inside the HVSFS torch.

## 8.3 Numerical Results and Discussions

This section provides a detailed analysis of the effects of the group-type angular injection and effervescent-type atomization on gas dynamics and droplet dynamics inside the HVSFS torch. The results are divided into different sections; firstly GTI effects on gas and droplet dynamics are discussed in section-***8.3.1***. Afterwards, a similar kind of analysis is developed for the ETI cases in section-***8.3.2***. Here, the Case 2.1 (STI), and Case 1 (Without droplets) are used as reference cases for the analysis and comparison with the GTI and ETI cases.

### 8.3.1 Group-Type Injection

This section illustrates the effects of varied angles of injection in the GTI on the gas and droplet dynamics inside the DJ2700 HVSFS torch. In all cases, the suspension droplets are injected with a constant diameter of 150µm, the average initial velocity of 42m/s and injection mass flow rate of $1\times10^{-4}$kg/s. In the GTI, the liquid feedstock is injected into the torch with different angles of injection of 5°, 10°, 15°, and 20° and named Cases 2.2, 2.3, 2.4 and 2.5, respectively (**Table 8-1**).

The flow physics in the thermal spray torch can be changed by using different types of liquid feedstock injections and varying injection parameters [115], [116], [119]. This section explains the effects on the gas flow dynamics and droplet dynamics by changing the angles of injection. **Figure 8-2**a–b demonstrate a comparison of gas temperature ($T_G$) and gas velocity ($V_G$) along the axis of the torch for the GTI with Case1 (Without Droplets) and Case 2.1 (STI). The heat is transferred from combustion gases to droplets, and then the droplets start evaporating after enough heating, which led to the cooling of combustion gases inside the torch's CC and barrel sections. **Figure 8-2**a, shows that the gas cooling is reduced with the increment in the injection angle from 0°–20°. Maximum cooling is observed for the 0° angle of injection as the P-E droplets extract heat from the hot gases and are evaporated along the torch's central axis, whereas minimum cooling effects are detected for 10°–20° angles of

injection as the droplets are injected into the core combustion regions. Thus, less cooling effect is observed along the torch's central axis (**Figure 8-2**a).

After the torch exit, in the free jet section-**III** at *x*=0.15m, an increase in temperature is observed for 0°–20° angles of injection, compared to Without Droplets (Case 1). This temperature rise in the free jet section proves the combustion of P-E vapours that add heat to the combustion gases (**Figure 8-2**a). Moreover, with an increase in the angle of injection, the droplet deviates from the centreline axis of the torch when injected into the core of the combustion zone. This technique increases the ethanol evaporation and combustion within the torch, hence improves the efficiency of the HVSFS process. From the graphical presentation in **Figure 8-2**a–b, a 10° angle of injection appears appropriate, as it enhances the $T_G$ and $V_G$ compared to all other cases. It proves that at a 10° angle of injection, ethanol droplets evaporated inside the CC, and non-premixed combustion started in the barrel section and added maximum heat and energy to the overall flow inside and outside the torch. Further, at 15º and 20º angles of injection the $T_G$ trend is similar to Without droplets Case 1; hence, it is evident from these graphs that no central cooling is observed at large angles of injection.

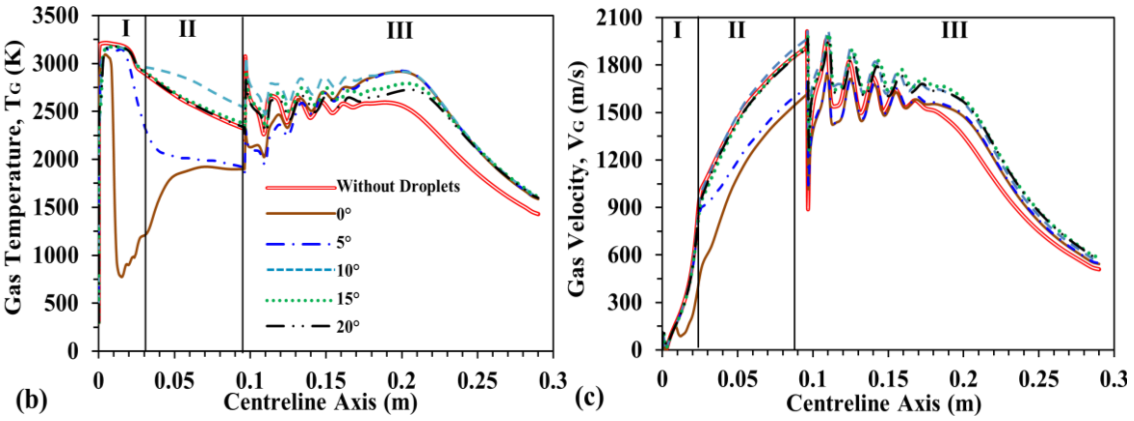


**Figure 8-2** Comparison of (a) gas temperature ($T_G$), and (b) gas velocity ($V_G$), for 150µm diameter droplet injection inside DJ2700 torch at varying angles of injection (GTI) (with P-E injection)

The interaction between high energy combustion gases and droplets is also governed by the relative velocity of droplets within the continuous gas, as the combustion gas has a higher kinetic energy which transfers the momentum to

the droplets. Therefore, the velocity of droplets keeps increasing throughout its flight. When flow passes through a C-D nozzle, the flow velocity and Mach number increase, which adds energy into the droplets and they fly from the nozzle towards the torch exit. **Figure 8-2**b shows that the gas velocity ($V_G$) decreases in the 0°, and 5° angles of injection along the torch axis as the droplets travel along the centreline axis. And, due to cooling of the combustion gas, reduction in the temperature and the velocity of flame is detected, while for higher angles of injection 10°–20° the droplets travel far away from the centreline axis, hence the reduction in velocity is not detected along the torch axis. However, in the free jet section-**III**, an increase in $T_G$ and $V_G$ confirms the addition of thermal and kinetic energy from the ethanol combustion with the remnant oxygen (**Figure 8-2**). Therefore, it can be stated that the angular injection increases the HVSFS process efficiency by increasing droplet evaporation and vapour combustion rates while decreasing the cooling effects on the gas thermal and kinetic energies.

Interesting effects of droplet breakup and evaporation in the CC are witnessed after the angular injection (GTI) of feedstock (**Figure 8-3**). The ethanol droplets convert into vapours, and maximum evaporation is observed inside the CC mid-region for 0°–15° angles of injection. For a 20° angle of injection, the droplets move toward the C-D nozzle throat region (**Figure 8-3**a). Compared to 0º-STI, the rate of evaporation is increased when droplets are injected at an angle of 5º–10º GTI. A small decrease in the maximum value of evaporation is observed for 15º and 20º angles of injection (**Figure 8-3**a) while lower mass fractions of liquid ethanol are observed in these cases (**Figure 8-3**b), which confirms the overall enhancement in the rate of evaporation. Moreover, the elongated evaporation regions are identified in Cases 2.4 and 2.5 (**Figure 8-3**a). This further proves that evaporation of liquid droplets is augmented while the maximum value of 15.2 $\times 10^{-7}$ and 20.4 $\times 10^{-7}$kg/s is illustrated in Cases 2.4 and 2.5, respectively (**Figure 8-3**a). Based on these results, increasing the angle of injection intensifies the rate of evaporation of ethanol droplets inside the torch. With the droplet evaporation, the location of the highest mass fraction of ethanol is observed around the throat region for all angles of injection (**Figure 8-3**b).

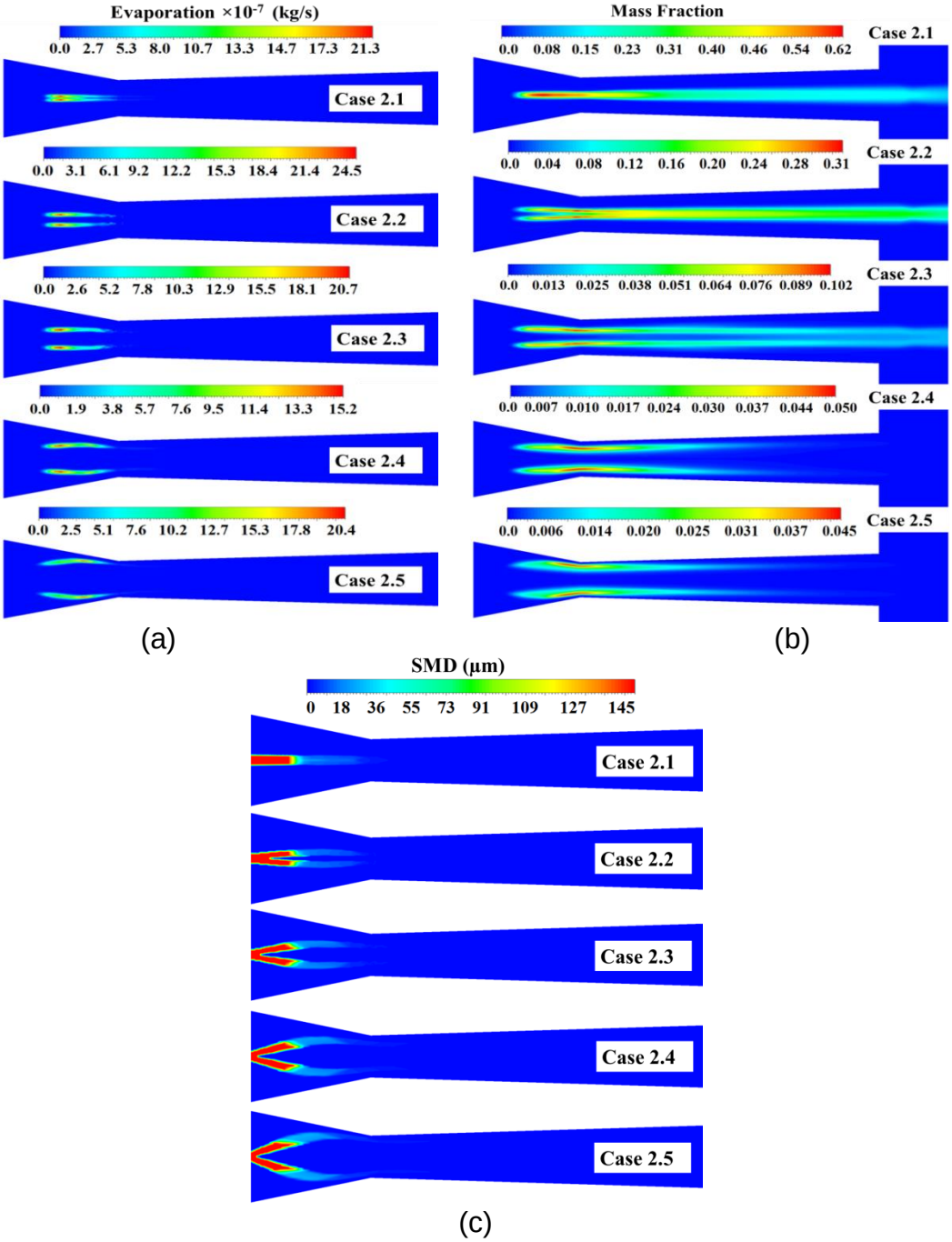


**Figure 8-3** Comparison of contours-map of (a) evaporation, (b) mass fraction and (c) SMD of the ethanol droplets at different angles of injection (**Table 8-1**)

After the non-premixed combustion of ethanol droplets with the oxygen residues, the gas temperature increases inside and outside the torch (**Figure 8-3**a). Gradually the mass fraction of ethanol decreases as the ethanol burns inside the torch. For 0°, 5° and 10° angles of injection the ethanol cannot completely burn even after the barrel exit, and it leaves the torch without prior combustion (**Figure 8-3**b). The reason for this delay in ethanol combustion for

smaller angular injection is the incomplete evaporation of ethanol droplets within the CC and barrel sections while with 15° and 20° angles of injection the droplets completely burn and disappear near the barrel exit. Moreover, at larger angles of injection of 15º and 20º, the droplet mass fraction reduces abruptly which verifies the complete evaporation and consumption of ethanol for combustion. At lower angles of injection (<10º), the ethanol evaporation and combustion is incomplete. However, at higher angles of injection (>20º), the suspension droplets can strike the CC walls. Therefore, to avoid the droplet impact on CC walls and to evaporate the liquid feedstock completely inside the torch, the better range for the angle of injection is from 10º–20°.

**Figure 8-3**c shows the values of SMD of the ethanol droplets; it clearly shows the variation in the angle of injection and its effects on the dispersion of droplets inside the CC. In all cases, the SMD decreases gradually from the initial size of 150µm due to droplets fragmentation inside the HVSFS torch. About 87% reduction in droplet diameter is observed from the inlet to the CC mid-section, and the droplet size decreases to 20µm. After that, in the nozzle throat region, the diameter of droplet reduces to 10µm and then in the barrel section remains well below 10µm. This trend is in good agreement with earlier studies in which the smaller diameter droplets evaporate quickly and give out nanoparticles in the mid-section of the barrel [119].

The results discussed above support that increasing the angle of injection from 0°–20° injects the droplets into the mainstream of the combustion flame and hence improves the suspension droplet dispersion, heating and evaporation. It also results in better consumption of flame kinetic energy to disintegrate the suspension droplets. The only drawback of the angular injection is the collision of suspension droplets with the CC walls. Thus, to protect the CC walls from droplets impingement while improving the overall flow physics, the angle of injection of 15° is a better choice. As seen and analysed at 15° angular injection the droplets do not strike the CC walls, and can breakup and evaporate completely within the core combustion region (section-**I, Figure 8-3**a–c), it also delivers extra thermal and kinetic energy to the HVSFS flame (**Figure 8-2**a, b).

### 8.3.2 Effervescent-Type Injection

As stated earlier, the effervescent atomization is based on the twin-fluid flow of gas and liquid that creates a bubbly flow inside the injection nozzle and disintegrates the suspension droplets into fine mist [93], [94], [102]. In ETI, the gas and liquid mixture are injected into the DJ2700 torch's CC, and the effects of varying GLR on the gas and droplet dynamics are investigated. The liquid injection mass flow rate remains similar as in the GTI case, i.e., $1\times10^{-4}$kg/s. The GFR are regulated according to the selected GLR (**Table 8-1**). In ETI, varied spray-half-angles of 4°, 6° and 8° are selected based on different GLR and named Case 3.1, 3.2, and 3.3, respectively (**Table 8-1**). The effects of varied GLR on the HVSFS gas dynamics and droplet dynamics are analysed in detail.

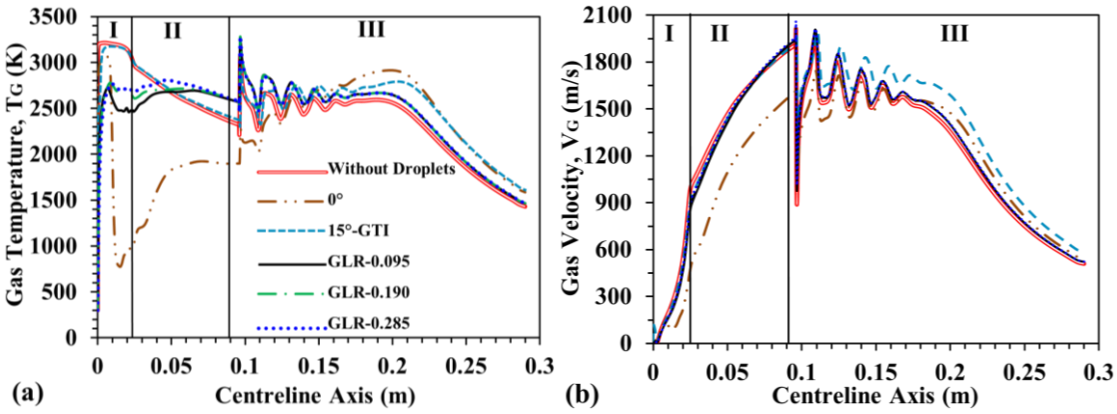


**Figure 8-4** Comparison of (a) gas temperature ($T_G$), and (b) gas velocity ($V_G$), for 150µm diameter droplet injection inside DJ2700 torch at varying GLR (ETI, with P-E injection)

It is assumed that by using ETI, droplet disintegration and droplet evaporation can be augmented, and this also helps to improve the gas dynamics inside the torch. **Figure 8-4** illustrates the effect of variation in GLR during ETI on $T_G$ and $V_G$. Compared with Case 1, ETI shows temperature decrement inside the CC and in the barrel sections due to heat absorbed by the evaporation of droplets. The temperature difference observed between Case 1, and the smallest GLR-0.095 (Case 3.1) is $\Delta T_G$=537.31K in the nozzle throat region (**Figure 8-4**a). Furthermore, the peak temperature is detected in the first shock diamond and is 200K higher than the Without Droplets case at *x*=0.1m (after the nozzle exit, **Figure 8-4**a). This is due to the heat addition by the ethanol combustion, which

increases the enthalpy of the flame in the free jet region, and will help to improve the heating and melting of the suspended nanoparticles.

Moreover, comparing the results of ETI and GTI illustrates that the cooling rate is significant in the case of ETI, whereas the angular injection at 15º (GTI) shows no cooling inside the torch (**Figure 8-4**a). This is due to the direct contact of droplets with the torch flame at a 15º angle of injection, while, in the effervescent atomization the spray-half-angles are small (4º, 6º, 8º), and improvement in gas cooling is only possible with higher spray-half-angles. This suggests that for improving the gas flow dynamics, 15º GTI performed better than the ETI cases (**Figure 8-4**a) and all other GTI cases (section-***8.3.1***), while, in comparison to the 0º STI (Case 2.1), the ETI technique has helped to reduce the gas cooling effects, and perform well compared to the STI method.

For evaluating the difference between ETI and GTI further, $V_G$ profiles are compared. They show that ETI and GTI have no significant effects on $V_G$ compared to Without Droplets-Case 1 in sections-**I** and -**II** (**Figure 8-4**b). The maximum variation in $T_G$ and $V_G$ is observed for 0º STI. This demonstrates that it is necessary to inject the suspension feedstock at an angle (GTI) and using atomization nozzle (ETI) to minimise the losses in the thermal and kinetic energies of the HVSFS flame (**Figure 8-4**). However, the biggest positive point of using the GTI and ETI is that these injection techniques further increase the thermal and kinetic energies of the HVSFS flame in the free jet section- **III** and thus improve the coating process. This is because the high enthalpy flame would help to improve the heating and melting of the suspended particles that would, in turn, support obtaining a dense coating. Moreover, a high gas velocity can provide high kinetic energy for accelerating the hot melted particulate matter and spreading the particles over the substrate to form a porosity free coating.

Similar kinds of contour map (section-***8.3.1***) are developed for the ETI case to analyse the effect of varied GLR on the droplet dynamics inside the HVSFS torch. **Figure 8-5** shows the variation in ethanol droplets' breakup, evaporation and decreasing mass fraction due to combustion while increasing GLR. **Figure**

**8-5**a, indicates the droplets dispersion and reduction in SMD as per increment in the GLR. The value of SMD reduces due to the increase in GLR and droplet atomization. As seen in the inlet region of the CC, droplets spread in the injection section, due to the difference in pressure between the liquid-gas mixture and high energy combustion gas, and the two-way turbulence interaction (**Figure 8-5**a). Due to these dissimilarities, the droplet diameter reduces much faster for the ETI.

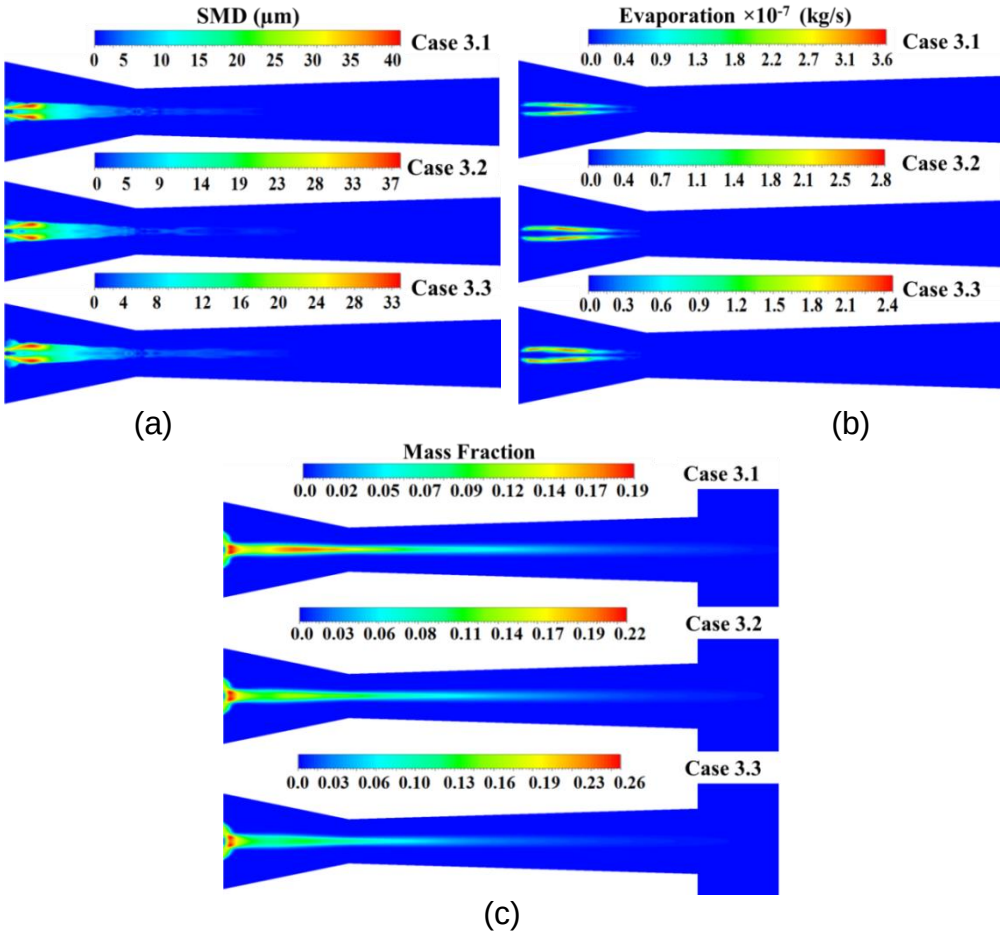


**Figure 8-5** Comparison of contours-map of (a) SMD, (b) evaporation and (c) mass fraction of the ethanol droplets at different GLR (**Table 8-1**)

The injection diameter is 150μm and with the atomization model, it suddenly decreases to 20μm at the point of injection, due to the gas cavity within the liquid layer. Thus, the thin liquid sheet rapidly breaks into smaller droplets due to the atomization gas effects and the highly energetic combustion gases inside the torch. It must be noted that this kind of disintegration and reduction in the droplet diameter has not been observed for GTI and STI. The benefit of the

smaller suspension droplets (d≤50µm), analysed by [119], is that they experience high evaporation in the mid-section of the nozzle and can be successfully used in applications where the suspension contains nanoparticles with a high melting point [119].

In **Figure 8-5a**, the value of the spray-half-angle is quite small. Consequently, the droplets cannot inject into the core of the combustion zone. Hence, the lower rate of evaporation is observed for ETI when compared to GTI (**Figure 8-3**a). The two red zones in **Figure 8-5**b for Case 3.3 demonstrate that the overall evaporation is augmented when GLR is increased. It is proved from **Figure 8-5**c that for Case 3.3, less ethanol is left in the barrel section, and it completely evaporated and was burned before the torch exit, while in Cases 3.1 and 3.2, some ethanol discharges outside the torch confirm the lower rate of evaporation and combustion for the small GLR cases. Additionally, it can be said that a further increment in GLR (to increase the spray-half-angle) can augment the efficiency of ETI. The main advantage observed for ETI is the enormous reduction in droplet diameter that can improve the deposition properties of the HVSFS process [108].

### 8.3.3 Comparison between Group-Type and Effervescent-Type Injection

Most of the comparative statements are already mentioned in section-***8.3.2*** while analysing the effects of using ETI in the HVOF torch. A further comparison between GTI and ETI droplet evaporation and droplet disintegration is shown in **Figure 8-6**. The maximum rate of evaporation is observed for homogeneous droplets (P-E) injection at 15º angle of injection (**Figure 8-6**a), while for ETI, even for homogeneous droplets, the rate of evaporation is significantly reduced as it is not directly injected into the CC hot flame region. Moreover, as stated earlier in Chapter 7, for increasing nanoparticles concentration, the rate of evaporation is reduced, and this is true in both cases of GTI and ETI (**Figure 8-6**a).

The second comparison between GTI and ETI is the droplet disintegration phenomena. As the ETI utilizes the twin-fluid criteria for droplet atomization, it

works significantly better than the single-fluid injection in the GTI technique. **Figure 8-6**b shows the initial droplet diameter reduced gradually inside the torch CC in GTI for both homogeneous and non-homogeneous suspension droplets. However, in ETI, due to the pressure difference between the atomizing gas and suspension liquid, the droplets are shattered at the beginning of the torch CC and the reduction in the droplet diameter is significantly higher than the GTI cases (**Figure 8-6**b). As explained in the LISA model details in section-***5.2.2.5***, the droplets may coalesce after the collision. In the ETI case, at the beginning of the torch's CC, the droplets firstly grow to a certain point and then start collapsing rapidly (**Figure 8-6**b). Further, the reduction in the droplet diameter has not been affected by the increment in the nanoparticles loading. Hence, it can be said that an increase in nanoparticles concentration has no significant effect on droplet fragmentation inside the DJ2700 torch for ETI and GTI cases. This examination agrees with the analysis of Esfarjani and Dolatabadi [106].

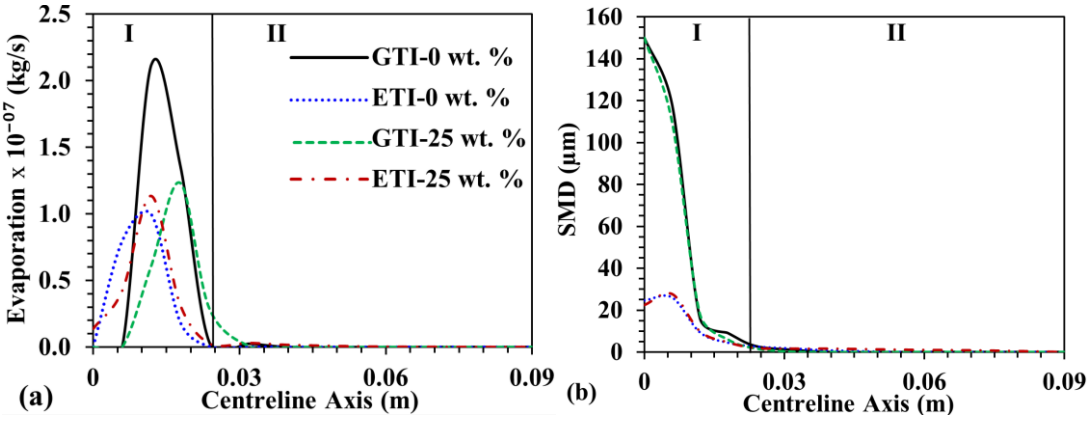


**Figure 8-6** Comparison of droplet (a) Evaporation, and (b) SMD, with different nanoparticles concentrations of 0 and 25wt.% at 15° angle of injection-GTI and with GLR-0.095-ETI

In the DJ2700 gun design, the carrier gas tube is located at the centre of the CC inlet wall and is surrounded by annular O/F inlets. Therefore, for STI and ETI injections, a recirculation zone is created close to the back wall in the injection area, and the particles start to spread out in that region. The hot combustion flame reaches the axis of the torch and interacts with the droplets. When the droplets inject at an angle of 10º–15° directed towards the combustion core they have direct interaction with the flame, which makes the evaporation process more efficient in comparison to the axial injection. For GTI technique, one has to

control the injection parameters and fix them to avoid droplet collision with the CC walls. After that, the droplets are evaporated and give out the nanoparticles in the barrel mid-section or after the torch exit, depending on the finishing point of the evaporation process.

In the HVSFS process, the coating efficiency is dependent on the torch operating parameters and on the injection parameters. The effectiveness of the HVSFS process can be increased by modifying the design of the liquid feedstock injection system and by controlling the injection parameters. The in-flight behaviour of suspension droplets, including breakup and evaporation, has a strong link with the deposition efficiency. For sufficient heating and melting of the suspended nanoparticles, a proper injection procedure must be selected that could increase the droplet breakup and evaporation inside the torch. Also, the injection should be in such a way that it improves the ethanol combustion and heat addition to result in increasing the efficiency of the HVSFS process. Hence, by the complete evaporation of droplets inside the CC and by sufficient heating and melting of suspended nanoparticles in the barrel section, the fine coating can be obtained. Furthermore, the atomization of precursor droplets inside the HVOF torch is necessary for the formation of nanoparticles dense coatings, as the injection of the liquid precursor without atomization may result in large-sized nanoparticles that may produce porous coatings.

## 8.4 Summary

Numerical simulations are performed for analysing the effects of angular injection and effervescent atomization. When suspension droplets are fed into the HVSFS by using the STI at a 0º angle of injection, the gas enthalpy and kinetic energy are observed to reduce, and the efficiency of the HVSFS flame is decreased significantly. To reduce this cooling effect and add more energy to the HVSFS flame, angular injection and effervescent atomization are selected which work successfully. The following conclusions are drawn from this work:

- The final location of evaporation of P-E is significantly varied with different injection parameters, and the suspension droplets may leave the torch without complete vaporization.

- To overcome the losses and delays in droplet evaporation the GTI can be used. It will reduce the thermal and kinetic energy losses in the HVSFS torch and thereby improves the coating formation.
- At lower angles of injection of 5º–10º, the suspension droplets could not completely evaporate within the torch and exit without prior evaporation which can create defects in the final coating. For higher angles of injection, 15º–20º, the droplets collide with the CC walls and may deposit on the torch's internal walls, and damage them. Hence, the angle of injection of 10º–15º is selected as the optimal value to avoid collision with the torch wall and improve the gas and droplet dynamics inside the torch.
- ETI also improves the gas and droplet dynamics inside the HVSFS torch, and it performs better than STI. In comparison to GTI, the effervescent atomization is not particularly efficient.
- To improve the atomization process of ETI, GLR must be increased to enlarge the spray-half-angle. It will inject the suspension liquid into the core combustion regions and improve the droplet evaporation as noticed for the GTI. Thus, it can work more efficiently with the HVSFS process.

# 9 EFFECT OF INCREASING GAS FLOW RATES ON DROPLET DISINTEGRATION AND EVAPORATION IN THE SOLUTION PRECURSOR HIGH-VELOCITY OXYGEN FUEL SPRAYING

## 9.1 Introduction

The major advantages of thermal spraying coating techniques are the usage of diverse ceramic and metallic materials [3]–[6], [78]. The technology of HVOF thermal spraying is commonly used for spraying metallic particles; however, with some modifications it can be used for spraying ceramic particles [3], [78]. Further advancements in the coating industry are moving towards spraying nanoparticles for dense, thick coating with excellent bonding strength. Recently, liquid feedstock has been utilized in HVOF spraying to generate dense coatings [12], [13], [17], [76]–[78]. The liquid feedstock is either suspension of nanoparticles or solutions. The former contains particles of nanometric, or a few micrometres in size dispersed in an organic solvent with dispersing agents, whereas the solution precursors are made by dissolving metal salts or organometallic or liquid metal precursors in a solvent [42], [50], [63].

The powder injection replacement with the liquid feedstock in the form of solution precursor is highlighted in the following, as the research gap, by presenting an in-depth literature review in Chapter 2 (section-***2.1.2***). However, the use of solution precursor thermal spraying over suspension thermal spraying purely depends on the application requirements, although the solution precursor offers some key benefits over the suspension spraying as described in Chapter 2 (section-***2.1.1***). Compared with the other thermal spray techniques, SP-HVOFS allows an excellent chemical homogeneity of coatings [50]. Furthermore, the SP-HVOFS eliminates the cumbersome process of nanosize powder manufacturing required for the suspension or conventional powder spraying processes.

The process of droplets disintegration is dependent on the preparation of the solution precursor. The main parameters required to be maintained during the precursor preparation process are precursor viscosity, surface tension, the

boiling point of the liquid solvent, solute chemistry and its solubility. The behaviour of small particles generated during the solution precursor flame spraying process depends on precursor droplet size distribution and injection velocities that need to be controlled during the HVOF process [42], [50]. These problems must be restrained by optimizing the process parameters that can be achieved by numerical modelling.

It should be noted that little work has been reported regarding experiments and numerical modelling of the SP-HVOFS process, so more research is required in this area. To date, no work has been reported to study the effects of increasing GFR on the gas and droplet dynamics inside the SP-HVOFS torch. It is realized that the size of nanoparticles needs to be controlled for the specific coating requirement [33], [50], [69]. In this chapter, the GFR are regulated to control the size of precursor droplets to form a nanosized coating. The time-temperature histories of the droplets in the HVOF flame are shown to control the size of the resultant particulate deposits. The SP-HVOFS process includes complex stages of droplets fragmentation, precursor/solvent evaporation, and chemical reactions while transferring heat, mass and momentum with the surrounding hot gas [33], [34]. This study aims to understand the influence of the key aspects of the SP-HVOFS process variables on gas and droplet dynamics during the process. A CFD-based model for the SP-HVOFS process is proposed to analyse the interaction between precursor droplets and the combustion flame.

## 9.2 Numerical Implementations

The modelling of the organometallic chemical precursor droplets injected into the HVOF spray system is analysed, and the effects of solution precursor droplet fragmentation and evaporation in HVOF are studied. A two-dimensional CFD model is developed to account for supersonic combustion and droplet dynamics by the Eulerian continuum approach coupled with the Lagrangian description of multicomponent spray droplets atomization, transport, breakup and evaporation. When the O/F GFRs are increased, (i) the velocity and (ii) the enthalpy of the HVOF flame are augmented. The former reduces the droplet residence time in the HVOF flame while the latter favours evaporation. Overall,

the results show that by controlling the GFR, droplets dispersion and disintegration is increased, which will improve the rate of evaporation of the solution precursor.

The governing equations for the conservation of mass, momentum, energy, turbulence, chemical species, and droplet species form the complete set of equations of the CFD model and were solved using the **Fluent** pressure-based 2D axisymmetric solver. A second-order upwind discretization scheme is used since it ensured accuracy, stability and convergence. Turbulence is described with the SST k-ω model (Chapter 3).

The DJ2700 HVOF torch geometry used in this study is similar to that presented in Chapter 3 (**Figure 3-1**, and **Table 3-1**). In the present chapter, the free jet domain length ($L_{FJ}$) is set as 500mm (section-**III**), to see the gas flow dynamics in the far field region after the gun's outlet. The torch geometry considered in the numerical simulations is also axisymmetric. The operating parameters are shown in **Table 9-1**. The premixed oxygen and methane are axially injected into the DJ2700 gun; the resulting hot combustion gases are accelerated inside the C-D nozzle and flow through the barrel section towards the exit of the gun. The formation of shock diamonds is observed after the ejection of flow in the free jet region (**Figure 9-1**). The lowest to highest O/F GFR selected for this study are designated as Cases 1, 2, 3, and 4 (**Table 9-1**). The initial precursor droplet diameter is 50µm with an injection temperature of 300K, and velocity of 15m/s. The droplet mass flow rate is $3.821\times10^{-4}$kg/s which gives $ZrO_2$ production rate of 100g/h. The solution precursor carrying mixture of 0.5M zirconium n-propoxide (ZnP 70wt.% in n-propanol) diluted in ethanol has a mass composition of about 72.3% ethanol, 19.4% ZnP, and 8.3% n-propanol solutions (**Table 9-1**). These multicomponent droplets are injected axially into the CC after complete simulations of combustion and turbulence of gaseous flow inside the torch.

In the SP-HVOFS process, the physical and chemical properties of nanoparticles are dependent on a large number of parameters, such as combustion gas temperature, pressure, velocity, C-D nozzle design, O/F

injection flow rates and feeding ratio, fuel and precursor properties and their concentration [33], [34], [78]. In this study, the effects of different O/F GFRs on the gas and droplet dynamics during the production of the $ZrO_2$ nanostructured coating are analysed in the SP-HVOFS process.

**Table 9-1 Working Conditions of DJ2700 SP-HVOFS torch**

| **Working Conditions** | Cases | | | |
|---|---|---|---|---|
| | 1 | 2 | 3 | 4 |
| Oxygen flow rate (kg/s) | 0.0035 | 0.007 | 0.014 | 0.021 |
| Fuel flow rate (kg/s) | 0.0015 | 0.003 | 0.006 | 0.009 |
| Droplet diameter and initial temp. | 50µm, 300K | | | |
| Droplet flow rates and initial velocity | $3.821\times10^{-4}$kg/s, 15m/s | | | |
| Solution precursor mass composition | 72.3% Ethanol, 19.4% ZnP, 8.3% n-propanol | | | |
| Precursor concentration | 0.5M ZnP solution | | | |

### 9.2.1 Gas-Phase Flame Structure

The modelling of droplet aerodynamic breakup and evaporation in the SP-HVOFS process involves the coupling of the gas dynamics with the droplet dynamics (**Figure 9-1**). It should be noted that the homogeneous solution used in this study is a mixture of 0.5M ZnP 70wt.% in n-propanol diluted with solvent (ethanol). The solid particles are not simulated after droplet evaporation, as the primary aim of this work is to numerically track the two-way coupling of the solution precursor droplet with the torch's gas dynamics and vice versa.

The droplets of solution precursor after being injected into the HVOF flame jet undergo several physical processes simultaneously. The first stage is the aerodynamic breakup, as the slow moving droplets are entrained into the high-velocity jet and accelerate in the high-velocity gas stream (**Figure 9-1**). Depending on the droplet initial size, thermophysical properties of the solution precursor and the surrounding gas conditions, droplets can undergo severe deformation and eventually breakup into smaller droplets. The secondary breakup of droplets into smaller ones is modelled by the TAB model (Chapter 3, section-***3.2.4.3***). The second stage is the evaporation of micron-sized precursor droplets after which the formation of particles begins when the precursor gas is going through a chemical reaction (**Figure 9-1**). The high-temperature is needed

to evaporate the precursor and provide the conditions for the chemical reactions. The temperature of high-velocity flames varies from 3000–4000K depending on the type of oxidizer and operating conditions [18], [26].

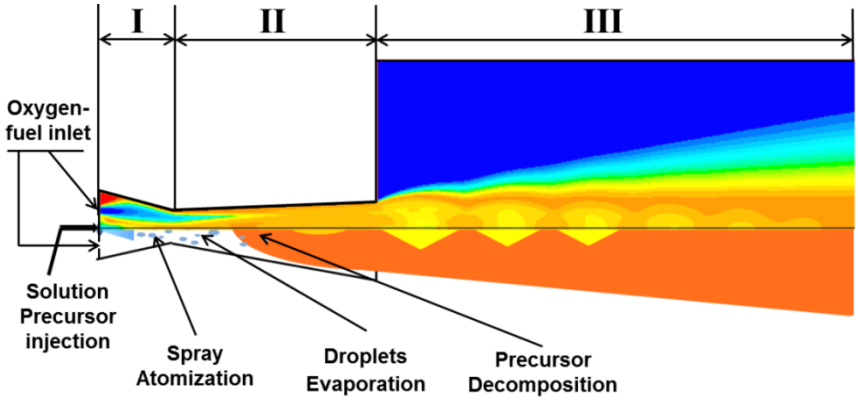


**Figure 9-1** Schematic representation of the SP-HVOFS process (Bottom) with CFD Temperature contours (Top)

For the supersonic combustion of methane inside the SP-HVOFS torch, a two-dimensional CFD model is employed using the Eulerian continuum approach. Then to capture the droplet dynamics in the domain, the Lagrangian model is coupled with the Eulerian continuum model for the description of multicomponent spray droplet breakup and atomization, transport, and evaporation (Chapter 3 and Chapter 6). Only the effects of droplet dynamics over the gas phase and the impact of combustion flame on the droplet dynamics in the SP-HVOFS are analysed. The flame combustion is modelled by using a single-step reaction mechanism. The complete stoichiometric combustion reactions are expressed as:

Zirconium n-propoxide: $C_{12}H_{28}O_4Zr + 18O_2 = ZrO_2 + 12CO_2 + 14H_2O$
1-Propanol: $C_3H_8O + 4.5O_2 = 3CO_2 + 4H_2O$
Ethanol: $C_2H_6O + 3O_2 = 2CO_2 + 3H_2O$
Methane: $CH_4 + 2O_2 = CO_2 + 2H_2O$

The eddy-dissipation model [132], [134], [135] is used to express the reaction rate to consider the interaction between eddy motion and chemical reaction, (Chapter 3). The governing equations for the conservation of mass, momentum, energy, turbulence, chemical species, and droplet species are fully explained in Chapter 3 and are not repeated here for brevity.

## 9.3 Results and Discussions

### 9.3.1 Effects of Increasing Gas Flow Rates on the Gas Dynamics

The combustion process inside the HVOF gun is mainly dependent on the CC design, total O/F GFR, and O/F gas ratio [10], [24], [26]. Four different levels of O/F GFRs are considered with a constant O/F ratio of 2.333, to analyse the effects of increasing O/F GFR over the combustion gas and droplet dynamics inside the SP-HVOFS process (**Table 9-1**, Cases 1–4).

The gas temperature ($T_G$), pressure ($P_G$), velocity ($V_G$) and Mach ($M_G$) number increase with a rise in GFR (**Figure 9-2**–**Figure 9-4**). In **Figure 9-2**, the maximum $T_G$ without multicomponent droplets injection is observed inside the CC (3000–4000K in section-**I** for all GFR) [18], [26], thereafter, it decreases gradually inside the barrel (section-**II**) and some peaks are observed in the shock jet (section-**III**). After the injection of precursor droplets, the value of $T_G$ goes down in the CC (ΔT is 750–1000 K for Cases 1 and 4, respectively), because heat is extracted from the gas for evaporating the precursor droplets (**Figure 9-3** and **Figure 9-4**a).

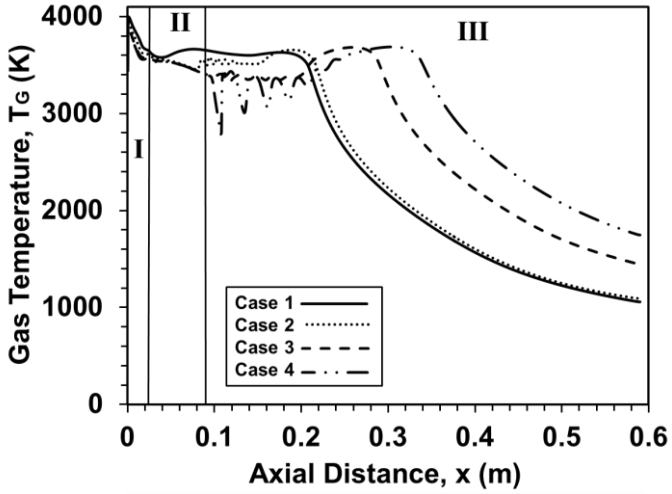


**Figure 9-2** Variations in the gas temperature (Without droplets injection) along the centreline axis [These legend description is applicable to all graphical representations]

The map of $T_G$ (**Figure 9-3**) demonstrates the high- and low-temperature regions from the gun inlet to some extent in the free jet section-**III** (near the gun's exit region indicated by a star). Lower temperatures are detected at the O/F inlets, and point of droplet injection in section-**I**. After the immediate start of droplet

evaporation, a sudden decrement is detected in the $T_G$ at the droplets injection port (along the gun axis), and then the $T_G$ increases inside the CC and barrel due to accelerating rates of O/F and multicomponent vapour combustion (section-**I** & **II**, **Figure 9-3** and **Figure 9-4**a). High GFR in Cases 3 and 4, augmented the combustion temperature in sections- **I** & - **II**, and more heat is added by the flammable precursor vapours. For each case, the temperature rise is observed after ejection of the flow in the atmosphere. The fluctuating temperature rise is due to the formation of shock jets at the exit of the torch as seen in section-**III** (**Figure 9-3** and **Figure 9-4**a).

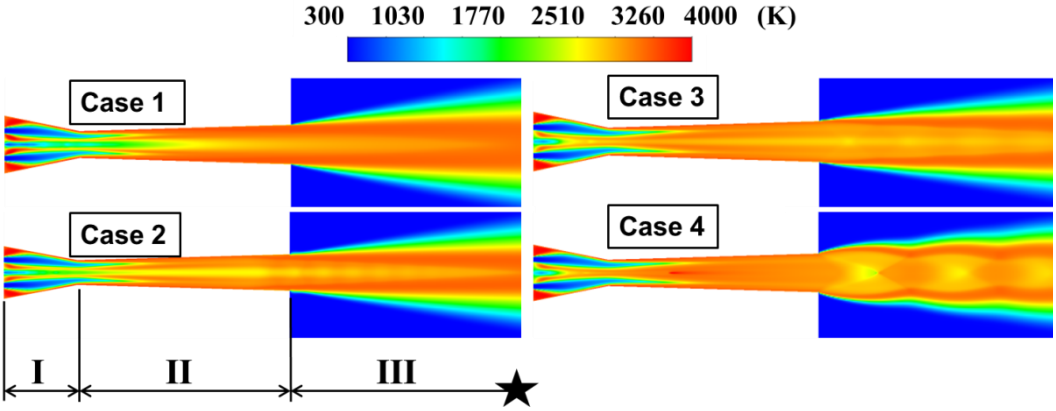


**Figure 9-3** Gas temperature maps for Cases 1–4 [Section-I-Combustion Chamber (CC), Section-II-Barrel, Section-III-Part of Free jet region]

The gas pressure ($P_G$) is also dependent on the injection of O/F mass flow rates; in section-**I**, the highest combustion inlet pressure value of 7.723bar is observed for Case 4, and the lowest value of 0.586bar is observed for Case 1 (**Figure 9-4b**). For each case, pressure sharply declines in the CC and barrel sections. Furthermore, for Cases 2, 3 and 4, the barrel exit pressure is less than the atmospheric pressure and the flow is under-expanded, which forms a Mach-disc at the downstream of the barrel's exit (**Figure 9-4b**). The flow settles down in the free jet region after a series of shock waves [24].

Similarly, the increment in $V_G$ is noticed inside the C-D nozzle and barrel section, while high values are observed in the shock jet. **Figure 9-4**c-d show the centreline profiles of gas velocity and Mach number for internal and external flow fields for Cases 1–4. The velocity field changes in each case due to enhancement in the rate of combustion, and becomes accelerated inside the C-D nozzle. The minimum velocity values are detected for Case 1 and the highest

velocity for Case 4. The obvious reason is the addition of kinetic energy to the gas during high rates of combustion with increased GFR. Moreover, the Mach number profiles are demonstrating the increased energy carried by the combustion gas for higher O/F flow rate cases. For Case 1, subsonic flow is observed at the C-D nozzle throat, $M_G$ <1.0 along the barrel axis and no shock diamonds are formed at the barrel exit. The supersonic jet with visible shock diamond appears in Cases 2, 3 and 4 as $M_G$ >1.0 at the gun discharge (**Figure 9-3** and **Figure 9-4**d). These high gas temperatures, pressures, velocities and Mach number will affect the precursor droplet breakup and evaporation inside the SP-HVOFS torch, discussed in the subsequent sections.

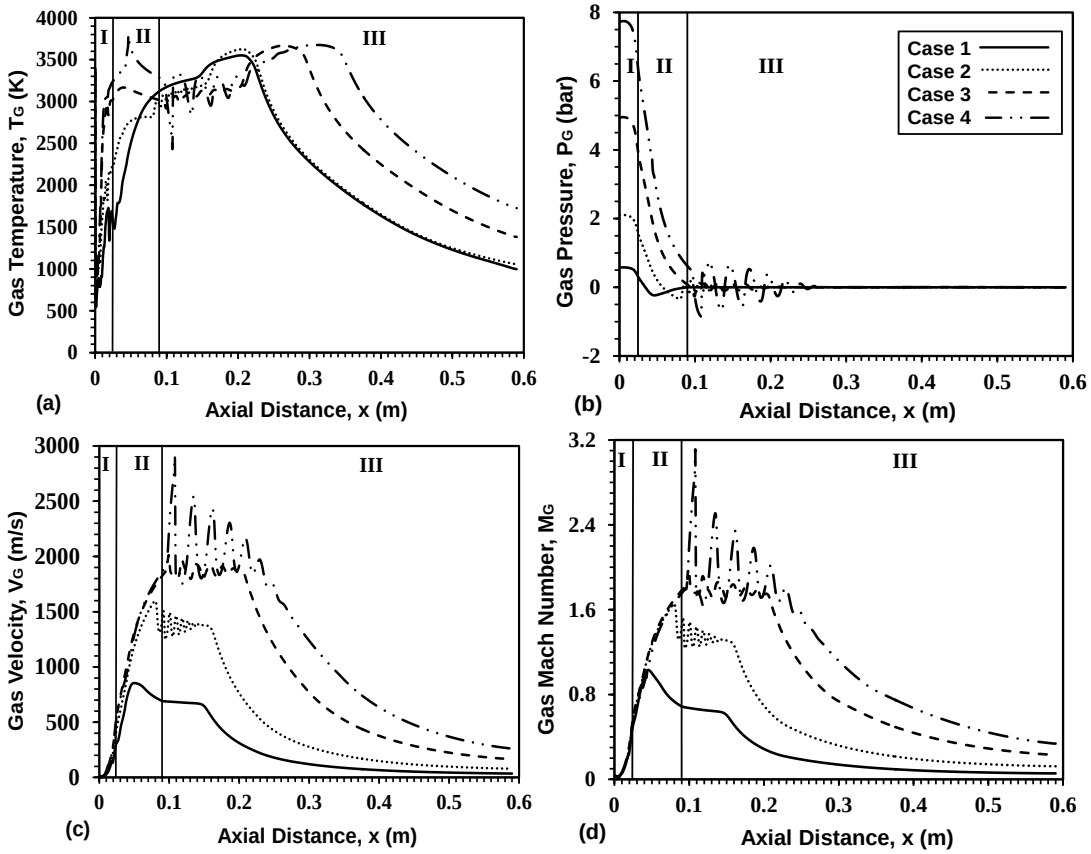


**Figure 9-4** Variation of (a) gas temperature, (b) gas pressure (c) gas velocity, and (d) gas-Mach Number along centreline axis for Cases 1–4

### 9.3.2 Effects of Increasing Gas Flow Rates on Precursor Droplet Dynamics and $ZrO_2$ Formation

Inside the SP-HVOFS gun, the chemical reaction started immediately as the precursor droplets absorb heat from the surrounding hot gas and are converted into vapours (section-**I**). The evaporation of the precursor liquid is dependent on

the combustion temperature, and under high GFR, the liquid boils rapidly and the evaporation rate increases. Similarly, in the SP-HVOFS process, the evaporation rate is augmented by increasing O/F flow rates. In Case 1, the highest rate of evaporation is detected in the C-D nozzle throat region along the gun axis while the precursor droplet evaporation continues in the barrel (section-**II**, **Figure 9-5**a). However, for Case 4, a high rate of evaporation is observed inside the barrel, and the maximum amount of ZnP precursor droplets are evaporated inside the barrel's mid-section (along the gun's axis; **Figure 9-5**b). In barrel section-**II**, the evaporation of precursor droplets is less in Case 1, compared to Case 4, due to lower gas temperatures ($T_G$) (**Figure 9-4**a). For total evaporation inside the SP-HVOFS torch, higher evaporation is detected for Case 1 than for Case 4. The understanding developed for the difference in the rate of evaporation has two points: (i) higher gas temperature with increased GFR augmented the rate of evaporation to some extent in the CC and barrel in Case 4; (ii) higher gas velocity reduces the interaction time between the gas and droplets in Case 4 which led to a smaller amount of overall evaporation compared to Case 1.

Due to these higher relative velocities, the process of evaporation decreases in the fast moving supersonic HVOF flame jet in Cases 2, 3 and 4, compared to the subsonic flow (Case 1). In Case 1, the precursor vapours had sufficient reaction time to interact with the combustion gases and formed the required $ZrO_2$ species. In **Figure 9-5**a, at the nozzle throat region, the highest rate of formation is identified and after the throat region, the formation rate decreases because of less available $T_G$, which is much lower when compared to Case 4 ($\Delta T_G$ = 1614K between Cases 1 and 4, **Figure 9-4**a). The opposite behaviour in $ZrO_2$ formation is observed for Case 4, i.e. the highest rate of formation is witnessed after the throat region (**Figure 9-5**b). The formation of $ZrO_2$ continues in section-**III** for both cases until all the precursor vapours are converted into $ZrO_2$ species (i.e., in the free jet region, section-**III** is not shown in **Figure 9-5**).

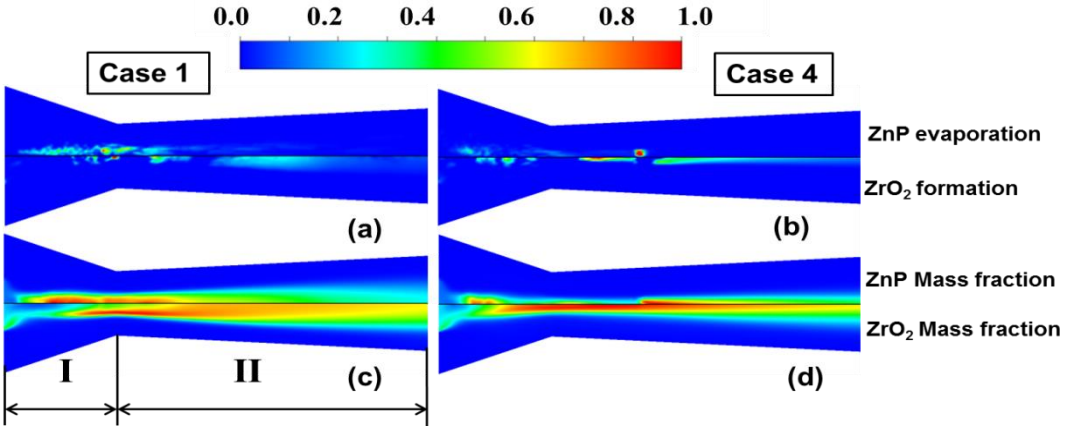


**Figure 9-5** Normalized contour plot of ZnP mass fraction and droplet evaporation rate (top) and $ZrO_2$ mass fraction and formation rate (bottom) for Case 1 (a & c), and Case 4 (b & d)

The $ZrO_2$ formation starts where the O/F combustion streams and precursor vapour streams are mixed inside the CC while the turbulence mixing occurs near the centreline axis of the torch as the precursor droplets are injected axially into the CC (from a central hole/opening). The mass fraction of ZnP and $ZrO_2$ (normalized by their maximum values) is shown for Cases 1 and 4 in **Figure 9-5**c, d, respectively. This clearly shows the higher formation of $ZrO_2$ near the nozzle throat and in the barrel inlet section, as excessive mass fractions of $ZrO_2$ are present near these regions (surrounding the gun axis). A large amount of ZnP appears in section-**I** and then reduces gradually after the C-D nozzle throat, which confirms the formation of $ZrO_2$ particles inside the SP-HVOFS gun (**Figure 9-5**c, d). Similar to the evaporation/formation rate more mass fraction of $ZrO_2$ is observed in the CC and barrel section for Case 1 compared to Case 4. In Case 4, ZnP has less interaction time available in high-temperature regions, and the droplets fly away without prior evaporation. Hence, less mass fractions are detected in the CC (**Figure 9-5**d).

For Cases 1–4, **Figure 9-6** shows the normalized contours of precursor droplets SMD inside the torch. The precursor droplet diameter decreases with droplets fragmentation as it travels inside sections-**I** and -**II**. In Case 1, due to the presence of the low-temperature field, the droplets will not fully evaporate but remain present till the exit of the barrel section (**Figure 9-6**a). The droplets' disintegration and evaporation rates increase with increment in the GFR as gas temperature, and pressure is augmented; hence, droplets start disappearing in

the middle of the barrel in Cases 2 and 3 (**Figure 9-6**b, and c). This is caused by the interaction of precursor droplets with higher GFR combustion gases having more kinetic energy and enthalpy. Therefore, the reduction of droplet size occurs by the augmentation in relative velocities.

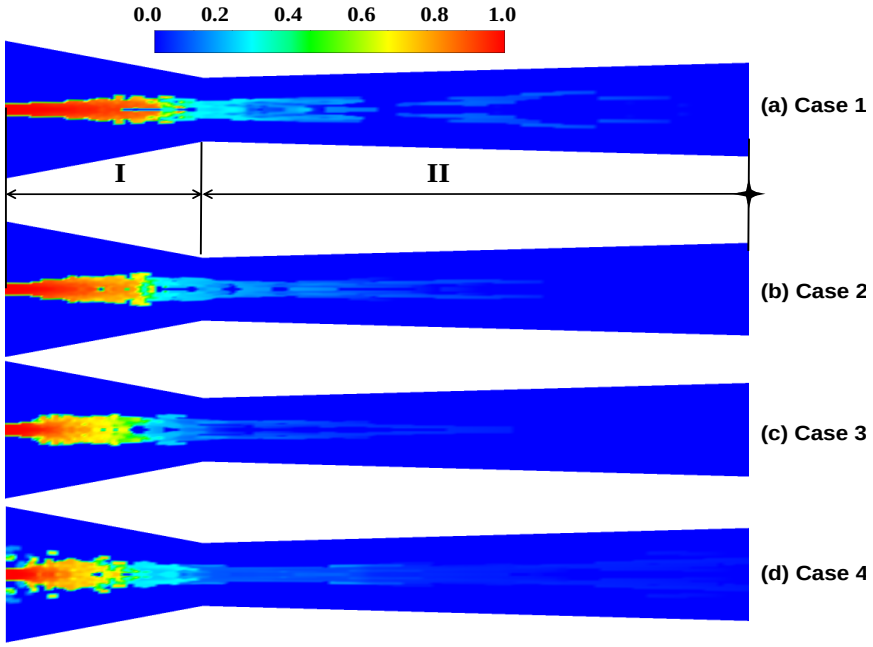


**Figure 9-6** Sauter mean diameter of the precursor droplets inside the SP-HVOFS torch (a) Case 1, (b) Case 2, (c) Case 3 and (d) Case 4

**Figure 9-6**c, d show that a high rate of combustion increases gas turbulence near droplets injection regions, which causes abrupt mixing of the hot gas and precursor droplets and intensifies the droplet breakup phenomenon. Moreover, an increase in the ratio of oxidant mixture to the mass of injected precursor is another dominant factor in reducing the droplet size near injection regions inside the CC. Smaller droplets with less precursor mass and having high kinetic energies (Case 4, **Figure 9-6**d) would leave the SP-HVOFS torch at a faster rate without complete evaporation. These droplets and vapours carrying higher kinetic energies will lower the formation of $ZrO_2$ in the higher GFR cases.

In summary, the increasing O/F GFRs significantly affected (i) the gas velocity and (ii) the gas enthalpy of the HVOF flame jet. The increased gas velocity reduces the droplet residence and interaction time in the HVOF flame while the higher gas enthalpy favours the vaporization of the precursor. Thus, the present study reveals that regulating the GFR can effectively control the droplet breakup

and evaporation processes that help to generate the required type of nanostructured, homogeneous coatings.

## 9.4 Summary

A CFD-based model for the SP-HVOFS process is proposed to analyse the interaction between precursor droplets with the combustion flame. The GFR are regulated to control the size of precursor droplets to form a nanosized coating. The time-temperature histories of the droplets in the HVOF flame are shown to control the size of resultant particulate deposits. The SP-HVOFS process includes complex stages of droplets fragmentation, precursor/solvent evaporation, and chemical reactions while transferring heat, mass and momentum with the surrounding hot gas. The following conclusions are drawn from the present work:

- The gas dynamics of the SP-HVOFS process are highly influenced by changing the O/F GFRs.
- By increasing the GFR, in the SP-HVOFS process, the gas enthalpy, gas temperature, gas pressure, gas velocity, and gas-Mach number increase significantly.
- The increase in gas enthalpy and gas temperature, in the SP-HVOFS process, augmented the rate of evaporation of precursor solution, and rate of formation of $ZrO_2$ nanoparticles.
- The higher gas velocities increase the relative velocities of ZnP vapours and $ZrO_2$ particles that reduce the vapours and particle residence time in the high-temperature regions of the SP-HVOFS torch.
- Furthermore, the increase in the O/F flow rates diluted the injected precursor and thus reduced $ZrO_2$ concentration in the process and decreased the rate of particle collision. As a result, it can be said that non-agglomerated nanoparticles can be obtained.
- Regulating the GFR can effectively control the droplet breakup and evaporation processes that help to generate the required type of nanostructured, homogeneous coatings.

# 10 RESEARCH SUMMARY, SCIENTIFIC CONTRIBUTIONS, AND RECOMMENDATIONS FOR FUTURE WORK

## 10.1 Research Summary

The present research studied the effects of varied injection parameters on the gas dynamics and droplet dynamics of the HVSFS and SP-HVOFS processes for improving the droplet breakup and evaporation to enhance the nanoparticles heating and deposition efficiency. In the solution precursor-fed-HVOF (SP-HVOFS) process various types of solvent, injection nozzle and solution concentration were studied to see the effect on the as-sprayed coating nanostructure and morphology. It is concluded that the increase in solute concentration would raise the surface tension of the solution precursor; thus, the fragmentation decreases with the augmentation of the surface tension. Therefore, the large size droplets form bigger $ZrO_2$ nanoparticles. Moreover, the intensification in droplets sizes delays the droplet evaporation and reduce residence time for particles in the torch high temperature zones which decreases sintering. Likewise, the higher precursor concentration resulted in the greater particle density that increased the rate of particle collision and further enhanced the growth of nanoparticles.

Moreover, P-W solvents have the higher heat of vaporization and high surface tension values, which limits its use. The process efficiency further decreases when the salt concentration increases in the P-W-based precursor. However, the addition of ethanol could reduce this deficiency, and improve the nanoparticles size and morphology. The efficiency of this process is also increased by using a proper atomization technique for precursor injection in the CH-2000 HVOF torch. These novel effervescent atomization techniques decreased the droplet size for both organic and inorganic solvents and improved the overall results. The best nozzle design for injecting the precursor is the effervescent-type injection (ETI) nozzle; it reduces the average diameter of nanoparticles, their size distribution and improves particle morphology.

For precursor droplets disintegration, numerical analysis is performed for the ETI nozzle. For numerical analysis, the LISA model is used and validated by previous results. The principle dependence of the effervescent atomization is on the delivery pressure ($P_{inj}$) and the GLR. The increment in the GLR and $P_{inj}$ can considerably increase the efficiency of the effervescent atomization and generate small size droplets. However, the effect of the nozzle exit diameter ($D_{inj}$) is minor. Smaller diameter nozzles can work efficiently at lower GLR and at lower $P_{inj}$ while a bigger sized orifice gives good atomization at higher GLR and $P_{inj}$. Thus, the combined effect of varying GLR, $P_{inj}$ and $D_{inj}$ can have a significant impact on the overall performance of the effervescent-type atomizer. The LISA model proved to predict the variations in spray atomization with respect to changing injection parameters and validated by the experimental results [92]. The effect of varied fluid properties such as viscosity and surface tension can affect the performance of these types of the atomizer. By analyses of the We, it is demonstrated that the liquids having higher surface tension (water) required more energy to disintegrate as compared to lower surface tension liquids (ethanol).

In the present thesis, a novel study is conducted by numerically modelling the effect of increasing nanoparticles concentration over the gas flow dynamics and droplet dynamics inside the HVSFS torch. It is shown that suspensions with higher concentrations of solid nano-loadings have greater surface tension and require higher heat of vaporization. The thermophysical properties of liquid feedstock with different nanoparticles concentrations (0, 5, 15 and 25 wt.%) are calculated and modified based on the proposed nanofluids models. It is concluded that the final location of evaporation of the homogeneous and non-homogeneous droplets is very different. The increment in the nanoparticles concentration delays the evaporation process of the droplets and adversely affects their disintegration. The finishing point of the droplet evaporation is an important aspect of the numerical analysis of suspension droplets in the HVSFS process. After that, nanoparticles formation begins in the computational domain as new entities.

Furthermore, the effects on the flow physics of the HVSFS process by using different injection types with increasing nano-loadings are studied for the first time. It is concluded that in surface-type (STI) and group-type (GTI) injections the effects on droplet breakup and evaporation are dependent on two parameters: nanoparticles concentration and droplet diameter. The diameter reduction and rate of evaporation are decreased with the increase in injection droplet size and solid nano-loadings. Smaller droplets (d≤50μm) can be effectively used in applications where the suspension has a high melting point material. The smaller diameter droplet improves the evaporation of suspension and results in better heating and melting of the remaining solid content. The larger droplets (150 and 300μm) with high concentration leave the gun without complete vaporization. This leads to serious consequences in real applications and can create defects in the final coating with increment in the coating porosity.

However, the droplets inserted by using GTI can inject the suspension into the core of the combustion zone and reach the evaporation point rapidly; thus, they evaporate completely inside the torch. The GTI increases the efficiency of droplets disintegration and evaporation, and the effects of gas cooling are reduced. At lower angles of injection of 5º–10º, the suspension droplets could not completely evaporate within the torch and exit without prior evaporation that can create defects in the final coating. For higher angles of injection 15º–20º, the droplets collide with the CC walls and may deposit on the torch's internal walls, and damage them. Hence, the angle of injection of 10º–15º is selected as the optimized value to avoid collision with the torch wall and improve the gas dynamics and droplet dynamics inside the DJ2700-torch.

The ETI also improves the gas and droplet dynamics inside the HVSFS torch as it performs better than STI. The droplets dispersion and size distribution are significantly improved after effervescent atomization. For further improving the atomization process of ETI, the gas-to-liquid ratio (GLR) must be increased to expand the spray-half-angle. It will inject the suspension liquid into the core combustion regions and improve the droplet evaporation as noticed for the GTI. Thus, it can work more efficiently with the HVSFS process.

Finally, it is also studied that the SP-HVOFS process gas dynamics can be regulated by changing the O/F GFRs. The increment in the GFR increases the gas enthalpy, gas temperature, gas pressure, gas velocity, and the gas Mach number in the SP-HVOFS process significantly. The increase in gas enthalpy and temperature augmented the rate of evaporation of precursor solution and the rate of formation of nanoparticles in the SP-HVOFS process. However, the higher gas velocities also increase the relative velocities of precursor vapours and form seed particles which reduced the vapours and particle residence time in the high-temperature regions of the SP-HVOFS torch. Furthermore, the increase in the O/F flow rates diluted the solution precursor in the torch; thus, reduced particle concentration in the overall process. It decreased the rate of particle collision, and as a result, non-agglomerated nanoparticles can be obtained. Effectively regulating the GFR would control the droplet breakup and evaporation processes which would help to generate the required type of nanostructured, homogeneous coatings.

## 10.2 Scientific Contribution

The CFD computations of the HVSFS and SP-HVOFS processes are essentially required because the internal flow physics of these processes cannot be examined experimentally. These processes include complex stages of droplets fragmentation, precursor and solvent evaporation, chemical reactions, particle formation, nucleation and growth of nanoparticles while transferring heat, mass and momentum with the surrounding hot gas [33], [34]. This thesis aimed to understand the influence of the key aspects of liquid feedstock-fed-HVOF process variables on the droplets disintegration and evaporation processes. CFD-based models for the HVSFS and SP-HVOFS processes are proposed that could analyse the interaction between the combustion flame and precursor droplets. Therefore, this CFD model can efficiently analyse the effects of any type of suspension or the solution precursor over the flow physics of the liquid-fed-HVOF torch. Different torch designs can be modelled with various liquid feedstock injection types. The novelty of this work is the utilization of the nanofluids model in determining the

thermophysical properties of suspension to analyse the effect of suspension disintegration and evaporation on the HVOF gas dynamics and vice versa.

Moreover, in this research for the first time, an effervescent twin-fluid nozzle is designed to inject the suspension or the solution precursor into the HVOF torch, and the improvement in the nanoparticles based coatings is analysed. The ETI nozzle is designed for the CH-2000 HVOF torch, and the coating morphologies are compared with the plain-orifice and angular injection nozzles. It is a novel study conducted to see the effects of atomization and non-atomization of solution droplets on the deposition of nanoparticles. The LISA model from **Fluent** is employed to investigate the liquid feedstock atomization effects over the gas and droplets dynamics. The modelling of the new effervescent atomization made the investigation process easier. Hence, this model can easily evaluate the impact of atomization on the torch's internal and external gas dynamics and conversely detect the effects of hot combustion gases over the atomization process.

The CFD modelling analyses provided in this thesis can be a cheap tool with which it is easy to study the use of different atomizing nozzle types in various HVOF torch designs. The setup of computational modelling can also be utilized for different kinds and designs of HVOF torch using different combustion fuels and liquid feedstocks. Moreover, atomization modelling can be used for various injection nozzles designs. It will reduce the burden of expensive experimental lab testing. Hence, it is an enormous piece of modelling work that can positively benefit the thermal spraying industry.

## 10.3 Recommendations for Future Research

The following studies could be conducted to extend further the understandings related to the liquid feedstock fed-HVOF processes:

1. The formation of solid nanoparticles inside the HVOF flame is also a challenging computational task that could be performed by writing a novel CFD code.
2. A model could be prepared to assign the in-flight liquid droplets' current position, velocity and temperature values to the newly released solid

nanoparticles as initial conditions after the complete evaporation of liquid droplets.

3. After the solid content starts moving inside the HVOF flame, the changes in their temperature, velocity and position can be captured numerically.

Modelling these three steps with different nanoparticle materials, varying O/F flow rates, various injection techniques, varied solid nano-loadings and other injection parameters could be highly significant to form a complete analysis of the liquid feedstock fed-HVOF torch mechanism.

4. With respect to designing a new atomizing nozzle that combines the effects of effervescent and angular injection could further improve the droplet disintegration, heating and evaporation of the suspension and solution precursor in the HVOF process.

# REFERENCES


[1] R. S. Lima and B. R. Marple, “Thermal spray coatings engineered from nanostructured ceramic agglomerated powders for structural, thermal barrier and biomedical applications: A review,” *J. Therm. Spray Technol.*, vol. 16, pp. 40–63, 2007.

[2] M. Oksa, E. Turunen, T. Suhonen, T. Varis, and S.-P. Hannula, “Optimization and characterization of high-velocity oxy-fuel sprayed coatings: techniques, materials, and applications,” *Coatings*, vol. 1, pp. 17–52, 2011.

[3] T. A. Dobbins, R. Knight, and M. J. Mayo, “HVOF thermal spray deposited Y2O3-stabilized ZrO2 coatings for thermal barrier applications,” *J. Therm. Spray Technol.*, vol. 12, pp. 214–225, 2003.

[4] R. Schwetzke and H. Kreye, “Microstructure and properties of tungsten carbide coatings sprayed with various High-Velocity Oxygen Fuel Spray systems,” *J. Therm. Spray Technol.*, vol. 8, pp. 433–439, 1999.

[5] T. Sudaprasert, P. H. Shipway, and D. G. McCartney, “Sliding wear behaviour of HVOF sprayed WC-Co coatings deposited with both gas-fuelled and liquid-fuelled systems,” *Wear*, vol. 255, pp. 943–949, 2003.

[6] M. Erne and D. Kolar, “Thermal spraying of oxide ceramic and ceramic metallic coatings,” in *Ceramic Coatings - Applications in Engineering*, S. Feng, Ed. InTech, 2012, pp. 167–194.

[7] P. Fauchais and A. Vardelle, “Thermal sprayed coatings used against corrosion and corrosive wear,” in *Advanced Spray Applications*, J. Hamid, Ed. InTech, 2012, pp. 3–39.

[8] A. G. Evans, D. R. Mumm, J. W. Hutchinson, G. H. Meier, and F. S. Pettit, “Mechanisms controlling the durability of thermal barrier coatings,” *Prog. Mater. Sci.*, vol. 46, pp. 505–553, 2001.

[9] D. Stover and C. Funke, “Directions of the development of thermal barrier coatings in energy applications,” *J. Mater. Process. Technol.*, vol. 92–93, pp. 195–202, 1999.

[10] E. Dongmo, R. Gadow, A. Killinger, and M. Wenzelburger, “Modeling of combustion as well as heat, mass, and momentum transfer during thermal spraying by HVOF and HVSFS,” *J. Therm. Spray Technol.*, vol. 18, pp. 896–908, 2009.

[11] E. Bemporad, G. Bolelli, V. Cannillo, D. De Felicis, R. Gadow, A. Killinger, L. Lusvarghi, J. Rauch, and M. Sebastiani, “Structural characterisation of High-Velocity Suspension Flame Sprayed (HVSFS) TiO2 coatings,” *Surf. Coatings Technol.*, vol. 204, pp. 3902–3910, 2010.

[12] G. Bolelli, V. Cannillo, R. Gadow, A. Killinger, L. Lusvarghi, and J. Rauch, “Properties of High-Velocity Suspension Flame Sprayed (HVSFS) TiO2 coatings,” *Surf. Coatings Technol.*, vol. 203, pp. 1722–1732, 2009.

[13] A. Killinger, M. Kuhn, and R. Gadow, “High-Velocity Suspension Flame Spraying (HVSFS), a new approach for spraying nanoparticles with hypersonic speed,” *Surf. Coatings Technol.*, vol. 201, pp. 1922–1929, 2006.

[14] E. Dongmo, A. Killinger, M. Wenzelburger, and R. Gadow, “Numerical approach and optimization of the combustion and gas dynamics in High-Velocity Suspension Flame Spraying (HVSFS),” *Surf. Coatings Technol.*, vol. 203, pp. 2139–2145, 2009.

[15] G. Bolelli, V. Cannillo, R. Gadow, A. Killinger, L. Lusvarghi, J. Rauch, and M.

Romagnoli, “Effect of the suspension composition on the microstructural properties of high-velocity suspension flame sprayed (HVSFS) Al2O3 coatings,” *Surf. Coatings Technol.*, vol. 204, pp. 1163–1179, 2010.

[16] R. Gadow, A. Killinger, and J. Rauch, “Introduction to high-velocity suspension flame spraying (HVSFS),” *J. Therm. Spray Technol.*, vol. 17, pp. 655–661, 2008.

[17] J. Rauch, G. Bolelli, A. Killinger, R. Gadow, V. Cannillo, and L. Lusvarghi, “Advances in High-Velocity Suspension Flame Spraying (HVSFS),” *Surf. Coatings Technol.*, vol. 203, pp. 2131–2138, 2009.

[18] E. Dongmo, M. Wenzelburger, and R. Gadow, “Analysis and optimization of the HVOF process by combined experimental and numerical approaches,” *Surf. Coatings Technol.*, vol. 202, pp. 4470–4478, 2008.

[19] S. C. Kamnis, “Development of multiphase and multiscale mathematical models for thermal spray process,” Aston University, 2007.

[20] S. Kamnis and S. Gu, “Numerical modelling of propane combustion in a high-velocity oxygen–fuel thermal spray gun,” *Chem. Eng. Process. Process Intensif.*, vol. 45, pp. 246–253, 2006.

[21] S. Kamnis and S. Gu, “3-D modelling of kerosene-fuelled HVOF thermal spray gun,” *Chem. Eng. Sci.*, vol. 61, pp. 5427–5439, 2006.

[22] M. Li and P. D. Christofides, “Multi-scale modeling and analysis of an industrial HVOF thermal spray process,” *Chem. Eng. Sci.*, vol. 60, no. 13, pp. 3649–3669, 2005.

[23] M. Li, D. Shi, and P. D. Christofides, “Diamond Jet hybrid HVOF thermal spray: Gas-Phase and particle behavior modeling and feedback control design,” *Ind. Eng. Chem. Res.*, vol. 43, pp. 3632–3652, 2004.

[24] M. Li and P. D. Christofides, “Modeling and control of high-velocity oxygen-fuel (HVOF) thermal spray: A tutorial review,” *J. Therm. Spray Technol.*, vol. 18, pp. 753–768, 2009.

[25] H. Tabbara and S. Gu, “Computational simulation of liquid-fuelled HVOF thermal spraying,” *Surf. Coat. Technol.*, vol. 204, pp. 676–684, 2009.

[26] S. Gu, C. N. Eastwick, K. A. Simmons, D. G. McCartney, G. McCartney, and D. G. McCartney, “Computational fluid dynamic modelling of gas flow characteristics in a high-velocity oxy-fuel thermal spray system,” *J. Therm. Spray Technol.*, vol. 10, pp. 461–469, 2001.

[27] S. Kamnis, S. Gu, T. J. Lu, and C. Chen, “Computational simulation of thermally sprayed WC-Co powder,” *Comput. Mater. Sci.*, vol. 43, pp. 1172–1182, 2008.

[28] S. Kamnis, S. Gu, and N. Zeoli, “Mathematical modelling of Inconel 718 particles in HVOF thermal spraying,” *Surf. Coatings Technol.*, vol. 202, pp. 2715–2724, 2008.

[29] N. Zeoli, S. Gu, and S. Kamnis, “Numerical simulation of in-flight particle oxidation during thermal spraying,” *Comput. Chem. Eng.*, vol. 32, pp. 1661–1668, 2008.

[30] S. Basu, E. H. Jordan, and B. M. Cetegen, “Fluid mechanics and heat transfer of liquid precursor droplets injected into high-temperature plasmas,” *J. Therm. Spray Technol.*, vol. 17, pp. 60–72, 2008.

[31] A. Ozturk and B. M. Cetegen, “Modeling of plasma assisted formation of precipitates in zirconium containing liquid precursor droplets,” *Mater. Sci. Eng. A*, vol. 384, pp. 331–351, 2004.

[32] S. Basu and B. M. Cetegen, “Modeling of thermo-physical processes in liquid ceramic precursor droplets injected into a plasma jet,” *Int. J. Heat Mass Transf.*,

vol. 50, pp. 3278–3290, 2007.

[33] B. M. Cetegen and S. Basu, “Review of modeling of liquid precursor droplets and particles injected into plasmas and high-velocity oxy-fuel (HVOF) flame jets for thermal spray deposition applications,” *J. Therm. Spray Technol.*, vol. 18, pp. 769–793, 2009.

[34] S. Basu and B. M. Cetegen, “Modeling of liquid ceramic precursor droplets in a high-velocity oxy-fuel flame jet,” *Acta Mater.*, vol. 56, pp. 2750–2759, 2008.

[35] D. Chen, E. H. Jordan, and M. Gell, “The solution precursor plasma spray coatings: Influence of solvent type,” *Plasma Chem. Plasma Process.*, vol. 30, pp. 111–119, 2010.

[36] C. Marchand, C. Chazelas, G. Mariaux, and A. Vardelle, “Liquid precursor plasma spraying: modeling the interactions between the transient plasma jet and the droplets,” *J. Therm. Spray Technol.*, vol. 16, pp. 705–712, 2007.

[37] A. Vardelle, C. Chazelas, C. Marchand, and G. Mariaux, “Modeling time-dependent phenomena in plasma spraying of liquid precursors,” *Pure Appl. Chem.*, vol. 80, pp. 1981–1991, 2008.

[38] K. Saha and B. M. Cetegen, “Modeling of precipitate formation in solution precursor droplets in a microwave plasma,” *J. Therm. Spray Technol.*, vol. 21, pp. 211–225, 2012.

[39] H.-B. Xiong and J.-Z. Lin, “Nanoparticles modeling in axially injection suspension plasma spray of Zirconia and Alumina ceramics,” *J. Therm. Spray Technol.*, vol. 18, pp. 887–895, 2009.

[40] P. Fauchais, M. Vardelle, S. Goutier, and A. Vardelle, “Key Challenges and Opportunities in Suspension and Solution Plasma Spraying,” *Plasma Chem Plasma Process*, vol. 35, pp. 511–525, 2015.

[41] P. L. Fauchais, J. V. R. Heberlein, and M. I. Boulos, *Thermal spray fundamentals: From powder to part*. London: Springer, 2014.

[42] P. Fauchais and G. Montavon, “Latest developments in suspension and liquid precursor thermal spraying,” *J. Therm. Spray Technol.*, vol. 19, no. 1–2, pp. 226–239, 2010.

[43] G. Bertolissi, C. Chazelas, G. Bolelli, L. Lusvarghi, M. Vardelle, and A. Vardelle, “Engineering the microstructure of solution precursor plasma-sprayed coatings,” *J. Therm. Spray Technol.*, vol. 21, pp. 1148–1162, 2012.

[44] E. H. Jordan, L. Xie, M. Gell, N. P. Padture, B. Cetegen, A. Ozturk, J. Roth, T. D. Xiao, and P. E. C. Bryant, “Superior thermal barrier coatings using solution precursor plasma spray,” *J. Therm. Spray Technol.*, vol. 13, pp. 57–65, 2004.

[45] M. Gell, E. H. Jordan, M. Teicholz, B. M. Cetegen, N. P. Padture, L. Xie, D. Chen, X. Ma, and J. Roth, “Thermal barrier coatings made by the solution precursor plasma spray process,” *J. Therm. Spray Technol.*, vol. 17, pp. 124–135, 2008.

[46] A. Saha, S. Seal, B. Cetegen, E. Jordan, A. Ozturk, and S. Basu, “Thermo-physical processes in cerium nitrate precursor droplets injected into high-temperature plasma,” *Surf. Coatings Technol.*, vol. 203, pp. 2081–2091, 2009.

[47] R. Vassen, A. Stuke, and D. Stöver, “Recent developments in the field of thermal barrier coatings,” *J. Therm. Spray Technol.*, vol. 18, pp. 181–186, 2009.

[48] E. Meillot, S. Vincent, C. Caruyer, D. Damiani, and J. P. Caltagirone, “Modelling the interactions between a thermal plasma flow and a continuous liquid jet in a suspension spraying process,” *J. Phys. D. Appl. Phys.*, vol. 46, p. 224017, 2013.

[49] E. Meillot, R. Vert, C. Caruyer, D. Damiani, and M. Vardelle, “Manufacturing

nanostructured YSZ coatings by suspension plasma spraying (SPS): effect of injection parameters," *J. Phys. D. Appl. Phys.*, vol. 44, p. 194008, 2011.

[50] P. Fauchais and A. Vardelle, "Solution and suspension plasma spraying of nanostructure coatings," in *Advanced Plasma Spray Applications*, J. Hamid, Ed. 2012, pp. 149–188.

[51] S. Noppakun, *Solution precursor plasma spray system*. Springer, 2014.

[52] O. Tingaud, R. Etchart-Salas, V. Rat, J.-F. Coudert, H. Ageorges, A. Grimaud, and A. Denoirjean, "Suspension plasma spraying of Zirconia coatings: Process and coating structure," in *18th International Symposium on Plasma Chemistry, Kyoto: Japan*, 2007, pp. 0–3.

[53] P. Fauchais, V. Rat, C. Delbos, J. F. Coudert, T. Chartier, and L. Bianchi, "Understanding of suspension DC plasma spraying of finely structured coatings for SOFC," *IEEE Trans. Plasma Sci.*, vol. 33, pp. 920–930, 2005.

[54] J. Fazilleau, C. Delbos, V. Rat, J. F. Coudert, P. Fauchais, and B. Pateyron, "Phenomena involved in suspension plasma spraying part 1: Suspension injection and behavior," *Plasma Chem. Plasma Process.*, vol. 26, pp. 371–391, 2006.

[55] B. Pateyron, N. Calve, and L. Pawłowski, "Influence of water and ethanol on transport properties of the jets used in suspension plasma spraying," *Surf. Coatings Technol.*, vol. 220, pp. 257–260, 2013.

[56] A. Joulia, G. Bolelli, E. Gualtieri, L. Lusvarghi, S. Valeri, M. Vardelle, S. Rossignol, and A. Vardelle, "Comparing the deposition mechanisms in suspension plasma spray (SPS) and solution precursor plasma spray (SPPS) deposition of yttria-stabilised zirconia (YSZ)," *J. Eur. Ceram. Soc.*, vol. 34, pp. 3925–3940, 2014.

[57] A. Vardelle, C. Moreau, N. J. Themelis, and C. Chazelas, "A Perspective on Plasma Spray Technology," *Plasma Chem. Plasma Process.*, pp. 491–509, 2014.

[58] R. Rampon, F. L. Toma, G. Bertrand, and C. Coddet, "Liquid plasma sprayed coatings of Yttria-Stabilized Zirconia for SOFC electrolytes," *J. Therm. Spray Technol.*, vol. 15, pp. 682–688, 2006.

[59] C. Delbos, J. Fazilleau, V. Rat, J. F. Coudert, P. Fauchais, and B. Pateyron, "Phenomena involved in suspension plasma spraying part 2: Zirconia particle treatment and coating formation," *Plasma Chem. Plasma Process.*, vol. 26, pp. 393–414, 2006.

[60] F. Tarasi, M. Medraj, A. Dolatabadi, J. Oberste-Berghaus, and C. Moreau, "Effective parameters in axial injection suspension plasma spray process of Alumina-Zirconia ceramics," *J. Therm. Spray Technol.*, vol. 17, pp. 685–691, 2008.

[61] C. Marchand, A. Vardelle, G. Mariaux, and P. Lefort, "Modelling of the plasma spray process with liquid feedstock injection," *Surf. Coatings Technol.*, vol. 202, pp. 4458–4464, 2008.

[62] R. Rampon, C. Filiatre, and G. Bertrand, "Suspension plasma spraying of YPSZ coatings: suspension atomization and injection," *J. Therm. Spray Technol.*, vol. 17, pp. 105–114, 2008.

[63] L. Pawlowski, "Suspension and solution thermal spray coatings," *Surf. Coatings Technol.*, vol. 203, pp. 2807–2829, 2009.

[64] A. Killinger, R. Gadow, G. Mauer, A. Guignard, R. Vaßen, D. Stöver, R. Vaben, D. Stöver, R. Vaen, and D. Stöver, "Review of new developments in suspension

and solution precursor thermal spray processes," *J. Therm. Spray Technol.*, vol. 20, pp. 677–695, 2011.

[65] D. Chen, E. H. Jordan, and M. Gell, "Effect of solution concentration on splat formation and coating microstructure using the solution precursor plasma spray process," *Surf. Coatings Technol.*, vol. 202, pp. 2132–2138, 2008.

[66] S. Govindarajan, R. O. Dusane, and S. V. Joshi, "In situ particle generation and splat formation during solution precursor plasma spraying of yttria-stabilized zirconia coatings," *J. Am. Ceram. Soc.*, vol. 94, pp. 4191–4199, 2011.

[67] A. Ozturk and B. M. Cetegen, "Experiments on ceramic formation from liquid precursor spray axially injected into an oxy-acetylene flame," *Acta Mater.*, vol. 53, pp. 5203–5211, 2005.

[68] N. Espallargas, *Future development of thermal spray coatings: Types, designs, manufacture and applications*, 1st ed. London: Elsevier Ltd, 2015.

[69] P. Fauchais, G. Montavon, R. S. Lima, and B. R. Marple, "Engineering a new class of thermal spray nano-based microstructures from agglomerated nanostructured particles, suspensions and solutions: an invited review," *J. Phys. D. Appl. Phys.*, vol. 44, p. 093001, 2011.

[70] J. O. Berghaus, J. G. Legoux, C. Moreau, R. Hui, C. Decès-Petit, W. Qu, S. Yick, Z. Wang, R. Maric, and D. Ghosh, "Suspension HVOF spraying of reduced temperature solid oxide fuel cell electrolytes," *J. Therm. Spray Technol.*, vol. 17, pp. 700–707, 2008.

[71] N. Stiegler, D. Bellucci, G. Bolelli, V. Cannillo, R. Gadow, A. Killinger, L. Lusvarghi, and A. Sola, "High-velocity suspension flame sprayed (HVSFS) hydroxyapatite coatings for biomedical applications," *J. Therm. Spray Technol.*, vol. 21, pp. 275–287, 2012.

[72] J. O. Berghaus and B. R. Marple, "High-Velocity Oxy-Fuel (HVOF) suspension spraying of mullite coatings," *J. Therm. Spray Technol.*, vol. 17, pp. 671–678, 2008.

[73] R. Gadow, A. Killinger, and J. Rauch, "New results in high-velocity suspension flame spraying (HVSFS)," *Surf. Coatings Technol.*, vol. 202, pp. 4329–4336, 2008.

[74] G. Bolelli, J. Rauch, V. Cannillo, A. Killinger, L. Lusvarghi, and R. Gadow, "Microstructural and tribological investigation of high-velocity suspension flame sprayed (HVSFS) Al2O3 coatings," *J. Therm. Spray Technol.*, vol. 18, pp. 35–49, 2009.

[75] M. Jadidi, S. Moghtadernejad, and A. Dolatabadi, "Numerical Modeling of Suspension HVOF Spray," *J. Therm. Spray Technol.*, no. DECEMBER, pp. 1–14, 2015.

[76] X. Q. Ma, J. Roth, D. W. Gandy, and G. J. Frederick, "A new High-Velocity Oxygen Fuel process for making finely structured and highly bonded Inconel alloy layers from liquid feedstock," *J. Therm. Spray Technol.*, vol. 15, pp. 670–675, 2006.

[77] J. Puranen, J. Laakso, M. Kylmälahti, and P. Vuoristo, "Characterization of high-velocity solution precursor flame-sprayed manganese cobalt oxide spinel coatings for metallic sofc interconnectors," *J. Therm. Spray Technol.*, vol. 22, pp. 622–630, 2013.

[78] D. Chen, E. H. Jordan, and M. Gell, "Solution precursor high-velocity oxy-fuel spray ceramic coatings," *J. Eur. Ceram. Soc.*, vol. 29, pp. 3349–3353, 2009.

[79] F.-L. Toma, G. Bertrand, D. Klein, C. Meunier, and S. Begin, "Development of

photocatalytic active TiO2 surfaces by thermal spraying of nanopowders," *J. Nanomater.*, vol. 2008, pp. 1–8, 2008.

[80] G. E. Kim, J. Falzon, J. Walker, F. Michael, and P. Nikki, "Use of nano-particle Titanium Dioxide (n-TiO2) thermal spray coatings for abrasion resistance in severe service applications," in *International Titanium Association*, 2010.

[81] A. Koutsomichalis, N. M. Vaxevanidis, A. Vencl, and P. Psyllaki, "Mechanical and wear behaviour of Titania plasma-sprayed coatings," in *Proceedings of the 11th International Conference "THE-A" Coatings in Manufacturing Engineering*, 2014, pp. 185–191.

[82] R. Yilmaz, A. O. Kurt, A. Demir, and Z. Tatli, "Effects of TiO2 on the mechanical properties of the Al2O3-TiO2 plasma sprayed coating," *J. Eur. Ceram. Soc.*, vol. 27, pp. 1319–1323, 2007.

[83] A. Ibrahim, R. S. Lima, C. C. Berndt, and B. R. Marple, "Fatigue and mechanical properties of nanostructured and conventional titania (TiO2) thermal spray coatings," *Surf. Coatings Technol.*, vol. 201, pp. 7589–7596, 2007.

[84] R. Roest, A. J. Atanacio, B. A. Latella, R. Wuhrer, and B. Ben-Nissan, "An investigation of sol gel coated zirconia thin films on anodised titanium substrate by secondary ion mass spectrometry and scanning electron microscopy," *Mater. Forum*, vol. 31, pp. 160–163, 2007.

[85] V. Thakare, "Progress in synthesis and applications of Zirconia," *Int. J. Eng. Res. Dev.*, vol. 5, pp. 25–28, 2012.

[86] T. Rudin, K. Wegner, and S. E. Pratsinis, "Uniform nanoparticles by flame-assisted spray pyrolysis (FASP) of low cost precursors," *J. Nanoparticle Res.*, vol. 13, pp. 2715–2725, 2011.

[87] L. Mädler and S. E. Pratsinis, "Bismuth oxide nanoparticles by Flame Spray Pyrolysis," *J. Am. Ceram. Soc.*, vol. 85, pp. 1713–1718, 2002.

[88] S. Tanvir and L. Qiao, "Surface tension of Nanofluid-type fuels containing suspended nanomaterials," *Nanoscale Res. Lett.*, vol. 7, p. 226, 2012.

[89] R. H. Perry and D. W. Green, *Perry's Chemical Engineers' Handbook*, 7th ed. McGraw-Hill, 1997.

[90] P. Fauchais, A. Joulia, S. Goutier, C. Chazelas, M. Vardelle, A. Vardelle, and S. Rossignol, "Suspension and solution plasma spraying," *J. Phys. D. Appl. Phys.*, vol. 46, p. 224015, 2013.

[91] A. Ozturk and B. M. Cetegen, "Morphology of ceramic particulates formed in a premixed oxygen/acetylene flame from liquid precursor droplets," *Acta Mater.*, vol. 53, pp. 2531–2544, 2005.

[92] L. Liu, M. Fu, and J. Wu, "The distribution of SMD downstream the discharge orifices of effervescent atomizers," *J. Eng. Thermophys.*, vol. 22, pp. 653–656, 2001.

[93] L. Qian, J. Lin, and H. Xiong, "A fitting formula for predicting droplet mean diameter for various liquid in effervescent atomization spray," *J. Therm. Spray Technol.*, vol. 19, pp. 586–601, 2010.

[94] J. D. Whitlow and A. H. Lefevbre, "Effervescent atomizer operation and spray characteristics," *At. Sprays*, vol. 3, pp. 137 – 155, 1993.

[95] R. A. Castleman, "The mechanism of the atomization of liquids," *Bur. Stand. J. Res.*, vol. 6, pp. 369–376, 1930.

[96] J. C. Lasheras, E. Villermaux, and E. J. Hopfinger, "Break-up and atomization of a round water jet by a high-speed annular air jet," *J. Fluid Mech.*, vol. 357, pp. 351–379, 1998.

[97] A. H. Lefebvre, X. F. Wang, and C. A. Martin, “Spray characteristics of aerated-liquid pressure atomizers,” *J. Propuls. Power*, vol. 4, pp. 293–298, 1988.

[98] T. C. Roesler and A. H. Lefebvre, “Studies on aerated-liquid atomization,” *International Journal of Turbo and Jet Engines*, vol. 6. pp. 221–230, 1989.

[99] L. Qian, J. Lin, and H. Xiong, “Simulation of droplet-gas flow in the effervescent atomization spray with an impinging plate,” *Chinese J. Chem. Eng.*, vol. 17, pp. 8–19, 2009.

[100] S. D. Sovani, P. E. Sojka, and A. H. Lefebvre, “Effervescent atomization,” *Prog. Energy Combust. Sci.*, vol. 27, pp. 483–521, 2001.

[101] L. Qian and J. Lin, “Modeling on effervescent atomization: A review,” *Sci. China Physics, Mech. Astron.*, vol. 54, pp. 2109–2129, 2011.

[102] J. Jedelsky, M. Jicha, J. Slama, and J. Otahal, “Development of an effervescent atomizer for industrial burners,” *Energy and Fuels*, vol. 23, pp. 6121–6130, 2009.

[103] M. T. Lund, P. E. Sojka, A. H. Lefebvre, and P. G. Gosselin, “Effervescent atomization at low mass flow rates. Part I: The influence of surface tension,” *At. Sprays*, vol. 3, pp. 77–89, 1993.

[104] L. Qian, J. Lin, H. Xiong, and T. Leung Chan, “Theoretical investigation of the influence of liquid physical properties on effervescent atomization performance,” *J. Fluids Eng.*, vol. 133, p. 101205, 2011.

[105] J. Lin, L. Qian, and H. Xiong, “Relationship between deposition properties and operating parameters for droplet onto surface in the atomization impinging spray,” *Powder Technol.*, vol. 191, pp. 340–348, 2009.

[106] S. A. Esfarjani and A. Dolatabadi, “A 3D simulation of two-phase flow in an effervescent atomizer for suspension plasma spray,” *Surf. Coatings Technol.*, vol. 203, pp. 2074–2080, 2009.

[107] S. A. Esfarjani, “Numerical simulation of two-phase flow in an effervescent atomizer for nano-suspension spray,” Concordia University, 2008.

[108] H. B. Xiong, L. J. Qian, and J. Z. Lin, “Simulation of effervescent atomization and nanoparticle characteristics in radio frequency suspension plasma spray,” *J. Therm. Spray Technol.*, vol. 21, pp. 226–239, 2012.

[109] J. Broukal and J. Hájek, “Validation of an effervescent spray model with secondary atomization and its application to modeling of a large-scale furnace,” *Appl. Therm. Eng.*, vol. 31, pp. 2153–2164, 2011.

[110] H. Xiong, J. Lin, and Z. Zhu, “Three dimensional simulation of effervescent atomization spray,” *At. Sprays*, vol. 19, pp. 75–90, 2009.

[111] J. Schröder, M. Schlender, P. E. E. Sojka, V. Gaukel, and H. P. P. Schuchmann, “Modeling of drop sizes from effervescent atomization of gelatinized starch suspensions,” in *ILASS – Europe 2010, 23rd Annual Conference on Liquid Atomization and Spray Systems*, 2010, pp. 1–7.

[112] R. D. Reitz and F. V. Bracco, “Mechanism of atomization of a liquid jet,” *Phys. Fluids*, vol. 25, pp. 1730–1742, 1982.

[113] R. D. Reitz, “Mechanisms of atomization processes in high-pressure vaporizing sprays,” *At. Spray Technol.*, vol. 3, pp. 309–337, 1987.

[114] M. C. Fung, K. Inthanvong, W. Yang, and J. Tu, “Experimental and numerical modelling of nasal spray atomisation,” in *Ninth International Conference on CFD in the Minerals and Process Industries*, 2012, pp. 1–6.

[115] E. Gozali, M. Mahrukh, S. Gu, and S. Kamnis, “Numerical analysis of multicomponent suspension droplets in high-velocity flame spray process,” *J.*

*Therm. Spray Technol.*, vol. 23, pp. 940–949, 2014.

[116] E. Gozali, S. Kamnis, and S. Gu, “Numerical investigation of combustion and liquid feedstock in high-velocity suspension flame spraying process,” *Surf. Coatings Technol.*, vol. 228, pp. 176–186, 2013.

[117] E. Gozali, S. Kamnis, and S. Gu, “Analysis of liquid feedstock behavior in High-Velocity Suspension Flame Spraying for the development of nanostructured coatings,” in *Proceedings of the International Thermal Spray Conference*, 2013, pp. 418–423.

[118] N. Zeoli, S. Gu, and S. Kamnis, “Numerical modelling of metal droplet cooling and solidification,” *Int. J. Heat Mass Transf.*, vol. 51, pp. 4121–4131, 2008.

[119] E. Gozali, M. Mahrukh, S. Gu, and S. Kamnis, “Numerical investigation on effects of nanoparticles on liquid feedstock behavior in High-Velocity Oxygen Fuel (HVOF) suspension spraying,” *Surf. Coatings Technol.*, vol. 280, pp. 370–377, 2015.

[120] Ansys, “Ansys fluent theory guide.” SAS IP, Inc., pp. 1–735, 2012.

[121] C. Li, H. Yang, and H. Li, “Effect of gas conditions on HVOF flame and properties of WC-Co coatings,” *Materials and Manufacturing Processes*, vol. 14. pp. 383–395, 1999.

[122] C. Li and Y. Wang, “Effect of particle state on the adhesive strength of HVOF sprayed metallic coating,” *J. Therm. Spray Technol.*, vol. 11, pp. 523–529, 2002.

[123] Y. Wang, C. Li, and G. Yang, “Effect of flame conditions on abrasive wear performance of HVOF sprayed nanostructured WC-12Co coatings,” *Trans. Nonferrous Met. Soc. China*, vol. 14, pp. 72–76, 2004.

[124] P. L. Davis, A. T. Rinehimer, and M. Uddin, “A comparison of RANS-based turbulence modeling for flow over a wall-mounted square cylinder,” in *20th Annual Conference, CFD Society of Canada, Canmore*, 2012.

[125] M. Jadidi, S. Moghtadernejad, and A. Dolatabadi, “A comprehensive review on fluid dynamics and transport of suspension/liquid droplets and particles in High-Velocity Oxygen-Fuel (HVOF) thermal spray,” *Coatings*, vol. 5, pp. 576–645, 2015.

[126] B. E. Launder and D. B. Spalding, *Lectures in mathematical models of turbulence*. London: Academic press, 1972.

[127] B. P. Stephen, *Turbulent flows*. Cambridge university press, 2001.

[128] K. M. Saqr and M. A. Wahid, “Comparison of four Eddy-Viscosity Turbulence Models in the Eddy Dissipation Modeling of Turbulent Diffusion Flames,” *Int. J. Appl. Math Mech.*, vol. 7, pp. 1–18, 2011.

[129] F. R. Menter, “Two-equation eddy-viscosity turbulence models for engineering applications,” *AIAA J.*, vol. 32, pp. 1598–1605, 1994.

[130] M. Taleby and S. Hossainpour, “Numerical investigation of high-velocity suspension flame spraying,” *J. Therm. Spray Technol.*, vol. 21, pp. 1163–1172, 2012.

[131] B. McBride and S. Gordon, “Computer program for calculation of complex chemical equilibrium compositions and applications II. users manual and program description,” 1996.

[132] B. F. Magnussen and B. H. Hjertager, “On mathematical models of turbulent combustion with special emphasis on soot formation and combustion,” in *16th Symposium on Combustion.The Combustion Institute*, 1976, vol. 16, pp. 719–729.

[133] B. F. Magnussen, “The eddy dissipation concept: A bridge between science and technology,” *Proc. ECCOMAS Themat. Conf. Comput. Combust. , Lisbon*, 2005.

[134] K. K. Kuo, *Principles of combustion*, 2nd ed. John Wiley & Sons, Inc., 1986.

[135] K. Fukumoto and Y. Ogami, “Simulation of CO-H2-Air turbulent nonpremixed flame using the eddy dissipation concept model with lookup table approach,” *J. Combust.*, vol. 2012, pp. 1–11, 2012.

[136] H. Tabbara and S. Gu, “A study of liquid droplet disintegration for the development of nanostructured coatings,” *AIChE J.*, vol. 58, pp. 3533–3544, 2012.

[137] D. Hu, “Comparison of numerical and experimental results of four liquid spray combustors,” Louisiana State University and Agriculture and Mechanical College, 2002.

[138] P. M. Bovat, “Computational analysis of water atomization in spray desuperheaters of steam boilers,” Rensselaer Polytechnic Institute, 2013.

[139] S. Morsi and A. Alexander, “An investigation of particle trajectories in two-phase flow systems,” *J. Fluid Mech*, vol. 55, pp. 193–208, 1972.

[140] A. Haider and O. Levenspiel, “Drag coefficient and terminal velocity of spherical and nonspherical particles,” *Powder Technol.*, vol. 58, pp. 63–70, 1989.

[141] M. Pilch and C. A. Erdman, “Use of breakup time data and velocity history data to predict the maximum size of stable fragments for acceleration-induced breakup of a liquid drop,” *Int. J. Multiph. Flow*, vol. 13, no. 6, pp. 741–757, 1987.

[142] W. E. Ranz and W. R. Marshall, “Evaporation from drops. Part I,” *Chem. Eng. Prog.*, vol. 48, p. 141, 1952.

[143] W. E. Ranz and W. R. Marshall, “Evaporation from drops. Part II,” *Chem. Eng. Prog.*, vol. 48, p. 173, 1952.

[144] V. V. Sobolev, J. M. Guilemany, and J. Nutting, “Gas-Particle interactions during spraying,” in *High Velocity Oxy-Fuel Spraying Theory, Structure-Property Relationships and Applications*, J. Shrikant, Ed. W. S. Maney and Son Ltd, 2004, pp. 29–61.

[145] V. V. Sobolev, J. M. Guilemany, J. C. Garmier, and J. A. Calero, “Modelling of particle movement and thermal behaviour during high-velocity oxy-fuel spraying,” *Surf. Coatings Technol.*, vol. 63, pp. 181–187, 1994.

[146] J. Marchal, T. John, R. Baranwal, T. Hinklin, and R. M. Laine, “Yttrium aluminum garnet nanopowders produced by Liquid-Feed Flame Spray Pyrolysis (LF-FSP) of metalloorganic precursors,” *Chem. Mater.*, vol. 16, pp. 822–831, 2004.

[147] S. Jain, D. J. Skamser, and T. T. Kodas, “Morphology of single-component particles produced by spray pyrolysis,” *Aerosol Sci. Technol.*, vol. 27, pp. 575–590, 1997.

[148] T. Hinklin, B. Toury, C. Gervais, F. Babonneau, J. J. Gislason, R. W. Morton, and R. M. Laine, “Liquid-Feed flame spray pyrolysis of metalloorganic and inorganic Alumina sources in the production of nanoalumina powders,” *Chem. Mater.*, vol. 16, pp. 21–30, 2004.

[149] R. Mahadevan, D. Lee, H. Sakurai, and M. R. Zachariah, “Measurement of condensed-phase reaction kinetics in the aerosol phase using single particle mass spectrometry,” *J. Phys. Chem. A*, vol. 106, pp. 11083–11092, 2002.

[150] C. Li, G. Yang, and Z. Wang, “Formation of nanostructured TiO2 by flame spraying with liquid feedstock,” *Mater. Lett.*, vol. 57, pp. 2130–2134, 2003.

[151] K. S. Shannon and B. W. Butler, “A review of error associated with thermocouple

temperature measurement in fire environments," *Int. Wildl. Fire Ecol.*, pp. 7–9, 2003.

[152] C. Suryanarayana and B. Prabhu, "Synthesis of nanostructured materials by inert-gas condensation methods," in *Nanostructured Materials: Processing, Properties, and Applications*, 2nd ed., C. K. Carl, Ed. William Andrew, Inc., 2007, pp. 47–90.

[153] A. J. Gröhn, S. E. Pratsinis, S.-F. Antoni, M. Raffaele, and K. Wegner, "Scale-up for nanoparticle synthesis by flame spray pyrolysis : The high-temperature particle residence time," *Ind. Eng. Chem. Res.*, vol. 53, pp. 10734–10742, 2014.

[154] A. J. Gröhn, S. E. Pratsinis, and K. Wegner, "Fluid-particle dynamics during combustion spray aerosol synthesis of ZrO2," *Chem. Eng. J.*, vol. 191, pp. 491–502, 2012.

[155] F. E. Kruis, K. A. Kusters, S. E. Pratsinis, and B. Scarlett, "A simple model for the evolution of the characteristics of aggregate particles undergoing coagulation and sintering," *Aerosol Sci. Technol.*, vol. 19, pp. 514–526, 1993.

[156] D. Shi, M. Li, and P. D. Christofides, "Diamond Jet hybrid HVOF thermal spray: Rule-Based modeling of coating microstructure," *Ind. Eng. Chem. Res.*, vol. 43, pp. 3653–3665, 2004.

[157] M. Li and P. D. Christofides, "Computational study of particle in-flight behavior in the HVOF thermal spray process," *Chem. Eng. Sci.*, vol. 61, pp. 6540–6552, 2006.

[158] E. Gozali, S. Kamnis, and S. Gu, "Numerical investigation of combustion and liquid feedstock in high velocity suspension flame spraying process," *Surf. Coatings Technol.*, vol. 228, pp. 176–186, 2013.

[159] P. K. Senecal, D. P. Schmidt, I. Nouar, C. J. Rutland, R. D. Reitz, and M. L. Corradini, "Modeling high-speed viscous liquid sheet atomization," *Int. J. Multiph. Flow*, vol. 25, pp. 1073–1097, 1999.

[160] N. Dombrowski and P. C. Hooper, "The effect of ambient density on drop formation in sprays," *Chem. Eng. Sci.*, vol. 17, pp. 291–305, 1962.

[161] C. Weber, "Zum Zerfall eines Flüssigkeitsstrahles," *J. Appl. Math. Mech. / Zeitschrift für Angew. Math. und Mech.*, vol. 11, pp. 136–154, 1931.

[162] P. J. O'Rourke, "Collective drop effects on vaporizing liquid sprays," Princeton University, 1981.

[163] X. F. Wang, J. S. Chin, and A. H. Lefebvre, "Influence of gas-injector geometry on atomization performance of aerated-liquid nozzles," *International Journal of Turbo and Jet Engines*, vol. 6. pp. 271–279, 1989.

[164] B. Breaux and B. Rouge, "The effect of elevated water content on ethanol combustion," Louisiana State University, Baton Rouge, Louisiana, 2012.

[165] P. Fauchais, R. Etchart-Salas, V. Rat, J. F. Coudert, N. Caron, and K. Wittmann-Ténèze, "Parameters controlling liquid plasma spraying: solutions, sols, or suspensions," *J. Therm. Spray Technol.*, vol. 17, pp. 31–59, 2008.

[166] F.-O. Bartz, D. R. Guildenbecher, R. Schmehl, R. Koch, H.-J. Bauer, and P. E. Sojka, "Model comparison for single droplet fragmentation under varying accelerations," in *ILASS – Europe 2011, 24th European Conference on Liquid Atomization and Spray Systems*, 2011.

[167] S. S. Sazhin, "Advanced models of fuel droplet heating and evaporation," *Prog. Energy Combust. Sci.*, vol. 32, pp. 162–214, 2006.

[168] Y. Xuan and W. Roetzel, "Conceptions for heat transfer correlation of nanofluids," *Int. J. Heat Mass Transf.*, vol. 43, pp. 3701–3707, 2000.

[169] D. A. Drew and S. L. Passman, *Theory of multicomponent fluids*, vol. 135. New York: Springer, 1999.

[170] A. Einstein, “Investigations on the theory of the Brownian movement,” *Ann. Phys.*, vol. 17, p. 549, 1905.

[171] M. Moosavi, E. K. Goharshadi, and A. Youssefi, “Fabrication, characterization, and measurement of some physicochemical properties of ZnO nanofluids,” *Int. J. Heat Fluid Flow*, vol. 31, pp. 599–605, 2010.

[172] S. S. Hosseini, A. Shahrjerdi, and Y. Vazifeshenas, “A review of relations for physical properties of nanofluids,” *Aust. J. Basic Appl. Sci.*, vol. 5, pp. 417–435, 2011.

[173] S. M. S. Murshed, K. C. Leong, and C. Yang, “Investigations of thermal conductivity and viscosity of nanofluids,” *Int. J. Therm. Sci.*, vol. 47, pp. 560–568, 2008.

[174] S. H. Kim, S. R. Choi, and D. Kim, “Thermal conductivity of metal-oxide nanofluids: Particle size dependence and effect of Laser irradiation,” *J. Heat Transfer*, vol. 129, p. 298, 2007.

[175] S. M. S. Murshed, K. C. Leong, and C. Yang, “Enhanced thermal conductivity of TiO2—water based nanofluids,” *Int. J. Therm. Sci.*, vol. 44, pp. 367–373, 2005.

[176] B. X. Wang, L. P. Zhou, and X. F. Peng, “A fractal model for predicting the effective thermal conductivity of liquid with suspension of nanoparticles,” *Int. J. Heat Mass Transf.*, vol. 46, pp. 2665–2672, 2003.

[177] R. H. Chen, T. X. Phuoc, and D. Martello, “Effects of nanoparticles on nanofluid droplet evaporation,” *Int. J. Heat Mass Transf.*, vol. 53, pp. 3677–3682, 2010.

[178] P. González-Tello, F. Camacho, J. M. Vicaria, and P. A. González, “A modified Nukiyama-Tanasawa distribution function and a Rosin-Rammler model for the particle-size-distribution analysis,” *Powder Technol.*, vol. 186, pp. 278–281, 2008.

[179] A. G. Bailey, W. Balachandran, and T. J. Williams, “The Rosin-Rammler size distribution for liquid droplet ensembles,” *J. Aerosol Sci.*, vol. 14, pp. 39–46, 1983.

[180] R. A. Mugele and H. D. Evans, “Droplet size distribution in sprays,” *Ind. Eng. Chem.*, vol. 43, pp. 1317–1324, 1951.

[181] G. Bolelli, V. Cannillo, R. Gadow, A. Killinger, L. Lusvarghi, and J. Rauch, “Processing and characterisation of high-velocity suspension flame sprayed (HVSFS) bioactive glass coatings,” *Ceram. - Silikaty*, vol. 54, pp. 1–7, 2010.

# APPENDICES

# Appendix A : Different Injection Types and Instruments used in the Nanoparticles Synthesis in SP-HVOFS process (Chapter 4)

## A.1 Liquid feedstock injection nozzles design

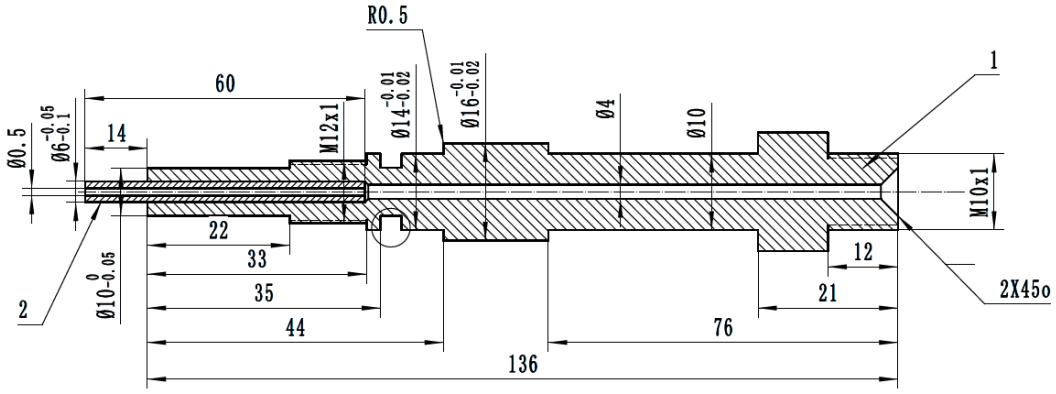


**Figure A-1** Liquid Feedstock injection plain-orifice nozzle N1, original design [Not to scale]

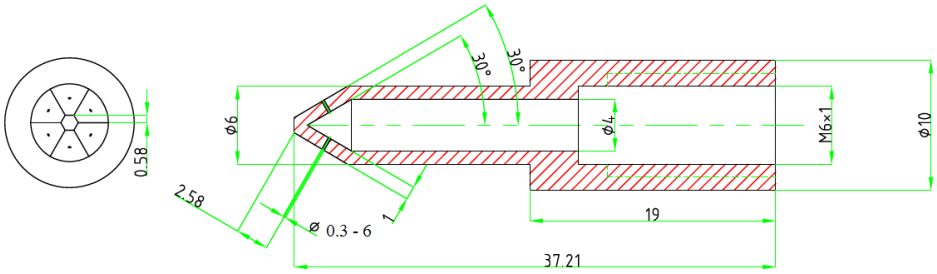


**Figure A-2** Liquid Feedstock angular injection nozzle N2, modified old nozzle with new angular head design [Not to scale]

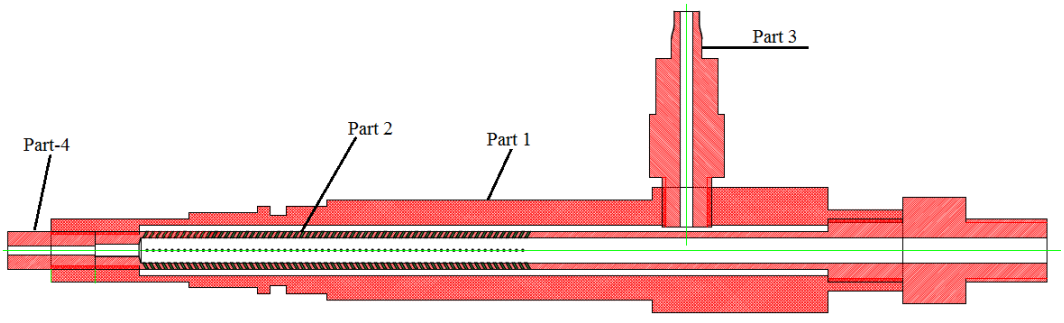


(a)

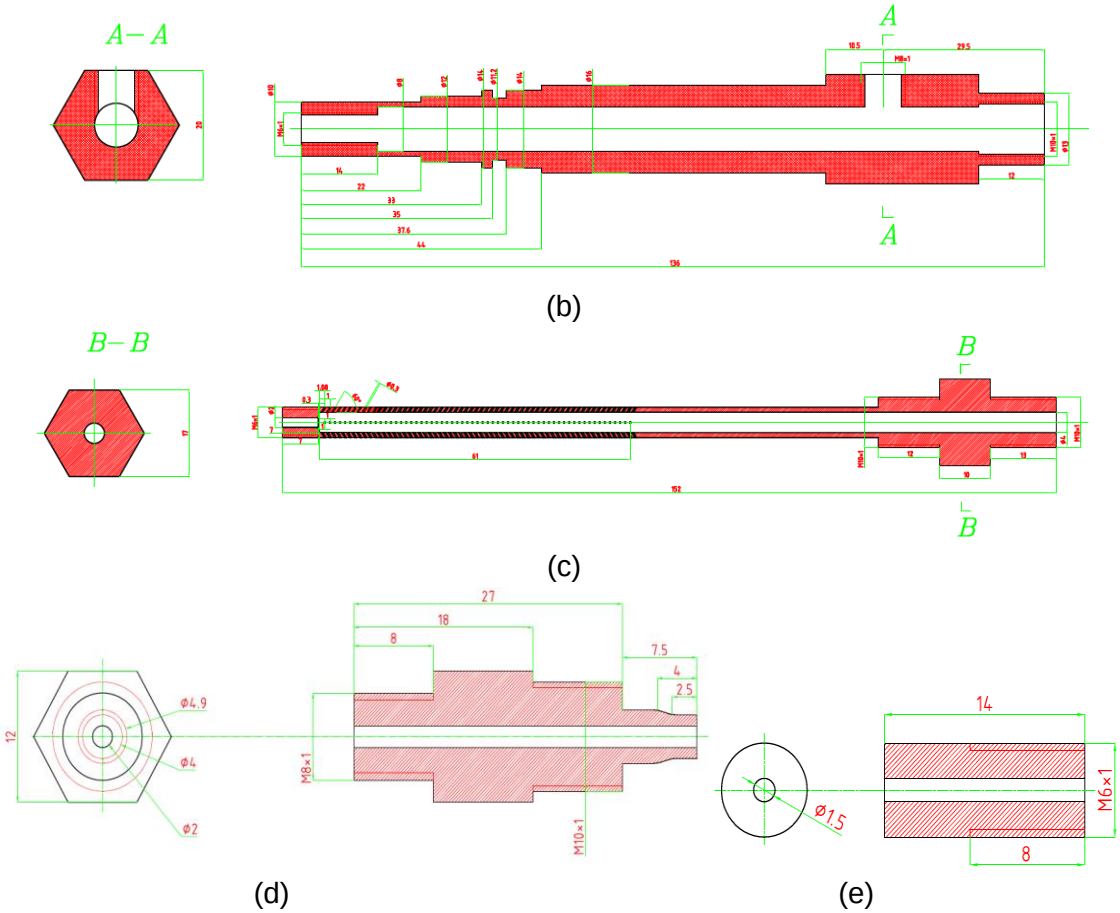


**Figure A-3** Liquid Feedstock injection (a) New effervescent nozzle N3, assembled (b) Part 1, (c) Part 2, (d) Part 3 and (e) Part 4 [Not to scale]

## A.2 CH-2000 Torch Geometry

**Figure A-4** CH-2000 torch (Original look)

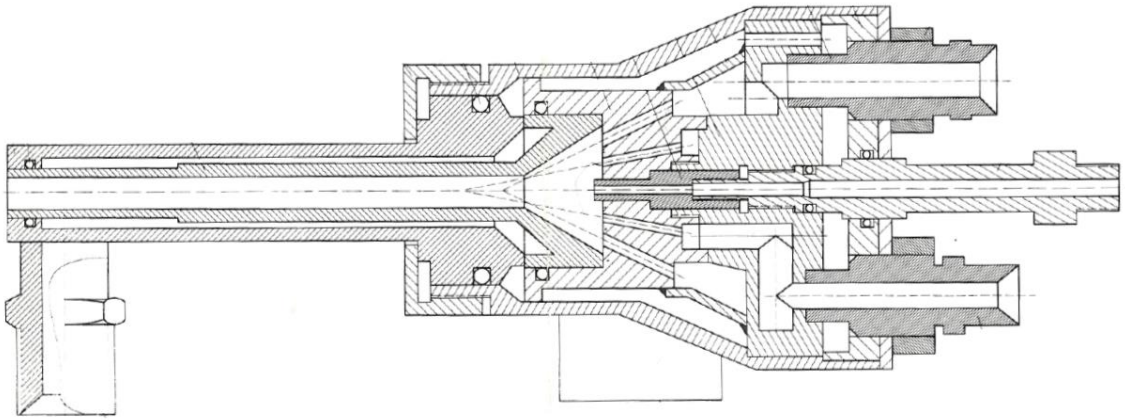

(a)

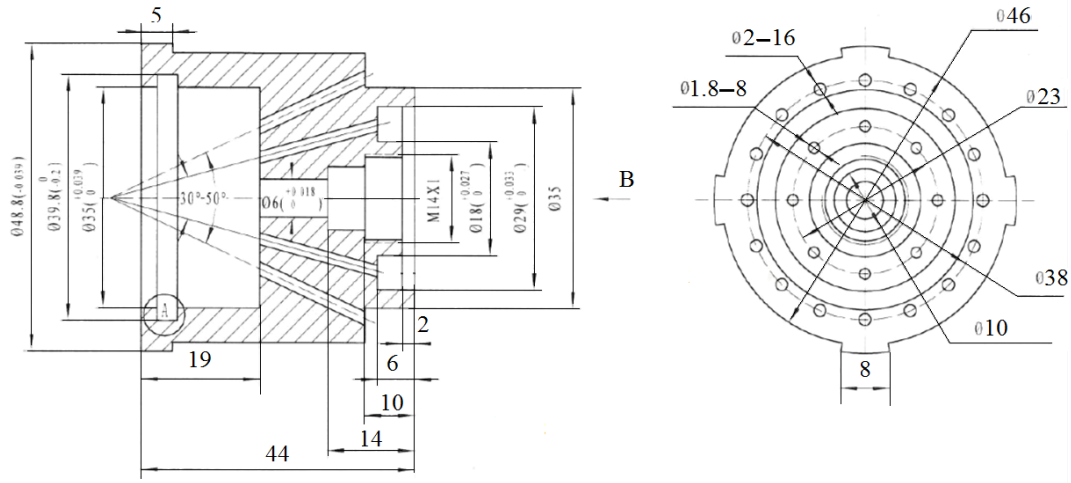


(b)

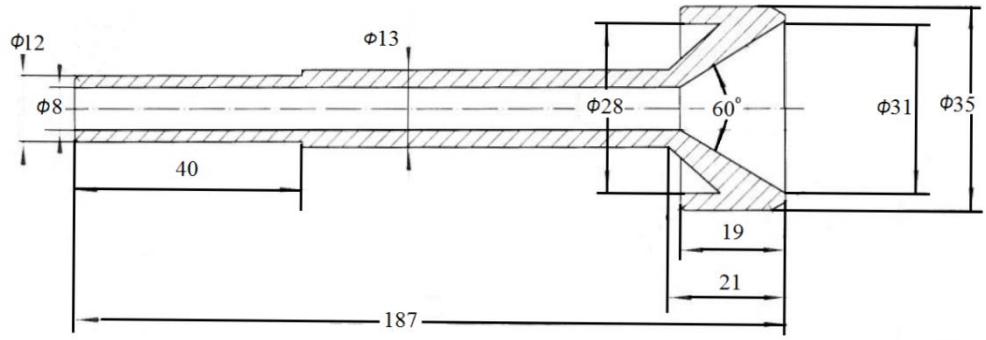


(c)

**Figure A-5** CH-2000 HVOF torch (a) torch and gas supply head assembled, (b) the CH-2000 head with oxygen, fuel and carrier gas inlets and (c) CH-2000 torch [Not to scale]

## A.3 The Instruments used during the Experiments


**Figure A-6** Oxygen and fuel flow rate controller for CH-2000 torch


**Figure A-7** Liquid feedstock injection pump

**Figure A-8** Substrate's grinding/-polishing equipment (AutoMet 250- Buehler)

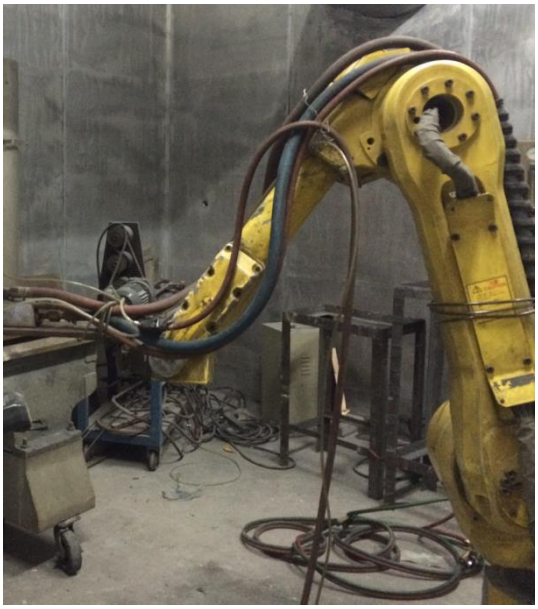

**Figure A-9** Automatic controller for the HVOF CH-2000 torch (the Moto-man)

### A.3.1 The instruments used in nanoparticles size and morphology analysis

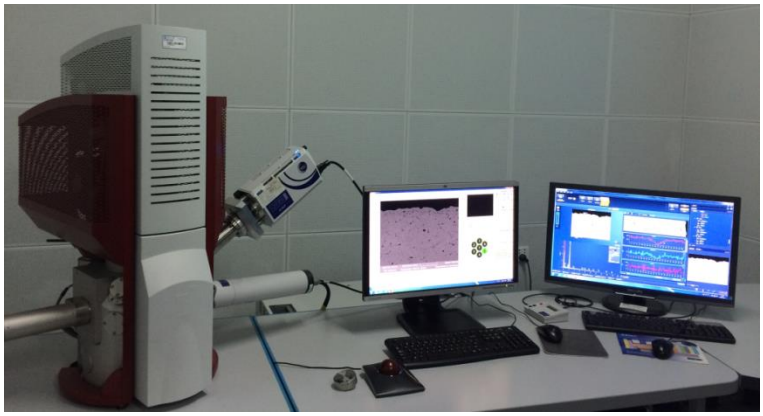

**Figure A-10** Scanning Electron Microscope (SEM) system

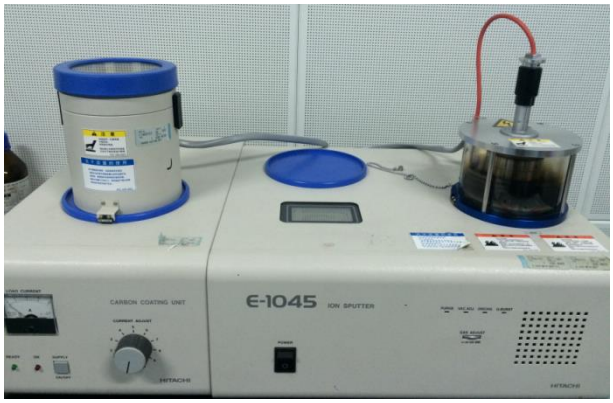


**Figure A-11** Ion Sputter